



## **Quantitative fluorescence microscopy for studying peptide transport and optimizing localization with structured illumination**

**Hundahl, Adam Coln**

*Publication date:*  
2022

*Document Version*  
Publisher's PDF, also known as Version of record

[Link back to DTU Orbit](#)

*Citation (APA):*  
Hundahl, A. C. (2022). *Quantitative fluorescence microscopy for studying peptide transport and optimizing localization with structured illumination*. DTU Health Technology.

---

### **General rights**

Copyright and moral rights for the publications made accessible in the public portal are retained by the authors and/or other copyright owners and it is a condition of accessing publications that users recognise and abide by the legal requirements associated with these rights.

- Users may download and print one copy of any publication from the public portal for the purpose of private study or research.
- You may not further distribute the material or use it for any profit-making activity or commercial gain
- You may freely distribute the URL identifying the publication in the public portal

If you believe that this document breaches copyright please contact us providing details, and we will remove access to the work immediately and investigate your claim.

**DTU Health Tech**  
Department of Health Technology

---

# **Quantitative fluorescence microscopy for studying peptide transport and optimizing localization with structured illumination**

Adam Coln Hundahl



**Supervisor:** Associate Professor Rodolphe Marie  
**Co-supervisors:** Assistant Professor Jannik Larsen

DTU Sundhedsteknologi  
Department of Health Technology  
Technical University of Denmark  
Ørsteds Plads  
Building 345B  
2800 Kongens Lyngby, Denmark

# Preface

---

The work done in this thesis was carried out at the Technical University of Denmark at the Department of Health Technology (DTU Health Tech). Associate Professor Rodolphe Marie was the primary supervisor, with Senior Researcher Kim Mortensen as co-supervisor. During the project, Assistant Professor Jannik Bruun Larsen joined as co-supervisor. All supervisors were from DTU Health Tech.

The Ph.D. project was done at DTU Health Tech from February 2019 to May 2022, besides a short external research stay in November 2021 at the University of Southern Denmark (SDU) at Eva Arnsparng Christensen's lab.

The Ph.D. was funded by the Novo Nordisk Foundation Challenge Programme (NNF16OC0022166). The Ph.D. was a part of the Novo Nordisk Center for Intestinal Absorption and Transport of Biopharmaceuticals (CitBIO) at the Technical University of Denmark, Department of Health Technology.





# Abstract

---

There is an increasing interest in oral administered biopharmaceuticals due to the high customer compliance. However, the bioavailability is only 1 – 2 % due to natural barriers, such as the intestinal barrier, protecting us from foreign molecules entering the cardiovascular system. Understanding the transport of drugs across barriers could help design novel drugs with higher bioavailability. However, cellular interaction with a drug can be complex and happen differently. For example, the transport can happen across a cell layer through active transportation involving biological processes, such as endocytosis. Alternatively, the drug can undergo passive transportation where diffusion dictates the transport.

Often, the investigation of drug transport through a cell layer is in systems that do not allow for imaging or tracking the drug, limiting the mechanistic insight into the transport of the drug. However, fluorescence microscopy offers an alternative way of investigating several biological problems by linking fluorescent dyes to the drug and possibly to cellular organelles. Here, two types of experiments can gain a mechanistic understanding of drug transport.

One type of experiment focuses on tracking single molecules over time. Here it is crucial to localize the molecule with the best precision possible to more accurately determine the interactions between the molecule and, e.g., cellular compartments. A recent approach to improve the localization precision is structured illumination microscopy. A second type of experiment quantifies drug amounts in various cellular compartments using single-cell analysis. A preferred microscope for single-cell analysis is a spinning disk confocal microscope.

The first part of the thesis deals with a novel method to improve the localization of single molecules. I first build an experimental setup that, combined with data analysis from collaborators, can localize fluorophores more precisely than conventional methods, such as camera-based localization microscopy. The structured illumination came from using a digital micro-mirror device as a spatial light modulator. As a proof-of-concept, single-bead and single-molecule samples were used to calibrate the structured illumination, achieving a structured illumination with a sinusoidal pattern with a period of approximately 230 nm and a modulation depth of 0.9. An alternative setup with non-harmonic structured illumination gave a period of roughly 400 nm and a modulation depth of 0.75. Ultimately, this led to an increase in precision localization of 2.1x and 1.3x, respectively.

The second part of the thesis addresses the challenges of quantifying peptide

transport through a monolayer of Caco-2 cells by developing a method to quantify peptides' transport by single-cell analysis by deconvoluting the axial intensity signal obtained by a spinning disk confocal microscope. The method was used to show that the lipidation of salmon calcitonin with two C8 lipid chains increases the transport significantly by a factor of 2.6x. The method was also used to gain mechanistic insight showing that the lipidation with two C4 lipid chains alters the transport mechanism of salmon calcitonin to a non-dynamin dependent process.

In the future perspective, combining the two types of experiments would extract the most amount of information possible in one experiment. A lattice light-sheet microscope would be able to facilitate that as it has structured illumination and is very suitable for live-cell imaging.

In conclusion, the results showed that the lipidation of salmon calcitonin significantly increases the transport of the peptide across a monolayer. Furthermore, we showed that optimal structured illumination could achieve a more than two-fold precision on localization.

# Resumé

---

Der er mange forskellige måder, at indtage medicin på, men den fortrukne metode er at indtage medicin oralt. Der er til gengæld det problem at kun 1 – 2 % af den indtagne medicin bliver optaget i blodstrømmen. Dette er fordi vi i kroppen har nogle naturlige barrierer, som beskytter os mod ikke-genkendte molekyler. Sådanne barriere er, for eksempel, tarmen, og ved at forstå hvordan molekyler bevæger sig igennem tarmbarrieren, kan man designe ny medicin med højere optag i blodstrømmen. Der er mere end én måde hvorpå medicin kan blive optaget igennem tarmen. Optaget kan ske ved aktiv transport af molekylet igennem tarmen ved brug af biologiske processer såsom endocytose. En anden måde hvorpå tarmen kan optage medicin er igennem passiv diffusion.

Når man vil undersøge om molekylet har den ønskede virkning og bliver transporteret igennem barrieren, benytter man sig oftest af nogle simple systemer som efterligner tarmen. Disse systemer består af celler som bliver groet i et enkelte lag som da virker som en barriere. Der er dog nogle begrænsninger ved disse systemer, da man oftest ikke kan tage billeder i høj opløsning af cellerne. Derfor er informationen begrænset til hvor meget der bliver transporteret igennem og ikke hvordan det bliver transporteret igennem.

Et alternativ er at brug fluorescens mikroskopi ved, at sætte et farvestof på molekylet man undersøger. Efterfølgende kan man lave to forskellige typer af eksperimenter. I det ene forsøg følger man enkelte molekyler gennem cellerne. Ved denne type forsøg handler det om at kunne lokalisere molekylerne med høj præcision for at kunne vide hvad molekylerne interagerer med. En nyere metode til at undersøge dette er ved at udnytte struktureret belysning. I det andet eksperiment kan man analysere celler på enkelt celle niveau og derved kvantificere hvor meget af molekylet der befinder sig inde i cellen. Ved denne type eksperimenter vil man benytte sig af et mikroskop, som er så skånsomt som muligt overfor cellerne, såsom et "spinning disk" konfokal mikroskop.

I den første del af denne afhandling gennemgår jeg processen af at bygge en eksperimentel opstilling som kan lave struktureret belysning. Her vises der, at ved brug af struktureret belysning kan man øge præcisionen man lokaliserer enkelte molekyler med. Jeg demonstrer dette ved brug af to opstillinger. Den første opstilling producerer struktureret belysning, som er ikke-harmonisk og har en periode på omkring 400 nm, samt en kontrast på ca. 0.75. Den anden opstilling producerer struktureret belysning, der følger en sinuskurve. Denne opstilling har en periode på ca. 230 nm

samt en kontrast på 0.9. Ved at bruge denne metode til at lokalisere enkelte molekyler viser vi, at vi kan øge lokaliseringen med henholdsvis en faktor 1.3 og 2.1.

Den anden del af afhandlingen fokuserer på at udvikle en model til at kvantificere transport af medicin igennem individuelle celler i et cellelag. Transporten kvantificeres ved at udvikle en model der beskriver den lodrette intensitetsprofil i forhold til når man måler på celler ved brug af et "spinning disk" konfokal mikroskop. Jeg benytter denne model til at kvantificere transporten af *salmon calcitonin* som er blevet lipideret med to C8 fedtkæder. Ved at sætte to C8 fedtkæder på *salmon calcitonin* steg transporten med en faktor 2.6 sammenlignet med ikke-modificeret *salmon calcitonin*. Denne metode blev også brugt til at vise, at når man sætter to C4 fedtkæder på *salmon calcitonin*, ændres mekanismen som transporterer molekylet.

Disse to projekter ville være ideelle at sammenføre, da man ved brug af struktureret belysning kan lokalisere transporten af *salmon calcitonin* igennem cellerne med høj præcision. Et "lattice-light sheet" mikroskop ville være et godt værktøj til dette, da det både kan producere struktureret belysning, men også er skånsomt med belysning af cellerne, hvilket gør det ideelt til at bruge på levende celler.

I denne afhandling viser jeg at ved at lipidere *salmon calcitonin*, vil man øge transporten igennem et lag af celler med en faktor 2.6. Ydermere, viser jeg at ved at bruge struktureret belysning kan man øge den præcision man lokaliserer enkelte molekyler med en faktor 2.1.

# Acknowledgements

---

I would like to thank the Nanofluidics and Bioimaging group for great working environment and a special thank to my supervisors Rodolphe Marie, Kim Mortensen, and Jannik Bruun Larsen for giving me the opportunity to work with my Ph.D. in a very interesting field and for great discussions. Furthermore, I would like to thank Martin Schmidt for a great collaboration and discussions throughout my Ph.D.

I want to thank Eva Arnsparng Christensen for allowing me to come do my external research stay in her lab and use her equipment.

Lastly, I would like to thank the Novo Nordisk Foundation Challenge Programme (NNF16OC0022166) for funding my Ph.D. project.



# List of publications

---

1. M. Schmidt, **A. C. Hundahl**, H. Flyvbjerg, R. Marie & K. I. Mortensen  
*Camera-based localization microscopy optimized with calibrated structured illumination*  
Published in: Communications Physics, vol. 4, no. 1, pp. 1–10, 2021 [1]  
Reprinted in Appendix B.1  
Experimental work presented in Chapter 2
2. **A. C. Hundahl**, A. Weller, J. B. Larsen, C. U. Hjørringgaard, M. B. Hansen, A. Mündler, K. Kristensen, E. A. Christensen, T. L. Andresen, K. I. Mortensen & R. Marie  
*Quantitative imaging of lipidated peptides: Towards a mechanistic understanding of their transport through an epithelial cell layer*  
In preparation  
Printed in Appendix B.2  
Work presented in Chapter 3 & 4
3. A. Weller, M. B. Hansen, R. Marie, **A. C. Hundahl**, C. Hempel, P. J. Kempen, H. L. Frandsen, L. Parhamifar, T. L. Andresen & J. B. Larsen  
Submitted to Advanced Healthcare Materials (2022)  
Work not included in thesis.





# Contents

---

<b>Preface</b>	<b>i</b>
<b>Abstract</b>	<b>iii</b>
<b>Resumé</b>	<b>v</b>
<b>Acknowledgements</b>	<b>vii</b>
<b>List of publications</b>	<b>ix</b>
<b>Contents</b>	<b>xi</b>
<b>1 Introduction</b>	<b>1</b>
1.1 Oral Delivery of Pharmaceuticals . . . . .	1
1.1.1 Transport studies . . . . .	1
1.1.2 Uptake mechanisms . . . . .	3
1.1.3 Model systems to study peptide transport . . . . .	3
1.1.4 Techniques to study peptide transport . . . . .	5
1.2 Fluorescence Microscopy . . . . .	6
1.2.1 Diffraction limit . . . . .	6
1.2.2 Super resolution techniques and localization . . . . .	7
1.2.3 Confocal Microscopy . . . . .	8
1.2.4 Quantification with confocal Microscopy . . . . .	9
1.3 Outline of thesis . . . . .	12
<b>2 Structured illumination utilizing a digital micromirror device</b>	<b>15</b>
2.1 Introduction . . . . .	15
2.2 Optical Setup . . . . .	19
2.2.1 First iteration of the optical setup . . . . .	19
2.2.2 Second iteration of optical setup . . . . .	21
2.2.3 Summary . . . . .	23
2.3 Experimental procedure . . . . .	23
2.3.1 Sample Preparations . . . . .	24
2.3.2 Imaging procedure . . . . .	25

2.4	Results . . . . .	27
2.4.1	Structured Illumination without Blaze Conditions . . . . .	27
2.4.2	Structured Illumination with Blaze Conditions . . . . .	28
2.4.3	Summary . . . . .	30
<b>3</b>	<b>Quantitative Assay for Peptide Transport Using Spinning Disk Confocal Microscopy</b>	<b>31</b>
3.1	Characterization of Spinning Disk Confocal Microscopy for Live Cell Imaging . . . . .	31
3.1.1	Summary . . . . .	36
3.2	Quantification of atto488 in Solution . . . . .	37
3.3	Simple Cell Model for Transport Study . . . . .	39
3.3.1	Method and materials . . . . .	40
3.3.2	Deconvolution of Intensity Signal . . . . .	42
3.3.3	Verifying Cell Model and Fluorescence Model for Quantification of Cellular Transport . . . . .	47
3.3.3.1	Uptake of TAT . . . . .	47
3.3.3.2	Tight Junction Integrity . . . . .	49
3.3.4	Summary . . . . .	51
<b>4</b>	<b>Quantitative imaging of lipidated Salmon Calcitonin Transport through an Epithelial Cell Layer</b>	<b>53</b>
4.1	Single Cell Analysis of Lipidated Peptide Cellular Transport . . . . .	54
4.1.1	Salmon Calcitonin C0/C0 . . . . .	54
4.1.2	Salmon Calcitonin C4/C4 . . . . .	55
4.1.3	Salmon Calcitonin C8/C8 . . . . .	57
4.1.4	Summary . . . . .	58
4.2	Verifying transport is successful . . . . .	58
4.2.1	Initial intensity before adding peptide . . . . .	59
4.2.2	Disrupting barrier integrity . . . . .	60
4.2.3	Solution equilibrium over time . . . . .	62
4.2.4	Summary . . . . .	62
4.3	Comparison of the three analogs . . . . .	62
4.3.1	Summary . . . . .	66
4.4	Temperature Dependency & Clathrin Dependent endosomes . . . . .	66
4.4.1	Summary . . . . .	74
4.5	TIRF stepwise bleaching . . . . .	74
4.5.1	Summary . . . . .	83
4.6	Outlook & Perspective . . . . .	83
4.6.1	Quantification of transport using a microfluidic model . . . . .	83
4.6.2	Expanding the model . . . . .	84
4.6.3	Summary . . . . .	87

---

<b>Conclusion</b>	<b>89</b>
<b>Appendices</b>	<b>91</b>
<b>Appendix A Additional Figures</b>	<b>93</b>
<b>Appendix B Journal articles</b>	<b>99</b>
B.1 Camera-based localization microscopy optimized with calibrated structured illumination . . . . .	99
B.2 Quantitative imaging of lipidated peptides: Towards a mechanistic understanding of their transport through an epithelial cell layer . . . . .	110
<b>Bibliography</b>	<b>153</b>



# CHAPTER 1

# Introduction

---

## 1.1 Oral Delivery of Pharmaceuticals

Often, therapeutic drugs are administered through injection [2], a direct path into the bloodstream resulting in high bioavailability, defined as the fraction of drug that has effectively entered the cardiovascular system [3]. However, this complicates the consumption of the drug and lowers customer compliance [4]. Therefore, many other non-invasive administering routes have been explored, such as nasal, inhalation, or oral delivery [5] as alternatives to invasive consumption. Oral drug delivery has received much focus in the past decade due to its high patient compliance [6]. However, the bioavailability of drugs administered orally is still very suboptimal (around 1-2 %) partly due to the gastrointestinal epithelium that acts as a physical barrier that the drug needs to cross [7].

A drug enters the gastrointestinal tract after oral delivery, where most orally administered biopharmaceuticals are absorbed [8]. Therefore, the biopharmaceuticals must pass through the intestinal barrier consisting of two defense systems. The first is a mucus layer lining the epithelial cell layer, preventing foreign molecules from reaching the cells immediately [9]. The epithelial cell layer is the second defense consisting of a monolayer composed of several cell types. The cells form a monolayer by establishing several types of junctions with neighboring cells. The junctions work to either stabilize the integrity of the monolayer (adherens junctions and desmosomes) or to create a tight barrier preventing molecules from passing through the interface of two cells (tight junctions) [10] as seen in Figure 1.1B.

### 1.1.1 Transport studies

Ideally, an orally delivered drug should either cross the intestinal barrier by transport between cells or transport through the cells of the intestinal barrier and then be released in the cardiovascular system to pass the intestinal barrier successfully, as seen in Figure 1.1A. The peptide can pass through paracellularly (between two cells) and thus overcome tight junctions. Another alternative is that the peptide passes through the cell's apical membrane and exits on the basolateral membrane. This type of transport is known as transcellular transport.

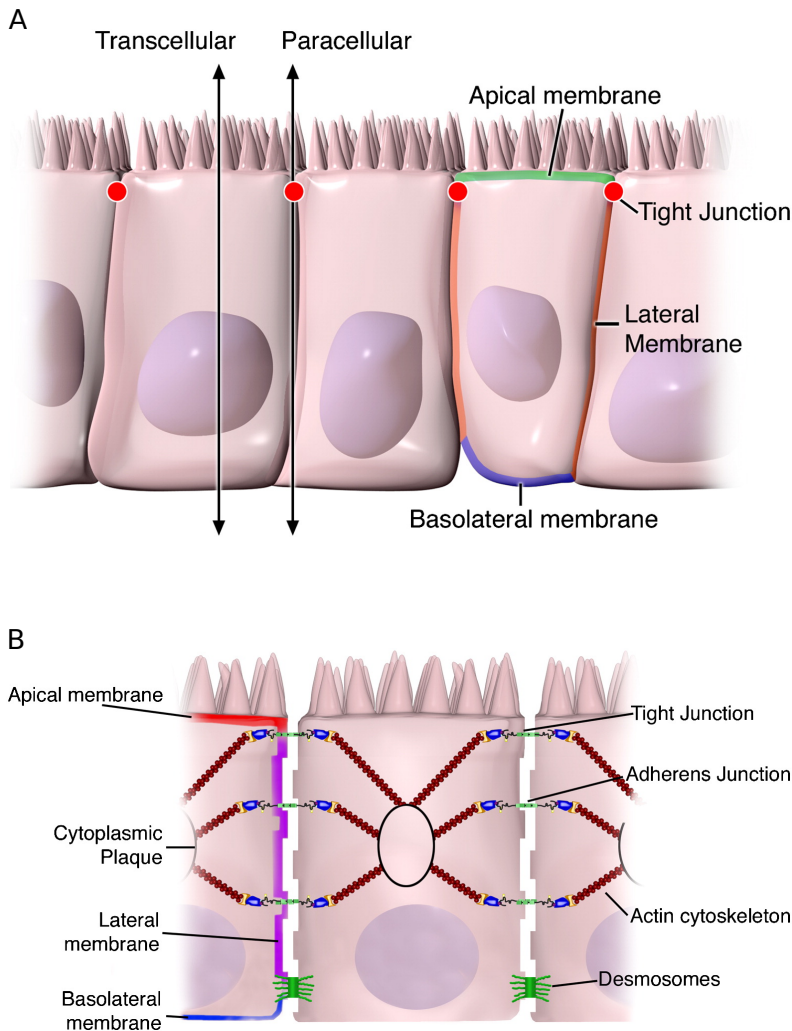


**Figure 1.1.** The structure and key functions of the cell intestinal barrier. A) Shows a cell layer where two transport pathways are highlighted. The transcellular pathway (transport through the cell) and the paracellular (transport between cells). The apical membrane of the cell layer is highlighted in green, the lateral membrane is highlighted in orange, and the basolateral membrane is highlighted in blue. Lastly, the tight junctions are marked as red dots. B) Shows a zoom in on the components in the cell layer. The tight junctions help prevent that every molecule passes through the cell layer. The adherens junction, actin cytoskeleton and desmosomes help keeping the integrity of the cell layer. The apical membrane is highlighted in red, lateral membrane in purple, and the basolateral membrane in blue. Figures are adapted from [10].

There are several ways of studying the transport of new drugs. One approach is a trial-and-error approach based on the quantification of bioavailabilities. However, an orthogonal approach is the *de novo* design of chemical modifications of the biopharmaceutical or a drug delivery scheme based on a mechanistic understanding of cellular transport.

### 1.1.2 Uptake mechanisms

Hence, in this context elucidating the transport mechanism that determines the fate of the drug is critical to optimizing its transport. Figure 1.2 shows some possible transport mechanisms, where two of them are passive. A passive transport mechanism does not require energy to transport across the cell layer. The driving force of the transport under passive transport is diffusion [11]. The other transport possibility is active transport, which is an energy-dependent pathway. Here, the transport happens by either a membrane protein acting as the peptide carrier through the cell. Another possibility is vesicle-mediated transport. In such a case, endocytosis might be the driving force of the transport of the peptide [12].

A common strategy to achieve transport from the gut to the blood or lymphatic system is to package the biopharmaceutical in nanoparticles. Doing so targets the uptake via the clathrin-mediated endocytosis [13]. Clathrin-mediated endocytosis is when cargo is packed into a vesicle with the help of clathrin and then transported into the cell [14]. Another approach is to use promoter molecules, and co-transport the molecule of interest [15, 16]. This is by utilizing the transport mechanism of proteins in the membrane to transport the protein of interest. An alternative route is to chemically modify the peptide with, e.g., polyethylene glycol (PEG) groups to protect the peptides and increase pharmacodynamics and pharmacokinetics [17]. However, recently another approach has proven successfully through the lipidation of peptides [18, 19] and particularly salmon Calcitonin [20] due to promoting interactions of the peptide with the cell membrane. One hypothesis is that partitioning the lipidated peptide to the cell membrane should increase the likelihood of uptake. The partitioning of peptides eventually leads to the subsequent release of the lipidated peptide into the cytosol and then on the basal membrane of the cell layer.

### 1.1.3 Model systems to study peptide transport

One way of quantifying the transport of biopharmaceuticals is *in vivo* because it provides live animal results. However, as an alternative, *in vitro* model systems are increasingly used because they shorten experiment time, reduce reagent consumption, thus increasing throughput, and circumvent costly and ethically debated use of model animals. Moreover, *in vitro* models may be suited to systematic studies toward the mechanistic understanding of transport. The human epithelial colorectal adenocarcinoma cell line (Caco-2) is an immortalized cell line. The Caco-2 cells often represent the cells of the gut epithelial in *in vitro* experiments [21]. Typically, a monolayer of



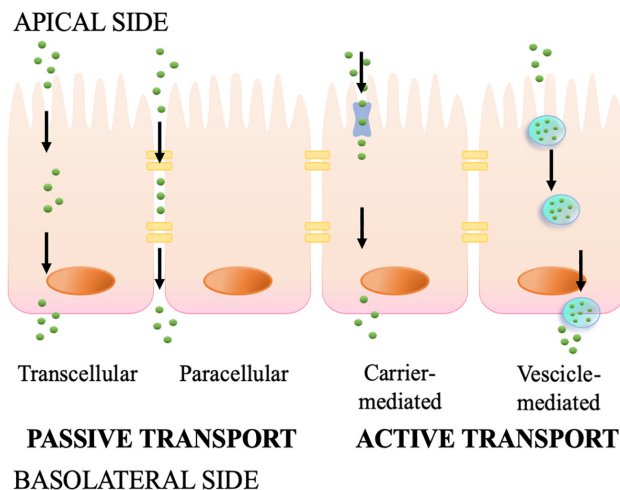


**Figure 1.2.** Showing the transport from the apical side to the basolateral side. Four different transport mechanisms are shown, two passive (no energy required) where the peptide transport across via diffusion through the transcellularly or paracellularly. Furthermore, two active (energy required) is shown where the peptide binds to, e.g., a receptor that mediates the transport, or the peptide is taken up by vesicles such as endosomes.

Figure adapted and modified from [11].

Caco-2 is cultured in a Transwell plate system as seen in Figure 1.3A to mimic the intestinal barrier. A porous membrane filter separates an apical chamber from the basolateral chamber in this system. The apical side is above the porous membrane, and the basolateral chamber is below. Cells typically grow for 18-21 days with media change every 1-2 days before the cells grow into a polarized monolayer with tight barriers [22]. Assessing the barrier integrity through an electrical measurement called TEER (transepithelial electrical resistance) confirms if the tight junctions are successfully made [23]. The tight junctions prevent diffusion freely between cells. Thus, they are a prerequisite to validating the uptake of biopharmaceuticals. However, the long cell culture time makes the experiment tedious and thus limits the applicability of the Transwell system for massive parallel studies and consequently leads to a trial-and-error approach to developing new drugs. Gupta et al. showed that growing Caco-2 cells in a Transwell plate system for as short as three days exhibit valid barrier integrity [24], which substantially increases the throughput of the Transwell plate system. The long wait for the cell to grow is something I try to address in this thesis by lowering the amount of days for the cells to grow into a monolayer, and also simplify the system.

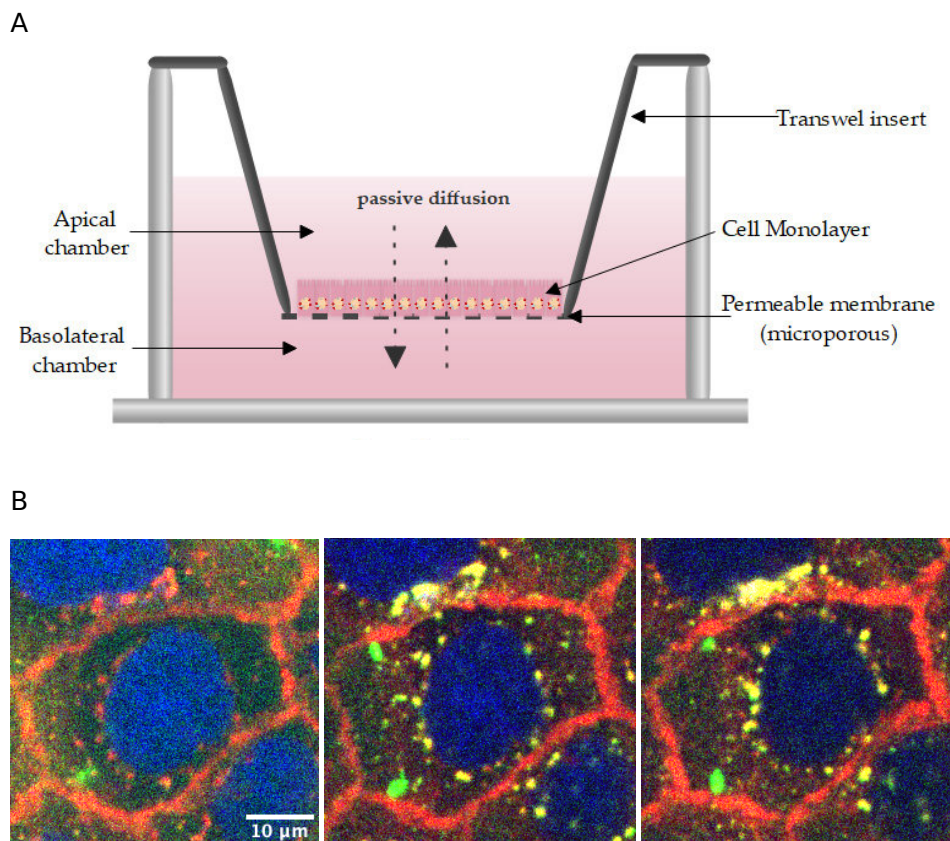


**Figure 1.3.** Two different examples experiments conducted for peptide transport. A) Shows a transwell system, where a cell monolayer is on top of a microporous permeable membrane inserted in a transwell insert. The insert is lowered into cell media where the peptide is added to the apical chamber. The peptide quantity is then measured on the basolateral chamber over time using various methods. Figure adapted and modified from [25]. B) Shows a single cell labelled with two different fluorophores. The red fluorophore labels the membrane and the blue labels the nucleus of the cell. The green spots represents the peptide added to the cells. The peptide is monitored over time.

#### 1.1.4 Techniques to study peptide transport

Once cells are cultured in the Transwell plate system, there are several methods to quantify the transport of biopharmaceuticals through the cell monolayer, such as mass spectrometry [26] and several other methods based on the detection of fluorescence, including ELISA [24]. By quantifying the amount of drug in the different compartments of the cells it can tell which transport mechanism is involved in an

uptake path. A compartment of the cell could be, e.g., the cytoplasm.

Fluorescence-activated cell sorting (FACS) [27] is a common tool used to investigate the cytosolic content of biopharmaceuticals by measuring the overall fluorescence signal of many individual cells. Extracting a fluorescence intensity distribution shows the intracellular content of a population of cells at a given time point. However, this method does not give information about the transport through a cell layer. Also, there is no information regarding the location of the biopharmaceutical in the cell.

## 1.2 Fluorescence Microscopy

To address the issue of a lack of qualitative information using a fluorescence microscope provides an alternative method. This method also relies on fluorescence and can give qualitative information regarding interactions with the biopharmaceuticals and organelles within the cell [28–30]. Figure 1.3B shows an example of using fluorescence microscopy to qualitatively show the uptake of a biopharmaceutical by single cells over time. It shows three different time points of the same cell. For each time point, it shows an increasing amount of the biopharmaceutical

As the intensity in an image is proportional to the amount of fluorophore, fluorescence microscopy can also provide quantitative information at the single-cell level and possibly at the single-molecule level, if appropriately utilized [31].

### 1.2.1 Diffraction limit

Imaging an isolated single molecule will produce a diffraction-limited spot. This happens because the signal from the fluorophore is convoluted with the PSF of the microscope. This means that the single molecule appears much bigger than it is in reality. The size of the diffraction limited spot depends proportionally on the emission wavelength and the numerical aperture of the objective. Abbe’s diffraction limit can estimate the resolution of the diffraction-limited spot [32], which states:

$$r = \frac{\lambda_{em}}{2NA} \quad (1.1)$$

Where  $\lambda_{em}$  is the wavelength of the emitted light of the fluorophore attached to the biopharmaceutical and NA is the numerical aperture of the objective. For a fluorophore with emission of  $\lambda_{em} = 500$  nm and an objective of  $NA = 1.45$ , the limited diffraction spot will be approximately 170 nm.

The radius of a protein, e.g., human growth hormone, is approximately 25 Å [33, 34], which is substantially smaller compared to the resolution of the diffraction limit. This would result in a single diffraction limited spot with the size of approximately 170 nm, but in reality the protein is much smaller. When only a few isolated molecules are present in a sample, the sample is a case of a sparsely labeled samples.

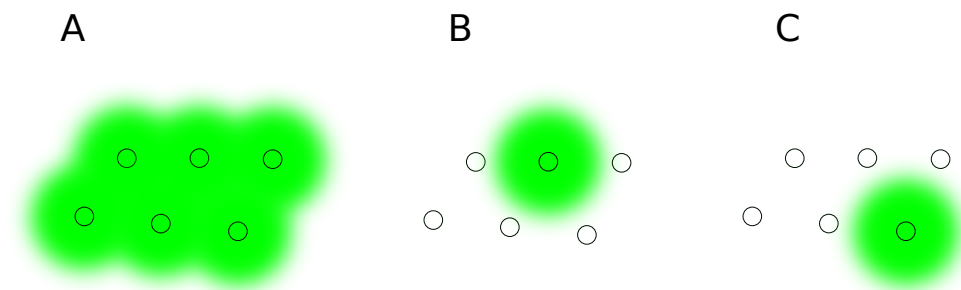


**Figure 1.4.** Diffraction limited spots when: A) six diffraction limited spots are closer than the diameter of the diffraction limited spot, hence it is not possible to resolve them. B) Shows when only one of the six fluorophores is emitting light. C) Shows when only one of the six fluorophores is emitting light, however, a different one compared to B).

### 1.2.2 Super resolution techniques and localization

In most cases, more than one molecule is close to one another, which is the case of densely labeled samples. Figure 1.4A shows an example where six molecules are closer than the diffraction limit. Hence they cannot be resolved individually but are perceived as one big unit. Fortunately, several techniques make it possible to overcome the diffraction limit. Such techniques are called super-resolution techniques and often rely on periodically turning on and off the fluorophores, such as Stochastic Optical Reconstruction Microscopy (STORM) [35, 36] and Photoactivated Localization Microscopy (PALM) [37–39]. Figure 1.4B and C shows two cases where two molecules emit at different times illustrating the blinking effect of turning the fluorophores on and off. Fitting all of the positions allows extracting a position estimate shown optimally by Mortensen et al. [40].

These methods are very harsh on the sample, so if the sample is, e.g., live cells it will cause phototoxicity. An alternative super-resolution method is structured illumination microscopy (SIM) [41, 42]. SIM is a technique capable of imaging at double the resolution and it is more suitable for live cell imaging [43] due to fewer exposure compared to STORM or PALM. However, the increase in resolution is less than STORM or PALM [44]. These techniques are all super resolution microscopy techniques and are great at resolving molecules with high resolution in densely labeled samples. However, it is a requisite that to resolve the structures, they do not move or drift during the experiment. As this thesis is about the transport of biopharmaceutical through cells, movement is needed for the transport to be successful. Therefore, instead of resolving the molecules at a high resolution one should track and localize them with high precision. Often when doing single molecule tracking it is advantages to have a sparsely labeled sample, or use a low concentration of drug [45, 46]. Furthermore, because of the moving drug it should be resolved with high temporal resolution and with low phototoxicity due to the live sample.

For unmatched precision it was showed recently that knowing the structure of the illumination source led to increased localization as seen with MINimal photon FLUXes (MINFLUX) [47–49]. For MINFLUX, the structure is a doughnut-shaped beam with minima in the doughnut’s center. Hence, if a fluorophore emits a few photons, it means that the fluorophore is near the doughnut’s center. Moving the doughnut beam around while recording the number of photons allows for localizing single molecules with very high precision [47].

MINFLUX opened up for a new field called Modulation Enhanced Localization microscopy (MELM) [50], where structured illumination enhances the precision of localization by optimizing the amount of information extracted per photon. In the case of MINFLUX, the structure is a doughnut structure. The drawback of MINFLUX is that it only tracks a single molecule at the time. However, recently numerous papers have utilized a sine wave as the structured illumination, as shown in ”repetitive optical selective exposure” [51], ROSE for short, ”structured illumination microscopy based point localization estimator” [52], SIMPLE for short, SIMFLUX [53], ”calibrated MELM” [1], C-MELM for short (experimental considerations explored in this thesis), and laser interference-based DMD-SIM (LiDMD-SIM) [54]. These methods have proven to enhance localization precision of multiple molecules simultaneously. The development of MELM with sine waves happened during my Ph.D project.

The structured illumination is made in many different ways, but creating the structured illumination by using a digital micromirror device (DMD) is a cheap and simple way, as shown in [1,52,54]. The DMD is a device with micromirrors that can be either turned ”on” or ”off”, which diffract incoming light in one of two directions. By configuring the DMD to have lines, it is possible to generate a structured illumination on the sample.

### 1.2.3 Confocal Microscopy

Regardless of how well we can localize single molecules, we still need an interesting system to work with, such as the transport of drugs in living cells. Fluorescence microscopy is a great tool to find interesting drug candidates for transport. There are many types of techniques that rely on fluorescence, but an often-used technique for live-cell imaging is confocal microscopy [55–57]. The confocal microscope works by focusing the light onto the sample. Furthermore, a pinhole is placed in front of the detector to reject light not from the focal point at the detector plane [58] as seen in the left image of Figure 1.5. For this type of confocal microscope it only detects one focal spot at a time. Hence the focal point is scanned across the live cell, leading to much exposure and, over time, might cause phototoxicity. This is a confocal laser scanning microscope (CLSM) [59]. Another type of confocal microscopy is the spinning disk confocal microscope (SDCM). This type of microscope also scans the sample, however it illuminates with multiple focal points simultaneously. The SDCM uses two spinning disks, one with lenses and one with pinholes (right image Figure 1.5) to excite and collect light from many focal points simultaneously. By collecting light from multiple

focal points at the same time it limits the phototoxicity toward the cells [60], but also increases imaging speed.

### 1.2.4 Quantification with confocal Microscopy

The confocal microscope is not a super resolution technique, which means during imaging fluorescently labeled molecules result in diffraction limited spots. The diffraction limited spot is a result of the point spread function. The lateral resolution of the diffraction limited spot is approximately 170 nm, whereas axial resolution is much larger, around 400 nm at a 500 nm excitation [61].

In an experiment of peptide transport through cells, the transport happens in the axial direction. Hence, during an imaging experiment, the transport is also quantified axially. Due to the low axial resolution, one should carefully quantify the fluorescence signal from the cytosol or around the cell membrane. The fluorescence signal from the cell surroundings significantly extends within the cell's interior and vice versa. Eventually, the signal from fluorescent molecules located outside the cell on both sides of the cell layer, i.e., the apical and basolateral sides, would overlap when the thickness of the cell approaches that of the size of the PSF, making data interpretation difficult. A way to mitigate this effect is by washing the cells after incubation with the drug. Removing the drug limits the amount of "contamination" in the signal in the cytosol from the solution. However, only an end-point measurement is possible in this case, thus failing to capture the uptake dynamics. Overcoming this by doing multiple experiments at different incubation times is cumbersome and time-consuming. So ideally, transport studies should be made via real-time live-cell imaging. Thus, in order to extract quantitative information from the intensity signal, it needs to be deconvoluted with the PSF [61]. The deconvolution of intensity signal has been used to quantify the fluorescence of puncta-like structures, typically in experiments where transport occurs via endosomes [62]. Still, little is put in to quantify the diffuse signal from the cell cytosol and the localized signal from the membrane [63].

In this thesis I worked on two projects with the ultimate goal of combining them into one. I wanted to combine increased localization utilizing MELM with an interesting molecule for peptide transport through cells. Therefore, in this thesis, I first showcase two different uses of a DMD first to produce non-harmonic and secondly produce harmonic structured illumination with the purpose of increasing localization precision. The first setup produces a non-harmonic structured illumination with three-beam interference (3BI). 3BI means that three beams entering the objective will interfere creating the structured illumination on the sample. Using 50 nm in diameter fluorescent beads allowed us to characterize the structured illumination by translating the beams across the illumination. The structured illumination had a period of approximately 400 nm with a modulation depth,  $C$ , of approximately 0.75.

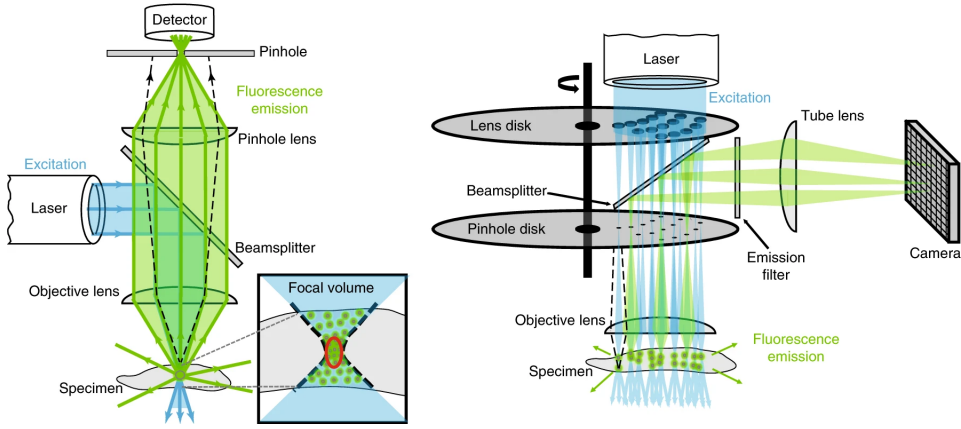


**Figure 1.5.** This figure shows two different confocal microscopes. The left image shows how a classic confocal microscope focuses light onto a sample and rejects out of focus light at the detector for a clear image. The right image shows a spinning disk confocal microscope. The light is passing through an array of microlenses and pinholes that focus multiple focal points onto the sample and reject any out of focus light at the detector. Figure adapted and modified from [58]

Defining the modulation depth as:

$$C = \frac{I_{max} - I_{min}}{I_{max} + I_{min}} \quad (1.2)$$

This simple expression for the modulation depth allowed for on-the-spot validation of the modulation depth at the microscope.

By characterizing the structured illumination, the bead was localized with a precision 1.3x better than camera-based localization. In the second setup, we controlled the beam's polarization more carefully, leading to a modulation depth of 0.9. Furthermore, the period of the second setup was only 230 nm. The low period of the structured illumination is due to blocking the central diffraction order from the DMD and controlling the polarization. Blocking the central diffraction order turned the setup into two-beam interference (2BI) structured illumination. 2BI refers to total internal reflection fluorescence structured illumination microscopy, TIRF-SIM [64]. TIRF is a great way to limit the power to just the surface of the sample but also to have a high signal-to-noise ratio [65–67].

Ultimately I wanted to use a lattice light sheet microscope (LLSM) to track the transport of drugs through cells. A LLSM is a microscope that illuminates an entire plane of a sample with very low phototoxicity, thus very great for live cell imaging. Furthermore, LLSM is capable of doing structured illumination microscopy [68]. Hence this would be the ideal setup to utilize the enhanced localization with C-MELM.

However, the LLS was not available at the time of my Ph.D. so I had to use a different microscope to study the peptide transport through cells. The best option I had available was a SDCM. Therefore, as the second part of my Ph.D. I developed a method to quantify the transport of peptides through a simple cell model. I did this by first measuring the PSF of the spinning disc microscope and then using it in combination with a simple physical model of the cell to interpret the fluorescence intensity of the cytosol, the cell membrane, and the transported molecule across the cell monolayer. Figure 1.6 shows the experimental setup for quantifying the transport of a peptide. Figure 1.6A shows how to do the typical experiment. The cells are grown for two days and labeled with a red membrane dye and a blue nucleus dye. After adding the peptide, the imaging begins. The imaging is done on a SDCM and captures multiple z-planes. We combine all z-planes, which results in a z-stack containing 3D information in time.

Figure 1.6B-D show sketches of the intensity profiles extracted from a single cell. Figure 1.6B shows the membrane intensity profile. Here it shows two peaks representing the bottom and top membrane of a cell by acquiring the z-stack from below the cells to above the cells. The dotted lines represent the center position of the peaks. The grey area represents the PSF of the SDCM. Figure 1.6C shows a sketch of the peptide intensity profile from below the cell, through the cell, and into the solution. The peptide intensity signal can be deconvoluted to extract the contribution from every part of the z-stack, e.g., the glass, cytosol, and the solution. The sum of these contributions is the total peptide intensity signal. The vertical dotted lines represent where the position of the membranes, and the grey shaded area is the PSF. Lastly, Figure 1.6D shows the nucleus intensity profile. Here the signal is within the two membranes (vertical dotted lines), and the shaded grey area is the PSF. To put the experimental procedure to the test, we start by confirming the validity of the cell model by measuring the known transport properties of TAT, Dextran, and Lucifer Yellow and showing how the intensity profile through a cell looks in different uptake scenarios. We then quantified the transport of the 3.4 kDa peptide salmon Calcitonin (sCT). We investigate the uptake of three various double-lipidated sCT analogs over 4 hours using a confocal fluorescence microscope to quantify the effects of lipidation on peptide transport through Caco-2 cells. Furthermore, we use this method to demonstrate that the model can show differences in the transport pattern of the peptide by adding an inhibitor for endocytosis and lowering the temperature below physiological temperatures.



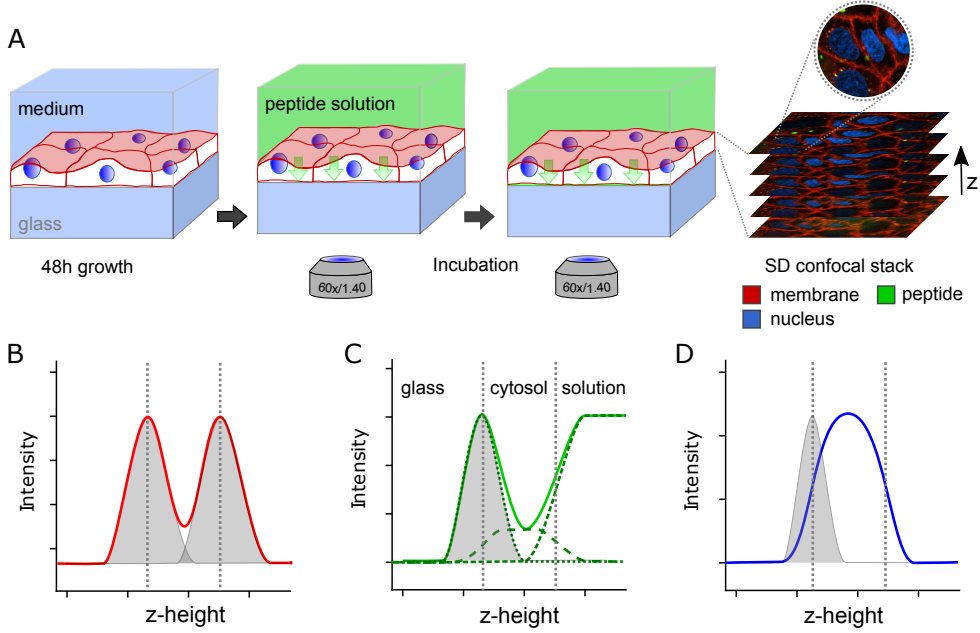


**Figure 1.6.** Description of the experimental setup used to investigate transport of peptides through a monolayer of Caco-2 cells. A) Shows the cell grown in a monolayer for 48 hours and labelled with a red membrane dye and a blue nucleus dye. The peptide solution is then added and imaged axially over four hours with a spinning disk confocal microscope. B) Shows the extracted membrane signal of a single cell. C) Shows the peptide intensity signal extracted from a single cell. The peptide intensity signal is deconvoluted and each component is plotted individually. The sum of the components result in the peptide intensity signal. D) Shows the nucleus intensity signal for a single cell. The dotted lines represent the positions of the bottom and upper membrane. The grey shaded area represents the PSF.

### 1.3 Outline of thesis

In this thesis, two different projects are investigated, with the main focus of the thesis being the utilization of fluorescence microscopy.

Chapter 2 will describe the work done in the first project, which is adapting a commercial wide-field microscope with free-space optics to generate wide-field structured illumination at the sample plane. The purpose of the structured illumination was to combine it with localization microscopy based on fitting the center in the XY-plane of a spot in an image to obtain a better localization precision. Two different experimental setups produce either non-harmonic structured illumination or sinusoidal structured illumination. Furthermore, it provides a detailed description of the sample preparation, sample alignment, imaging protocol, and pre-processing of data. This

project collaborated with a fellow Ph.D. student Martin Schmidt who was responsible for the data analysis and development of the model to combine structured illumination localization fitting with center-based image localization, whereas I have focused on the experimental aspects of the project. This collaboration resulted in a paper called "Camera-based localization microscopy optimized with calibrated structured illumination" [1].

Chapter 3 describes the work done in the second project, where the focus has been on developing a model to quantify the transport of biopharmaceuticals through a cell layer consisting of epithelial cells. Adding Lucifer Yellow and dextran to the cell validated the barrier integrity of the cells. Estimating the point spread function of a spinning disk confocal microscope allowed us to derive an analytical expression describing the transport of the peptide by deconvoluting the axial intensity peptide. Adding TAT to the cells confirmed that the model can quantify the transport of peptides.

In Chapter 4 the model was used to quantify the transport of three different analogs of salmon calcitonin (sCT): sCT(C0/C0), sCT(C4/C4), and sCT(C8/C8), where sCT(C8/C8) show the highest amount of transport of the three analogs. Increasing the lipid chain increases the transport of the peptide, but it also changes the transportation mechanism. Furthermore, a preliminary study investigated the membrane partitioning of the various analogs. Lastly, applying the quantification model of a microfluidic system showed similar results as the simple cell model.

Chapter 3 and 4 are the subject of a paper in preparation and the current version is printed in Appendix B.2.



## CHAPTER 2

# Structured illumination utilizing a digital micromirror device

---

### 2.1 Introduction

This chapter will give an introduction to the concepts used when producing structured illumination. This will include how to manipulate the polarization of light. Furthermore, it will describe two optical setups used to produce structured illumination by modifying an epifluorescence widefield microscope.

Epifluorescence produces a uniform illumination across the entire FOV and can be used to do camera based localization where each molecule is localized by fitting the position of it. Generally, the more photons available the better is the localization. As the illumination is uniform there is no information to gather from the illumination. However, when using a structured illumination on the sample it varies in space. This can be used to enhance the localization of each molecule in the FOV, hence extracting more information per photon available. The first setup aims to be as simple as possible using a DMD to produce the structured illumination. The second setup aims to produce a better structured illumination by achieving a higher contrast and a shorter period.

Finally, both setups are used to localize single molecules showing a 2.1 fold increase in localization precision for the second setup and a 1.3 fold increase in localization precision for the first setup. However, before working with DMD based structured illumination, we need to understand two important phenomena: polarization of light and the diffraction of light. It is important to understand this because the polarization of light hitting the sample will change the contrast of the structured illumination, ultimately meaning how much information we can extract from the structured illumination. This means that we need to make sure that at the sample, the incoming light is polarized linearly and in the same direction as the lines produced on the DMD. To manipulate the polarization of light I will use various optical components. Hence, the following will be a short introduction to how to produce two different

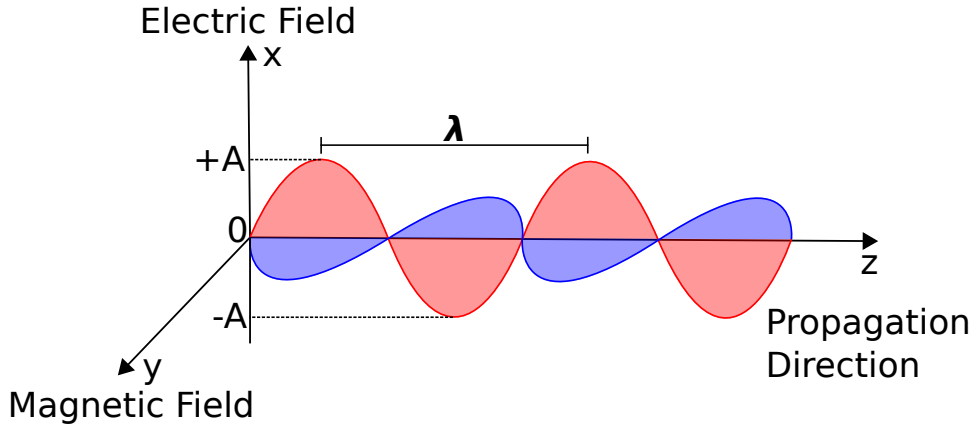


**Figure 2.1.** Electromagnetic wave described by the electric field (red curve) and magnetic field (blue curve). The wavelength of the electromagnetic wave is shown as  $\lambda$  and the amplitude of the wave ranges between  $\pm A$ .

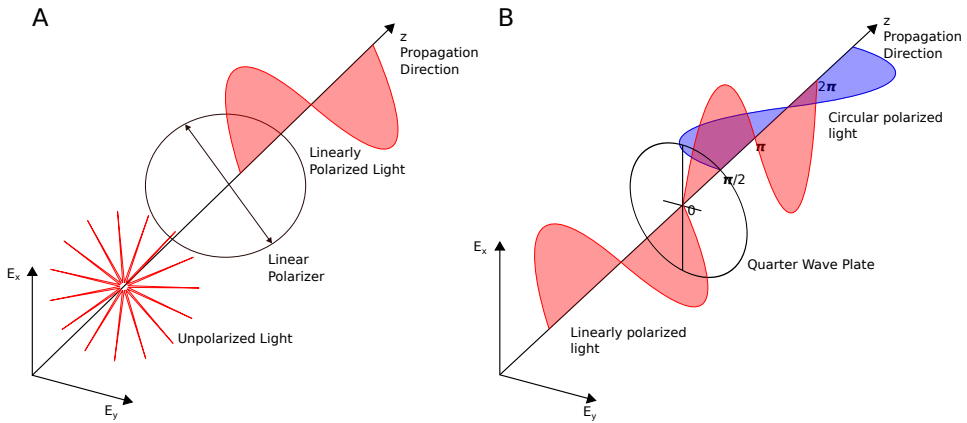


**Figure 2.2.** Describing the effect of two optical components on the polarization of light. A) Unpolarized light travelling along z, the propagation axis, entering a linear polarizer which allows only one plane of light to pass through, as seen by the red curve. B) Linear light traveling towards a quarter-wave plate set at a  $45^\circ$  angle to the linear polarization resulting in circularly polarized light.

types of polarized light, linear and circular.

In our setup we use a monochromatic light sources to excite fluorophores in our sample. Monochromatic light consists of an electromagnetic field traveling in one direction. The electromagnetic field consists of two components, an electric field and a magnetic field, which oscillate with a specific wavelength and they are perpendicular

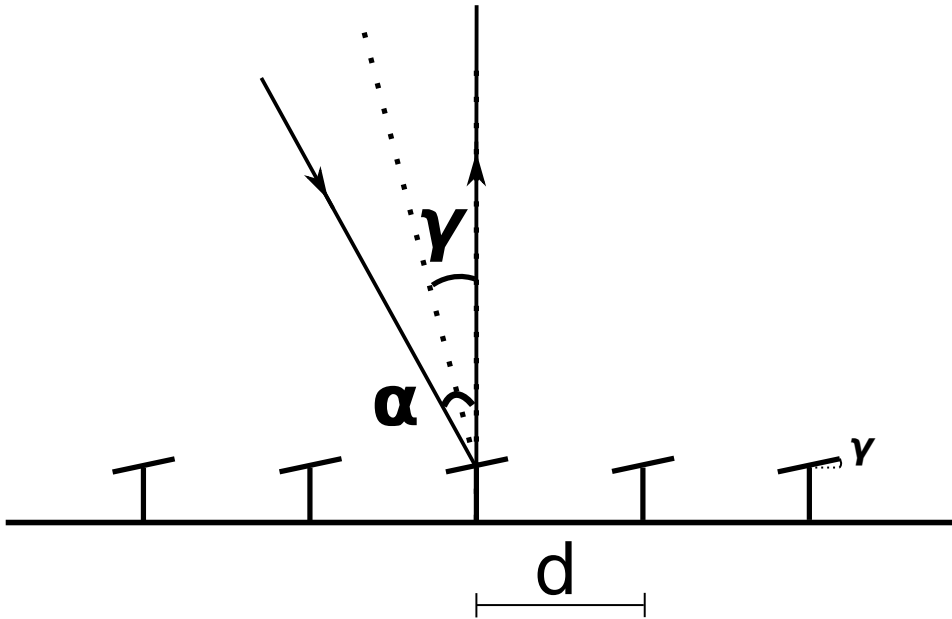


**Figure 2.3.** Diffraction off of a DMD represented as a blazed grating.  $\gamma$  is the tilt angle of the grating.  $\alpha$  is the angle of the incident light with respect to the normal of the surface.  $d$  is the distance between the consecutive mirrors. The light is reflected normal to the surface of the DMD.

to one another, as seen in Figure 2.1. The red curve in Figure 2.1 describes the electric field traveling along  $z$ . Similarly, the blue curve represents the magnetic field traveling along  $z$ . The electromagnetic wave will oscillate, reaching a maximum amplitude at the peak of the wave and dropping down to a minimum amplitude at the bottom of the wave, denoted  $+A$  and  $-A$  in Figure 2.1, respectively.

It is possible to change the polarization of the light by, e.g., passing the light through a linear polarizer. The light going through a linear polarizer, polarizes in the same plane as the rotation of the linear polarizer, as seen in Figure 2.2A. In this case, unpolarized light (meaning that the light comes from multiple planes) passes through a linear polarizer set at an angle. Thus, creating linearly polarized light in a specific direction. Furthermore, the linearly polarized light can be turned into circularly polarized light as seen in Figure 2.2B. To get circularly polarized light, linearly polarized light must pass through a quarter-wave plate. A quarter-wave plate is an optical component that consists of a birefringent material, which is a material that has two different refractive indexes. This means that the light passing through the quarter-wave plate will travel at different speeds. As an example, Figure 2.2B show three different axes  $E_x$ ,  $E_y$  and  $z$ , where the light travels in the direction of  $z$  and separates the electric field into two components,  $E_x$  and  $E_y$ . Imagine that a

circular polarizer has a fast axis (the light travels fastest along this axis) and a slow axis (the light is traveling slower along this axis) that follow  $E_x$  and  $E_y$ , respectively. Then, as linearly polarized light enters at a  $45^\circ$  angle with respect to the fast axis, the  $E_x$  component will travel fast through the material, whereas the  $E_y$  component will travel slower. As the two components exit the quarter-wave plate, they shift along the z-direction by a quarter of a wave.

The final phenomenon is the diffraction of light entering at an angle at a blazed grating, as seen in Figure 2.3. It shows that at an incident angle,  $\alpha$ , traveling towards a blazed grating with blaze angle,  $\gamma$ , it is possible to diffract the outgoing light such that it is parallel to the normal of the surface. To optimize the intensity of the outgoing ray, the blaze conditions must be fulfilled. The factors in the blaze condition are the pitch length ( $d$ ), the wavelength of the laser, the blaze angle, the incident angle, and the diffraction order, as demonstrated by Li et al. [54].

## 2.2 Optical Setup

This section will describe the two optical setups used to demonstrate Calibrated Modulation Enhanced Localization Microscopy (C-MELM). The first setup produced a non-harmonic structured illumination, whereas the second setup produced a harmonic structured illumination.

### 2.2.1 First iteration of the optical setup

The idea behind this setup is that we want to have a simple way of producing structured illumination in the sample plane. We did this by putting the DMD in a 4f configuration with the microscope lens and the microscope objective. This means that the BFP is inside of the microscope objective, hence we cannot block the central order, nor control the polarization. This led to a non-harmonic structured illumination. Figure 2.4 shows the first version of the optical setup used to produce structured illumination. We used the setup extensively to optimize imaging procedures and sample preparation. Prior to using the setup seen in Figure 2.4 we tested the optical components in the setup. The beam splitter (BS) was put in the laser path, followed by an analyzer (A) and a power meter (PM). The analyzer is a linear polarizer inserted into a rotation mount, and by rotating the analyzer, it adjusts how much light is passing through. Figure 2.5A shows the effect of turning the analyzer 180 degrees in increments of 10 degrees as blue data points and the experimental setup. At  $\theta = 0$  the highest intensity is observed, and at  $\theta = 90$  the intensity hits a minimum. At  $\theta = 180$ , the intensity reaches a maximum intensity again. The black line in Figure 2.5A fits the data following Malus Law, stating that  $I(\theta) = I_0 \cos^2(\theta)$  [69], where  $I_0$  is the initial intensity value. Figure 2.5B shows the intensity through the beam splitter and a quarter-wave plate from 0 to 360 with 10 degrees increments as the blue data points and the experimental setup. The solid black line in Figure 2.5B is a circle with a radius equal to the mean value of the blue data points. The black circle is meant as a visual to see how much the blue data points deviate from a circle. The results in Figure 2.5B is as circular as we could get the polarization. After verifying that the BS and QWP in combination produce circularly polarized light, we built the setup seen in Figure 2.4.

First, we used a 473 nm monochromatic laser as the excitation source. However, the power of the laser was unstable unless kept at 100 mW. Thus, by using a series of neutral density (ND) filters, we lowered the power from 100 mW to 30 mW. We needed to lower the power to avoid saturating the camera. Next, we guided the light through a beam splitter, coupled with a quarter-wave plate set at a 45-degree angle to the BS, which resulted in circularly polarized light. M1 and M2 guide the laser light through a beam expander (L1  $f = 30$ mm, L2  $f = 200$  mm) for a beam expansion of 6.6x. 4 mirrors, M3, M4, M5, and M6, then guide the laser onto the digital micromirror device (DMD) at an approximately 24-degree angle such that the first-order diffraction was diffracted normal to the DMD, following the procedure of



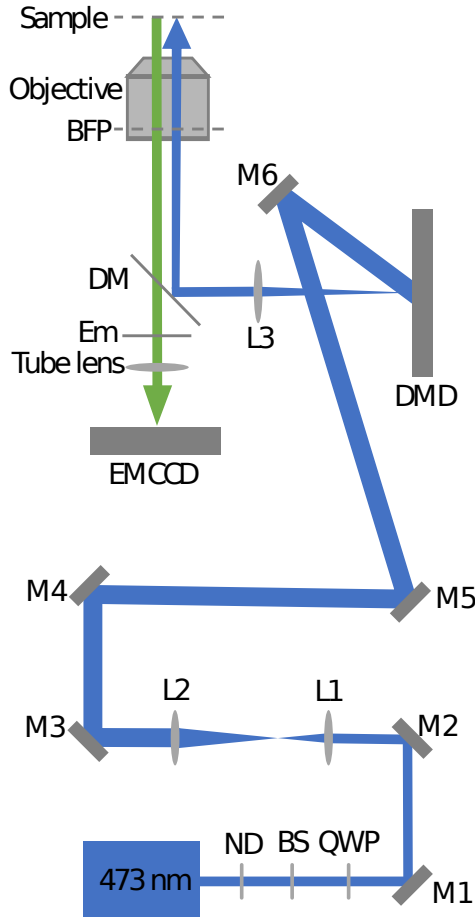


**Figure 2.4.** 473 nm laser light is guided through neutral density filters (ND), a beam splitter (BS), and a quarter-wave plate (QWP) to lower the intensity and make circularly polarized light. M1 and M2 guide the light through a beam expander (L1  $f = 30\text{mm}$ , L2  $f = 200\text{ mm}$ ) for an expansion of 6.6x. M3, M4, M5, and M6 then guide the light onto the digital micromirror device (DMD) at an approximately 24-degree angle, diffracting light normal to the DMD onto the sample through a 4f-configuration with L3 ( $f = 300\text{ mm}$ ) and the objective. The dichroic mirror then guides the light to the objective of the microscope. The emission coming from the sample is transmitted through the dichroic mirror and an emission filter before being focused onto the EMCCD camera by a tube lens.

York et al. [70]. A lens, L3 ( $f = 300\text{ mm}$ ), then focused the light in the objective's back focal plane (BFP), forming an image on the sample sequentially. The DMD, L3, BFP, and the sample were in a 4f-configuration. A dichroic mirror (DM) reflects the

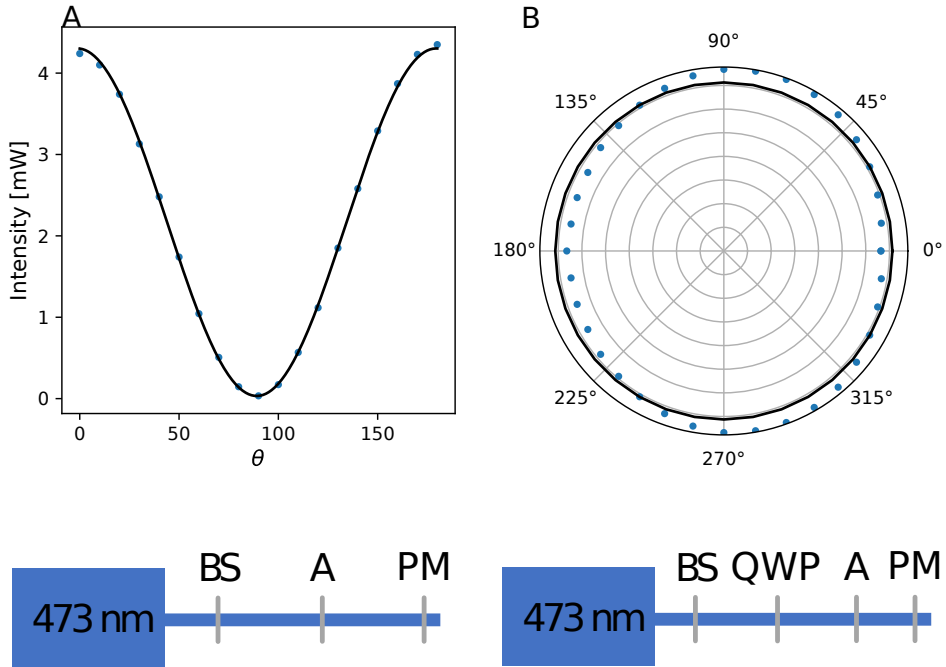


**Figure 2.5.** Intensity through a beam splitter and a quarter wave plate. A) shows the intensity through a beam splitter at various angles on the analyzer as blue points. The black line is a fit following Malus law. Below is a sketch of the setup. B) Shows the intensity through a beam splitter and a quarter-wave plate at various angles on the analyzer as blue points. The black line shows a circle with radius = mean of data. Below is shown a sketch of the setup.

excitation light onto the sample after L3. Still, it transmits the emitted light from the sample through an emission filter and into a tube lens, focusing the light onto the EMCCD camera. The dichroic mirror and L3 are inside the microscope body.

### 2.2.2 Second iteration of optical setup

In the second setup we controlled the polarization of light hitting the sample, but we also blocked the central spot in the BFP. To be able to control the polarization and block the central spot we needed access to the BFP. In order to get access to the BFP we introduced another set of lenses between the DMD and the microscopes objective, such that the BFP was available. At the BFP we then blocked the central order, and made sure that the polarization of the light going to the sample was linear and in the same direction as the lines on the DMD. This led to a shorter period, higher contrast and that the structured illumination was a sine wave.

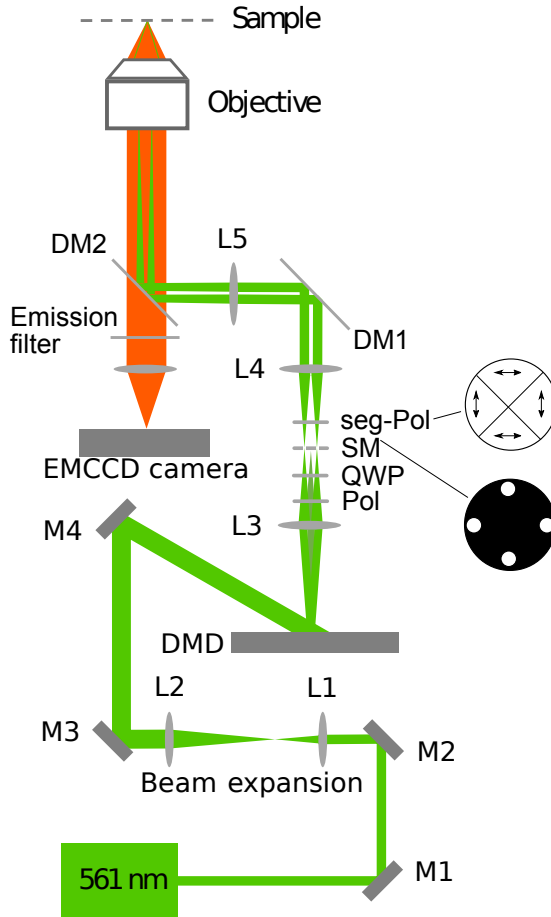


**Figure 2.6.** 561 nm excitation laser is guided by two mirrors, M1 and M2, through L1 ( $f = 30$  mm) and L2 ( $f = 200$  mm) to expand the beam 6.6 times. M3 and M4 guide the light onto the DMD at an angle of  $24^\circ$ , such that the on-mirrors of the DMD is diffracting the first diffraction order in a direction normal to the surface of the DMD. The light passes through L3 ( $f = 300$  mm) and through a linear polarizer coupled with a quarter-wave plate set at a  $45^\circ$  angle to create circularly polarized light. A spatial mask (SM) blocks the central spot in the BFP, and a segmented polarizer (seg-Pol) polarizes the light. L4 collimates the light, and the first dichroic mirror (DM1) guides the light through L5 ( $f = 300$ ), focusing the light in the BFP of the objective. A second dichroic mirror (DM2) guides the light from L5 to the objective, which focuses the light on the sample. The emission from the sample passes through DM2, and the emission filter, before getting focused onto the EMCCD camera by the tube lens.

We built the second experimental setup using inspiration from [52,54] by utilizing a DMD as a spatial light modulator to create structured illumination. Figure 2.6 shows the optical setup, and in this setup, the excitation source is a 561 nm monochromatic laser. It is guided by two mirrors (M1 and M2) through a telescope (L1  $f = 30$  mm and L2  $f = 200$  mm), expanding the beam by 6.6x. Two additional mirrors (M3 and M4) then direct the light to the DMD at a 24-degree angle, guiding the first-order diffraction spot away from the DMD along the normal of the DMD plane. The light passes through a lens (L3,  $f = 300$  mm) and a linear polarizer coupled with a quarter-wave plate. The quarter-wave plate was set at a 45-degree angle with the linear polarizer to create circularly polarized light. L3 focuses the light from the DMD in the BFP, and a spatial mask (SM) is inserted in the BFP to block the central spot. The spatial mask consists of four holes because of the structured illumination in the horizontal and vertical directions.

The light then passes through a segmented polarizer (seg-Pol). The segmented polarizer consists of four pieces, where each piece is a linear polarizer. Each piece in the segmented polarizer polarizes the light in the same direction as the lines produced on the DMD. For example, if the DMD made horizontal lines, then the polarization would be in the horizontal direction. Then the light was collimated by L4 ( $f = 300$  mm) and guided via a dichroic mirror to L5 ( $f = 300$  mm), focusing on the BFP of the objective, which then focused the structured illumination onto the sample. After L5, another dichroic mirror guides the excitation light to the sample and transmits the emission light from the sample to the EMCCD camera. Having two dichroic mirrors is to remove any retardation of the light. With one DM in the setup, any retardation of the light would not be fixable. However, including the second DM would cancel out the effect of the first DM. By introducing additional lenses in the setup in Figure 2.6 it allows to manipulate the light more as there is easier access to the BFP compared to the setup in 2.4.

### 2.2.3 Summary

This section showed the two setups that makes structured illumination. The two setups differ by using two different excitation sources, but we also see that in Figure 2.6 the polarization is more carefully controlled compared to the setup in Figure 2.4.

## 2.3 Experimental procedure

This section will provide details regarding the experimental procedure. The experimental procedures include preparing the various samples and how to mount the samples onto the microscope. Furthermore, the experimental procedure explains how to image with structured illumination and how to characterize the structured illumination.

### 2.3.1 Sample Preparations

#### Slide preparation

During the preparations for C-MELM experiments, one key component was to clean the coverslips prior to anything else. Therefore, we cleaned the coverslips using UV/ozone treatment for approximately 60 minutes. The UV/Ozone treatment removes any biological material on the surface of the coverslip. Furthermore, it also creates a hydrophilic surface for better adhesion.

#### 51 nm beads

The 51 nm bead (Duke Scientific Corporation cat no G50) stock concentration was diluted  $10^4$  times in PBS and sonicated for 30 minutes to break up any aggregating beads. Next, 10  $\mu\text{L}$  of the sonicated bead solution was deposited on a cleaned coverslip for approximately 1 minute. After incubation, the coverslip was briefly dipped in first PBS and secondly in MiliQ water. We then dried the coverslip using nitrogen before mounting the coverslip in 8  $\mu\text{L}$  mowiol onto a microscope slide. The sample was left to harden overnight and was stable for multiple imaging sessions.

#### 46 nm beads

The 46 nm beads (Invitrogen, FluoroSphere carboxylated) stock concentration was diluted  $10^4$  times in MiliQ water and sonicated for 30 minutes. While sonicating the beads, an oven was preheated to 50 °C. After sonication, the beads were diluted 10 times in 99% ethanol to reach a final dilution of  $10^5$ . Next, 5  $\mu\text{L}$  of the bead solution was deposited on the coverslip and placed in the oven to dry for 1 hour. Subsequently, 10  $\mu\text{L}$  of 1xTE was deposited on the coverslip as mounting media before sealed with epoxy glue. This sample was used right away after the glue had hardened. This sample was stable for approximately a week.

#### Single molecule

The single molecule sample was single streptavidin (SA) atto590 molecules. Before adding SA-atto590, the cleaned coverslips were coated with 10  $\mu\text{g}/\text{mL}$  BSA and 1  $\mu\text{g}/\text{mL}$  in a ratio of 10:1. 100  $\mu\text{L}$  of this mixture was added to the coverslips for 20 minutes to allow tethering to the surface, followed by washing in 1xTE for 2 minutes to remove any unbound BSA:BSA/Biotin mixture. Secondly, 100  $\mu\text{L}$  of a 1  $\mu\text{g}/\text{mL}$  SA-atto590 fluorophore was added to the coverslip for 10 minutes before washing in 1xTE for 10 minutes. Lastly, the coverslip was mounted on a microscope slide with degassed 1xTE with nail polish and imaged immediately. This sample was only stable for one day.

### 2.3.2 Imaging procedure

Two different types of experiments were carried out using structured illumination. The first experiment was to characterize the pattern of the structured illumination. This was done such that the maximum amount of information was able to be extracted from the structured illumination. The second type of experiment was a proof-of-concept experiment, where the information gained from characterizing the structured illumination led to increased localization of point emitters.

#### Characterization of illumination pattern

This section will describe how the structured illumination was characterized. The characterization of the structured illumination is a crucial part of the C-MELM, hence much time was put into developing a protocol that allowed for the best experimental results possible.

Before every characterization experiment, the piezo stage was calibrated to have as precise movement as possible of the sample. The sample was mounted to the piezo stage before putting the piezo stage onto the sample holder of the microscope. For this type of characterization, the sample is moved, hence the sample must be level. Otherwise, the sample can get out of focus, leading to inaccurate measurements. To level the sample, a LED source localized the sample. Then, after finding the sample, the sample was leveled in the horizontal direction by moving the sample back and forth and adjusting a screw manually to remove any tilt on the sample. After leveling the horizontal direction, the sample was leveled vertically following the same procedure.

To make the structured illumination, a laser was illuminating the DMD, such that the mirror of the DMD in the "on" position would diffract the light normal to the DMD and through the rest of the optical setup as seen in Figure 2.7A. The "on" mirrors are seen as white squares, and the "off" mirrors are seen as black squares in Figure 2.7A. The optical setup seen in Figure 2.6 uses a duty cycle of 3/9. This means that 3 mirrors are turned to the "on" position followed by 6 mirrors in the "off" position, thus the numerator means how many mirror are in the "on" position and the denominator is the sum of the "on" and "off" mirrors. This duty cycle is then repeated across the entire DMD. An example of this is seen in Figure 2.7C, where structured illumination is seen in the vertical direction.

The structured illumination consisted of three different phases in both a horizontal and vertical direction, resulting in a total of six phases. Each phase had the same duty cycle of 3/9, but it is shifted, which means that it is not the same mirrors turned on and off in the different phases. Going from, e.g., phase one to phase two, the "on" mirrors would have been shifted by three places, hence yielding an identical, but shifted, illumination on the sample as seen in Figure 2.7B. The sample was illuminated first with three phases with horizontal lines and then three phases with vertical lines. Each phase was illuminated onto the sample for 50 ms, thus the total exposure of one cycle of the structured illumination was 300 ms. This cycle was repeated for a total of 10 times at this position. After repeating the illumination 10

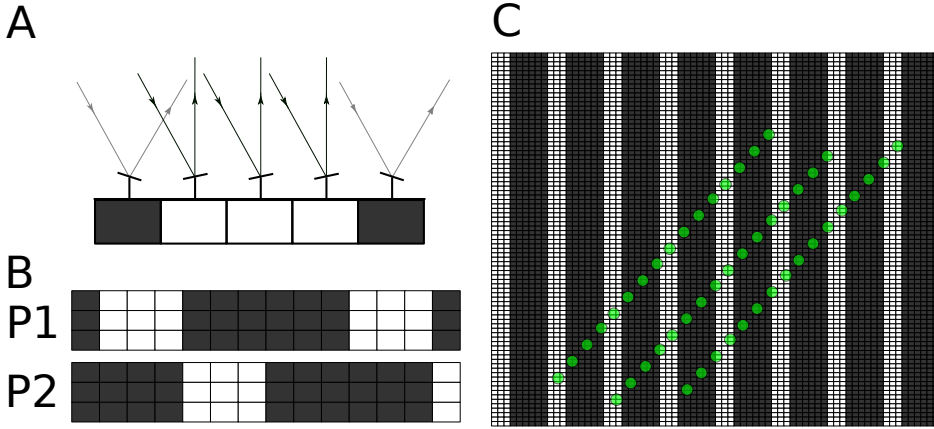


**Figure 2.7.** Utilizing a DMD as a spatial light modulator allows for making structured illumination. A) Shows a series of 5 mirrors of the DMD. The first and last mirror is in the "off" position guiding the incoming light away from the normal of the DMD. The three middle mirrors are in the "on" position guiding the light normal to the DMD and through the rest of the setup. B) Shows an example of two phases of the structured illumination. P1 represents phase 1, and P2 represents phase 2. Both phases have three mirrors in the "on" position followed by 6 mirrors in the "off" position. The difference between the phases is that the position of the "on" mirrors has been shifted three mirrors. C) Shows a schematic of a single phase of structured illumination and how three beads are translated diagonally across the structured illumination.

times, the sample was moved 50 nm in the x and y direction, approximately 70 nm diagonally. After moving to the new position, the whole cycle of illuminating with the structured illumination was repeated. Figure 2.7C shows a schematic of a single phase of structured illumination with the white columns representing the "on" mirrors and the black columns representing the "off" mirrors. The green dots represent a bead at a given position and the trajectory it has as it is moved across the structured illumination. The process of illuminating and moving the sample was repeated until the sample had moved approximately  $2\ \mu\text{m}$ , or 30 steps. Moving the sample across the structured illumination is what allows us to characterize the structured illumination. For the optical setup in Figure 2.4 the duty cycle was  $1/8$ . Furthermore, the setup uses four phases, hence the total illumination duration was 400 ms for this setup. The rest of the procedure was identical between the two setups.

### C-MELM measurement

The C-MELM measurement is when the characterized structured illumination is used to localize point emitters on the sample more accurately. The measurement is simply done by imaging the same field of view for 100 cycles. One cycle is illumination by

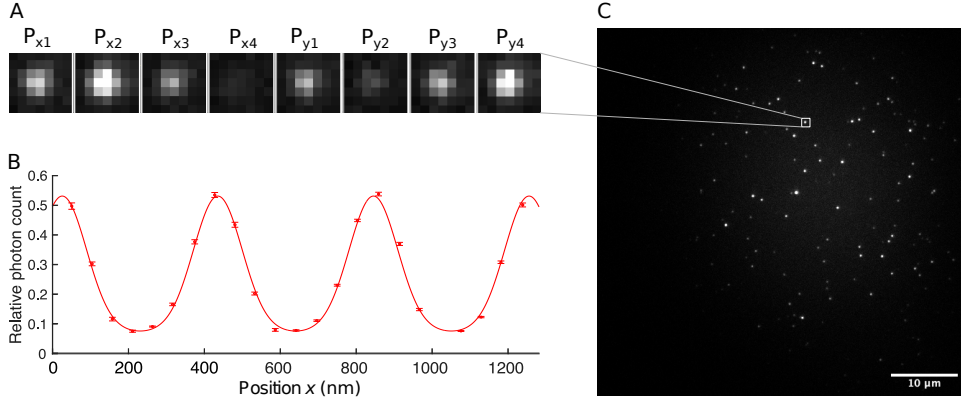


**Figure 2.8.** Shows the pattern produced by the DMD in the sample plane. A) Shows a single 51 nm fluorescent bead under excitation in 8 different frames. Each frame with a different phase of the structured illumination results in different intensities. B) Shows the characterized illumination pattern for the x-periodic structured illumination. C) Shows a single frame of a typical FOV with 51 nm beads. B) Was adapted and modified from [1].

all of the phases. For the setup in Figure 2.6 this is 300 ms (6 phases of 50 ms each) and for the setup in Figure 2.4 this is 400 ms (8 phases of 50 ms each).

## 2.4 Results

Here are the results of characterizing the structured illumination using the two optical setups seen in Figure 2.4 and 2.6. This section will show the results individually and compare the differences between the two setups.

### 2.4.1 Structured Illumination without Blaze Conditions

The first type of structured illumination characterized was from the first setup seen in Figure 2.4. We used a sample with 51 nm beads to characterize the structured illumination for this setup. Figure 2.8C shows a typical FOV with the beads. For this setup, we used a duty cycle of  $1/8$  with 4 phases in both the vertical and horizontal direction, resulting in a total of 8 phases. The illumination on the sample was 50 ms for each phase. Hence, the entire exposure time was 400 ms for one series. A zoom-in of a single bead in the FOV in Figure 2.8C is seen in Figure 2.8A. For each phase, there is a different intensity emitting from the bead. We repeated the exposure for each series of exposure 10 times before moving the stage to another position to have better statistics. 30 positions were imaged in total, each illuminated 10 times with the 8 phases resulting in 2400 exposures, or approximately 2 minutes of imaging.



Figure 2.8B shows an example of the calibrated structure illumination for a single bead in the FOV. The structured illumination is non-harmonic because the width of the peak and the valley of the structured illumination is not the same. The illumination period was approximately 400 nm, and the modulation depth was roughly 0.75. One thing to note is that the modulation depth was not the same for horizontal and vertical lines. The modulation depth of the horizontal lines for the bead shown in Figure 2.8A was 0.8, but for the vertical lines, it was only 0.67.

Applying C-MELM to this type of structured illumination results in an improvement in localization precision of approximately 1.3x compared to regular camera-based localization [1]. For an in-depth data analysis see [1].

## 2.4.2 Structured Illumination with Blaze Conditions

The second iteration of the experimental setup (Figure 2.6) was a bit more sophisticated than the first iteration and involved a few more optical components but performed much better.

Here, the characterization was performed on a sample with 46 nm beads or single molecules. Regardless of the sample, the procedure and the results are the same. We used a duty cycle of 3/9 to characterize the structured illumination produced with the setup seen in Figure 2.6. Figure 2.9C shows a FOV of a sample with 46 nm beads. We illuminated the sample with three phases of horizontal lines and three phases of vertical lines for a total of 6 phases. Figure 2.9A shows an example of a single bead exposed by each of the phases. The total exposure for all six phases was 300 ms. Repeating the process 10 times increases the quality of the characterization of the structured illumination. We moved the sample approximately 70 nm diagonally for 30 repetitions, which allowed for fully characterizing the structured illumination. The imaging resulted in 1800 exposures or 1.5 minutes of imaging. The characterization of the structured illumination happened for every bead in the FOV that was well isolated. Figure 2.9B shows the characterized structured illumination for a single bead for the setup in Figure 2.6. The period of the structured illumination was approximately 230 nm, which is much smaller than that of the structured illumination created using the setup in Figure 2.4. Furthermore, the structured illumination pattern follows a sinusoidal, making it a much simpler pattern to fit.

The modulation depth of the structured illumination produced with the setup in Figure 2.6 was 0.9 in the horizontal and vertical directions. Applying C-MELM with this type of structured illumination resulted in an improvement of the localization precision of more than 2x compared to regular camera-based localization [1]. For a detailed description of the data analysis, see [1].

The two methods of making structured illumination utilize a DMD as a spatial light modulator. However, they produce very different types of structured illumination, and there are two reasons for this. The first reason is that the polarization is controlled differently in the two setups. In Figure 2.4 the polarization is made circular at the beginning of the setup, but the polarization does not last throughout

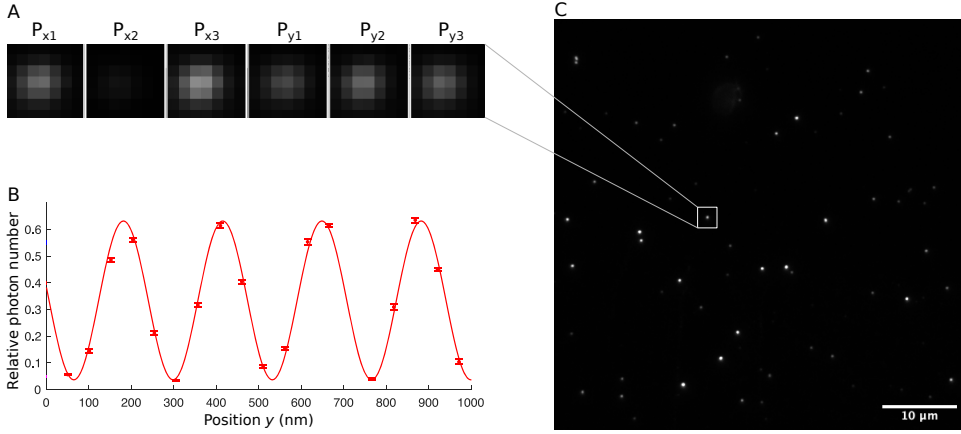


**Figure 2.9.** Shows the pattern produced by the DMD in the sample plane. A) Shows a single 40 nm fluorescent bead under excitation in 6 different frames. Each frame with a different phase of the structured illumination results in different intensities. B) Shows the characterized illumination pattern for the x-periodic structured illumination. C) Shows a single frame of a typical FOV of 40 nm beads. B) Was adapted and modified from [1].

the setup. Throughout the setup, the polarization changes from circular to elliptical. Hence, there is a phase difference that is not equal to  $\frac{\lambda}{4}$ . The phase difference ultimately leads to a difference in intensity of the interference beams on the sample plane, which affects the modulation depth of the structured illumination [54]. In Figure 2.6 the polarization is controlled later in the setup, after the DMD. Here, the polarization is circular to ensure equal intensity in the diffraction spots. Furthermore, removing the central diffraction spot also increases the modulation depth and makes the period of the structured illumination shorter. After removing the central diffraction spot, the polarization is changed again in the same direction as the lines on the DMD. Also, inserting an extra DM purposely induces a difference in polarization, which is then undone by the second DM guiding the light to the sample. By controlling the polarization, the interference on the sample plane overlaps much more, resulting in an increased modulation depth.

These two features, higher modulation depth and a shorter period, are why the setup in Figure 2.6 performs better compared to Figure 2.4. A shorter period and higher modulation depth result in a steeper gradient of the structured illumination, hence making it more sensitive toward the position of the, e.g., bead it illuminates. Thus, having characterized the structured illumination, one can extract the localization of the bead more precisely. Additionally, by improving the structured illumination we reduce the imaging time by 25 %, which decreases the phototoxicity on the sample and also lowers the amount of bleaching.

### 2.4.3 Summary

This section shows that producing structured illumination with a DMD as a spatial light modulator can produce structured illumination with a modulation depth of approximately 0.75 and a period of 400 nm with a simple setup. The structured illumination was non-harmonic using this setup. By using this setup we achieved a 1.3-fold increase in localization precision.

By accessing the BFP and blocking the central diffraction spot while also controlling the polarization of the light resulted in structured illumination with a modulation depth of 0.9 and a period of 230 nm. The structured illumination produced with this version of the setup was harmonic and we achieved a 2.1-fold increase in localization precision.

## CHAPTER 3

# Quantitative Assay for Peptide Transport Using Spinning Disk Confocal Microscopy

---

To do quantitative data analysis on the transport of peptides through a cell layer, we first needed to develop a protocol that allowed us to do this. This includes a characterization of the microscope's point spread function such that it was incorporated into the quantification model. Furthermore, we used a simple cell setup where the cells were grown for two days before the experiment, thus we needed to verify the integrity of the cell barriers. This was done by adding two different types of molecules with known transport properties. One type known to not transport across cell barriers, and another type known to transport across cell barriers. This serves as a control both for the cell model and also the quantification model.

Lastly, we made a calibration curve to calculate the concentration of peptide in solution. We did this by making a dilution series of atto488 fluorophore.

### 3.1 Characterization of Spinning Disk Confocal Microscopy for Live Cell Imaging

There are multiple imaging modalities suitable for fluorescent live cell microscopy, including widefield microscopy, laser scanning confocal microscopy, or spinning disk confocal microscopy. Using a SDCM, one can do live cell imaging for several hours due to the limited excitation of light on the sample and the high temporal resolution. However, the spatial resolution of the SDCM is still limited by the diffraction limit, where the lateral resolution goes down to 170 nm, and the axial resolution goes

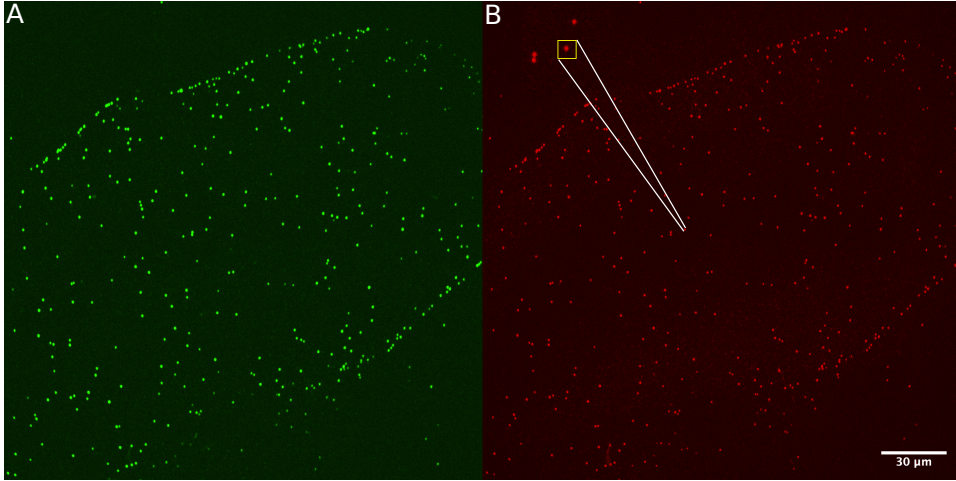


**Figure 3.1.** 100 nm tetraspek beads illuminated with A) 488 nm laser and B) 640 nm laser used for approximating the PSF of the spinning disk. Inset shows a zoom in of a single bead, where the sum of the intensity in the yellow square is extracted.

down to 500 nm [71]. We want to extract quantitative information about the peptide transport through cells. Therefore, to interpret the data obtained with the SDCM, we estimated the microscope's point spread function (PSF). To do so, diffraction-limited fluorescent beads, 100 nm in diameter, were deposited on a glass-bottom surface. The beads are multi-fluorescence beads with four different fluorescent dyes with different excitation and emission spectrums: 365/430 nm (blue), 505/515 nm (green), 560/580 nm (orange), and 660/680 nm (red). Here, only two of the fluorophores are excited as seen in Figure 3.1. Figure 3.1A shows the image when excited by a 488 nm laser, and Figure 3.1B shows the image when excited by a 640 nm laser.

To get information about the axial PSF, we did a z-stack on the beads. Here, we used a z-step of 0.1  $\mu\text{m}$  with a total z-stack of 10  $\mu\text{m}$ , thus yielding 101 steps in total. We then extract the intensity from a single bead by choosing a small region of interest (ROI) around a bead, as seen in Figure 3.1B. For this experiment, the ROI around the bead was 20x20 pixels to make sure we only worked with isolate beads. By extracting the intensity in each of the planes of the z-stack results in a z intensity profile. Figure 3.2A shows a typical example of an intensity profile. The green dots represent the emission of the tetraspek beads. Figure 3.2B shows an example of the intensity profile of the same bead but excited with a red laser. The z-stack recorded is in total 10  $\mu\text{m}$  high, but only 7  $\mu\text{m}$  of the z-stack is used to estimate the axial PSF of the SD, which is why the intensity profiles in Figure 3.2 is only shown between 0 and 7  $\mu\text{m}$ . The intensity profiles in Figure 3.2 show a Gaussian-like structure but with wider tails, thus to estimate the PSF, the intensity profiles were fitted to a double Gaussian distribution. The double Gaussian is a sum of two Gaussians, where one has

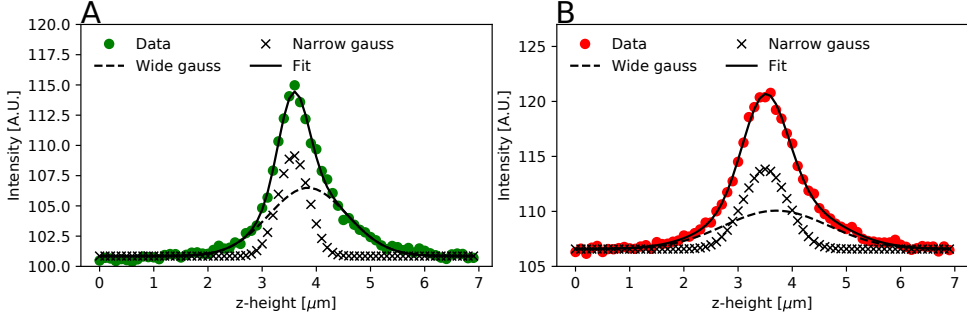


**Figure 3.2.** Intensity profile of a tetraspek bead and the fit to the intensity profile. A) The intensity profile for 488 nm laser excitation is shown as green data points. The two individual Gaussians (crosses and dashed lines) used to fit the data (solid black line) is shown. B) The intensity profile for 640 nm laser excitation is shown as red data points. The two individual Gaussians (crosses and dashed lines) used to fit the data (solid black line) is shown

a high amplitude and narrow width, and the other Gaussian has a small amplitude but a larger width. Using a double Gaussian to fit the axial PSF was recently shown in [72]. Figure 3.2A and B show the fit to the data as a solid black line. Furthermore, the wide and narrow Gaussian is the dashed and crossed lines in Figure 3.2A and B. The expression used to fit the PSF of the SDCM is as defined below.

$$I(z) = a \left[ \left( c \frac{1}{\sigma_1 \sqrt{2\pi}} e^{-\frac{(z-\mu_1)^2}{2\sigma_1^2}} \right) + \left( (1-c) \frac{1}{\sigma_2 \sqrt{2\pi}} e^{-\frac{(z-\mu_2)^2}{2\sigma_2^2}} \right) \right] + b \quad (3.1)$$

Here a total of 7 parameters are included, where  $a$  is the amplitude of the sum of the two Gaussian.  $c$  is a factor weighing each Gaussian, e.g., how much of the PSF fit should be described by the first Gaussian and how much should be described by the second Gaussian.  $\mu_1$  and  $\sigma_1$  are the mean and standard deviation of the tall and narrow Gaussian.  $\mu_2$  and  $\sigma_2$  are the mean and standard deviation of the low and wide Gaussian. Lastly,  $b$  is estimating the background level where the tails of the Gaussian have flattened out. By fitting the intensity trace in 3.2A and B we extract the different parameters described above.

This procedure was carried out for a total of 16 beads. Their intensity profiles were extracted, and each intensity profile was fitted with the expression for the PSF seen above. For each fit, every parameter was stored and plotted as seen in Figure 3.3 for

$\lambda_{488ex}$	$\mu_\Delta$	$\sigma_1$	$\sigma_\Delta$	A	b	c1	c2
	$0.19 \mu\text{m}$	$0.29 \mu\text{m}$	2.78	18.98 A.U.	100.9 A.U.	0.4	0.6

**Table 3.1.** The mean value of the parameters found by fitting tetraspek beads with Equation 3.1 for 488 nm excitation.

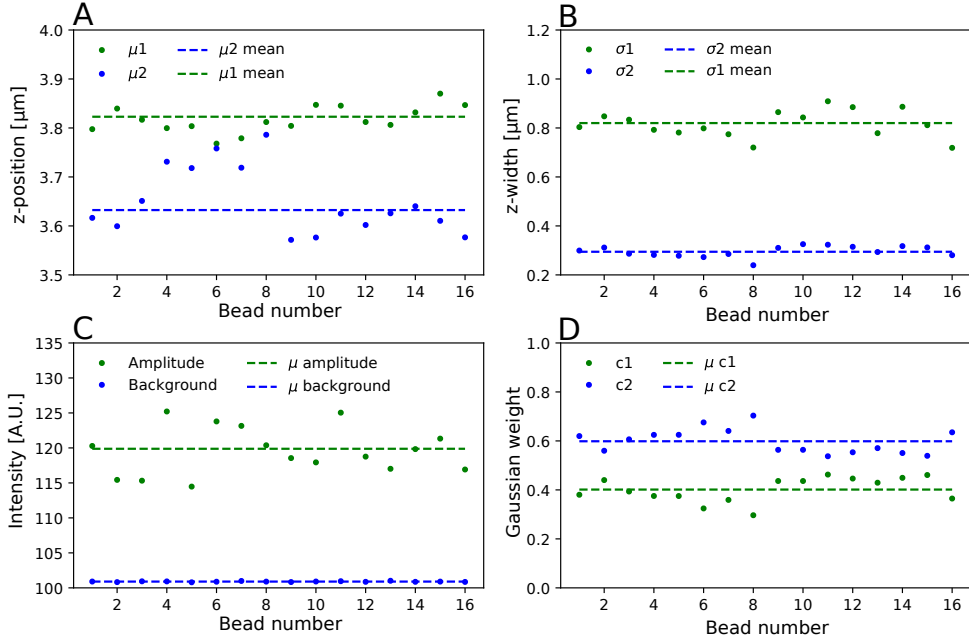


**Figure 3.3.** The parameters extracted from fitting 16 beads for the 488 nm laser. A) The green dots represent the position,  $\mu_1$ , of the tall and narrow Gaussian. The green dashed line represents the mean of  $\mu_1$ . The blue dots represent the position,  $\mu_2$ , of the small and wide Gaussian, where the blue dashed line represents the mean position of  $\mu_2$ . B) The green and blue dots represent the value of  $\sigma_1$  and  $\sigma_2$ , for the tall and narrow and the small and wide Gaussian, respectively. The dashed lines represent the mean for  $\sigma_1$  (green) and  $\sigma_2$  (blue). C) Shows the amplitude for each bead as green dots and the background for each bead as blue dots. The dashed green line shows the mean amplitude, and the dashed blue line shows the mean background level. The background level is added to the amplitude signal for easier visualization. D) Shows the parameter  $c_1$ , which distributes the weight on each Gaussian in green dots and  $c_2$  (defined as  $1-c_1$ ) in blue dots. The dashed lines show their respective means.

488 nm laser and Figure 3.4 for 640 nm laser. It should be noted that the PSF is not estimated for 488 nm or 640 nm excitation, but rather the emission, approximately 520 nm, and 680 nm. Figure 3.3A shows the fitted positions of the two Gaussians for each bead and the mean position as the dashed lines. Figure 3.3B shows the fitted

$\lambda_{640ex}$	$\mu_\Delta$	$\sigma_1$	$\sigma_\Delta$	A	b	$c_1$	$c_2$
	0.16 $\mu\text{m}$	0.38 $\mu\text{m}$	2.43	18.8 A.U.	106.8 A.U.	0.41	0.59

**Table 3.2.** The mean value of the parameters found by fitting tetraspek beads with Equation 3.1 for 640 nm excitation.

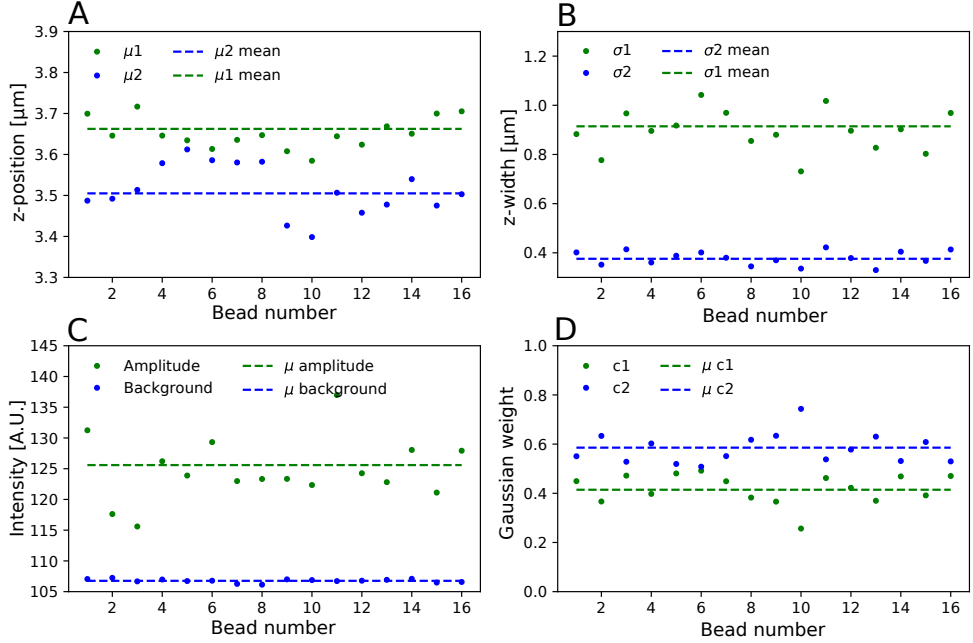


**Figure 3.4.** The parameters extracted from fitting 16 beads for the 640 nm laser. A) The green dots represent the tall and narrow Gaussian position,  $\mu_1$ . The green dashed line represents the mean of  $\mu_1$ . The blue dots represent the position,  $\mu_2$ , of the small and wide Gaussian, where the blue dashed line represents the mean position of  $\mu_2$ . B) The green and blue dots represent the value of  $\sigma_1$  and  $\sigma_2$ , respectively, for the tall and narrow and the small and wide Gaussian. The dashed lines represent the mean for  $\sigma_1$  (green) and  $\sigma_2$  (blue). C) Shows the amplitude for each bead as green dots and the background for each bead as blue dots. The green dashed line shows the mean amplitude, and the blue dashed line shows the mean background level. The background level is added to the amplitude signal for easier visualization. D) Shows the parameter  $c_1$ , which distributes the weight on each Gaussian in green dots and  $c_2$  (defined as  $1-c_1$ ) in blue dots. The dashed lines represent their respective means.

width of the two Gaussians, and the dashed lines represent the mean value of the fitted widths. Figure 3.3C shows the fitted amplitude and background intensity level. Lastly, Figure 3.3D shows the fitted weight on each of the Gaussians. Here  $c_1$  is the weight on the tall and narrow Gaussian and  $c_2$  is the weight on the low and wide Gaussian.  $c_2$  is defined as  $1-c_1$ .

The mean values extracted from fitting the intensity profiles from the 16 beads using Equation 3.1 is summarized in Table 3.1. Here,  $\mu_\Delta$  is the difference between  $\mu_1$  and  $\mu_2$ , and  $\sigma_\Delta$  is the ratio between  $\sigma_1$  and  $\sigma_2$ . Figure 3.4A-D shows the extracted parameters when fitting the intensity profiles of the beads, but when exciting with a 640 nm laser. A summary of the mean of the extracted fitting parameters is seen in



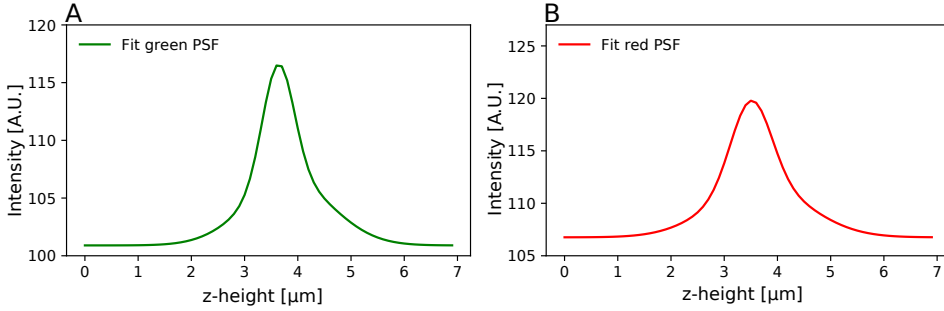


**Figure 3.5.** The PSF for A) 488 nm laser and B) 640 nm laser.

Table 3.2.

Equation 3.1 is used to fit the intensity profile of tetraspek beads to estimate the PSF of the spinning disk confocal microscope. After fitting the intensity profiles and extracting the parameters we can simplify the expression of the PSF by expressing  $\mu_2$  and  $\sigma_2$  as  $\mu_1$  and  $\sigma_1$  with the appropriate shift. The shifts are seen in Table 3.1 and 3.2. Thus, the new expression for the PSF is as follows:

$$I(z) = a \left( c \frac{1}{\sigma_1 \sqrt{2\pi}} e^{-\frac{(z-\mu_1)^2}{2\sigma_1^2}} \right) + a \left( (1-c) \frac{1}{\sigma_1 \sigma_{\Delta} \sqrt{2\pi}} e^{-\frac{(z-(\mu_1+\mu_{shift}))^2}{2(\sigma_1 \sigma_{\Delta})^2}} \right) + b \quad (3.2)$$

Using the values from Table 3.1 and 3.2 and inserting them into Equation 3.2 we simulated how the point spread function looks like for 520 emission and 680 emission. Figure 3.5A shows the PSF for 520 nm emission and 3.5B shows the PSF for 680 nm emission.

### 3.1.1 Summary

In this section we have estimated the axial PSF of a spinning disk confocal microscope at two different wavelengths. We want to estimate the PSF in the axial direction as it is in this direction peptide transports through cells and we need the PSF to quantify the transport. To estimate the axial PSF we excited multi-spectral beads (tetraspek beads) with 488 nm and 640 nm in a z-stack to get emission intensity profiles at 520 nm and 680 nm. We then fit the intensity profiles with a double Gaussian to approximate the axial PSF. From the fit we extracted the parameters describing the PSF in the axial direction.

## 3.2 Quantification of atto488 in Solution

Before using atto488 to study peptide transport it was characterized in the SD. This serves the purpose of knowing if the fluorophore self-quenches, which is a process that can happen when using high molecular concentrations of a fluorophore [73]. Furthermore, the experiment will provide a calibration curve, which will make it possible to convert fluorescent intensity into molecular concentration. To characterize atto488 we made a dilution series starting at 5  $\mu\text{M}$  atto488. In the dilution series we halved the concentration seven times to get concentration ending at 0.08  $\mu\text{M}$  as seen in Table 3.3. We sampled from inside the coverslip's glass and into the atto488 solution in a z-stack. The total depth of the z-stack was 40  $\mu\text{m}$ . We used the same well for each concentration, starting with 0.08  $\mu\text{M}$ . We added 100  $\mu\text{L}$  and imaged three separate FOVs in the same well. After imaging one concentration we removed the fluorophore solution and washed the well once with a buffer before adding the next concentration in the dilution series. We used a fixed laser power of 8 % throughout the experiment. Furthermore, we used a constant exposure time on the camera of 50 ms for each z-plane. Figure 3.6 shows 4 examples of different intensity profiles at various fluorophore concentrations.

From Figure 3.6 it shows that the background level inside of the glass changes with the concentration of the solution. For the blue curve in Figure 3.6 the background level is approximately 200 A.U., whereas for the red curve it is 100 A.U. This highlights that we need to estimate the background for each concentration. The background was estimated by averaging the intensity signal from inside of the glass at  $z = 0 \mu\text{m}$  up until the first vertical dotted line as seen in Figure 3.6 at  $z = 12.5 \mu\text{m}$ . Similarly, the intensity in the solution also changes with the concentration of the fluorophore. To estimate the intensity level in solution the average intensity was found from  $z = 25.5 \mu\text{m}$  (second dotted line in Figure 3.6) until the end of the z stack at  $z = 40 \mu\text{m}$ . The estimated background and solution level is seen in Table 3.3. Figure 3.7 shows the intensity in the solution with the background intensity subtracted as a function of concentration. Each data point is the average of 3 FOVs and the error

Concentration [ $\mu\text{M}$ ]	Volume [ $\mu\text{L}$ ]	Background [A.U.]	Solution [A.U.]
5	100	$100.05 \pm 0.023$	$1.22 \pm 0.030$
2.5	100	$101.66 \pm 0.037$	$2.85 \pm 0.033$
1.25	100	$105.08 \pm 0.085$	$6.16 \pm 0.13$
0.63	100	$111.87 \pm 0.22$	$12.83 \pm 0.41$
0.31	100	$124.52 \pm 0.59$	$25.65 \pm 0.83$
0.16	100	$149.90 \pm 0.49$	$50.98 \pm 0.55$
0.08	100	$199.77 \pm 1.5$	$104.41 \pm 1.9$

**Table 3.3.** Concentrations and volumes used for making the calibration curve for atto488. The estimated background level and the background subtracted solution level. The results are an average of 3 FOVs  $\pm$  SEM.

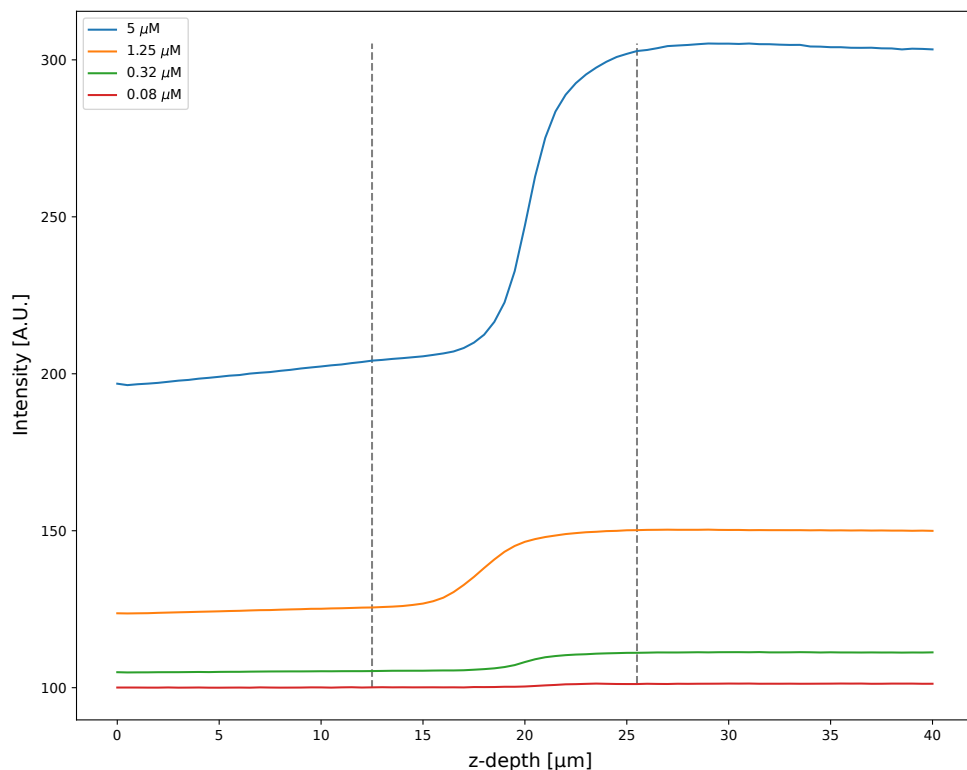


**Figure 3.6.** Examples of fluorescence intensity profiles sampled from in the coverslip glass into the solution with free atto488 fluorophores. The background is estimated from  $z = 0 \mu\text{m}$  to the first dashed line. The solution level is estimated from the second dashed line to  $z = 40 \mu\text{m}$ . Each curve is an average of 3 FOVs.

bars represent the SEM. We fit the data to a straight line, where the intercept on the y-axis has to cross through 0 A.U. The reason for this is because the data in Figure 3.7 is background corrected, so any signal in solution should only arise from atto488 molecules. Thus, at a concentration of  $0 \mu\text{M}$ , where no atto488 molecules are present, there should be no signal at all, hence the fit is forced to 0 A.U. The fit to the data show great agreement with the data with a slope of  $20.8 \text{ A.U./}\mu\text{M}$ . It is possible to convert intensities obtained under the same experimental conditions to concentrations. Furthermore, it is also clear that there is no self-quenching of the atto488 fluorophore in this concentration range. Had this been the case, then the intensity values seen in Table 3.3 would have not doubled between from concentration to concentration.

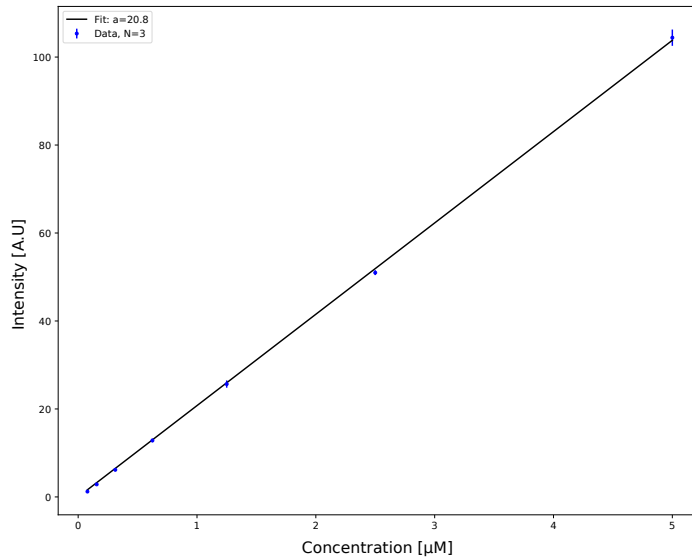


**Figure 3.7.** Background corrected calibration curve. The blue dots represents the solution level at a given concentration. Each point is an average of 3 FOVs  $\pm$  SEM. Black line is a linear fit to the data forced to intercept y axis at 0 A.U.. The fitted slope is 20.8 A.U./ $\mu$ M

### 3.3 Simple Cell Model for Transport Study

Generally, when studying peptide transport through a monolayer the transport is quantified as the amount of peptide going from the apical side to the basolateral side. Transwells are often used to study the peptide transport. However, the cells grow in the transwell for 18-21 days before the transport experiment, and it does not allow for high magnification imaging. To overcome this I want to develop a simple cell model where the cells only grow for two day and still exhibit tight barriers. Furthermore, I was to combine this with an assay to quantify peptide transport from the apical to the basolateral side. I will achieve this by letting the cells are grow for 48 hours, and validate that this is enough time to form valid barriers by adding two molecules, Dextran and Lucifer yellow, that are known not to transport through the cells [74,75]. Secondly, I add TAT to quantify the transport from the apical side to the basolateral side of the monolayer [76], thus confirming the quantification of peptide transporting.

### 3.3.1 Method and materials

#### Cell Culture

We used a human colon adenocarcinoma cell line (Caco-2) and cultured them in an Eagle's Minimum Essential Medium (MEM). The MEM was supplemented with 10 % fetal bovine serum (FBS), 1 % penicillin/streptomycin (P/S), 1 % L-glutamine and 1 % Non-essential amino acids (NEAA). This mixture is the cell culture media. The cells were kept and grown in a 75 cm<sup>2</sup> culture flask with approximately 12 mL of cell culture media inside a humidified incubator at 37 °C and 5 % CO<sub>2</sub>. We did all experiments with cells split between 45 and 60 times.

#### Cell seeding

Upon reaching approximately 80-90 % confluence, the cells were washed with 10 mL of PBS before splitting the cells with 1 mL of a mixture of trypsin and EDTA (T/E) for 5 minutes in the incubator. Next, we added 9 mL cell culture media to stop the T/E process of detaching the cells. Next, the cell density was estimated using a cell counter. Then 30000 cells were seeded in each well in an ibidi treat 8-well plate at a volume of 300 µL per well. The cells were then left to grow in a humidified incubator at 37 °C and 5 % CO<sub>2</sub> for 48 hours.

#### Cell labeling

We labeled the cells with two fluorophores staining either the nucleus or the cell membrane.

The nucleus staining used is called Hoechst and we used a concentration of 1 µg/mL diluted in cell culture media. The cells were incubated at 37 °C in a humidified incubator and 5 % CO<sub>2</sub> with the staining solution for 30 minutes before washing three times with cell culture media.

After washing, we labeled the cells with CellMask DeepRed to stain the cell membrane. The labeling concentration was 2.5 µg/mL and diluted in cell culture media. The cells were incubated at 37 °C in a humidified incubator and 5 % CO<sub>2</sub> for approximately 10 minutes before washing three times with an imaging medium. The imaging medium consists of fluorobrite mixed with 2 % glutamax. The cells were in the imaging medium approximately 1 hour before the uptake experiments.

#### Imaging of Cells and Peptide

We imaged the cells using an inverted Nikon spinning disk confocal microscope. Before adding the cells to the microscope sample holder, the heating chamber around the microscope heated it to 37 °C, 5 % CO<sub>2</sub> under humid conditions. To visualize the cells, a 60x/1.4 NA oil objective was used. The ibidi treat 8-well plate has a total of 8 wells, hence multiple fields of views were marked in both the same well but also in multiple

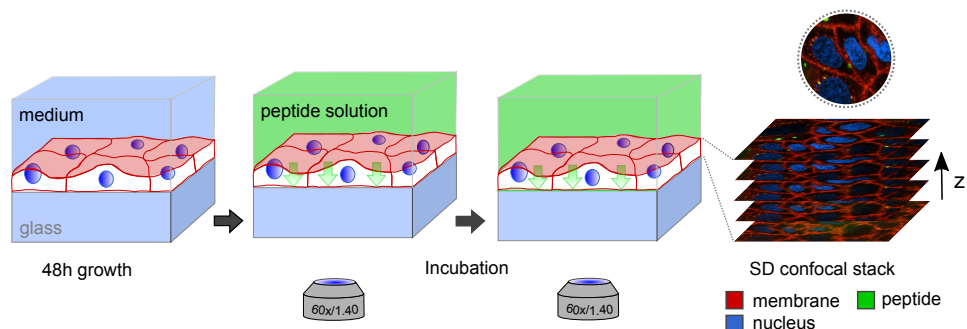


**Figure 3.8.** Cartoon of experimental procedure. Cell membrane and nucleus are labelled in red and blue, respectively, after 48 of grow in ibidi-wells. Peptide solution is added and the transport is monitored over time by z-stack imaging.

other wells. Typically, for every single well, we chose three fields of view based on a few criteria: 1) The entire field of view contains cells, 2) the cells look healthy, e.g., no membrane protrusion due to cell death, and 3) the cells would need to have a certain height. Figure 3.8 shows a schematic of the experimental procedure. For each field of view, we imaged a z-stack with 71 z-steps. Each step was  $0.5\ \mu\text{m}$ , resulting in a  $35\ \mu\text{m}$  tall z-stack. There are many different peptides used depending on the goal of the experiment. For negative controls to validate the barrier integrity of the cells we used  $1\ \mu\text{M}$  of Dextran or  $100\ \mu\text{M}$  of Lucifer yellow. For the positive control to validate that we can quantify transport through the cell layer we used  $3.5\ \mu\text{M}$  of TAT. We used salmon calcitonin (sCT) as the model peptide. sCT was used as the native molecule (sCT(C0/C0)), or modified with either two C4 chains (sCT(C4/C4)) or two C8 chains (sCT(C8/C8)). When using any of the sCT analogs  $1\ \mu\text{M}$  peptide was added. Regardless of what peptide added we imaged each field of view before adding the peptide. We did this by imaging the field of views as a z-stack with 8 % laser power on the 405 nm laser (to excite the Hoechst staining of the nucleus) and 10 % laser power on the 640 nm laser (to excite the CellMask DeepRed staining of the membrane). The exposure time on the scientific CMOS (sCMOS) camera for each laser excitation was 50 ms. We used these images to correct for movement in x, y, and z due to adding the peptide solution. This means that  $t = 0$  min after adding the peptide is approximately 1-2 minutes after adding the peptide. We used three different peptides: sCT(C0/C0), sCT(C4/C4), and sCT(C8/C8). We diluted the peptide stock solution to approximately  $2\ \mu\text{M}$  in an imaging medium. We added a total volume of  $100\ \mu\text{L}$  peptide solution to each well containing  $100\ \mu\text{L}$  imaging medium, thus getting diluted to  $1\ \mu\text{M}$ . This way of adding peptide showed the least movement.

Immediately after adding the peptide solution, we checked the marked positions to see if they had moved due to the disturbance of adding the peptide solution. After adjusting the positions, we did a time series experiment, where we imaged the cells

for four hours every 40 minutes for seven time points. We imaged each field of view as a z-stack of 71 steps. We illuminated each z-plane with 50 ms exposure of 8 % 405 nm laser, 8 % 488 nm laser (exciting the fluorophores on the peptides), and 10 % 640 nm laser for a total exposure of 150 ms per z-plane. Due to a large amount of exposure to each field of view, it is important to minimize unnecessary light exposure to the sample. One way of minimizing the unnecessary exposure and limiting the latency between exposures is by utilizing hardware triggering of the lasers rather than software triggering [77]. Furthermore, using a quad-band emission filter rather than single band emission filters minimizes the latency between exposures.

### Processing of data

After the experiment, we loaded the data into a python script for choosing regions of interest (ROIs) to analyze within a cell. Due to the small movement of the stage and the cells throughout the experiment we loaded every time point to correct the small movements. We saved the position of the ROI for later data analysis. Each of the ROIs was a 10x10 pixel square inside the cell's cytosol. We picked the ROIs to be close to the nucleus, as seen in Figure 3.9. After finding ROIs for all cells in a FOV and extracting the intensity profiles for each time point we plot it. Figure 3.10 shows an example of an intensity profile for each of the fluorophores. The intensity profiles are the mean intensity of the ROI as a function of the z-plane of the z-stack. The right intensity profile seen in Figure 3.10 is from the nucleus of the cell. Given that the ROI is not inside the nucleus, there should be no or little signal. The left plot in Figure 3.10 shows the intensity profile of the membrane of the cell. Approximately at 12  $\mu\text{m}$  we see a peak in the signal, which arises from the bottom membrane of the cell. Similarly, at approximately 17  $\mu\text{m}$  we see a second peak, which comes from the upper membrane of the cell. Lastly, the center plot in Figure 3.10 comes from the peptide signal

## 3.3.2 Deconvolution of Intensity Signal

### Cell Membrane Signal

We use the membrane intensity profile to localize the position of a given cell's bottom and top membrane. The intensity signal needs to be fitted to a model describing the signal. To do so, one needs to know what the membrane of the Caco-2 cell looks like. The width of the membrane of a Caco-2 cell is approximately 5 nm [78] and thus can be thought of as a point emitter. Since the emission from the membrane is recorded through an optical system, it is not possible to resolve the membrane down to 5 nm as the signal is convolved with the PSF. Thus, the model used to localize the cells' membrane is the convolution of the point emitter and the PSF. The point emitter is thought of as a delta function only yielding a signal at the location of the membrane. Section 3.1 describes the PSF for the optical system. Thus, we fit the intensity signal

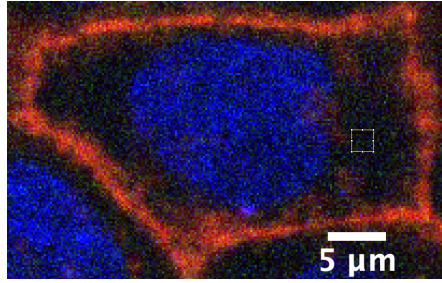


**Figure 3.9.** An example of a single cell. The membrane is seen in red and the nucleus is seen in blue. The 10x10 pixel yellow square indicates the ROI where the intensity is sampled from.

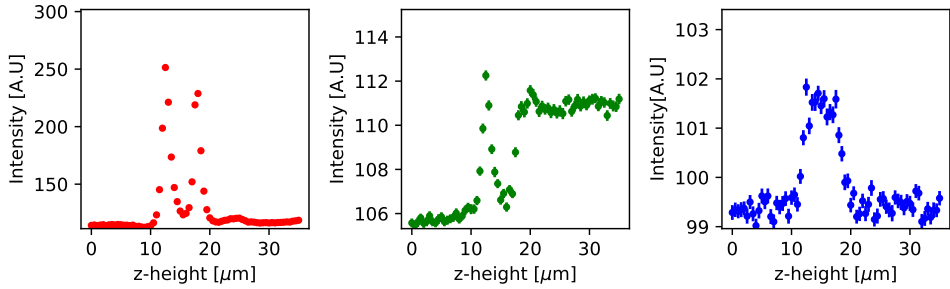


**Figure 3.10.** Intensity extracted from a single cell. The left plot with the red data points represents the membrane, where the first peak is the bottom membrane of the cell and the second peak is the upper membrane of the cell. The center plot with the green data points represents the intensity coming from a peptide. Lastly, the right plot represents the nucleus intensity with the blue data points. The data points are all the mean intensity in the ROI  $\pm$  SEM.

with the following equation:

$$\begin{aligned}
 I(z) = & a_1 \left[ c \frac{1}{\sigma\sqrt{2\pi}} e^{-\frac{(z-\mu_1)^2}{2\sigma^2}} + (1-c) \frac{1}{\sigma\sigma_\Delta\sqrt{2\pi}} e^{-\frac{(z-(\mu_1+\mu_\Delta))^2}{2(\sigma\sigma_\Delta)^2}} \right] \\
 & + a_2 \left[ c \frac{1}{\sigma\sqrt{2\pi}} e^{-\frac{(z-\mu_2)^2}{2\sigma^2}} + (1-c) \frac{1}{\sigma\sigma_\Delta\sqrt{2\pi}} e^{-\frac{(z-(\mu_2+\mu_\Delta))^2}{2(\sigma\sigma_\Delta)^2}} \right] + b
 \end{aligned} \tag{3.3}$$

Here, 5 different parameters are fitted:  $a_1$  and  $a_2$  are the amplitudes of the signal coming from the bottom and top membrane of the cell, respectively.  $\mu_1$  and  $\mu_2$  are the positions of the bottom and top membrane, respectively. Lastly,  $b$ , is the background intensity level. The other parameters,  $c$ ,  $\mu_\Delta$  and  $\sigma_\Delta$  were found previously in Section 3.1 for a 640 nm laser excitation. Figure 3.11 A shows an example as a cartoon of



how such a fit would look, where the two vertical dotted line represent the position of the bottom and top membrane of the cell. The grey area at each position of the membrane shows the PSF.

### Peptide Signal

We used the same approach when fitting the signal from the peptide. However, the signal is different, so we split it up to simplify it. The intensity signal was split up into three different sections as seen in Figure 3.11 B. In the glass section, we estimate the background. It starts at  $z = 0$  (inside of the glass of the sample) and ends at  $z = \mu_1$ , which is the position of the first membrane. The cytosol section starts at  $z = \mu_1$  and ends at  $z = \mu_2$ . In this part, we quantify the amount of peptides inside the cell. The last section is called the solution and starts at  $z = \mu_2$  and ends at  $z = 35 \mu\text{m}$ , which is the end of the  $z$ -stack. The last thing to mention is that at the position  $z = \mu_1$ , if any peptide is transported through the cells and accumulates at the bottom membrane, then the signal at the interface between the two sections, glass and cytosol, will increase. This results in 4 different contributions. The sum of these will fit the peptide's intensity profile.

The first contribution comes from the background, which is assumed a constant that has to be added to take the offset of the camera into account.

The second contribution comes from the peptide accumulating at the bottom membrane. Like the membrane of a cell, the peptide can be thought off as a point emitter confined at the bottom membrane, hence the contribution is the convolution of a point emitter with the PSF at 488 nm excitation. The contribution from this part is then:

$$a_1 \left[ c \frac{1}{\sigma \sqrt{2\pi}} e^{-\frac{(z-\mu_1)^2}{2\sigma^2}} + (1-c) \frac{1}{\sigma \sigma_\Delta \sqrt{2\pi}} e^{-\frac{(z-(\mu_1+\mu_\Delta))^2}{2(\sigma \sigma_\Delta)^2}} \right] \quad (3.4)$$

Where  $a_1$  represents the amplitude of the peptide transported through the cell and is also the only parameter that needs to be fitted of this contribution, as  $\mu_1$  were found previously in the membrane fit and  $c$ ,  $\sigma$ ,  $\sigma_\Delta$  and  $\mu_\Delta$  were found experimentally as described in Section 3.1. The third contribution comes from the intensity level inside the cell. This contribution is a step function, where the step happens at the bottom membrane. The step goes from the background level into some intensity level inside the cell. It is this intensity level that we fit. The PSF and the step function need to be convoluted to obtain the intensity profile needed. A.1 shows a schematic the convolution, but the following will show the derivation of it.

The convolution is:

$$y(t) = s(t) * g(t) = \int_{-\infty}^{\infty} s(x)g(z-x)dx \quad (3.5)$$

In this scenario  $s(t)$  would be the step function and  $g(t)$  would be the PSF. The step function is defined such that from the position of the bottom membrane,  $\mu_1$ , and into

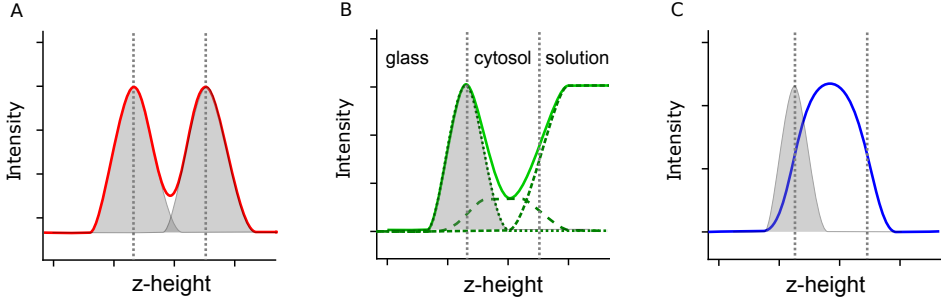


**Figure 3.11.** Cartoon of intensity profiles. A) shows the membrane intensity profile as a red line. B) Shows the peptide intensity profile as a green line. The four components of the fit is shown individually and the sum of contributions of each part of the fit is seen as a solid green line. C) Shows the nucleus signal as a blue line. The vertical lines in the graphs represent the positions of the membranes of the cell. The grey plots represent the point spread function.

the cell the step function returns a value,  $a_2$ . Below the cell the step function returns a value of 0. Because of this Equation 3.5 reduces to

$$y(t) = a_2 \int_{\mu_1}^{\infty} g(z - x) dx$$

Inserting the PSF yields

$$y(t) = a_2 \int_{\mu_1}^{\infty} c \frac{1}{\sigma_1 \sqrt{2\pi}} e^{-\frac{(z-x_1)^2}{2\sigma_1^2}} dx_1 + a_2 \int_{\mu_{01}}^{\infty} (1-c) \frac{1}{\sigma_2 \sqrt{2\pi}} e^{-\frac{(z-x_2)^2}{2(\sigma_2)^2}} dx_2$$

We approximate the PSF as the sum of two Gaussians, where one is tall and narrow, and the other is wide and flat, as shown in Section 3.1. For simplicity, the two Gaussians here are expressed with two different positions and two different widths. Focusing on only the first integral, one can see that it is simplified significantly by substitution.

$$a_2 \int_{\mu_1}^{\infty} c \frac{1}{\sigma_1 \sqrt{2\pi}} e^{-\frac{(z-x_1)^2}{2\sigma_1^2}} dx_1 = a_2 c \frac{1}{\sigma_1 \sqrt{2\pi}} \int_{\frac{z-\mu_1}{\sqrt{\pi}\sigma_1}}^{-\infty} -e^{-U^2} dU \sqrt{2}\sigma_1$$

Where  $U = (t - x_1)/\sqrt{2}\sigma_1$  and  $dU/dx_1 = -1/\sqrt{2}\sigma_1$  meaning  $dx_1 = -dU\sqrt{2}\sigma_1$ . By flipping the limits and identifying that  $\sqrt{2} = 2/\sqrt{2}$  and multiplying with  $\sqrt{\pi}/\sqrt{\pi}$  the expression ends up being

$$a_2 c \frac{1}{\sigma_1 \sqrt{2\pi}} \frac{\sqrt{\pi}\sigma_1}{\sqrt{2}} \int_{-\infty}^{\frac{z-\mu_1}{\sqrt{\pi}\sigma_1}} \frac{2}{\sqrt{\pi}} e^{-U^2} dU \sqrt{2}\sigma_1 \quad (3.6)$$

Here a lot of constants cancels out and realizing that

$$\frac{2}{\sqrt{\pi}} \int_{-\infty}^z e^{-t^2} dt = \operatorname{erfc}(-z) = 1 + \operatorname{erf}(z)$$

where  $\operatorname{erf}(z)$  is the error function, then Equation 3.6 reduces to

$$\frac{a_2}{2} c \left( 1 + \operatorname{erf} \left( \frac{z - \mu_1}{\sqrt{\pi} \sigma_1} \right) \right) \quad (3.7)$$

The same process is repeated for the second Gaussian yielding similar expression

$$\frac{a_2}{2} (1 - c) \left( 1 + \operatorname{erf} \left( \frac{z - \mu_{01}}{\sqrt{\pi} \sigma_2} \right) \right)$$

Where  $\mu_{01}$  and  $\sigma_2$  is then the position and width of the second Gaussian. Introducing the notation from Section 3.1  $\mu_{01}$  is then  $\mu_1 + \mu_\Delta$  and  $\sigma_2$  is  $\sigma_1 \sigma_\Delta$ , hence the equation turns into

$$\frac{a_2}{2} (1 - c) \left( 1 + \operatorname{erf} \left( \frac{z - (\mu_1 + \mu_\Delta)}{\sqrt{\pi} \sigma_1 \sigma_\Delta} \right) \right) \quad (3.8)$$

Summing the two equations (3.7 and 3.8) result in the total contribution of fluorescence intensity arising from the peptide in the cytosol of the cell and yields the following expression

$$\frac{a_2}{2} \left[ c \left( 1 + \operatorname{erf} \left( \frac{z - \mu_1}{\sqrt{\pi} \sigma_1} \right) \right) + (1 - c) \left( 1 + \operatorname{erf} \left( \frac{z - (\mu_1 + \mu_\Delta)}{\sqrt{\pi} \sigma_1 \sigma_\Delta} \right) \right) \right] \quad (3.9)$$

The fourth and last contribution comes from the intensity level in the solution. Similar to the third contribution, this is also a step function, where the step is happening at the top membrane of the cell and the step amplitude is  $a_3$ . Repeating the process that yields Equation 3.5 - 3.9 the resulting equation for the fourth contribution is then:

$$\frac{a_3}{2} \left[ c \left( 1 + \operatorname{erf} \left( \frac{z - \mu_2}{\sqrt{\pi} \sigma_1} \right) \right) + (1 - c) \left( 1 + \operatorname{erf} \left( \frac{z - (\mu_2 + \mu_\Delta)}{\sqrt{\pi} \sigma_1 \sigma_\Delta} \right) \right) \right] \quad (3.10)$$

Each contribution has been described, and the sum of the four contributions will fully describe the intensity profile of the peptide channel. The expression used to fit the intensity profile is:

$$\begin{aligned} I(z) = & a_1 \left[ c \frac{1}{\sigma \sqrt{2\pi}} e^{-\frac{(z - \mu_1)^2}{2\sigma^2}} + (1 - c) \frac{1}{\sigma \sigma_\Delta \sqrt{2\pi}} e^{-\frac{(z - (\mu_1 + \mu_\Delta))^2}{2(\sigma \sigma_\Delta)^2}} \right] \\ & + \frac{a_2}{2} \left[ c \left( 1 + \operatorname{erf} \left( \frac{z - \mu_1}{\sqrt{\pi} \sigma_1} \right) \right) + (1 - c) \left( 1 + \operatorname{erf} \left( \frac{z - (\mu_1 + \mu_\Delta)}{\sqrt{\pi} \sigma_1 \sigma_\Delta} \right) \right) \right] \\ & + \frac{a_3}{2} \left[ c \left( 1 + \operatorname{erf} \left( \frac{z - \mu_2}{\sqrt{\pi} \sigma_1} \right) \right) + (1 - c) \left( 1 + \operatorname{erf} \left( \frac{z - (\mu_2 + \mu_\Delta)}{\sqrt{\pi} \sigma_1 \sigma_\Delta} \right) \right) \right] + b \end{aligned} \quad (3.11)$$

In Equation 3.11 only 4 parameters are fitted because the position of bottom and top,  $\mu_1$  and  $\mu_2$ , were found using the membrane signal.  $\sigma$ ,  $\sigma_\Delta$  and  $\mu_\Delta$  were all found previously in Section 3.1. The 4 parameters fitted are  $a_1$ , which is the amplitude of the peptide that is accumulated at the membrane of the bottom cell.  $a_2$ , which is the amplitude of the intensity level inside of the cell.  $a_3$ , which is the intensity of the solution and lastly,  $b$  is the background level and is assumed constant.

### Nucleus signal

The nucleus signal is only used to make sure that the sampling of the intensity is not inside of the nucleus.

## 3.3.3 Verifying Cell Model and Fluorescence Model for Quantification of Cellular Transport

After deconvoluting the intensity signal, the next step was to verify the quantification of peptide transport over time. To do so, a cell-penetrating peptide, TAT, with a FITC ( $\text{Ex}_\lambda = 490 \text{ nm}/\text{Em}_\lambda = 525 \text{ nm}$ ) fluorophore attached to it was used. TAT is known to penetrate the cell membrane [76] hence it is expected that this molecule is suitable for testing the quantification method. However, the Caco-2 cells are only grown in a monolayer for 48 hours in this simple cell model. Thus, to ensure that the transport of TAT, or any other molecule, is not due to paracellular transport occurring due to inadequate barriers, we used two different molecules to verify the integrity of the barriers. The two molecules were 4 kDa FITC-dextran and 400 Da Lucifer Yellow ( $\text{Ex}_\lambda = 430 \text{ nm}$  and  $\text{Em}_\lambda = 544 \text{ nm}$ ). They are both used to validate barrier integrity for endothelial cell monolayers [74] [75].

### 3.3.3.1 Uptake of TAT

To investigate if the physical model resulting in Equation 3.11 worked, TAT-FITC was added to the solution and measured over time. The cells were imaged every 40 minutes for 240 minutes (4 hours) before ending the experiment. Figure 3.12 shows the intensity profile of the TAT. The top row in Figure 3.12 shows the intensity profile for the membrane signal in red and the intensity profile for the peptide signal in green. The two intensity profiles are from right after adding TAT-FITC to the solution of the cells. The bottom row shows the same cell, but 40 minutes after adding TAT-FITC.

Here we see two things: a shift in the cell's position in  $z$  and an increase in the peptide signal at the position of the bottom membrane of the cell. Because of the change in  $z$  over time, we need to fit the position of the cell membranes at each time point. To verify that there is an increase in the accumulated peptide we fit the peptide intensity signal. The image in Figure 3.13 shows a  $z$ -slice of a typical example of a cell, where the red represents the membrane of the cell, the blue represents the nucleus, and the green represents the peptide, TAT. The TAT is seen as either aggregates

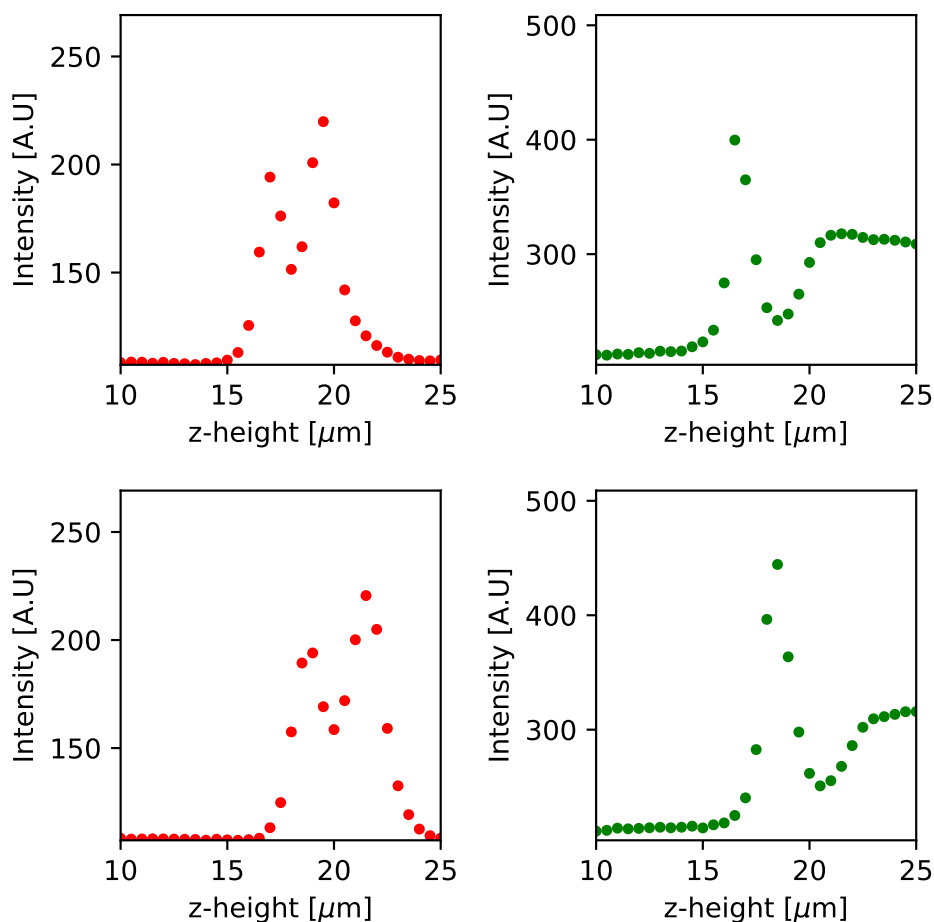


**Figure 3.12.** The membrane intensity profile is shown as red points and peptide intensity profile is shown as green points. The upper row shows the membrane and peptide intensity signal just after adding TAT-FITC. The bottom row shows the membrane and peptide intensity signal of the same cell, but 240 minutes later.

or TAT in organelles inside of the cell, but also as a diffusive signal. The graph in Figure 3.13 shows three of the four fitted parameters from Equation 3.11 because all of the parameters are background subtracted. The blue dots represent the solution level of TAT-FITC, which is stable at around 90 A.U. over the four hours of imaging. The red dots represent the intensity level of TAT-FITC inside of the cells, where the intensity level starts around 2 A.U. (see Figure A.3 for a zoom in) and ends at around 40 A.U, which is a 20 fold increase of the cytosolic content over four hours.

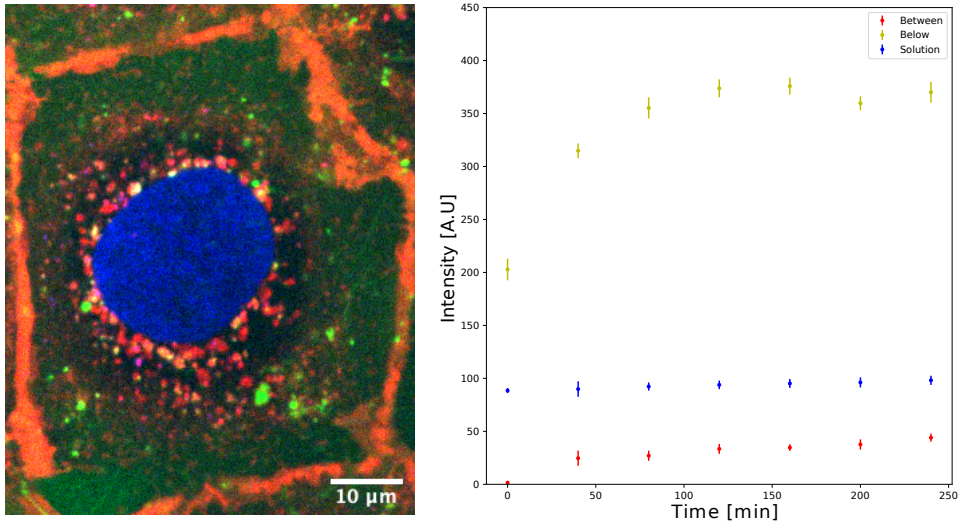


**Figure 3.13.** The left image shows a typical example of a cell with the membrane in red, the nucleus in blue, and the peptide, TAT-FITC, in green. The right graph shows three parameters used to fit the intensity profile of multiple cells of TAT-FITC: below (yellow), between (red), and solution (blue) plotted over time.  $N = 10$  cells. Error bars are S.E.M. Background is subtracted from each of the parameters.

Lastly, the yellow dots show the amount of peptides co-localizing with the bottom membrane as a function of time. The initial intensity for TAT-FITC under the cell is 200 A.U., and over the period of 4 hours, it increases to 350 A.U. for a 1.5 fold increase. These results show that the model can quantify transport accumulating TAT at the bottom membrane and the cytosolic content. From the calibration curve seen in Figure A.2 we calculate the concentration of TAT-FITC in solution to be 3.5  $\mu\text{M}$ . At approximately 2  $\mu\text{M}$  the mechanism of uptake of TAT goes from translation to endocytosis [76]. This explains the endosome-like structure seen in Figure 3.13.

### 3.3.3.2 Tight Junction Integrity

The previous section showed that the physical model describing the intensity profile could detect and quantify changes in the amount of peptide in the cytosol and the amount of peptide co-localized with the bottom cell membrane. To make sure that the peptide signal at the bottom membrane of the cells is coming from the peptide being transported through cells with adequate barrier integrity, we did two negative controls. We used Four kDa Dextran-FITC and 400 Da lucifer yellow for this purpose. Figure 3.14 shows the three parameters that describe the intensity level below the cell, in the cell, and the solution level. Figure 3.14A shows the three parameters describing the intensity profile of 4 kDa dextran-FITC over time. The solution level

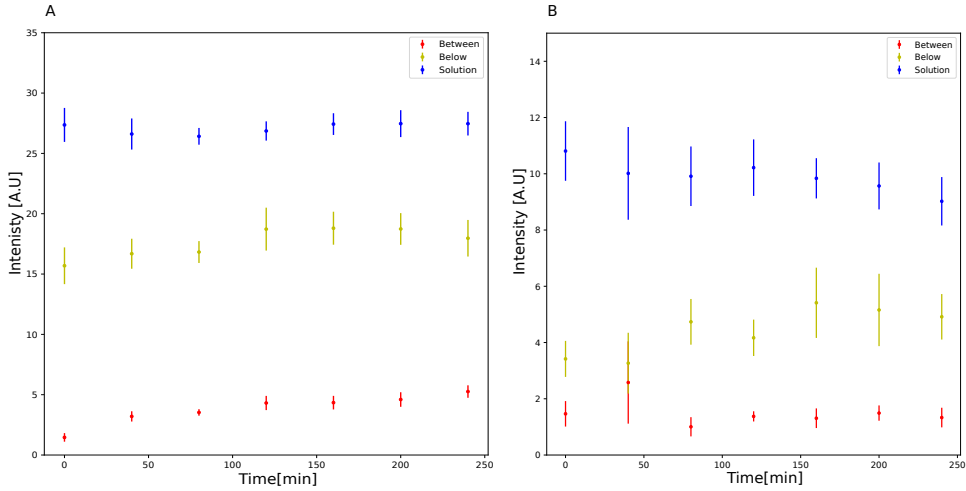


**Figure 3.14.** Shows the results of two negative controls to verify the barrier integrity. The molecules used are 4kDa dextran-FITC and lucifer yellow. A) shows the three parameters used to fit the intensity profile of dextran-FITC. The yellow data points represent the amount of peptide transport through the cells. The red data points represent the amount of peptides inside the cells. Lastly, the blue data points represent the solution level.  $N = 6$  cells. B) show the three parameters describing the intensity level for lucifer yellow. The yellow data points represent the amount of peptide transport through the cells. The red data points represent the amount of peptides inside the cells. Lastly, the blue data points represent the solution level.  $N = 5$  cells. Error bars are S.E.M.

and the amount of peptide accumulating at the bottom membrane are both stable over time. From the calibration curve of FITC (seen in the appendix, Figure A.2) the concentration of dextran-FITC in solution is approximately  $1 \mu\text{M}$ . Furthermore, it means that the barrier is tight for molecules with a size of 4 kDa. The cytosolic content increases of dextran over time. The signal increases slightly from approximately 2 A.U to 4 A.U, resulting in a two-fold increase in cytosolic content. These results indicate that the tight junctions formed are tight when adding a peptide of 4 kDa, but it also shows that the model can detect when the peptide is only taken up by the cell but not transported through the cell. Figure 3.14B shows the three parameters describing the intensity profile for Lucifer yellow. Lucifer yellow is a small molecule of approximately 400 Da, which is 10x smaller than dextran. All three parameters are stable over time and within the error bars. This means that the barriers formed by the cells growing for two days are also tight with small molecules of 400 Da.

### 3.3.4 Summary

By deconvoluting the peptide intensity signal, it was possible to obtain the physical model, describing the peptide intensity profile with an analytical expression. This allowed for the quantification of four parameters in total: background level, accumulated peptide at the bottom of a cell membrane, the cytosolic content, and the solution level. The three last parameters were all background subtracted to get the pure intensity contribution from each parameter. This model was tested by adding TAT-FITC to the solution and imaging a z-stack of the cells every 40 minutes for 4 hours. This showed that the model could detect and quantify changes in the cytosolic content but also the amount of accumulated peptide underneath the cells, as seen in Figure 3.13.

Furthermore, the model was used to verify the barrier integrity of the simple cell model. The cells are only grown for 48 hours thus, so to make sure that the barriers function, we added dextran and Lucifer yellow to the solution. These molecules are known not to undergo paracellular transport, which means no accumulation of peptides underneath the cells if the tight junctions are tight. Figure 3.14 shows that we see no transport across the cell layer for either dextran or lucifer yellow, meaning that the cell had adequate barriers within the 48 hours of growth.





## CHAPTER 4

# Quantitative imaging of lipidated Salmon Calcitonin Transport through an Epithelial Cell Layer

---

In this chapter, three different sCT peptide analogs were tested against each other. The first sCT analog is the native sCT called sCT(C0/C0). The second analog is modified with two C4 chains and is called sCT(C4/C4). The third analog is modified with two C8 chains and is called sCT(C8/C8). The peptides were modified to test if the modifications will improve the uptake or transport across cells. All of the peptide analogs has an atto488 molecule attached for detection of fluorescence and ultimately to quantify the transport.

Next, we investigated the uptake mechanism by inhibiting endosome formation dependent on dynamin, or lowering the temperature. We wanted to change the conditions to show if the peptide modifications change the transport mechanism through the cells.

We then characterize the number of peptides in a peptide aggregate with the goal of knowing the oligomeric state of the peptide. We wanted to know if the difference in transport arises from a difference in oligomeric state. To characterize the number of peptides in a peptide spot, each sCT analog was deposited on a glass surface and bleached with TIRF. From the intensity time trace we counted the number of bleaching steps, which corresponds to the number sCT molecules in a spot.

Lastly, we give an outlook of how the model can be applied to a different cell model. More specifically we used a microfluidic model called an OrganoPlate where the cells are fully differentiated and polarized, meaning they are more alike to their native

environment. We add the three sCT analogs and measure the transport across the cells for four hours and quantify the transport. Furthermore, we expand the model to also quantify the membrane partitioning at the upper membrane of the cell. We do this by sampling the intensity profile through the nucleus to increase the distance between the upper and bottom membrane of the cell for less overlap in the signal, and by adding an additional fitting parameters to the fitting model.

## 4.1 Single Cell Analysis of Lipidated Peptide Cellular Transport

This section will show the results of adding sCT(C0/C0), sCT(C4/C4), and sCT(C8/C8) to a monolayer of Caco-2 cells and imaging every 40 minutes for four hours. The purpose of adding the lipidated sCT is to quantify if the uptake or transport across intestinal barriers is dependent on the lipid chain size.

### 4.1.1 Salmon Calcitonin C0/C0

The reasoning behind modifying sCT with fatty acid lipid chains is to increase the ability to transport across the Caco-2 cell layer. Hence, to establish a transport baseline, the native sCT was investigated initially by adding 1  $\mu$ M of sCT(C0/C0). Figure 4.1A shows the peptide intensity profile just as sCT(C0/C0) was added to the solution. Figure 4.1B shows the intensity profile for the same cell as in 4.1A, but 240 minutes after adding sCT(C0/C0). Figure 4.1C shows three different parameters describing the intensity levels in the cell experiment. The red data points represent the cytosol intensity level. Here it shows that the peptide is not taken up into the cytosol of the cell. The blue data points represent the solution level, where it is stable at 15 A.U. From the calibration curve in Figure 3.7 we can convert the intensity to a concentration. The concentration in the solution level is calculated to be 0.75  $\mu$ M. This is slightly lower than the expected concentration of 1  $\mu$ M. It should be noted that the calibration curve in Figure 3.7 is made with free atto488 fluorophore, hence it is an assumption that the peptide in solution is behaving as free fluorophores. The yellow data points in Figure 4.1C represent the amount of peptide co-localizing with the bottom membrane and it shows that the signal increases from 10 A.U. to 15 A.U. for 1.5x increase. We use the results as a baseline for transport of unmodified sCT, we can compare the effects of lipidation of sCT. Furthermore, as there is no increase over time in the cytosol it suggests that the transport mechanism across the cells does not depend on transport through the cytosol.

For the rest of the figures in this chapter, the blue data points will represent the solution level, red data points will represent the intensity level in the cytosol and the yellow data points will represent the accumulation at the bottom membrane.

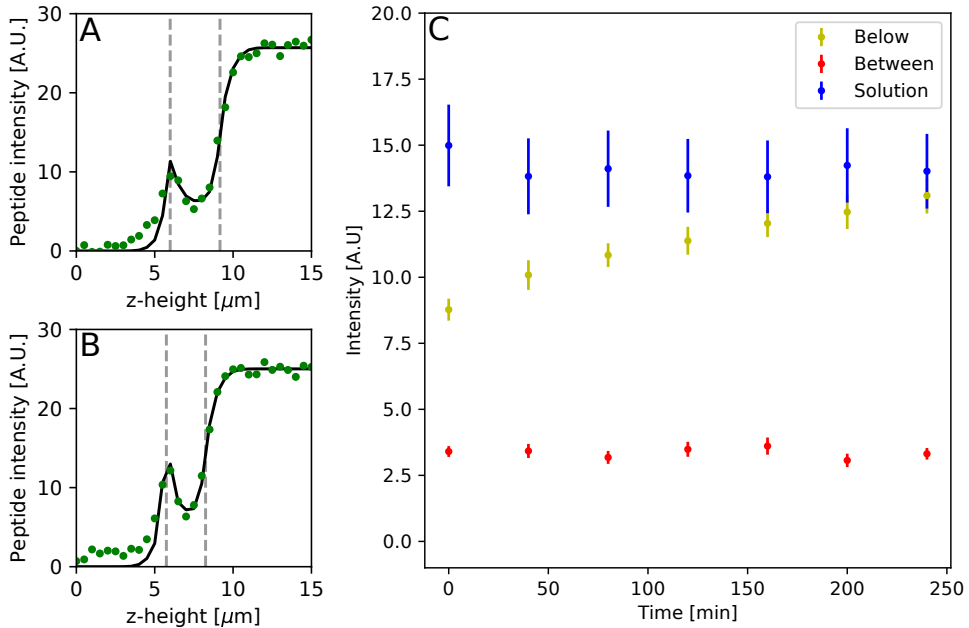


**Figure 4.1.** Overview of Caco-2 cells with sCT(C0/C0) added. A) Shows the intensity profile for sCT(C0/C0) just after adding sCT(C0/C0) at  $t = 0$  min as the green dots. Vertical dashed lines indicate the positions of the membranes, and the solid black line is the fit to the data. B) Shows the intensity profile for the same cell as in A), but at  $t = 240$  min as green data points. Vertical dashed lines indicate the positions of the membranes. The solid black line is the fit to the data. C) Shows the three parameters, with the estimated background subtracted, used to fit the intensity profile: solution level in blue, cytosolic content in red, and accumulated peptide underneath the bottom cell in yellow. The experiment was running for 4 hours total and imaged every 40 minutes for seven time points. Error bars are SEM.  $N = 24$  cells.

#### 4.1.2 Salmon Calcitonin C4/C4

The second peptide analog tested was sCT(C4/C4)-atto488. Like with sCT(C0/C0),  $1 \mu\text{M}$  of sCT(C4/C4) was added to the solution of the cells. Figure 4.2A shows the intensity profile just as sCT(C4/C4) was added to the cells. Figure 4.2B shows the intensity profile of the same cell but 240 minutes after adding sCT(C4/C4). Figure 4.2C shows the parameters used to quantify the intensity profiles. The solution level is around 15 A.U., which corresponds to  $0.75 \mu\text{M}$ . This is slightly lower than the expected concentration of  $1 \mu\text{M}$ . The cytosolic intensity level is stable around 4 A.U. throughout the experiment, suggesting that lipidating sCT with two C4 chains does not increase the uptake into to cytosol. The amount of co-localized peptide with the bottom membrane of the cell increases from 10 A.U. to 15 A.U., for a total increase

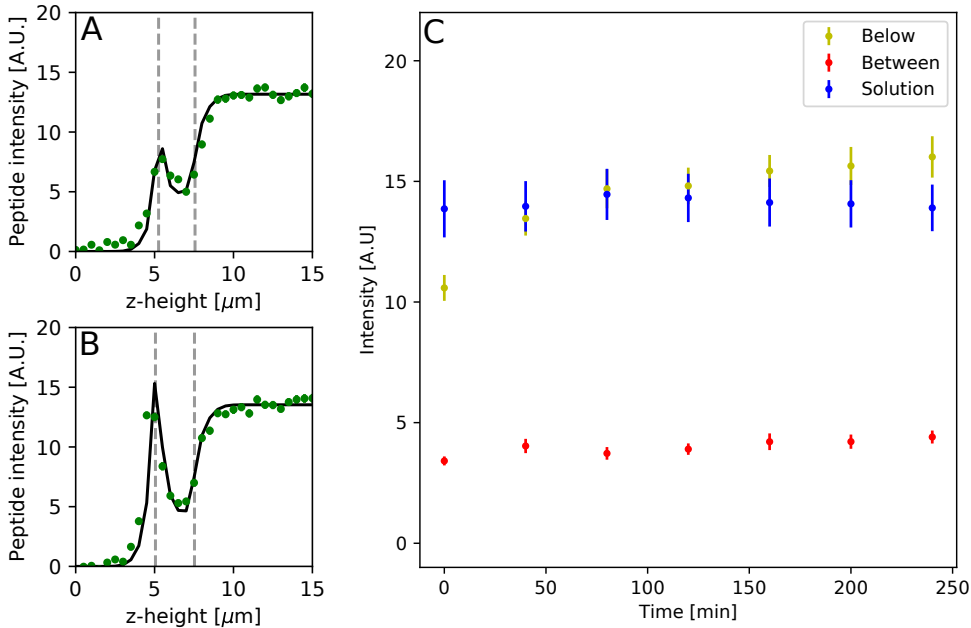


**Figure 4.2.** Overview of Caco-2 cells with sCT(C4/C4) added. A) Shows the intensity profile of a cell just after adding sCT(C4/C4) at  $t = 0$  min as the green points. The black line is the fit to the data. The two vertical lines represent the position of the two membranes. B) Shows the intensity profile for the same cell as in A), but at  $t = 240$  min, shown as the green points. The black line is the fit to the data. The vertical lines represent the position of the membranes. C) Shows the three parameters, with the estimated background subtracted, used to fit the intensity profile of sCT(C4/C4) for each time point. The blue data points represent the solution level, the red data points represent the cytosolic content, and the yellow data points represent the accumulated peptide underneath the cells. Error bars are SEM.  $N = 38$  cells.

of 1.5x. Comparing sCT(C0/C0) and sCT(C4/C4) we see that the accumulation at the bottom membrane stagnates at the same total increase, however sCT(C4/C4) reaches an increase of 1.5x already after 80 minutes, whereas sCT(C0/C0) reaches 1.5x increase after 240 minutes. This shows that sCT(C4/C4) transports faster through the cell layer comped to sCT(C0/C0). This also highlights the importance of doing live cell imaging, and not only endpoint measurements. Had we only done endpoint measurements, then we would not have observed the differences between sCT(C0/C0) and sCT(C4/C4).

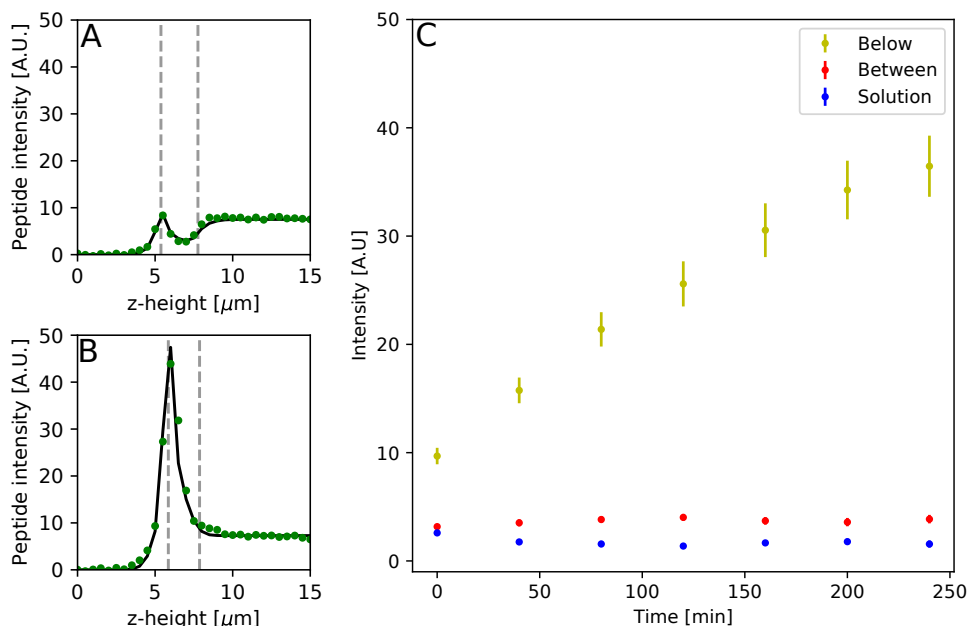


**Figure 4.3.** Overview of Caco-2 cells with sCT(C8/C8) added and imaged every 40 minutes for four hours. A) Shows the intensity profile for a single-cell after adding sCT(C8/C8) at  $t = 0$  min, seen as the green dots. The black line is the fit to the data. B) Shows the intensity profile of the same cell as in A) but at  $t = 240$  minutes, seen as green dots. The black line is the fit to the data. The vertical lines in A) and B) represent the position of the bottom and top membrane of the cell. C) Shows the three parameters used to fit the intensity profile of sCT(C8/C8), with the background-subtracted. The red and blue data points represent the cytosolic content and solution level, respectively. The yellow data points represent the accumulated peptide underneath the cells. Error bars are SEM.  $N = 30$  cells

### 4.1.3 Salmon Calcitonin C8/C8

The last analog tested was sCT(C8/C8). Similar to the experiments with sCT(C0/C0) and sCT(C4/C4), we added  $1 \mu\text{M}$  of the peptide to the solution. Figure 4.3A shows the intensity profile just after adding sCT(C8/C8). Figure 4.3B shows the intensity profile of the same cell, but 240 minutes after adding sCT(C8/C8). Just from comparing Figure 4.3A and B it is clear to see that sCT(C8/C8) transport a lot compared to sCT(C0/C0) and sCT(C4/C4). Figure 4.3C shows the parameters describing the intensity profiles. The solution level is 2.5 A.U., which is very low compared to sCT(C0/C0) and sCT(C4/C4). The concentration of sCT(C8/C8) was only  $0.13 \mu\text{M}$ , which is much lower than the expected concentration of  $1 \mu\text{M}$ . The low concentration is probably due to poor peptide solubility due to increasing the length of the lipid chains.

Furthermore, we see that the intensity level in the cytosol does not change over time. This suggests that increasing the length of the lipid chains does not increase the cytosolic uptake. Lastly, the amount of peptide co-localizing with the bottom membrane increases 10 A.U. to 37 A.U., which is an increase of 3.7x. By comparing this to sCT(C0/C0) and sCT(C4/C4) it shows that sCT(C8/C8) transports through the cells much faster, but also much more. Between  $t = 0$  minutes and  $t = 160$  minutes the peptide transports at a constant rate before it slows down. We can also see that the amount of sCT(C8/C8) accumulating at the bottom membrane of the cells increases well above the solution level. This suggests that it is some sort of active transport that facilitates the accumulation of sCT(C8/C8) at the bottom membrane. Another factor could be that if the peptide is transported across the bottom membrane, then there is no way for the peptide to move, hence it is stuck at the surface underneath the cells.

#### 4.1.4 Summary

This section showed the transport across cells of three different sCT analogs: sCT(C0/C0), sCT(C4/C4), and sCT(C8/C8). We fitted the intensity profiles and extracted parameters describing the transport and uptake through a monolayer of Caco-2 cells. By finding the intensity in the solution level we were able to calculate the peptide concentration in the experiments using a calibration curve. For sCT(C0/C0) and sCT(C4/C4) we had a concentration of  $0.75 \mu\text{M}$ , which is slightly lower than the expected concentration of  $1 \mu\text{M}$ . For sCT(C8/C8) the concentration was only  $0.13 \mu\text{M}$  due to poor peptide solubility. More interestingly, all analogs showed no increase in the cytosol, but shows a very different transport across the cell layer. sCT(C8/C8) showed the highest amount of accumulation at the bottom cell membrane of 3.7-fold increase, whereas sCT(C4/C4) and sCT(C0/C0) showed a 1.5-fold increase. For sCT(C0/C0) and sCT(C4/C4) they reached this level at very different time points, thus showcasing the need for live cell imaging.

Furthermore, the transport of sCT(C8/C8) increases well above the solution level, which indicates that is an active transport. For sCT(C0/C0) and sCT(C4/C4) it looks as if the transport stops when the intensity level of the peptide at the bottom membrane of the cell reaches the same intensity level as in the solution. This would indicate that it is some sort of equilibrium.

## 4.2 Verifying transport is successful

In this section, we show results to verify that the peptide passes through the bottom membrane of the monolayer. This is done by adding EDTA to disrupt the cells after incubating with sCT(C8/C8) for four hours. Furthermore, we want to know if the cells have any form of autofluorescence. We do this by measuring through cells before adding any peptide and plot the intensity profile. Lastly, Figure 4.3 shows that the

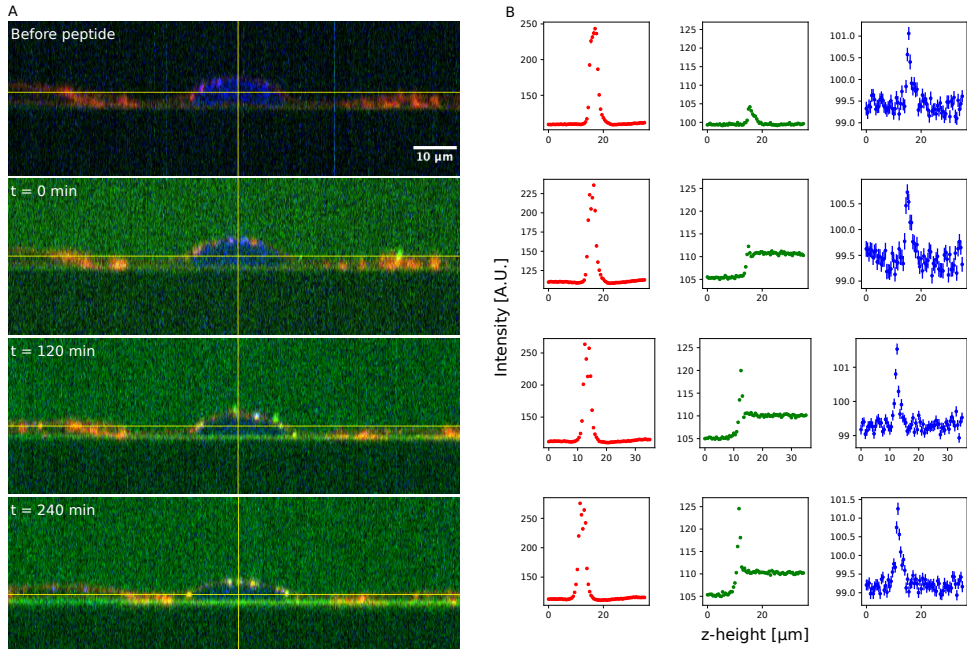


**Figure 4.4.** A qualitative overview of a single cell before, and after adding sCT(C8/C8) compared to the extracted intensity profiles. A) Four images with the membrane stained in red, the nucleus stained in blue, and the peptide in green. The top image is before adding the peptide. The next image is just as we added sCT(C8/C8). The next two images are at 120 minutes after adding sCT(C8/C8) and 240 minutes after adding sCT(C8/C8), respectively. B) Shows the intensity profiles of the cell seen in A) at the specified timepoints when sampling through the cell's cytosol. The red signal shows the membrane intensity signal, the peptide intensity signal in green, and the nucleus intensity signal in blue.

solution level drops slightly from  $t = 0$  minutes to  $t = 40$  minutes. To investigate this a peptide solution was imaged in a well only containing buffer to see how fast it reaches equilibrium.

#### 4.2.1 Initial intensity before adding peptide

Figure 4.3 shows that at  $t = 0$  min (just after adding the peptide and readjusting any movement) the intensity level in the solution is below the intensity level of accumulated peptide at the bottom membrane. To better understand why the initial intensity is so high, we imaged a FOV with cells labeled with CellMask DeepRed (for the membrane) and Hoechst (for the nucleus) before adding any peptide. Figure 4.4A shows an XZ view of a single cell in the imaged FOV. The red color represents the labeled cell membrane, and the blue color represents the labeled nucleus. Before



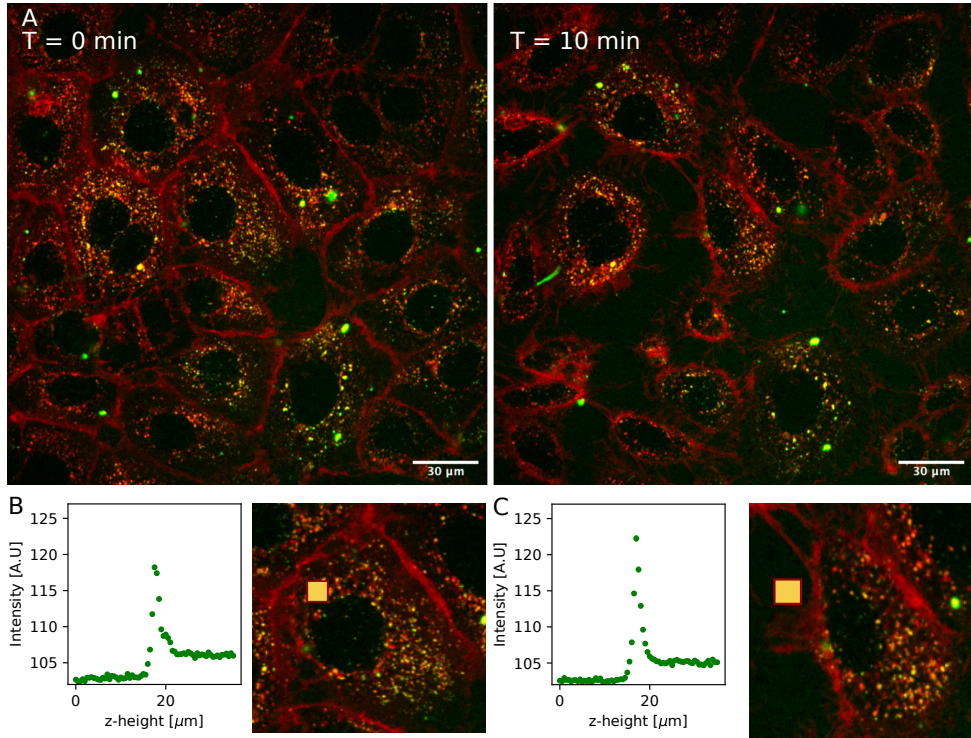
adding any peptide to the FOV, there is no apparent signal in the green channel.

Figure 4.4B shows the extracted intensity profiles for all three imaging channels. From the extracted intensities, we see that for the green peptide channel, there is a small peak of approximately 5 A.U. at the same place as the membranes, seen in red. We suspect that this comes from auto fluorescence from the cells. After imaging with no peptide present, we added sCT(C8/C8) to the FOV and started imaging. Figure 4.4A second row shows a qualitative image of the same cell as before adding the peptide. The Figure shows a clear peptide signal in the solution and that some peptides as larger aggregates at the cell membrane, or individual peptides in organelles. By looking at the intensity profiles in Figure 4.4B just after adding the peptide, the intensity profile has also changed. The solution level is only 5 A.U. above the background level. We also see a tiny peak at the position of the bottom membrane. The amplitude of the peak is approximately 7 A.U. above the background level. Following the same cell at 120 and 240 minutes after adding the peptide shows a higher and higher degree of accumulation of peptide near the membrane of the cell in Figure 4.4A, but also in the intensity profiles in Figure 4.4B.

From 4.3 we see that the intensity below the cells is higher than the solution level. In Figure 4.4 we show that this is because we have some intensity from the cell that is higher than the solution level in 4.3. Furthermore, sCT(C8/C8) show a fast transport over time, hence it is not unlikely that the peptide has transported a bit before we start the imaging. We don't see that the initial value for sCT(C0/C0) and sCT(C4/C4) at  $t = 0$  min is higher than the solution level because we have a higher concentration of sCT(C0/C0) and sCT(C4/C4). Another contributing factor could be because of the kinetics of sCT(C0/C0) and sCT(C4/C4) are slower than for sCT(C8/C8).

## 4.2.2 Disrupting barrier integrity

As the cells are grown on a glass surface, there is no space underneath the cells where the peptide can move after transporting through the cells. Therefore, it is impossible to know if the peptide is inside the cells or transported across the membrane. When looking at the intensity profiles it is not possible to tell if this is the case due to the diffraction limit. To verify that the peptide transports through the monolayer, we did an experiment where we added sCT(C8/C8) to a well with cells labeled with CellMask deep red and Hoechst. After a four-hour incubation period, we removed the peptide solution and added 1  $\mu$ M of EDTA to the cells. Adding the EDTA disrupts the tight junctions and shrinks the cells. After adding the EDTA, we imaged the cells every 5 minutes for an hour. However, after only 10 minutes, the cells had already shrunk from one another, as seen in Figure 4.5A. Here the same cells are seen just after adding EDTA (left image) and 10 minutes after adding the EDTA (right image). Figure 4.5B shows a single cell at  $t = 0$  min with a yellow square inside of it. We sample the intensity inside this ROI in each z-slice. Figure 4.5B also shows the resulting intensity profile. The intensity profile shows a peak in the center of the



**Figure 4.5.** Disrupting the tight junctions and cell to cell adhesion with EDTA verifying the transport of the peptide through the cells. The cells were incubated with sCT(C8/C8) for four hours before adding 1  $\mu$ M EDTA. A) shows just as we added EDTA (left) and 10 minutes after (right). The red is the membrane, and the green is the peptide dots. For better visualization, we left the nucleus stain out. B) Shows the intensity profile of a single cell from just as we added EDTA. We sampled the intensity at the position of the yellow box. C) shows the same cell and sampling the intensity in the same location as in B) but 10 minutes after adding EDTA.

z-stack, overlapping with the position cell membrane. After the 10 minutes in the same ROI, we sampled the intensity as seen in Figure 4.5C. However, the ROI is not in the cell anymore as the cell has detached from neighboring cells and shrunk down. Nevertheless, the intensity profile still shows a peak in the same position as in Figure 4.5B.

The results in Figure 4.5 confirms that the peptide has been transported through the cell and is now binding to the surface. This means that the model can be used to study the transbarrier transport.

### 4.2.3 Solution equilibrium over time

By inspecting Figure 4.3 it shows that the initial solution level at  $t = 0$  min is higher than that of  $t = 40$  min. To investigate why that is sCT(C8/C8) was added to some cells and imaged continuously for 5 minutes. Here, we initiated the imaging acquisition by a z-stack of a single FOV. For the first minute, no peptide is present, so the solution level is 0 A.U. After 1 minute of imaging, the peptide was added, which resulted in a significant increase to around 75 A.U. The intensity level decreases for the next three minutes from 75 A.U. to 5 A.U., where it reaches an equilibrium. The plot can be seen in the appendix Figure A.4.

The same FOV is only imaged every 40 minutes during a typical experiment. This time far exceeds the time needed for the peptide to distribute in the solution. Figure 4.3 shows that the initial solution level is higher than that of the later time points. The drop in intensity is likely due to initiating imaging before the peptide has distributed evenly in the solution. One could, of course, wait approximately 5 minutes after adding the peptide before starting the imaging. However, by doing that, one will lose the initial transport of the peptide. As it is the transport of the peptides that are of interest, we opted to start the experiment as soon as possible after adding the peptide.

### 4.2.4 Summary

In this section, we verified that the peptide transports through the cells. We did this by adding EDTA to disrupt the tight junctions and shrink the cells. Furthermore, we explained how the peak in the intensity signal of sCT(C8/C8) is higher than the solution level at  $t = 0$  min, which is due to fluorescence from the cells. Lastly, we explained why the intensity in the solution drops from  $t = 0$  min to  $t = 40$  min in Figure 4.3 because imaging is initiated before the peptide solution has fully mixed.

## 4.3 Comparison of the three analogs

This section will compare the various peptide analogs with statistical tests to show if there is a significant difference in the transport when increasing the size of the lipid chains. To see if the three peptides show different transport patterns, the amount of accumulated peptide over time is plotted for each of the peptides as seen in Figure 4.6. Plotting the data as the relative increase makes it easier to compare and visualize differences between the peptide analogs. We find the relative increase by dividing the intensity level at every time point by the intensity level of the first time point. In Figure 4.6, the blue data points represent the amount of sCT(C0/C0) transported through over time. The yellow data points represent the transport of sCT(C4/C4) over time. The transport happens rapidly for the first 80 minutes before stagnating. Comparing sCT(C0/C0) and sCT(C4/C4), they have a relative increase of roughly

1.5x after 240 minutes. Lastly, the green data points represent the relative increase of sCT(C8/C8) over time. Compared to sCT(C0/C0) and sCT(C4/C4), sCT(C8/C8) exhibits a much higher degree of transport. After 40 minutes, the relative increase has passed that of sCT(C0/C0) and sCT(C4/C4) for the whole experiment duration. The transport of sCT(C8/C8) continues to increase linearly until 160 min through the experiment when the increase slows down. The experiment did not run long enough to know if the transport would reach a plateau.

Looking at Figure 4.6 it is clear to see by eye that there is a difference between transport of sCT(C8/C8) and the other two analogs. However, to quantify if they are significantly different, we needed to do statistical tests on the data. Before doing any tests, we need to verify whether the data consistent with a normal distributed to determine which statistical test to use. To test if the data is consistent with a normal distributed, we used a  $\chi^2$  goodness of fit ( $\chi^2$ -GOF) test. The  $\chi^2$ -GOF is defined as:

$$\chi^2 = \sum_{i=1}^n \left( \frac{E_i - O_i}{E_i} \right)^2$$

where  $E_i$  is the expected value of bin number  $i$ ,  $O_i$  is the observed value in bin number  $i$ , and  $n$  is the number of total data points. Therefore, to calculate the  $\chi^2$ , we plotted the relative increase of the peptides as histograms. Figure 4.7 shows three different histograms, showing the relative increase at  $t = 240$  min for each of the peptides in blue and the resulting normal distribution with the expected values in green. Figure 4.7A shows the distribution of the relative increase after 240 min transport of sCT(C8/C8). Most data centers around a relative increase of 3, but a few extreme points at around 8x relative increase. After finding the observed values, we need to find the expected value to get a  $\chi^2$  value.

We fit the sCT(C8/C8) data to a Gaussian distribution to estimate the mean value and a standard deviation. We then used the mean and standard deviation to calculate the expected values like this:

$$E = \sum O \frac{1}{\sigma\sqrt{2\pi}} \exp \left( -\frac{1}{2} \left( \frac{bins - \mu}{\sigma} \right)^2 \right)$$

where  $E$  is the expected values at the positions given in the bins, which come from the observed data.  $\mu$  is the estimated mean of the data, and  $\sigma$  is the estimated standard deviation of the data.  $O$  is the sum of the observed values, which in this case is the number of data points in the histogram. The expected values for sCT(C8/C8) is seen in Figure 4.7A as the green bars.

We tested if the data is consistent with a normal distribution in our data which means this is the null hypothesis,  $H_0$ , and the alternative hypothesis,  $H_1$ , is that the data is not consistent with a normal distribution. We calculated the  $\chi^2$  value, and found a p-value. For sCT(C8/C8), the p-value is  $5.8 \times 10^{-6}$  with seven degrees of freedom, and with an  $\alpha$  value of 0.05, we reject the null hypothesis. Figure 4.7B shows the distribution of sCT(C4/C4) at  $t = 240$  min. Most of the observations are

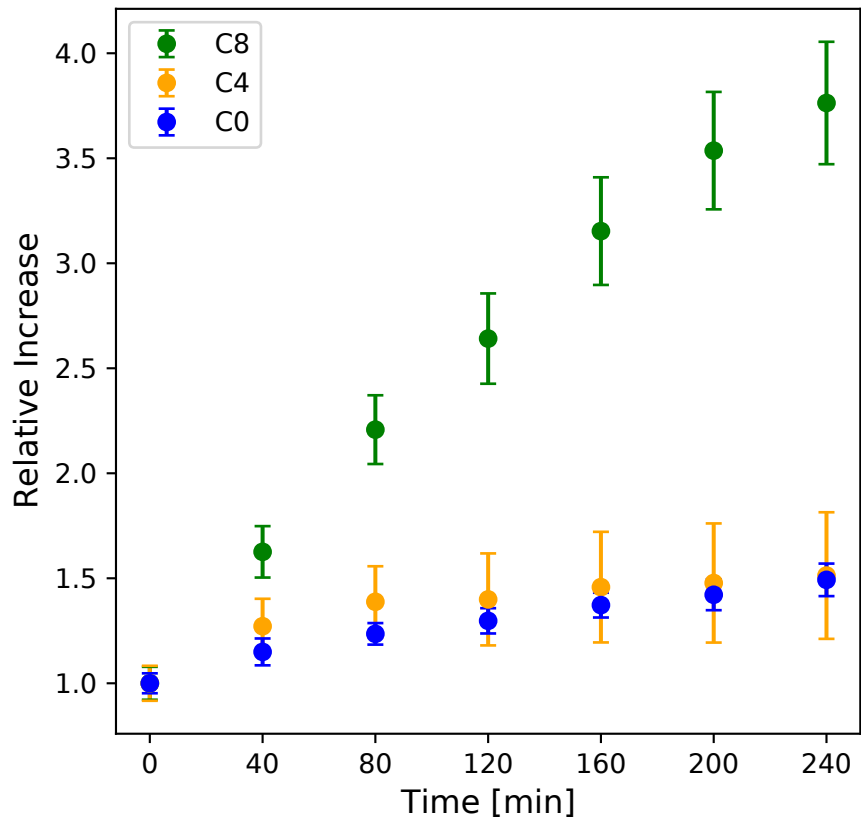


**Figure 4.6.** A comparison of the three sCT analogs and how much is transported over time relative to  $t = 0$  min. The blue data points represent the accumulation of sCT(C0/C0) over time.  $N = 24$  cells, error bars are  $\pm$  SEM. The yellow data points represent the accumulation of sCT(C4/C4) over time.  $N = 38$  cells error bars are  $\pm$  SEM. The green data points represent the accumulation of sCT(C8/C8) over time.  $N = 30$  cells error bars are  $\pm$  SEM.

around the 1.5x relative increase. However, there is one outlier, around a 3x relative increase. By doing the  $\chi^2$ -GOF test on the data from sCT(C4/C4), we got a p-value

	sCT(C8/C8)	sCT(C4/C4)	sCT(C0/C0)
sCT(C8/C8)	1	$5.4 \times 10^{-16}$	$6.24 \times 10^{-15}$
sCT(C4/C4)	$5.4 \times 10^{-16}$	1	0.65
sCT(C0/C0)	$6.24 \times 10^{-15}$	0.65	1

**Table 4.1.** The p-values of pairwise testing sCT(C0/C0), sCT(C4/C4) and sCT(C8/C8) against each other.

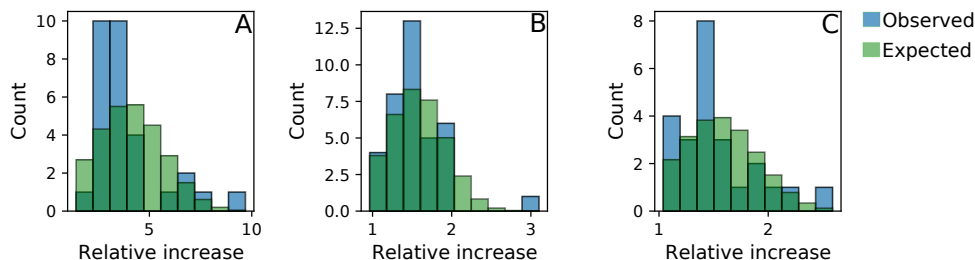


**Figure 4.7.** The transport of the sCT analogs after four hours was tested if they followed a normal distribution by using the  $\chi^2$  goodness of fit test. A) Shows the distribution of sCT(C8/C8) at  $t = 240$  min in blue compared to the expected values of a Gaussian with mean and sigma estimated from the sample. B) Shows the distribution of sCT(C4/C4) at  $t = 240$  min in blue compared to the expected values of a Gaussian with mean and sigma estimated from the sample. C) Shows the distribution of sCT(C0/C0) at  $t = 240$  min in blue compared to the expected values of a Gaussian with mean and sigma estimated from the sample.

p-value for A) is  $5.8 \times 10^{-6}$ . p-value for B) is  $4.3 \times 10^{-4}$ . p-value for C) is 0.038.

of  $4.3 \times 10^{-4}$ . With an  $\alpha$  value of 0.05, we reject the null hypothesis, meaning that the sCT(C4/C4) data is not consistent with a normal distribution. Figure 4.7C shows the distribution of the transport of sCT(C0/C0) at  $t = 240$  min. We calculated the  $\chi^2$  test statistics with 7 degrees of freedom and found a p-value of 0.038. At an  $\alpha$  value of 0.05 the null hypothesis is rejected. Hence the data from sCT(C0/C0) is not consistent with a normal distribution.

After verifying that the data is not consistent with a normal distribution, we use a non-parametric test to test if the three distributions seen in blue in Figure 4.7 come from the same distribution. To this end, we use a Kruskal-Wallis test. The null hypothesis using this Kruskal-Wallis test is that sCT(C0/C0), sCT(C4/C4) and sCT(C8/C8) come from the same/identical distribution with the same/identical median value. The alternative hypothesis is that at least one of the three peptides is different from one another [79]. The p-value returned from the Kruskal-Wallis test was  $2.2 \times 10^{-12}$ , and with an  $\alpha$  value of 0.05 the null hypothesis is rejected hence the alternative hypothesis is accepted, meaning that at least one of the peptides has values drawn from a different distribution, meaning that the transport properties are different. Because the Kruskal-Wallis test showed that there is a difference between the three peptides, a *post hoc* test can be performed, which will test the three peptides pairwise. The test used is a pairwise Mann Whitney test [79]. The results are seen in Table 4.1, where the p-values are shown for the pairwise testing. Here it shows that sCT(C8/C8) is significantly different from both sCT(C4/C4) and sCT(C0/C0). However, sCT(C4/C4) and sCT(C0/C0) are not significantly different. The results from Table 4.1 show that sCT(C8/C8) is from a different distribution compared to sCT(C4/C4) and sCT(C0/C0), which are from the same distribution. Or in other words, by lipidating salmon calcitonin with two lipid chains with a length of 4 car-

bon does not change the transport of salmon calcitonin after four hours, compared to sCT(C0/C0). However, increasing the size of the lipid chains from 4 to 8 does significantly increase the transport of salmon calcitonin after four hours compared to both sCT(C0/C0) and sCT(C4/C4).

### 4.3.1 Summary

This section showed that lipidating sCT with two C8 fatty acid lipid chains increases the transport through a monolayer after four hours significantly compared to the transport observed with native sCT and sCT modified with two C4 fatty acid lipid chains.

## 4.4 Temperature Dependency & Clathrin Dependent endosomes

In this section we will build a mechanistic understanding of how the peptide transports through the monolayer. To verify that we can detect differences between two systems, we lower the temperature from 37 °C to 25 °C and compare the relative increase between them. By lowering the temperature active transport processes such as endosome transport is lowered [80,81] and it also changes the membrane permeability by changing the membrane fluidity [82]. Furthermore, we inhibit transport through an endosomal route that depends on dynamin by using dynasore as the inhibitor [83].

So far, we have seen that the sCT(C8/C8) analog significantly shows the highest amount of transport. Furthermore, we have seen that sCT(C4/C4) and sCT(C0/C0) are not different from each other regarding the total amount of transport over 4 hours. Hence we wanted to test if the difference in transport stems from different mechanisms. First, we lowered the temperature from 37 °C to 25 °C. We lowered the temperature to see if we could see any difference when altering the system. By lowering the temperature, we would expect that the overall transport would decrease [80, 81]. Figure 4.8 shows the deconvoluted intensity signal for all three peptide analogs. Figure 4.8A shows the three intensity contributions of the peptide signal of sCT(C0/C0). When lowering the temperature, peptide transport through the cells stops. Figure 4.8B shows the parameters used to fit the peptide intensity signal of sCT(C4/C4). The initial solution level is 20 A.U. at  $t = 0$  min, but at  $t = 40$  min, it drops to approximately 15 A.U. and stabilizes. This is explained by starting the imaging before the peptide solution has reached equilibrium. The cytosolic content and the transport across the cells both show no increase over time when lowering the temperature. This shows that by lowering the temperature from 37 °C to 25 °C, then the transport across the monolayer for sCT(C0/C0) and sCT(C4/C4) stops. This suggests that the transport mechanism for sCT(C0/C0) and sCT(C4/C4) are energy dependent.

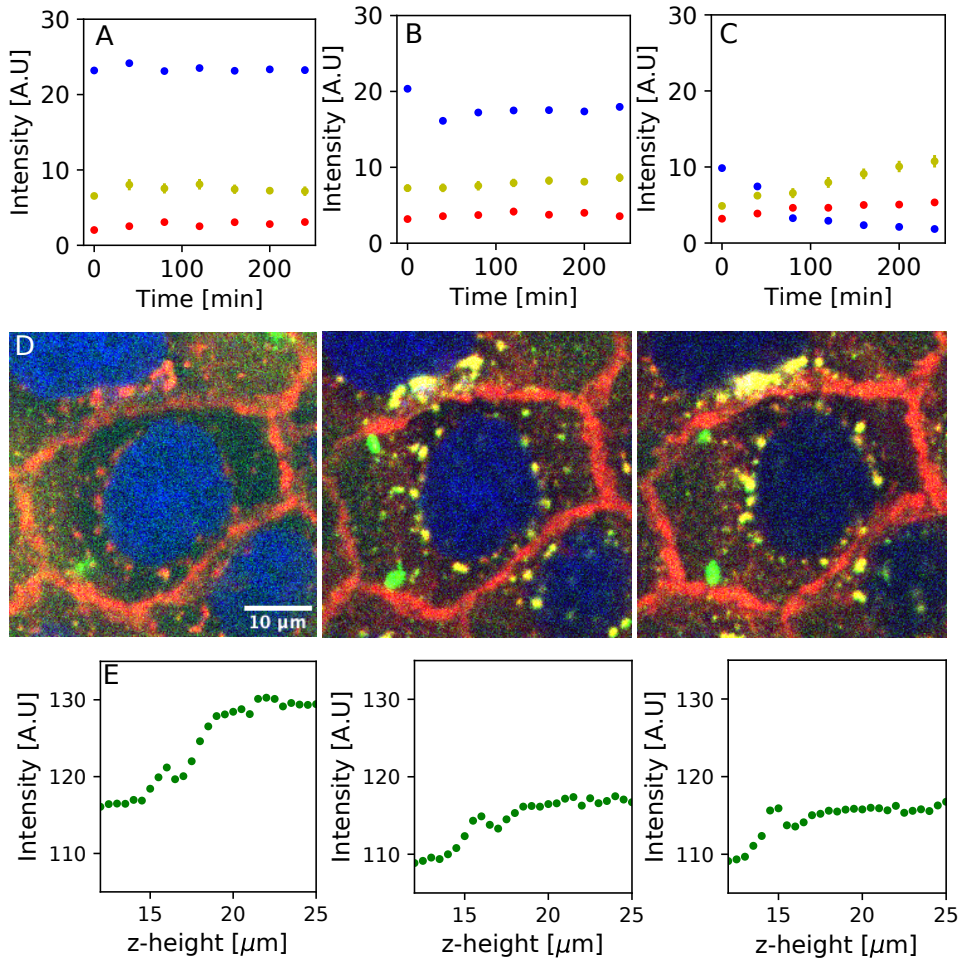


**Figure 4.8.** The transport of the sCT analogs was monitored at 25 °C for four hours with imaging every 40 min. A) Shows the three parameters used to fit the intensity profile of sCT(C0/C0)  $N = 24$  cells  $\pm$  SEM, B) shows the three parameters used to fit the intensity profile of sCT(C4/C4)  $N = 20$  cells  $\pm$  SEM and C) shows the three parameters used to fit the intensity profile of sCT(C8/C8)  $N = 12$  cells  $\pm$ . All the parameters are background corrected. The blue data points represent the solution level, and the red data points represent the intensity level in the cytosol. The yellow data points represent the accumulated peptide underneath the cells. D) Shows a cell with sCT(C8/C8) added at three different time points,  $t = 0$  min,  $t = 80$  min, and  $t = 240$  min going from left to right. E) Shows the intensity profiles through a cytosol of a cell at  $t = 0$  min,  $t = 80$  min, and  $t = 240$  min going from left to right.

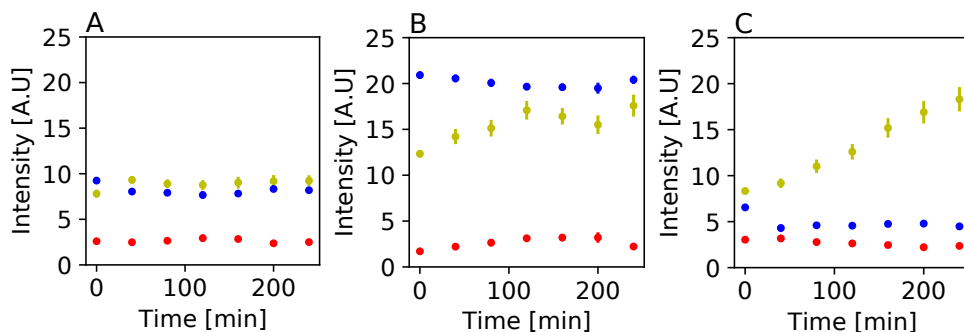


Figure 4.8C shows the parameters describing the fit to the intensity profile of sCT(C8/C8). The initial value of accumulated peptide underneath the cells is approximately 5 A.U. and increases to approximately 10 A.U. resulting in a relative increase of 2.0x. The cytosolic intensity level does not increase over time. Lastly, the intensity in the solution is seen decrease from  $t = 0$  min until  $t = 240$  min. From  $t = 0$  min to  $t = 80$  min, it decreases from 10 A.U. to approximately 2 A.U. From  $t = 80$  min to  $t = 240$  min, it decreases to 1 A.U. This is not explained by the phenomenon seen in Figure A.4. This is unexpected as it would indicate that the solution level empties over the 4 hours of imaging. To see what is happening with the cells, Figure 4.8D shows the same cell at three different time points. The left image is just after adding sCT(C8/C8). Here we see a diffuse signal, making the z-slice look green, and we also see a few green aggregates already forming on the cell. The middle image shows the same cell at  $t = 80$  min. Here the diffusive signal is almost gone, but we do see the peptide with some form of endocytic organelles. The right image in Figure 4.8D shows the cell at  $t = 240$  min. Here we see even more the formation of aggregates. Figure 4.8E shows three examples of how an intensity profile is sampled through the cytosol of a cell. The left intensity profile is just adding the peptide. The center intensity profile is at  $t = 80$  min, and the last intensity profile in Figure 4.8E is at  $t = 240$  min. From the intensity profiles, it is clear that it is not only the solution level that decreases over time but the entire system that is lower in intensity over time. In the fitting model given in Equation 3.11, everything is divided into separate parts and estimated for each time point, which means that the peak under the cell, intensity level in the cell, and the solution are estimated separately independent on what the intensity level is in the other regions. The only common thing between the parameters is that they have all been background subtracted. This means that the accumulated peptide increase does not arise artificially from the solution level decreasing. Even though the entire intensity profile is shifting toward lower intensity levels over time, it still shows the expected results, namely that we would see a lower relative increase of transported peptide over time at 25 °C compared to at 37 °C.

It should be noted that these results only come from a single day of experiments. Thus, it would be nice to repeat the experiment to see if this behaviour is only an artefact for this experiment. The data in Figure 4.8A - C was all obtained in the same experiment. As the intensity is stable for Figure 4.8A and B it means that the decrease in the solution level in Figure 4.8C does not arise from any issues with the microscope, such as lack of oil on the objective.

To not just lower the general uptake and transport, we wanted to inhibit a specific mechanism. By adding 80  $\mu$ M of dynasore, the recruitment of dynamin is inhibited, thus inhibiting endocytotic pathways depending on dynamin. For the dynasore to effectively inhibit dynamin, 80  $\mu$ M was added 30 minutes before adding the peptide [83]. After 30 minutes of incubation with dynasore, we added a mixture of the peptide and dynasore.

Figure 4.9 shows the parameters describing the fit to the intensity profiles of the three peptide analogs. Figure 4.9A shows that the transport of sCT(C0/C0) does not increase over time. Both the solution and cytosolic intensity levels are constant



**Figure 4.9.** The transport of the sCT analogs was monitored at 37 °C with 80  $\mu$ M dynasore present for four hours with imaging every 40 min. A) Shows the three parameters with the background subtracted used to fit the intensity profile of sCT(C0/C0). B) Shows the three parameters with the background subtracted used to fit the intensity profile of sCT(C4/C4). C) Shows the three parameters with the background subtracted used to fit the intensity profile of sCT(C8/C8). The blue data points represent the solution level, and the red data points represent the cytosolic content. Lastly, the yellow data points represent the accumulated peptide underneath the cells.

over the four hours of imaging. Figure 4.9B shows the parameters describing the fit to the intensity profile of sCT(C4/C4). The initial peptide intensity level underneath the cells is approximately 12 A.U. and increases to approximately 17 A.U. This is a similar relative increase of 1.4x, which is the same relative increase observed under physiological temperatures (see Figure 4.2). The solution and cytosolic intensity levels does not change over time. Figure 4.9C shows the transport of sCT(C8/C8) where the initial peptide intensity level underneath the cell is approximately 9 A.U., increasing to approximately 20 A.U. at  $t = 240$  min. This is a relative increase of just above 2x, which is similar to the transport of sCT(C8/C8) at 25 °C. The solution level has an initial value of 6 A.U. at  $t = 0$  min and drops to 5 A.U. at  $t = 40$  min, and then stays stable for the rest of the experiment. This slightly higher value at  $t = 0$  min is due to the mixing of the peptide not fully complete yet, which is shown in Figure A.4 to take a few minutes after adding the peptide. Lastly, the cytosolic content of sCT(C8/C8) over time, which is not increasing.

Figure 4.9 shows that the transport accumulating sCT(C0/C0) at the bottom cell membrane is inhibited. By inhibiting the function of dynamin the transport of sCT(C8/C8) is lowered from a 3.7-fold increase at 37 °C to approximately 2.5-fold increase at 37 °C with 80  $\mu$ M dynasore. Interestingly, the transport of sCT(C4/C4) is not lowered when comparing the transport at 37 °C and at 37 °C with 80  $\mu$ M dynasore.

From the results seen in Figure 4.8 and 4.9 we can say that the process involved with the transport of sCT(C0/C0) across the cell barrier is an endosome process that depends on dynamin as the transport is inhibited at 25 °C, but also at 37 °C with dynasore present. For sCT(C4/C4) the transport is inhibited at 25 °C, but not

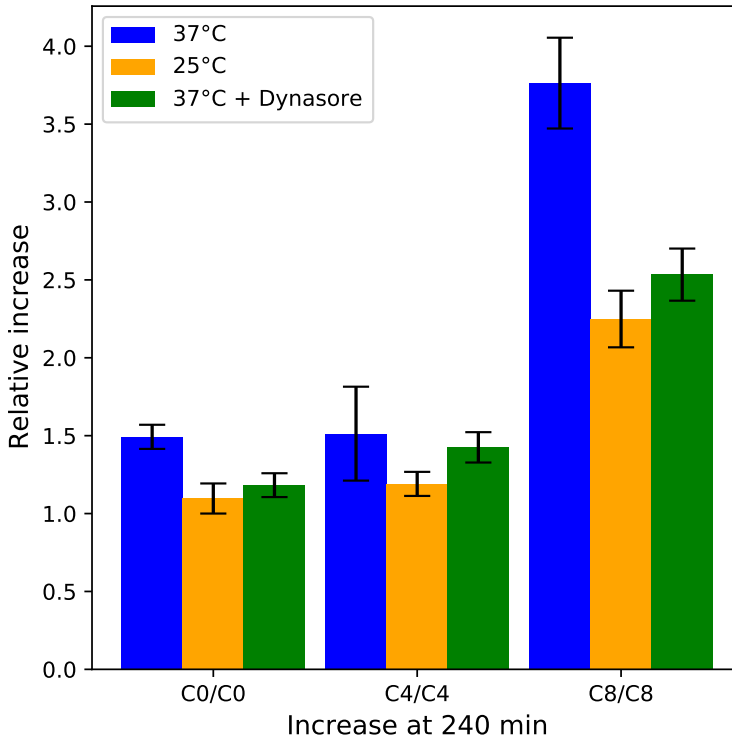


**Figure 4.10.** Overview of the relative increase of peptide signal underneath the cells after 240 minutes of transport for all three analogs at three different conditions. The blue bars represent the transport under physiological conditions. The yellow bars represent transport at 25 °C, and the green bars represent transport at the physiological condition in the presence of 80  $\mu$ M dynasore.

at 37 °C with dynasore present. This means that the transport mechanism is not dependent on dynamin, but does depend on another energy dependent mechanism, or passive diffusion in the membrane. Lastly, these results tell us that the transport of sCT(C8/C8) through the cells depends on dynamin as the transport is lower when dynasore is present. Furthermore, it shows that a second mechanism is also in play as the transport is not fully inhibited, either at 25 °C or when dynasore is present.

We have data of three different peptides, each under three different conditions. The point of lipidating the peptides was to increase their transport through the monolayer. Hence, to better be able to visualize the effect of the lipidation of the peptide but also visualize the effect of changing the temperature or adding dynasore, the relative increase at  $t = 240$  min is shown in Figure 4.10 for all three peptides at each of the experimental conditions. The blue bars represent the relative uptake at

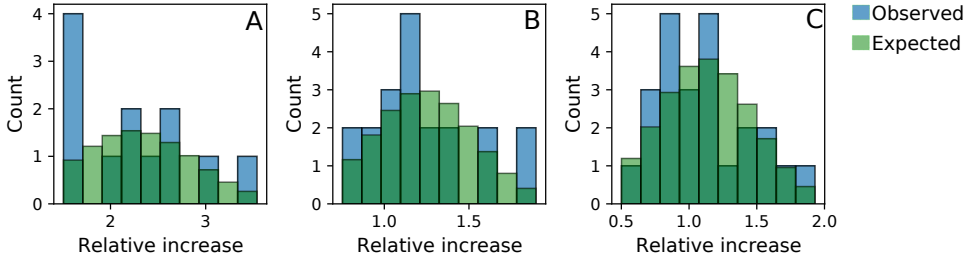
$t = 240$  min for each peptide under physiological conditions. The yellow and green bars in Figure 4.10 show the relative increase at  $t = 240$  min for the three peptide analogs at  $25^\circ\text{C}$  and under physiological conditions +  $80\ \mu\text{M}$  dynasore, respectively. For sCT(C0/C0), both the yellow and green bars are lower than the blue bars. For sCT(C4/C4), we see the same relative increase at physiological temperature with and without dynasore present. However when lowering the temperature, then it also lowers the relative increase. Lastly, sCT(C8/C8) shows the highest amount of transport under physiological conditions. At  $25^\circ\text{C}$  and at  $37^\circ\text{C}$  with dynasore added, the transport levels are similar.

However, to say that they are significantly different, we need to do statistical tests. Before doing any statistical tests, we tested the data to see if it follows a normal distribution or not, as this will determine what type of test needs to be applied. To test for normality, we used a  $\chi^2$ -GOF test with an  $\alpha$  level of 0.05. The null hypothesis is that the data is consistent with a normal distribution, and the alternative hypothesis is that the data is not consistent with a normal distribution.

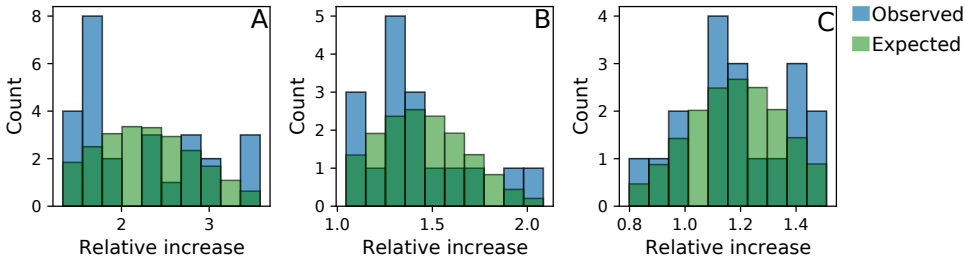
Figure 4.11 shows the distribution of the relative increase at  $t = 240$  min for sCT(C0/C0), sCT(C4/C4) and sCT(C8/C8). The blue bars represent the observed data, and the green bars represent the expected data. Figure 4.11A shows the distribution of observed and expected values for sCT(C8/C8). The p-value calculated for sCT(C8/C8) is 0.025, and with an  $\alpha$  level of 0.05, the null hypothesis is rejected, meaning that the data is not consistent with a normal distribution. We repeated the same process for sCT(C4/C4) and sCT(C0/C0) as seen in Figure 4.11B and C, respectively. The calculated p-value for sCT(C4/C4) is 0.097. Hence the null hypothesis cannot be rejected, which means that the data of sCT(C4/C4) is consistent with a normal distribution. The p-value for sCT(C0/C0) is 0.66, which means that the null hypothesis cannot be rejected, meaning that the data of sCT(C0/C0) is consistent with a normal distribution.

Figure 4.12 shows the distributions of sCT(C0/C0), sCT(C4/C4) and sCT(C8/C8) under physiological conditions, but with  $80\ \mu\text{M}$  dynasore added. The blue bars represent the observed data, and the green bars represent the expected data. Figure 4.12A shows the data of sCT(C8/C8). The calculated p-value is  $1.0 \times 10^{-4}$ , which is below the  $\alpha$  level; hence we reject the null hypothesis. This means that the data for sCT(C8/C8) is not consistent with a normal distribution. For sCT(C4/C4) (Figure 4.12B) the p-value is calculated to 0.12. This is higher than the  $\alpha$  level of 0.05; thus the null hypothesis cannot be rejected, and the data is consistent with a normal distribution. Figure 4.12C shows the distribution of sCT(C0/C0). The calculated p-value is 0.31, and with an  $\alpha$  level of 0.05, the null hypothesis cannot be rejected, which means that the data is consistent with a normal distribution.

We have previously tested if there is a difference between the three peptide analogs. Now, we are testing if there is a difference between the transport of the peptide under various conditions after four hours. We are looking at sCTC(C0/C0) first, and here we test if the three distributions are from the same distribution. Since they are not all consistent with a normal distribution, we perform a Kruskal-Wallis test. The null hypothesis is that all the distributions are the same, whereas the alternative



**Figure 4.11.** We tested if the transport of the sCT analogs at 25 °C after four hours follow a normal distribution by using a  $\chi^2$  goodness of fit test. A) Shows the distribution of sCT(C8/C8) at t = 240 min in blue compared to the expected values of a Gaussian with mean and sigma estimated from the sample. B) Shows the distribution of sCT(C4/C4) at t = 240 min in blue compared to the expected values of a Gaussian with mean and sigma estimated from the sample. C) Shows the distribution of sCT(C0/C0) at t = 240 min in blue compared to the expected values of a Gaussian with mean and sigma estimated from sample  
p-value for A) is 0.025. p-value for B) is 0.097. p-value for C) is 0.66.



**Figure 4.12.** We tested the transport of the sCT analogs at 37 °C + 80  $\mu$ M dynasore after four hours to see if they follow a normal distribution by using the  $\chi^2$  goodness of fit test. A) Shows the distribution of sCT(C8/C8) at t = 240 min in blue compared to the expected values of a Gaussian with mean and sigma estimated from the sample. B) Shows the distribution of sCT(C4/C4) at t = 240 min in blue compared to the expected values of a Gaussian with mean and sigma estimated from the sample. C) Shows the distribution of sCT(C0/C0) at t = 240 min in blue compared to the expected values of a Gaussian with mean and sigma estimated from the sample.  
p-value for A) is  $1.0 \times 10^{-4}$ . p-value for B) is 0.12. p-value for C) is 0.31.

hypothesis is that at least one of the three distributions is different. The Kruskal-Wallis test gives a p-value of  $4.0 \times 10^{-4}$ . With an  $\alpha$  level of 0.05, we reject the null hypothesis, meaning at least one of the distributions is different. With at least one distribution being different, we can do a *post hoc* analysis of pairwise testing as seen in Table 4.2. The test shows that there is a significant difference between transport of sCT(C0/C0) at 37 °C compared to at 25 °C and at 37 °C with dynasore present. The

test also shows that there is no significant difference in the transport of sCT(C0/C0) at 25 °C and at 37 °C with dynasore. This means that one of the transport mechanisms involved in sCT(C0/C0) transport depends on dynamin.

We repeated the same process for sCT(C4/C4). The calculated p-value for the Kruskal-Wallis test was 0.0025, which is lower than the  $\alpha$  level, which means we reject the null hypothesis. This means that at least one of the distributions is different from the others. As we reject the null hypothesis in the Kruskal-Wallis test, we can do a *post hoc* pairwise test. The results of the pairwise test for sCT(C4/C4) is seen in Table 4.3. This shows that there is a significant difference between the transport of sCT(C4/C4) at 37 °C and at 25 °C. It also shows that there is not a significant difference between the transport of sCT(C4/C4) at 37 °C with or without dynasore. Furthermore, Table 4.3 shows that there is no significant difference in the transport of sCT(C4/C4) at 25 °C and at 37 °C with dynasore added. This means that the transport mechanism for sCT(C4/C4) does not depend on clathrin-mediated endocytosis, but another transport mechanism affected by temperature.

Lastly, we also tested sCT(C8/C8) using the Kruskal-Wallis test. The p-value calculated for sCT(C8/C8) when comparing the three different experiments is  $8.5 \times 10^{-7}$ . With an  $\alpha$  level of 0.05 we reject the null hypothesis, which means that at least one of the distributions of sCT(C8/C8) differs from the others. This means that we can do a *post hoc* pairwise test. Table 4.4 shows the results of the pairwise test. The test shows that the transport of sCT(C8/C8) at 37 °C is significantly different than the trans-

	T = 37°C	T = 25°C	T = 37°C + dynasore
T = 37°C	1	$1.7 \times 10^{-4}$	$7.0 \times 10^{-3}$
T = 25°C	$1.7 \times 10^{-4}$	1	0.34
T = 37°C + dynasore	$7.0 \times 10^{-3}$	0.34	1

**Table 4.2.** The p-values of pairwise testing of sCT(C0/C0) at different T = 37°C, T = 25°C and T = 37°C + dynasore.

	T = 37°C	T = 25°C	T = 37°C + dynasore
T = 37°C	1	0.0011	0.16
T = 25°C	0.0011	1	0.13
T = 37°C + dynasore	0.16	0.13	1

**Table 4.3.** The p-values of pairwise testing of sCT(C4/C4) at different T = 37°C, T = 25°C and T = 37°C + dynasore.

	T = 37°C	T = 25°C	T = 37°C + dynasore
T = 37°C	1	$1.6 \times 10^{-5}$	$1.2 \times 10^{-7}$
T = 25°C	$1.6 \times 10^{-5}$	1	0.98
T = 37°C + dynasore	$1.2 \times 10^{-7}$	0.98	1

**Table 4.4.** The p-values of pairwise testing of sCT(C8/C8) at different T = 37°C, T = 25°C and T = 37°C + dynasore.

port at 25 °C and at 37 °C with dynasore. Comparing the transport at 25 °C with the transport at 37 °C with dynasore, there is no significant difference. This means that one of the transport mechanisms for sCT(C8/C8) involves clathrin-dependent endocytosis.

#### 4.4.1 Summary

The results in Tables 4.2 to 4.4 shows the p-values when comparing the same peptide analog at different conditions. Here it shows lowering the temperature lowers the transport significantly for all the analogs. However, only sCT(C0/C0) and sCT(C8/C8) significantly decrease in transport after adding dynasore. The transport of sCT(C4/C4) is unchanged when adding dynasore. This shows that sCT(C0/C0) and sCT(C8/C8) undergo endocytosis as part of the transport. We cannot say if sCT(C4/C4) undergoes active transport or not, but we can say that the transport mechanism involved does not depend on dynamin.

### 4.5 TIRF stepwise bleaching

From the previous section we can see that some of the transport mechanisms involve endocytosis. Therefore, we wanted to test if the peptides aggregate into big clumps and therefore undergo endocytosis. To characterize the number of sCT molecules in a puncta spot, we utilize total internal reflection fluorescence (TIRF) microscopy to do stepwise bleaching. We can count the number of peptides in an aggregate by doing stepwise bleaching [84]. TIRF microscopy yields a high signal-to-noise ratio (SNR) compared to epifluorescence, a shallow illumination depth, and low power on the sample [65] [66]. The principle behind TIRF is that if light is sent toward a sample with a different refractive index than, e.g., the glass of the coverslip, with a certain critical angle, then all of the light will be reflected. This, however, produces an evanescent field into the sample. The special thing about this field is that the energy into the sample decreases exponentially with the distance from the interface. This means that only the part of the sample that is very close to the interface will get illuminated with high power [67]. This is why there is a high SNR.

To do stepwise bleaching, an ibidi 8-well glass bottom plate was cleaned following a protocol from Snaar-Jagalska et al. [85]. In brief, the glass slides are deposited for 15 min in an ultrasonic bath in a 1 % triton solution followed by rinsing in Milli-Q water. Secondly, we cleaned the glass slides for 15 minutes in an ultrasonic bath in Milli-Q water, then another 15 minutes in an ultrasonic bath for 15 min with 0.1M KOH. Lastly, we washed the glass slides in Milli-Q water for 15 min in an ultrasonic bath and dried them under a nitrogen flow.

We deposited 100  $\mu$ L of approximately 100 fM peptide to a well and let sit for 10 minutes to allow the peptides to adhere to the glass surface. After 10 minutes, we removed the peptide solution, and a fresh imaging medium was added (FluoroBrite

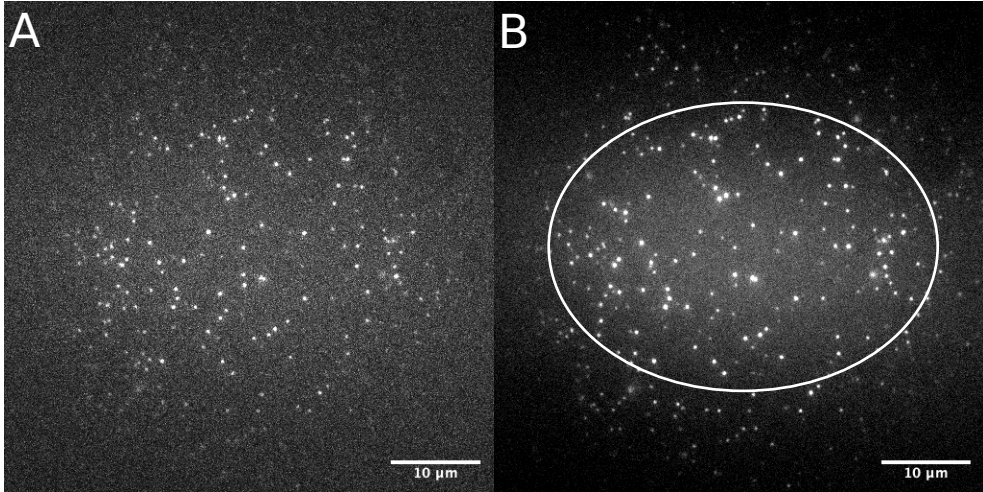


**Figure 4.13.** A typical field of view of a sample used for TIRF bleaching. A) An example of the first frame of sCT(C4/C4)-atto488 on deposited on a glass surface. B) Shows an average of the 10 first frames of the same field of view as in A). The white circle indicates spots eligible for analysis.

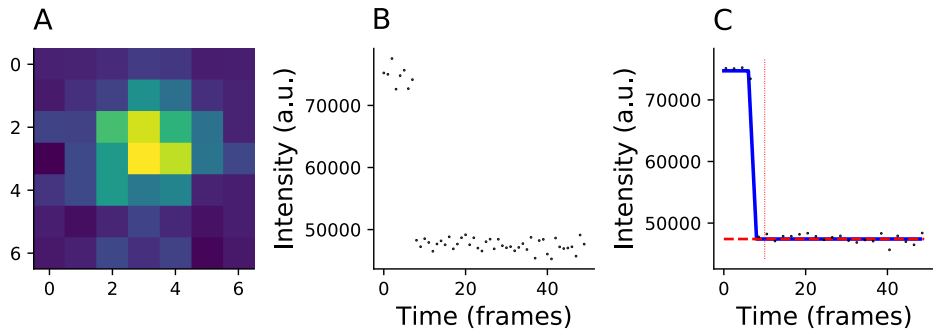


**Figure 4.14.** Shows a typical peptide spot and bleaching steps of it. A) Shows a peptide spot in a 7x7 pixel bounding box, were all the intensity in the box is summed and used for analysis. B) Shows the intensity trace as a function of number of frames for the peptide seen in A). C) Shows the fit of using the step finding algorithm as the blue line. The intensity values starting from the dotted vertical line and to the end of the time trace is used to estimate the background intensity, and the red dashed horizontal line represents the background intensity.

from sigma). We used a homebuilt TIRF to image the peptide. We used a 100x objective with a numerical aperture of 1.45 to make objective-based TIRF illumination. This works by making sure that the laser is focused in the BFP of the objective. Then,



we used a mirror to guide the laser to the edge of the objective. By doing this we were able to reach the critical angle for total internal reflection to create the evanescence field.

The camera used was an EMCCD 512 Evolve with 50 ms exposure and an EM gain set to 300. We used a 473 nm cobolt laser set to 1 mW power as an illumination source. The power density at the sample plane was approximately  $40 \text{ W/cm}^2$ . Figure 4.13A shows the first frame in a bleaching movie where the bright spots represent peptides with an atto488 fluorophore attached to them. Each experiment ran for 500 frames or until all spots had bleached. As seen in Figure 4.13B, the TIRF illumination profile is not homogeneous. Thus, we only used isolated spots in the white circle for analysis.

We picked out a single spot in a region of  $7 \times 7$  pixels to perform the analysis. We summed all the intensity for each frame in this spot, which resulted in an intensity trace. We then used the intensity trace to estimate the number of steps and the size of the step. The number of steps equals the number of monomers in the peptide spot. Figure 4.14 shows an example of the analysis. Figure 4.14A shows an isolated spot and the region used to sum the intensity. As we sum the intensity in a region around the peptide, the spot must be isolated, thus yielding an intensity trace coming from only one spot. Figure 4.14B shows the intensity trace of the spot in Figure 4.14A. After extracting the intensity, we used a step-finding analysis on the intensity trace. Figure 4.14C shows the result of using the step-finding analysis. In the step-finding analysis, we binned the intensity so that each data point averages two time points from the raw intensity trace. We did this to limit the contribution of variation in intensity value in each frame due to noise.

From the vertical dotted line in Figure 4.14C until the end of the intensity trace, we estimated the background. The red dotted horizontal line represents the estimated background. The algorithm then utilizes a maximum likelihood estimator to find the number of steps and the step size in the intensity trace. The algorithm works by giving a range of step sizes as input to know where to start searching. It then tries the different possible step sizes until it finds the step size and number of steps in the trace that produces the lowest Akaike information criterion value. If not careful picking a correct range of searching, it might show multiple steps, even though the intensity trace only shows a single step when inspecting by eye. The blue line in Figure 4.14C is a simulated intensity trace with the number of steps and step size found from the data. The blue line is a final check that the algorithm finds the correct parameters. We repeat this process for all of the spots found in all different fields of view for all three peptide analogs. We then plot the distribution of the step sizes and the number of steps.

Figure 4.15A shows the distribution of photons in the 88 spots found in 5 different FOVs for sCT(C4/C4). We convert the arbitrary intensity to the number of photons through a conversion. The conversion is dependent on the gain, offset, and quantum efficiency (QE) of the camera. We used an EMCCD camera for this experiment so the EM gain is included in the conversion. The combined gain for the camera and the EM gain is 25 at 300 EM gain and camera gain of 1. The offset cancels out as we

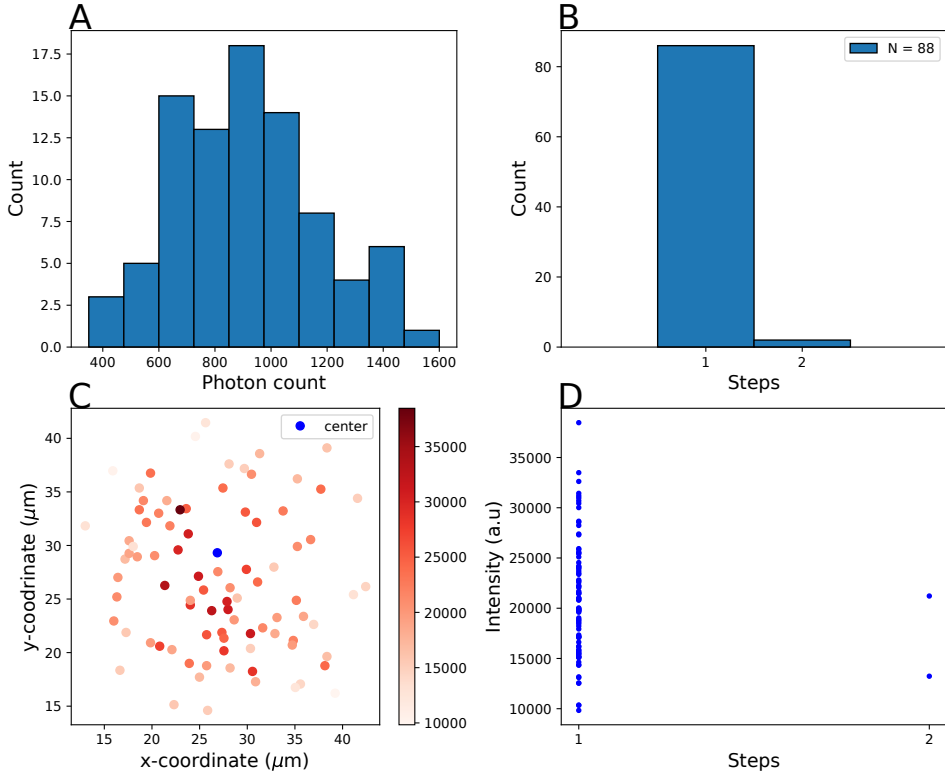


**Figure 4.15.** The results of the bleaching step analysis of all 88 peptide spots for sCT(C4/C4)-atto488. A) Shows the distribution of photons emitted from each spot and B) shows the distribution of the number of steps found by the step algorithm. C) Shows the intensity of each spot as a function of the distance away from the center of illumination, showcasing the highest intensity toward the center (blue dot). D) shows the intensity of the spots as a function of the number of steps in each spot.

subtract the background from the intensity spots. Lastly, quantum efficiency refers to how efficiently the camera converts the incoming photons to electrons and then into intensity. The EMCCD camera has a QE of 90 %. Thus the conversion from intensity to photons is done by the following equation:

$$photon = \frac{\frac{intensity}{totalgain}}{QE} \quad (4.1)$$

The distribution in Figure 4.15A seems evenly distributed around 800-1000 photons and ranges from 400 – 1600 photons per peptide spot. Given this range of photons, one would expect a polydisperse distribution of peptide sizes, however, this is not the case. Figure 4.15B shows the distribution of the number of steps for sCal(C4/C4).

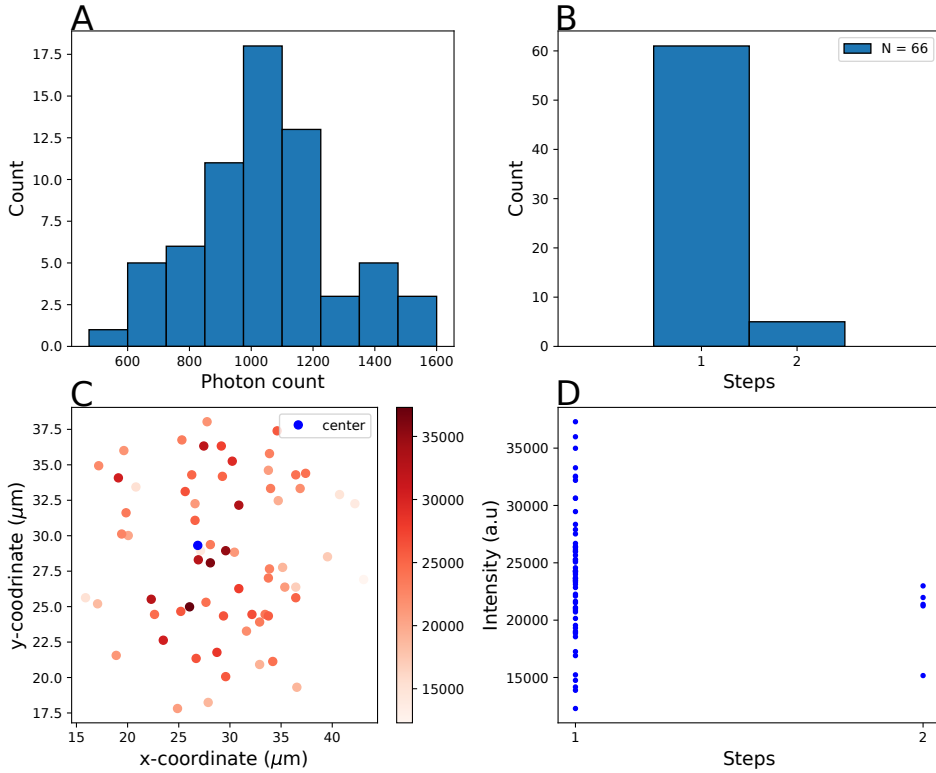


**Figure 4.16.** The results of the bleaching step analysis of all 66 peptide spots for sCT(C0/C0)-atto488. A) Shows the distribution of photons emitted from each spot and B) shows the distribution of the number of steps found by the step algorithm. C) Shows the intensity of each spot as a function of the distance away from the center of illumination, showcasing the highest intensity toward the center (blue dot). D) shows the intensity of the spots as a function of the number of steps in each spot.

Here it is clear that the majority of the population is monomers with only a few dimers present. The reason for the large distribution of photons might come from the fact that the illumination of our FOV is non-uniform (Figure 4.13B). Figure 4.15C shows the intensity of the spot as a function of the distance from the center of the illumination in Figure 4.13B. The blue dot represents the center of the illumination, and from this, we can see that the further away we get from the center, the less intensity we gain from every single spot. This explains why the distribution of the photons is as wide as it is. Figure 4.15D shows the intensity step size as a function of the number of steps. This shows that most of the steps are single steps but have a wide range of step sizes because of the non-uniform illumination. We did this analysis for the remaining two peptide analogs. Figure 4.16 and 4.17 show the results.

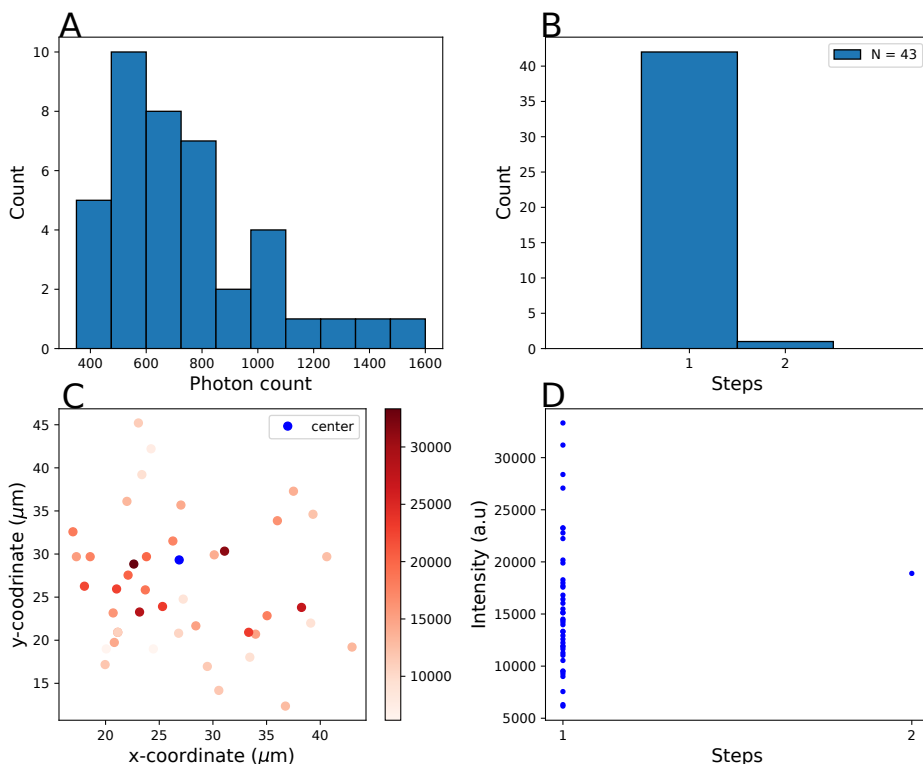


**Figure 4.17.** The results of the bleaching step analysis of all 43 peptide spots for sCT(C8/C8)-atto488. A) Shows the distribution of photons emitted from each spot and B) shows the distribution of the number of steps found by the step algorithm. C) Shows the intensity of each spot as a function of the distance away from the center of illumination, showcasing the highest intensity toward the center (blue dot). D) shows the intensity of the spots as a function of the number of steps in each spot.

Figure 4.16A shows the distribution of photons from 66 spots of sCT(C0/C0) in 4 different FOVs. Similar to sCT(C4/C4), the photons distribute around a photon count of 1000 photons per peptide. Figure 4.16B shows the number of steps per spot where it is primarily monodisperse. Figure 4.16C and D shows that the spread of the photon count arises from the uneven illumination. Lastly, Figure 4.17 shows the output of analyzing 43 spots in 9 different FOVs of sCT(C8/C8). The high amounts of FOVs are due to a low density of isolated spots on the surface in each FOV. Figure 4.17A shows the distribution of the photons emitted from sCT(C8/C8). Here we see a different story when comparing the photon distribution of sCT(C0/C0), and sCT(C4/C4) (Figure 4.15A and Figure 4.16A, respectively) as it distributes around 600 photons per spot and has a longer tail towards higher photon counts. Figure 4.17B

shows the distribution of the number of steps in each spot found for sCT(C8/C8), and we see that the distribution is also monodisperse with only a few dimers. Looking at Figure 4.17C, we can see that the most intense spots do not arise from the center of the illumination (blue dot in Figure 4.17C) but a bit towards the left of the FOV. Figure 4.17D shows similar results to Figure 4.17A, namely a lower intensity level per spot.

Given that the molecule responsible for the emission is the same on all three peptide analogs, we wanted to investigate why the three distributions are not alike. We compared the photon count to show the differences between the three analogs. Figure 4.18 shows the distribution of photon counts for each of the peptide analogs, where for sCT(C0/C0) (blue bars) and sCT(C4/C4) (orange bars) show similar distributions. sCT(C8/C8) (green bars) shows a distribution towards lower photon counts per peptide. We did this by analyzing the local background of the ROI of the peptide spot. Figure 4.19A shows the distribution of photons for sCT(C0/C0) in blue, sCT(C4/C4) in orange and sCT(C8/C8) in green. With the same color representations, Figure 4.19B shows the distribution of photons in the background in each of the spots. Here we see that the background is higher for sCT(C8/C8). Given that the background of sCT(C8/C8) is slightly higher than the two other peptides we tried to sum the contributions from the peptide and the background to see if it could eliminate some of the differences observed. Figure 4.19C shows the summed contribution of the background and peptide spot for all three peptide analogs. Still, sCT(C8/C8) has a slightly lower photon output compared to sCT(C4/C4) and sCT(C0/C0).

Another possible reason for the slight variation in the photon output might arise from a small sample to sample variation. Such variations could be the angle of the laser beam through the objective being different. At the critical angle, the intensity at the glass interface is at its highest and will exponentially decrease in intensity at angles around the critical angle [67]. Given that in the TIRF setup, we have the incident angle adjusted manually, it is a cause of error. To verify the result from Figure 4.15 to 4.17 we repeated the experiment on a commercial Nikon TIRF microscope. There are a few differences between the two setups, such as the objective used, the camera, the illumination source, and the beam's tilting through the objective is done automatically by the software. The objective used was still a 100x objective, but the numerical aperture was 1.49 versus a numerical aperture of 1.45. The higher numerical aperture means that a bigger angle is possible through the objective. The illumination source was a 488 nm laser as opposed to a 473 nm laser. The camera used at the Nikon setup was a Camera ORCA-Flash 4.0 sCMOS camera from Hamamatsu with a camera gain of 2, and a mean offset of 100 [86]. As the camera is not an EMCCD camera, there is no EMgain. Lastly, the software will minimize the sample to sample fluctuations as the incident angle is controlled better due to the motorized mirrors.

Figure 4.20 shows the photon count for all of the three peptides after repeating the bleaching experiment on the Nikon setup. Figure 4.20A shows the distribution of photons for sCT(C0/C0) (blue bars), sCT(C4/C4) (orange bars) and sCT(C8/C8) (green bars). The distributions are all overlapping nicely, which suggests that the

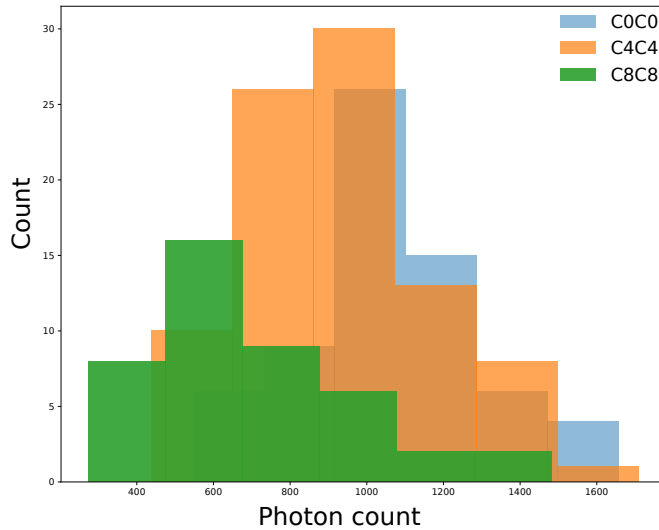


**Figure 4.18.** The distribution of photons from each of the three sCT analogs. The blue distributions represents sCT(C0/C0)-atto488. The orange distribution represents sCT(C4/C4)-atto488. Lastly, the green distribution represents sCT(C8/C8)-atto488.

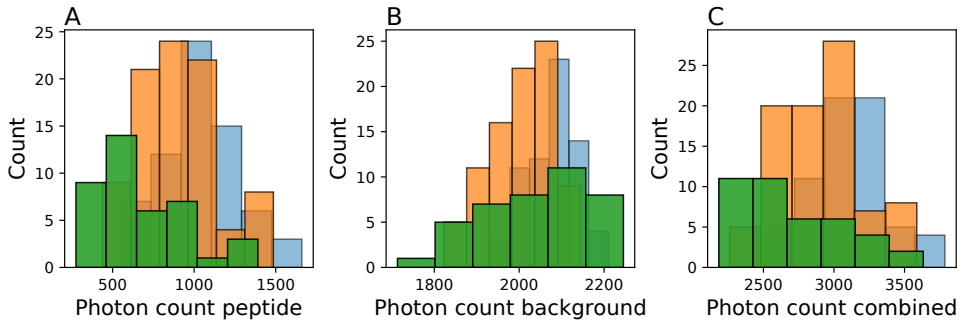


**Figure 4.19.** Comparing the different contributions in the bleaching step analysis. We did the experiment at a homebuilt TIRF setup. It shows the distribution of photons for sCT(C0/C0)-atto488 as blue bars. The orange bars show the distribution of sCT(C4/C4) and sCT(C8/C8)-atto488 as green bars. A) Shows the photon count contribution from the sCT analogs. B) Shows the distribution of the photon count of the background, and C) shows the distribution of the combined photon count.

discrepancy seen in the distributions seen in Figure 4.19 comes from the tuning of the incident angle. Figures 4.20B and C confirm that the distributions of the background photon and the summed contribution of the peptide and background overlap as well. The number of steps is independent of the number of photons coming from

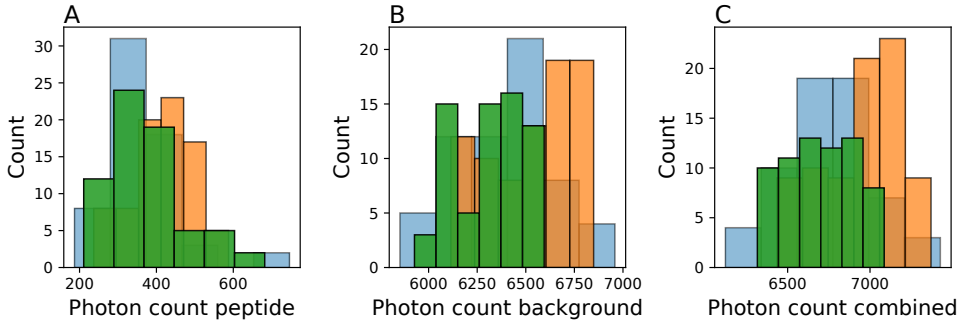


**Figure 4.20.** Comparing the different contributions in the bleaching step analysis using a commercial Nikon TIRF setup. It shows the distribution of photons for sCT(C0/C0) as blue bars. The orange bars show the distribution of sCT(C4/C4) and sCT(C8/C8) as green bars. A) Shows the photon count contribution from the sCT analogs. B) Shows the distribution of the photon count of the background, and C) shows the distribution of the combined photon count.

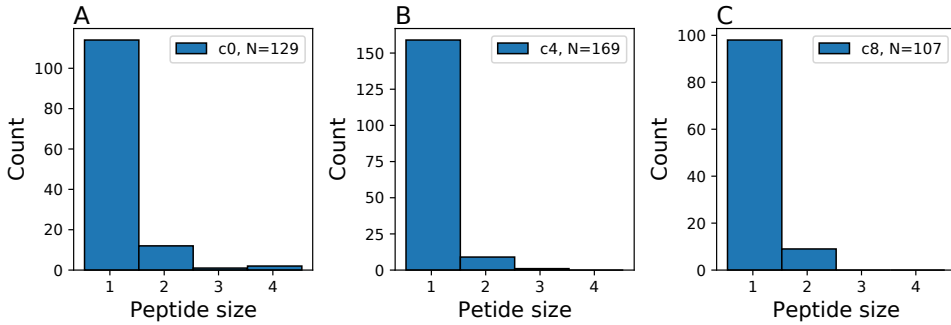


**Figure 4.21.** The data acquired from both TIRF setups are pooled and the distribution of the peptide size is shown. A) Shows the distribution of peptide size for sCT(C0/C0)-atto488. B) Shows the distribution of the peptide size of sCT(C4/C4)-atto488 and lastly, C) shows the distribution of the peptide size of sCT(C8/C8)-atto488.

the peptides as long as the step is detectable. As this is the case, we pool the number of steps from each experiment, as seen in Figure 4.21. For sCT(C0/C0), we analyzed 129 spots (Figure 4.21), showing the majority of the peptide is monomers with approximately 10 % dimers and very few higher-order polymers. Figures 4.21B and C show sCT(C4/C4) and sCT(C8/C8), respectively, and a majority of the peptides are present as monomers.

### 4.5.1 Summary

With these experiments, we show that sCT(C8/C8), sCT(C4/C4), and sCT(C0/C0) are all primarily monomers as puncta spots. These results are obtained under quite different conditions compared to when doing a transport experiment. The concentration when bleaching the peptide is in the femto-molar range, whereas under the cell transport experiment the concentration of peptide is in the micro-molar range. As the concentration is much lower in the bleaching experiment it might change the equilibrium toward a state with only monomers. This is the drawback of trying to do bleaching of single peptide spots, however it is a necessity. This also means that the results in this section only says that under these conditions, we observe that the majority of the peptide puncta spots are monomers.

## 4.6 Outlook & Perspective

### 4.6.1 Quantification of transport using a microfluidic model

We wanted to test if the quantification model would also be suitable with other cell models, such as a microfluidic model where the cells are fully polarized. However, as we base our model on imaging, it needed to be a platform suitable for imaging with the same conditions as the simple cell model. Therefore, we opted to try a system called an OrganoPlate. Luckily, a colleague in the CitBIO center has worked extensively with this system and helped us with cell seeding and operating the system. The cells were seeded and grown as described by Trietsch et al. [87]. The process yields fully polarized cells and forms a leak-tight intestinal tubule inside of the chip.

The three different peptide analogs were added to other chips and imaged over a four-hour period every 40 minutes for seven time points. Figure 4.22 shows the transport of the peptides over time. The blue data points represent the accumulation of sCT(C0/C0) underneath the cells. Here we observe an increase of approximately 1.4x relative increase. For sCT(C4/C4), yellow data points, the relative increase is approximately 1.2x. Lastly, the green data points represent the relative increase of sCT(C8/C8). The relative increase for sCT(C8/C8) is approximately 2.2x. We see the same trend when comparing this to the results seen in Figure 4.6 in regards to sCT(C8/C8) in the sense that it shows the highest increase of the three analogs. Comparing sCT(C0/C0), we see the same relative increase between the two experiments. Lastly, looking at sCT(C4/C4) and comparing that to the transport seen in Figure 4.6 the error bars overlap. This means that the data is within the uncertainty and from this pilot experiment is the same. sCT(C8/C8) is still the peptide analog performing the best. This shows that we can use the simple cell model for the early investigation of drug candidates.

Future experiments would repeat the temperature and dynasore experiment with the OrganoPlate, but also increase the number done at 37 °C.



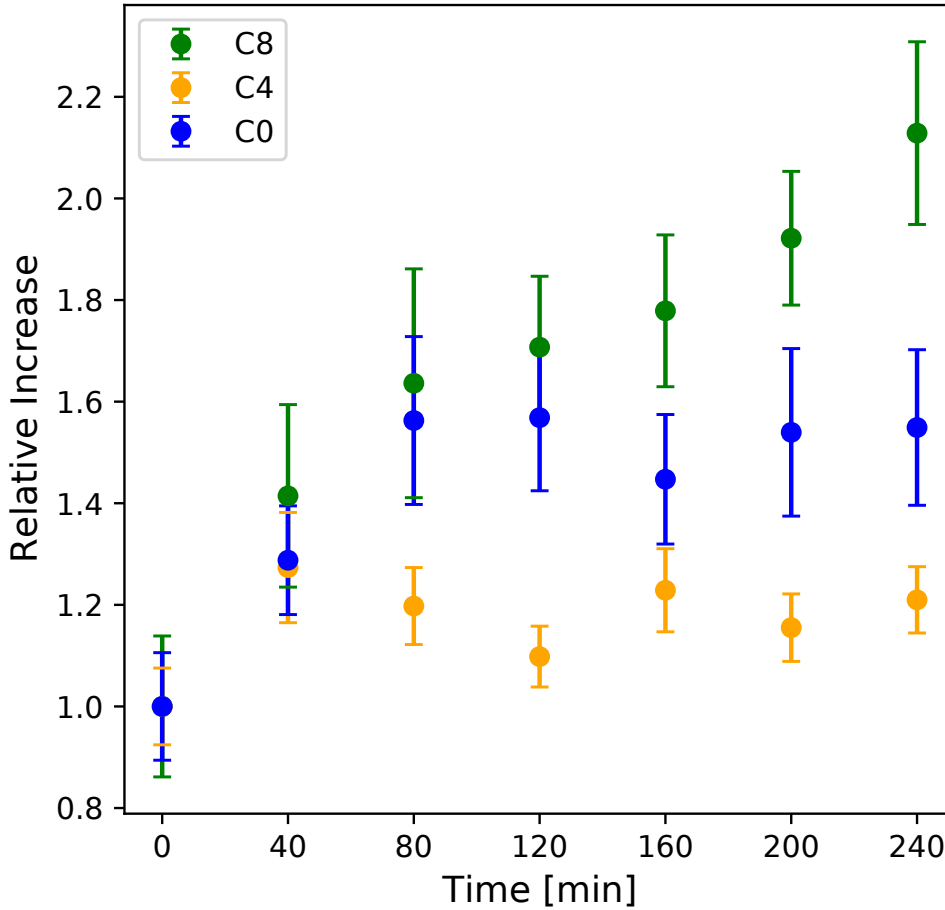


**Figure 4.22.** Transport of sCT(C0/C0) (blue,  $N = 16 \pm \text{SEM}$ ), sCT(C4/C4) (yellow,  $N = 17 \pm \text{SEM}$ ) and sCT(C8/C8) (green,  $N = 9 \pm \text{SEM}$ ) in an OrganoPlate. The dashed lines are not fit to the data but to help follow the trend of the data.

#### 4.6.2 Expanding the model

We wanted to investigate if sCT(C8/C8) is partitioning to the membrane of the cell. When analyzing through the cytosol of the cell, there is no apparent accumulation of the peptide on the upper membrane of the cell as seen in, e.g., Figure 4.3 A and B. To try and overcome this, we sampled the intensity through the nucleus. This is shown in Figure 4.23. Figure 4.23A shows the intensity profile of the membrane (red data points) at  $t = 0$  min just after adding sCT(C8/C8). Here, two well-separated peaks are observed, one for each cell membrane. The green points represent the intensity profile of the peptide channel. We see an initial peak below the cell, similar

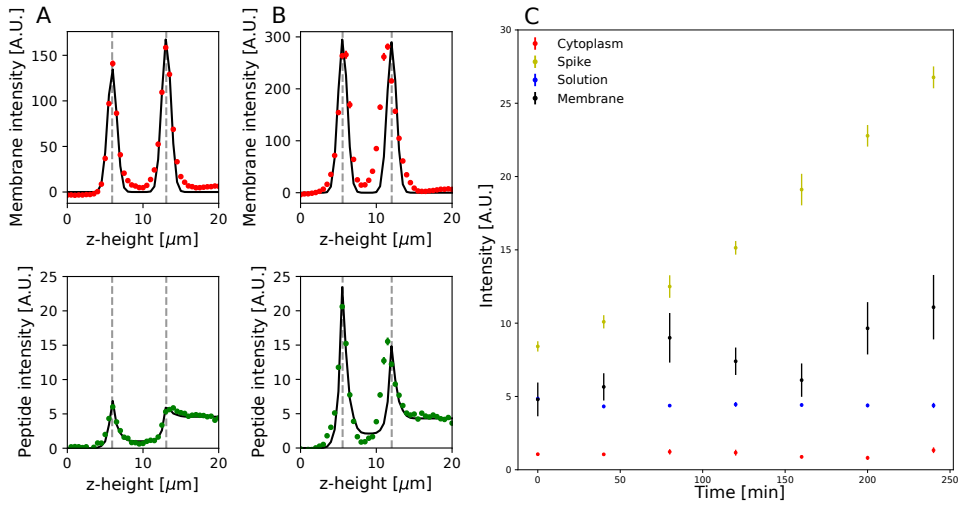


**Figure 4.23.** Sampling through the nucleus of a cell A) shows the membrane and peptide intensity profiles just after adding sCT(C8/C8), B) shows the same as in A), but 240 minutes after adding sCT(C8/C8). The red data points show the membrane intensity profile, and the green data points show the peptide intensity profile. Black lines represent fit to the intensity profiles. Vertical dashed lines represent the position of membranes. C) Shows four parameters over time. Solution level is shown in blue, cytosol level shown in red, and accumulated peptide below the cells shown in yellow. The accumulation of peptides on top of the cells shown in black.  $N = 9 \pm \text{SEM}$

to when sampling through the cytosol. But, there is also a small peak at the top membrane. Figure 4.23B shows the same cell as in Figure 4.23A, but at  $t = 240$  min. The membrane intensity profile is the same at the two time points, but the peptide intensity profile has changed. The accumulated peptide underneath the cell has increased from approximately 7 A.U. to 25 A.U. Looking at the peak at the upper membrane of the cell, it has also increased. However, the current quantification model is not able to detect changes on the upper membrane.

To quantify the binding of the peptide to the upper membrane, the model needs to be changed. We use a modified version of Equation 3.11 for this purpose. In Equation 3.11 there is a fitting parameter at the position of the bottom membrane used to quantify the amount of peptide transported through the cells. In the modified model, there is an additional fitting parameter at the position of the top membrane with the same function; quantify the amount of peptide binding to the upper membrane. The equation used to fit the intensity profiles seen in Figure 4.23 is as follows:

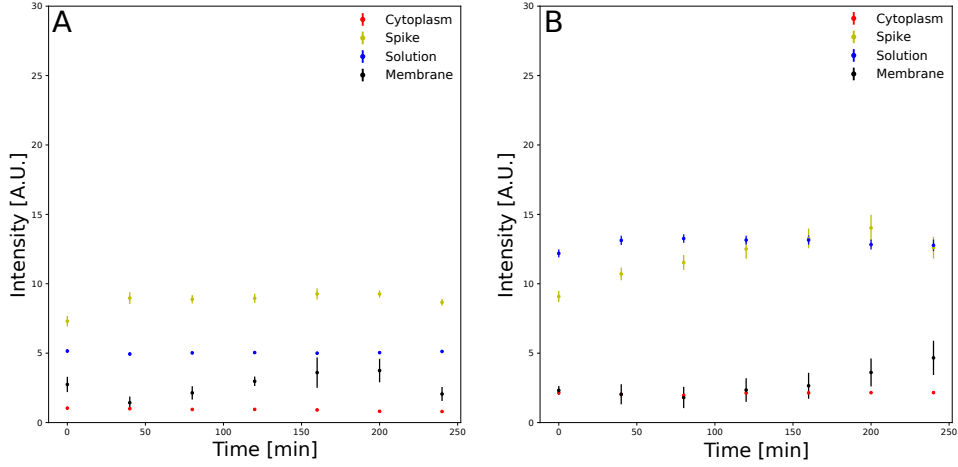


**Figure 4.24.** The intensity level extracted from sampling through the nucleus. A) Shows the transport of sCT(C0/C0) in yellow, the solution level in blue, the intensity level inside in red and the upper membrane binding in black.  $N = 5 \pm \text{SEM}$ . B) Shows the transport of sCT(C4/C4) in yellow, the solution level in blue, the intensity level inside in red and the upper membrane binding in black.  $N = 10 \pm \text{SEM}$

$$\begin{aligned}
 I(z) = & a_1 \left[ c \frac{1}{\sigma \sqrt{2\pi}} e^{-\frac{(z-\mu_1)^2}{2\sigma^2}} + (1-c) \frac{1}{\sigma \sigma_\Delta \sqrt{2\pi}} e^{-\frac{(z-(\mu_1+\mu_\Delta))^2}{2(\sigma \sigma_\Delta)^2}} \right] \\
 & + \frac{a_2}{2} \left[ c \left( 1 + \text{erf} \left( \frac{z-\mu_1}{\sqrt{\pi} \sigma_1} \right) \right) + (1-c) \left( 1 + \text{erf} \left( \frac{z-(\mu_1+\mu_\Delta)}{\sqrt{\pi} \sigma_1 \sigma_\Delta} \right) \right) \right] \\
 & + \frac{a_3}{2} \left[ c \left( 1 + \text{erf} \left( \frac{z-\mu_2}{\sqrt{\pi} \sigma_1} \right) \right) + (1-c) \left( 1 + \text{erf} \left( \frac{z-(\mu_2+\mu_\Delta)}{\sqrt{\pi} \sigma_1 \sigma_\Delta} \right) \right) \right] \\
 & + a_4 \left[ c \frac{1}{\sigma \sqrt{2\pi}} e^{-\frac{(z-\mu_2)^2}{2\sigma^2}} + (1-c) \frac{1}{\sigma \sigma_\Delta \sqrt{2\pi}} e^{-\frac{(z-(\mu_2+\mu_\Delta))^2}{2(\sigma \sigma_\Delta)^2}} \right] + b
 \end{aligned} \tag{4.2}$$

The black lines in Figure 4.23A and B show the fit to the intensity profiles using the equation seen in 4.2. Figure 4.23C shows the four parameters used to fit the peptide intensity profile when sampling through the nucleus. The blue data points represent the solution level. The red data points represent the intensity level inside of the cell. The yellow data points represent the accumulated peptide underneath the cells. Lastly, the black data points represent peptide binding at the top membrane. The accumulated peptide increases over time from approximately 8 A.U. to 27 A.U., which is a relative increase of 3.4x. This relative increase is similar to when sampling the intensity through the cell's cytosol. The intensity level inside the cell should be 0 A.U. and should not change over time as we are sampling through the nucleus. The

red data points in Figure 4.23 show that the intensity level does not increase over time. The solution level should not change between the two sampling places in the cell, which we show as blue data points. The black data points in Figure 4.23 show the peptide binding to the upper membrane. Here the intensity increases from 5 A.U. at  $t = 0$  min to approximately 10 A.U. at  $t = 240$  min, yielding a relative increase of 2x.

Seeing that sCT(C8/C8) is binding to the membrane, we also wanted to test if the other two analogs have any membrane-binding properties. Figure 4.24 shows the different intensity levels extracted when sampling through the nucleus. Figure 4.24A shows the results for sCT(C0/C0). Here it shows that the peptide is not binding to the membrane over time but only fluctuates around the initial value. Furthermore, We do not detect the same accumulation underneath the cells when sampling through the nucleus for sCT(C0/C0). Here the relative increase is 1.2x, which is slightly lower than when sampling through the cytosol. The cytosol intensity level and solution intensity level are both stable over time.

Figure 4.24B shows the intensity levels of sCT(C4/C4) when sampling through the nucleus. For the first 160 minutes, the peptide does not seem to bind to the upper membrane, but after 160 minutes, it starts to increase over time. The increase begins at the same time as the accumulated peptide underneath the cells starts to hit a plateau. This suggests that upon reaching saturation of transport of the peptide, it starts binding to the upper membrane as a secondary phase. However, the experiment would need to run for more than four hours to investigate this further. The cytosol intensity level and solution intensity level are both stable over time.

The next step in developing the model and extracting additional information would be to let the experiment run for longer, which would let the transport of all three analogs reach a plateau. If the transport reaches a plateau, it can be fit and the kinetics of the transport rates can be extracted.

### 4.6.3 Summary

Using a microfluidic model we show that we can use the analytical expression to quantify the transport of peptides in another system than just the simple cell model. Furthermore, it validates that the simple cell model is a great tool for early investigation of drug candidates.

By expanding the model and sampling through the nucleus, we get additional information about the properties of the peptide. However, by sampling through the nucleus, one also loses some information regarding the uptake in the cytosol. Furthermore, the model becomes more complicated with an additional fitting parameter. The data is available from the same experiment, so regardless of the model used and where we sample the intensity, there is no need to do extra experiments.



# Conclusion

---

The thesis investigates two different projects with the ultimate goal of combining the knowledge obtained from the projects. The first part of the thesis focused on structured illumination created with a digital micromirror device (DMD) as the spatial light modulator. Here the characterization of the structured illumination was done with single molecules or single polymer beads by translating them across two different types of structured illumination.

By blocking the 0th diffraction order in the back focal plane of the diffracted light from the DMD, it optimizes the structured illumination. Furthermore, controlling the polarization of the light resulted in a sinusoidal structured illumination pattern with a period of approximately 230 nm and a modulation depth of approximately 0.9 with both horizontal and vertical lines. However, by not blocking the 0th order diffraction spot or controlling the polarization correctly, the structured illumination was non-harmonic, with a period of approximately 400 nm and a modulation depth of approximately 0.75.

C-MELM still localized the point emitters with higher precision than camera-based localization with either of the two types of structured illumination. C-MELM increased the localization by 1.3x for the non-harmonic structured illumination and 2.1x for the sinusoidal structured illumination compared to camera-based localization.

The second focus of the thesis was to develop a method quantifying the transport of biopharmaceuticals through a monolayer of cells. To quantify the transport of peptides through a cell monolayer, deriving an analytical expression describing the axial intensity profile was crucial. Estimating the point spread function of a spinning disk confocal microscope led to an analytical expression that quantifies the transported peptide, cytosolic peptide content, the solution level, and the background level of the system. Adding Lucifer Yellow and dextran to the cells showed fully functioning barriers of the cell monolayer. Adding TAT to the cells showed a 1.5x increase in transport over four hours. Furthermore, the cytosolic content of TAT increased 20-fold over four hours, proving that 1) the cell model has tight barriers and 2) that the quantification method can quantify the transport of peptides over time.

Three different analogs of sCT were tested against each other: native sCT (sCT(C0/C0)), sCT modified with two four carbon lipid chains (sCT(C4/C4)), and sCT modified with two eight carbon lipid chains (sCT(C8/C8)). Each peptide was added to the cells and monitored for four hours. Applying the quantification method showed that sCT(C8/C8) transports approximately 2.6 more than the other two

analogs.

Investigating the transport mechanisms of the three analogs showed some exciting results. First, lowering the temperature from 37 °C to 25 °C means lowering the general transport, both active transport and passive diffusion of the peptide. All three analogs showed a lower transport at 25 °C compared to 37 °C. Secondly, Adding 80  $\mu$ M of dynasore inhibits the function of dynamin, which is a molecule needed in clathrin-dependent endocytosis. The transport of sCT(C0/C0) and sCT(C8/C8) was significantly lower than when the dynasore was absent. However, it did not lower the transport for sCT(C4/C4), suggesting that the transport mechanism of sCT(C4/C4) does not depend on clathrin-mediated endocytosis, but sCT(C0/C0) and sCT(C8/C8) do.

# Appendices





## APPENDIX **A**

# Additional Figures

---

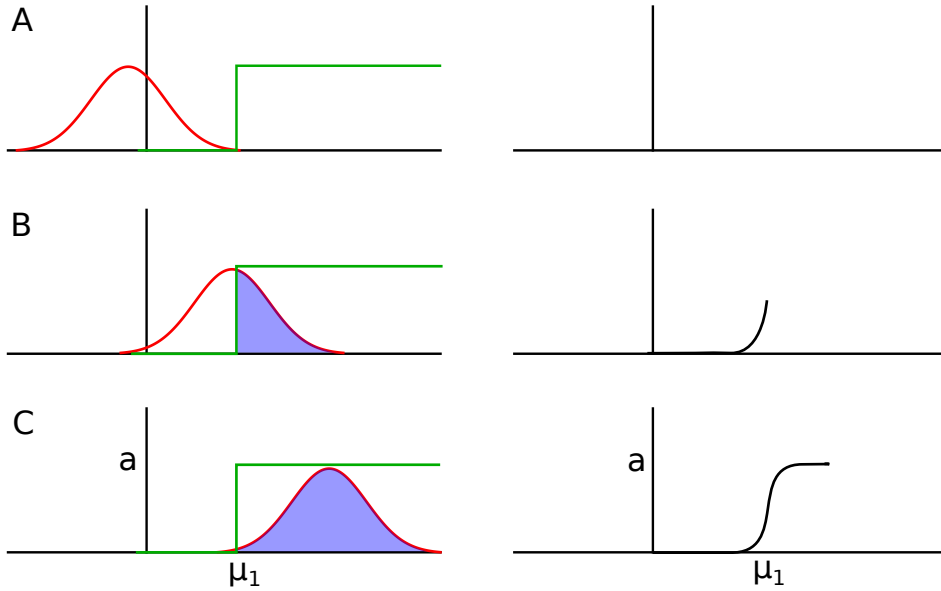


**Figure A.1.** Convolution of a PSF (red curve) and a step function (green curve). A) Shows the two functions (on the left) and the convoluted function (on the right) when no overlap between the two input functions. B) Shows the two functions with partial overlap (on the left) with blue area representing overlap. The convoluted function is seen on the right and show the area of the two input functions. C) Shows the two functions at full overlap (on the left) with the blue area representing the overlap. The convoluted function is an error function and is seen on the right. The position  $\mu_1$  is the inflection point of the error function and also where the step function goes from a value of 0 to a, where a is the amplitude of the step.

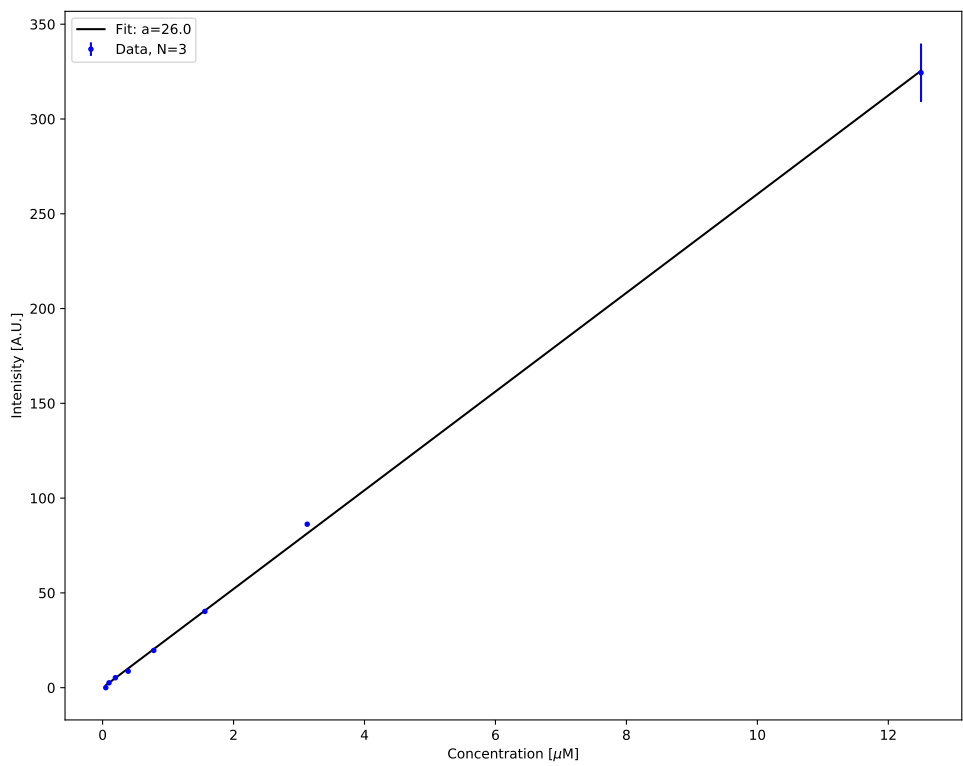


**Figure A.2.** Calibration curve of FTIC fluorophore.

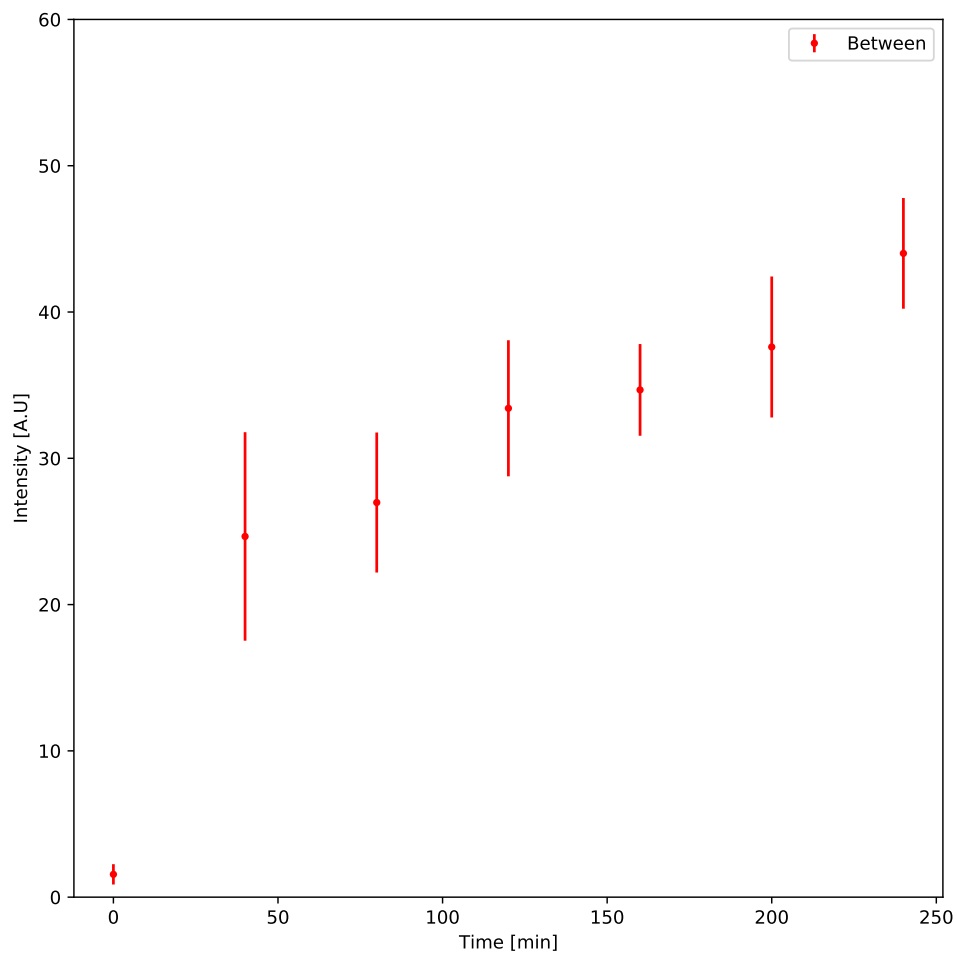


**Figure A.3.** The between parameter of TAT.

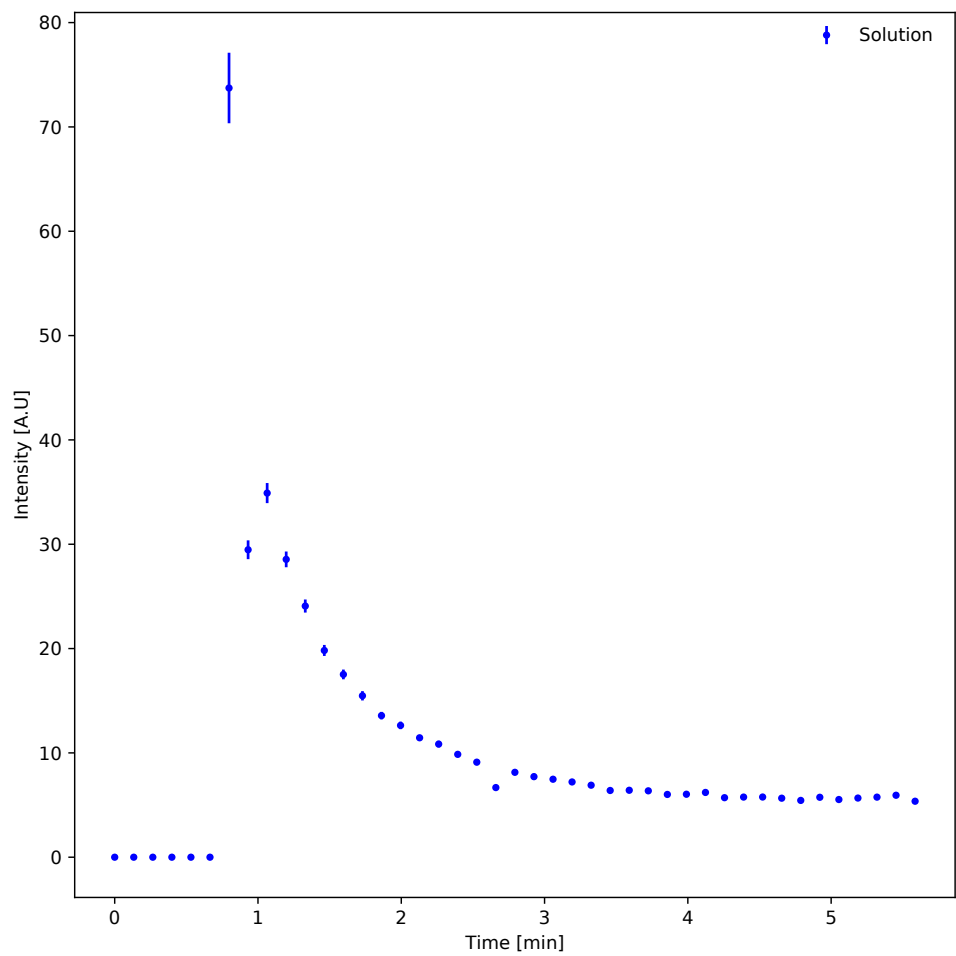


**Figure A.4.** Adding sCT(C8/C8) live during acquisition.



# APPENDIX B

## Journal articles

---

- B.1 Camera-based localization microscopy optimized with calibrated structured illumination



# Camera-based localization microscopy optimized with calibrated structured illumination

Martin Schmidt <sup>1</sup>, Adam C. Hundahl <sup>1</sup>, Henrik Flyvbjerg <sup>1</sup>, Rodolphe Marie <sup>1</sup> & Kim I. Mortensen <sup>1✉</sup>

Until very recently, super-resolution localization and tracking of fluorescent particles used camera-based wide-field imaging with uniform illumination. Then it was demonstrated that structured illuminations encode additional localization information in images. The first demonstration of this uses scanning and hence suffers from limited throughput. This limitation was mitigated by fusing camera-based localization with wide-field structured illumination. Current implementations, however, use effectively only half the localization information that they encode in images. Here we demonstrate how all of this information may be exploited by careful calibration of the structured illumination. Our approach achieves maximal resolution for given structured illumination, has a simple data analysis, and applies to any structured illumination in principle. We demonstrate this with an only slightly modified wide-field microscope. Our protocol should boost the emerging field of high-precision localization with structured illumination.

<sup>1</sup>Department of Health Technology, Technical University of Denmark, Lyngby, Denmark. ✉email: [kimo@dtu.dk](mailto:kimo@dtu.dk)

Fluorescently labeled molecules and particles are localized and tracked with super-resolution throughout the nano- and biosciences. The structure and processes of life at the nanoscale are probed with these tools<sup>1–4</sup>. The spatio-temporal resolution of these techniques improves with improving microscopy modalities<sup>5</sup>, fluorescent probes<sup>6</sup>, and cameras<sup>7</sup>. But resolution also improves with improving localization methods<sup>1,8</sup> and image analyses<sup>9</sup>. In a recent such improvement, MINFLUX<sup>8</sup> vastly improved the “photon economy”<sup>10</sup> of localization by utilizing a doughnut-shaped illumination structure for localization, albeit with low throughput due to its scanning implementation. A new class of localization methods (ROSE<sup>11</sup>, SIMPLE<sup>12</sup>, SIMFLUX<sup>13</sup>), sometimes referred to as modulation-enhanced localization microscopy (MELM)<sup>14</sup> methods, avoid the bottleneck of scanning by combining the use of wide-field structured illumination with camera-based imaging. While current implementations compare favorably to conventional methods, they, unfortunately, use only half the localization information encoded by their structured illuminations in actual measurements, as detailed below.

In camera-based (wide-field) localization microscopy, any structure in the illumination of the sample is unintended but predominantly varies slowly across the image<sup>15–18</sup>. Regardless, fluorescent point-emitters image as diffraction-limited spots<sup>9,19</sup> (Fig. 1a, Supplementary Note 1). The location of the emitter is determined with high precision by fitting a theoretical model of the point-spread function (PSF) to the spot<sup>9</sup> (Fig. 1a, Supplementary Note 1–3). Such PSF-fitting is used extensively to track molecules and particles with nanometer resolution<sup>19</sup> and is leveraged by various super-resolution methods (e.g., PALM<sup>20</sup>, STORM<sup>21</sup> and DNA PAINT<sup>22</sup>) to overcome the diffraction limit.

Since the spot registers a finite number of photons,  $N$ , the position coordinates of the emitter can be determined only with limited precision. The variance of estimates for a position coordinate  $x$  is

$$\text{Var}(x) = \frac{\sigma^2}{N_i} = \frac{\sigma^2}{N_{\text{effective}}} \quad (1)$$

where  $\sigma$  is a constant length that is specific to the experiment and proportional to the wavelength of the emitted light, while  $i$  quantifies the localization information per photon achieved with a given image analysis. It is not always possible to reduce this variance by increasing  $N$ : The value of  $N$  may be limited by, for example, a desired temporal resolution (frame rate), and/or photobleaching of the emitter, and/or phototoxicity to the sample. Instead of increasing  $N$ , one may maximize  $i$  and thereby increase the effective photon number,  $N_{\text{effective}}$ . While other methods exist<sup>15,23</sup>, it is well established that maximum likelihood estimation (MLE) with a correct model of the PSF is one optimal method to this end<sup>9,10,24,25</sup>. It achieves the minimal possible variance allowed theoretically by the so-called Cramér-Rao lower bound (CRLB<sup>26</sup>), by using all localization information present in a spot<sup>9,10,24,25</sup>. Thus, it is impossible to do better than that for a given image.

MINFLUX<sup>8,27</sup>, on the other hand, localizes and tracks fluorescent particles with up to 22-fold improvement of  $N_{\text{effective}}$  compared to that of optimal fitting of PSFs<sup>8</sup>. This is achieved by comparing the particle's total intensity from exposures to different doughnut-shaped illumination structures. This allows ultra-fast tracking of individual particles, but the scanning implementation limits throughput severely.

For localization purposes, the bottleneck in throughput can be mitigated by use of wide-field structured illumination, which amounts to camera-based MINFLUX (Supplementary Note 4–6). Conceptually, for each of two orthogonal directions in the image

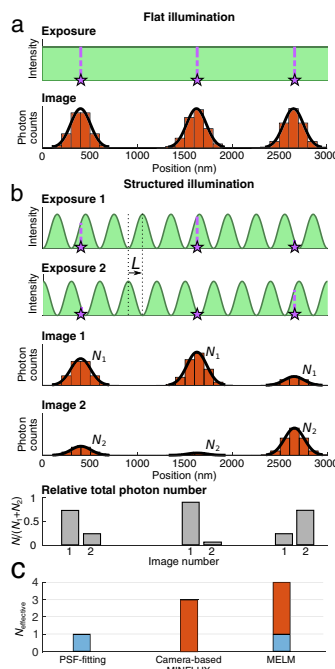


**Fig. 1 | Illustration of MELM and its theoretical performance.** **a** In conventional camera-based localization microscopy, the illumination is spatially constant (green line). Thus, all fluorescent point-source (purple stars) are illuminated with the same intensity. Consequently, the diffraction-limited images (spots) of identical sources (orange bars) are equally intense on average. If those spots are non-overlapping, the position of each point-source can be determined by fitting its spot with a model point-spread function (PSF) (black solid lines, Methods). **b** Under structured illumination (Exposure 1, green line), the average number of photons,  $N_1$ , in the diffraction-limited spot of each point-source (Image 1, orange bars) depends on the position of the source relative to the illumination. If the structured illumination is phase-shifted (Exposure 2, green line), the average number of photons,  $N_2$ , in the diffraction-limited spot of each point-source changes (compare Image 1 to Image 2, orange bars). Regardless of intensity, the position of a point-source thus imaged twice is determined by fitting a model-PSF that has the position coordinate among its fitted parameters (black solid lines). Since we know the structure of the illumination from calibration and the distance,  $L$ , it was translated (Methods), the relative number of photons  $N_{1,2}/(N_1 + N_2)$  in the two spots from a point-source reveal its position modulo  $L$  (Methods). **c** The resulting effective photon number of an optimized MELM method ( $N_{\text{effective}}$  in Eq. 1), is the sum of the effective photon numbers for PSF-fitting and camera-based MINFLUX, assuming identical total exposure time (Methods, Supplementary Fig. 1). Note that the values for  $N_{\text{effective}}$  correspond to the values realized in our 2D C-MELM experiment below (Supplementary Fig. 1, Supplementary Note 7–8).

plane, it works as follows: The sample is illuminated with a spatially periodic intensity and imaged with a camera through a microscope (Fig. 1b). An isolated point source images as a diffraction-limited spot. The intensity of each such spot depends

on where its point-source is located in the structured illumination (Fig. 1b). After a translation (phase shift) of the illumination, each spot appears at its unchanged position in a new image, but typically with different intensity (Fig. 1b). If the position-dependent intensity of both illuminations is known, the relative intensity of a spot in its two images determines the position of its source, modulo the period of the structured illumination. SIMPLE<sup>12</sup> is a recent protocol to this end. It determined the relative intensities with masks.

The relative intensities are, however, optimally determined by fitting a theoretical PSF to the spots recorded under different illuminations (Fig. 1b, Methods). Such fits determine both the intensities and, simultaneously and directly, the position of each point-source. This extra position-information resolves the ambiguity caused by the periodicity of the structured illumination. It also improves position-estimates because the total intensity and the source coordinates are statistically independent aspects of a spot.

ROSE<sup>11</sup> and SIMFLUX<sup>13</sup> are recent implementations of such a hybrid approach. ROSE generates the structured illumination with electro-optical modulators and cycles repeatedly between phase-shifts during the recording of a “frame”, where a “frame” is the set of images recorded of one sample with differently phase-shifted illumination structures. Each image in a “frame” is recorded in a separate area of the camera by changing the emission path in synchrony with the phase-shift. SIMFLUX, on the other hand, records each image in a “frame” in a single exposure. Its structured illumination is generated and shifted with a set of piezo-mounted gratings. Both methods calibrate the structured illumination using the sample itself. This requires a dense sample, a complicated data-processing pipeline, and illumination structures that are purely harmonic with no excess spatial variation due, e.g., to imperfect optics. Thus, for sparse samples and/or in the presence of excess variation in the structured illumination, this strategy may fail. Even if it does not fail, however, its calibrating-while-localizing uses information for calibration that could have improved localization. A better “photon economy”<sup>10</sup> uses all photons from point-sources to be localized for localization and calibrates the structured illumination *before* it is used, with other, less precious sources.

Additionally, and importantly, while ROSE<sup>11</sup> and SIMFLUX<sup>13</sup> do realize ~2–3-fold improvements on  $N_{\text{effective}}$  relative to conventional localization applied to the same data, this is only half the improvement possible with these methods. Specifically, the CRLB for SIMFLUX allows a ~5-fold improvement, but only ~2.3-fold improvement was realized in actual measurements (additional improvements were achieved during brief measurements lasting less than one second)<sup>13</sup>. The CRLB for ROSE allows ~6-fold improvement, but only a ~3-fold improvement was realized<sup>11</sup>. In both cases, residual drift in the system was invoked to explain these shortcomings.

Below, we demonstrate that the CRLB can be realized in actual measurements with a pre-calibrated structured illumination: We extract all structured illumination-encoded localization information from images. Specifically, for each emitter we fit its theoretical PSF to its image simultaneously in every illumination employed, using MLE and a model of the structured illumination which was already calibrated locally and independently. This vastly simplifies the data analysis by reducing it to just a single fit of a model to recorded images. The resulting method, C-MELM (Calibrated Modulation Enhanced Localization Microscopy), localizes point-sources in camera-acquired images with maximal  $N_{\text{effective}}$ , the maximal value allowed by the CRLB for the experiment (Fig. 1c). This maximal  $N_{\text{effective}}$  is the sum of values for  $N_{\text{effective}}$  from each of a MELM method’s constituent camera-based localization methods (Fig. 1c, Supplementary Fig. 1, Supplementary Note 7–8) since these provide statistically independent information. With C-MELM, we thus

localize single molecules with an  $N_{\text{effective}}$  of ~4.4, amounting to an increase in localization precision by a factor of ~2.1. This compares favorably to previous camera-based MELM implementations. Finally, C-MELM also localizes point-sources with theoretically maximal precision if the structured illuminations are distinctly non-harmonic, we show.

## Results

**Experimental implementation and calibration of C-MELM.** For experimental demonstration, we used a commercial epifluorescence microscope with a modified excitation light path (Fig. 2a, Methods, Supplementary Fig. 2). Specifically, we used a collimated laser beam to image a digital micromirror device (DMD) through the objective using two-beam interference<sup>28</sup> (Methods). This served as illumination of the sample<sup>12,29</sup>. We configured the mirrors to create lines<sup>12,29</sup> with a duty ratio of 3/9 (Fig. 2b, Methods). We translated (i.e. phase shifted) the structured illumination as needed by using our control of the positions of the lines from the DMD. This simple setup provided optimized, consistent, and controllable structured illumination of the sample.

The local intensity of the illumination is required input to C-MELM. We therefore characterized the illumination by translating bright 46-nm fluorescent beads across the stationary structured illumination (Fig. 2c, d, Methods). We repeated this characterization for all three phases of the structured illumination that we would use (Fig. 2c, d) and along both coordinate axes (Supplementary Fig. 3), to check that the profile of the structured illumination is conserved under its translations (phase shifts). We repeated these checks and analyses for multiple beads distributed randomly in the field of view (FOV), in order to account for smooth excess spatial variations in the structured illumination caused by the optics<sup>15–18</sup>. For practical application, we interpolated between the nearest five such characterizations of the structured illumination in order to determine the illumination at a given position in the FOV (Methods, Supplementary Note 10). We found the structured illumination resulting from this illumination scheme to be harmonic with a period of ~230 nm and a contrast of up to ~0.9 (Fig. 2c). Importantly, however, our calibration assumes neither that the structured illumination is harmonic nor that it is free from excess spatial variation<sup>15–18</sup>. By abstaining from assumptions, (i) eliminates a potential source of error present in ROSE, SIMPLE and SIMFLUX, which all assume such ideal conditions (ii) ensures that C-MELM estimates may be calculated directly with a single MLE fit to images with no need for subsequent iterative refinement of particle positions and/or structured illumination parameters, and (iii) ensures that C-MELM also works with other microscopy modalities and sources of structured illumination (see below).

**C-MELM localizes single molecules with maximal precision.** To demonstrate C-MELM’s performance, we imaged single Atto-590-labeled Streptavidin molecules immobilized on a coverslip as a time-lapse recorded movie (Methods). Each “frame” in this movie consists of six images of the sample, one for each of three phase-shifted illumination structures along each of two orthogonal coordinate axes (Fig. 3a, Methods). For each isolated single molecule, we obtained the C-MELM estimate of its position by assuming that its six diffraction-limited images (“spots”) in a “frame” could be modeled with six 2D Gaussians produced by a common point-source at a single position, but with intensities that were constrained by the calibrated structured illumination (Methods, Supplementary Note 7). The theoretical images resulting from this fitted model agree with the experimental data

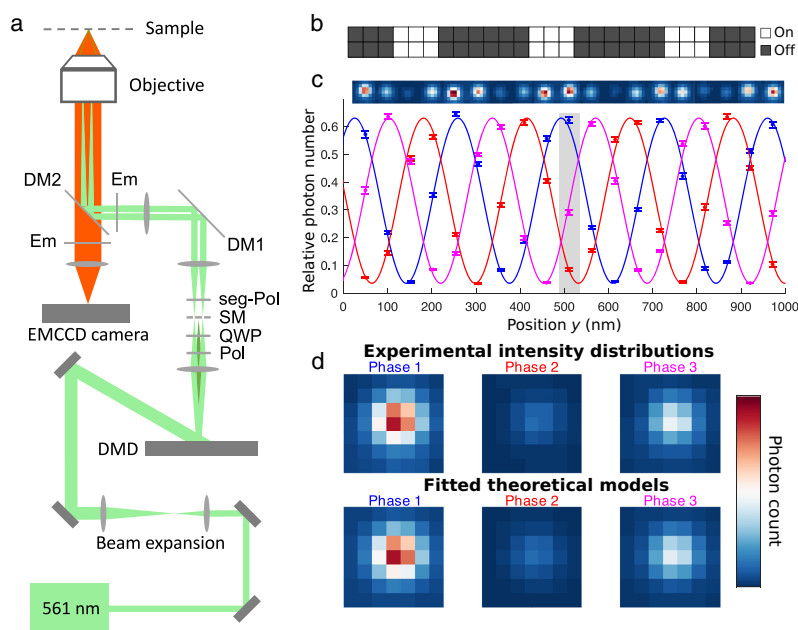


**Fig. 2 Implementation of C-MELM using a digital micromirror device (DMD).** **a** Experimental setup consisting of a commercial wide-field epi-fluorescence microscope with a modified excitation path (Methods): The excitation light (green) is reflected off the DMD before it is relayed by a telescope, undergoes diffraction through the objective and results in structured illumination in the sample plane. See Supplementary Fig. 2 for details. **b** Subset of the DMD array configured in a periodic series of “on” and “off”-mirrors. **c, d** Example characterization of the structured illumination using a single 46-nm fluorescent bead (Methods). **c** We translated a fluorescent bead relatively to the structured illumination generated with the DMD configuration in **b** and recorded the number of photons in its resulting diffraction-limited spots (top row) for each position (blue dots) during 50-ms exposures. For each position of the bead, this was repeated for a total of three phases of the structured illumination (colored dots). A harmonic function with parameters obtained by a fit to data (colored curves, Methods, Supplementary Note 3) describes the data perfectly and thus characterizes the structured illumination. For each position, the total intensities were normalized by the total photon number observed in the three diffraction-limited spots recorded at that position. Error bars represent standard error of the calculated relative photon number. **d** Experimental bead images (top row) obtained at a single stage position (gray area in **c**) under illumination from three different phases as in **c**. All three images are fitted with a point-spread function model (bottom row) for a point-source under assumption that its position is identical in the three images (Methods, Supplementary Note 3). This enables accurate estimation of total intensity also in dim images (e.g., for Phase 2). The effective pixel size was 107 nm.

(Fig. 3a), which indicates that our 2D-Gaussian approximation to the PSF (Methods) is accurate.

For comparison with state-of-the-art fitting of PSFs to images recorded with uniform illumination, we used the set of six exposures as input to ensure that the total number of photons was identical between the localization methods (Supplementary Note 3). We localized each molecule multiple times with both methods. Typically, we obtained ~300 position estimates for each localization method from which we calculated the localization precision as the s.d. of the positions (Fig. 3b). For the example molecule shown in Fig. 3a, b, we found that C-MELM more than doubled the localization precision: it yielded an  $N_{\text{effective}}$  of ~4.4. Note that both localization methods achieved their optimal performance with the available photons, since their position estimates scattered as standard normal distributions when rescaled by their theoretical s.d. calculated from the CRLB (Fig. 3c, Supplementary Fig. 4, Supplementary Note 8).

We repeated this analysis for 14 well-isolated molecules in the FOV of the time-lapse movie. For each molecule, we thus calculated the sample variance of position estimates obtained using, respectively, C-MELM and state-of-the-art fitting of PSFs to images (effectively) recorded with uniform illumination. The localization variances obtained from the molecules agree with their theoretically predicted values (Fig. 3d), which demonstrates that C-MELM makes optimal use of the information content in both of its constituent camera-based localization methods: it achieves the theoretical limit for performance, its CRLB. This shows that C-MELM is consistently superior to PSF-fitting by a factor of ~4.4 on  $N_{\text{effective}}$ , which is a significant improvement relative to the experimentally realized values of previous camera-based MELM methods.

**C-MELM localizes particles with maximal precision under non-harmonic illumination.** In order to demonstrate that C-MELM

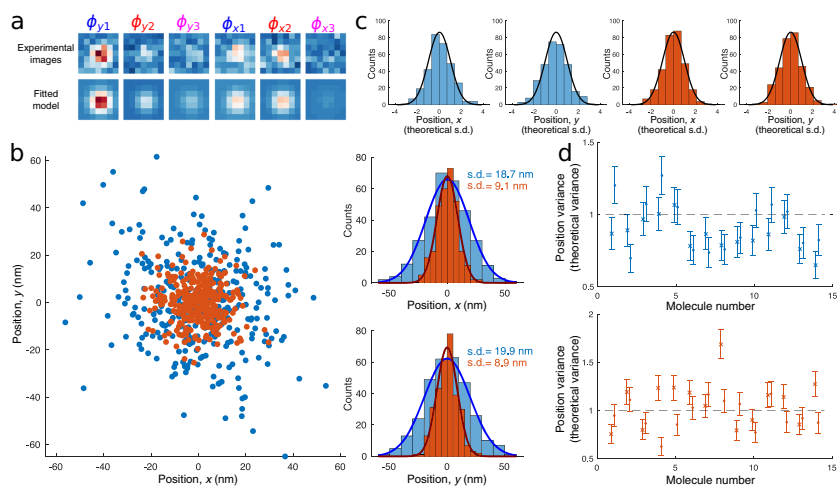


**Fig. 3 Experimental demonstration of C-MELM for localization of single molecules.** **a** Single Atto590-labeled Streptavidin molecules were subjected to six 50-ms exposures of structured illumination: three phases of, respectively, y-periodic ( $\phi_y$ ) and x-periodic illumination ( $\phi_x$ ). Each molecule thus produced six diffraction-limited images (top row), which constitute one measurement. The molecule's position and six spot intensities were estimated by a simultaneous maximum likelihood estimation fit of six model point-spread functions (PSFs) with shared point-source location, in which we constrained the relative intensities in spots as expected from the illumination structures (bottom row, Methods). For display, each image was averaged over ten frames for noise-reduction, but all position estimates obtained below were done on individual frames. The effective pixel size was 107 nm. **b** 310 positions of the molecule in **a** obtained, respectively, by PSF-fitting (blue) and C-MELM (orange). The estimates are centered on their respective mean values. Position estimates for each coordinate and localization method are normally distributed yielding a localization precision as given by the s.d. in the legend. **c** Histograms of all position estimates for PSF-fitting (blue) and C-MELM (orange) centered on their mean values and in units of their theoretically predicted s.d. calculated from the Cramér-Rao lower bound (CRLB). Agreement with a standard normal distribution with unit variance (black curve) demonstrates that localization in each case is optimal. **d** Sample variances of x- (crosses) and y- (circles) coordinates of positions obtained, respectively, with PSF-fitting (blue) and the C-MELM (orange) for 14 isolated single molecules in the field of view in units of their respective theoretical variance (calculated from the CRLB). The data fluctuate around 1, which is expected when estimates achieve the theoretical limit for performance, the CRLB. Error bars indicate the s.d. of the sample variance.

does not require harmonic illumination structures in order to localize with theoretically optimal precision, we modified our excitation light path in an alternative manner (Supplementary Fig. 5). Most notably, instead, we used three-beam interference for generation of the structured illumination<sup>28</sup> (Methods). For this setup, we used a 1/8 duty ratio on the DMD, which optimized the period/contrast relationship in this case. The realized structured illumination was distinctly non-harmonic but perfectly described by a single, simple theoretical model with phase-shifts (Methods, Supplementary Figs. 6 and 7 and Supplementary Note 9). For characterization of the resulting structured illumination, we used 51-nm fluorescent beads (Methods).

For demonstration, we imaged another set of 51-nm fluorescent beads as a time-lapse recorded movie (Fig. 4a, Methods). Due to the non-harmonic structure of the structured illumination, we used four phases to ensure that C-MELM's performance is independent of the particle's position relative to the structured illumination (Supplementary Fig. 8). For analysis, we used a set of eight 2D Gaussians produced by a common point-source at a single position, but with intensities that were constrained by the calibrated structured illumination in Fig. 4c, d (Methods, Supplementary Note 7, Supplementary Fig. 9). Also, in this case, the theoretical images resulting from this fitted model agree with the experimental data (Fig. 4b), which indicates that our 2D-Gaussian approximation to the PSF is accurate also for fluorescent beads<sup>9</sup>.

We repeated this analysis for all 40 well-isolated beads in the FOV of the time-lapse movie (Fig. 4a). For each bead, we thus calculated the sample variance of position estimates obtained using, respectively, C-MELM and state-of-the-art fitting of PSFs to images recorded with uniform illumination (Fig. 4e, f). The total photon number obtained from beads varied due to spatial variations in the excitation laser intensity and variations in the size of beads. Regardless, C-MELM is consistently superior to PSF-fitting by a factor of  $\sim 1.7$  on  $N_{\text{effective}}$ , thus nearly doubling the photon efficiency. Since this structured illumination has a poorer period/contrast relationship than the harmonic structured illumination realized above, each of C-MELM's constituent camera-based localization methods here contribute substantially to the resulting photon efficiency, and C-MELM makes optimal use of both: it achieves the theoretical limit for performance, its CRLB (Fig. 4e, f, Methods, Supplementary Note 8). Consequently, no other unbiased estimator can do better with this structured illumination.

The duration of recording of each calibration and test movie was around three minutes during which fluorescent particles were imaged for four seconds at each position (Methods). We observed negligible sample and focal drift, and thus no correction for drift was required. The presence of significant sample and/or focal drift would have prevented C-MELM from achieving its CRLB, which assumes no drift. The time between recordings of data for

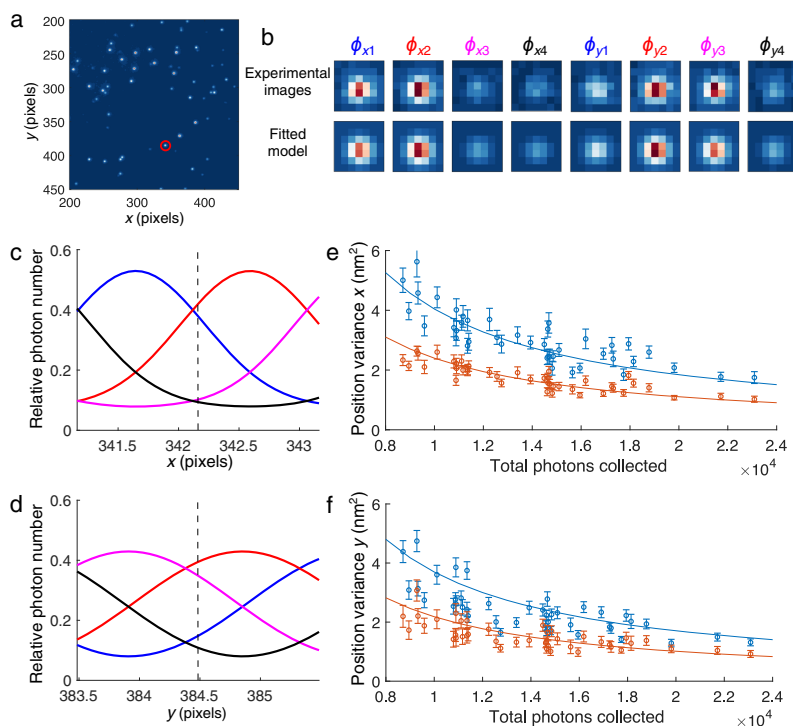


**Fig. 4 Experimental demonstration of C-MELM with non-harmonic structured illumination.** **a** Camera-based microscopy image of a sample containing multiple isolated fluorescent 51-nm beads (Methods). Effective pixel width, 107 nm. A bead used as example for demonstration in subsequent panels is indicated (red circle). **b** The sample in **a** was subjected to eight 50-ms exposures of structured illumination (Methods): four phases of  $x$ -periodic illumination ( $\phi_x$ ) and four phases of  $y$ -periodic illumination ( $\phi_y$ ). This resulted in eight recordings of diffraction-limited spots (top row) from the same bead, which constitute one measurement. The fluorescent bead's position and eight intensities were estimated by a simultaneous maximum likelihood estimation fit of eight model point-spread functions with shared point-source location, in which we constrained the relative intensities in spots as expected from the illumination structures (bottom row, Methods). **c, d** Relative photon numbers expected from the characterization of four phases of structured illumination (solid lines with various colors, Methods, Supplementary Note 9, Supplementary Fig. 9) along the  $x$ - (**c**) and  $y$ -axes (**d**), respectively. The bead's approximate position is indicated (dashed lines). **e, f** Sample variance of position estimates, for  $x$ - (**e**) and  $y$ -coordinates (**f**), for all 40 isolated particles in the field of view in **a** for C-MELM (orange) and conventional camera-based localization (blue). Error bars represent the s.d. of the sample variance. The information-theoretical lower bound (Cramér-Rao lower bound (CRLB), Supplementary Note 8) for the variance is indicated for both methods (solid lines). C-MELM achieves its lower bound and is uniformly the superior method as it has the smaller variance, corresponding to an  $N_{\text{effective}}$  larger by a factor  $\sim 1.7$  (Eq. 1).

calibration and measurement typically was a couple of hours and included a change of experimental sample in the case of single-molecule imaging. During such time periods, we observed a slight drift of the structured illumination, which gave rise to a bias for the C-MELM position estimates. We corrected our estimates for this bias (Methods). Note, however, that the drift of the structured illumination had negligible effect on the precision of C-MELM position estimates (Figs. 3 and 4). This demonstrates the stability and feasibility of C-MELM in practical settings.

Finally, we extended our results using computer-simulated data to confirm C-MELM's ability to localize particles with accuracy and maximal precision according to the CRLB over a range of experimentally relevant total photon numbers (Supplementary Fig. 10).

## Discussion

The attainable resolution in a structured illumination-enhanced localization experiment depends crucially on the total number of source photons (Supplementary Fig. 10), on the background, and on the contrast and period of the structured illumination (Supplementary Note 11 and Supplementary Fig. 11). In our single-molecule experiments, our structured illumination yielded a contrast of  $\sim 0.9$  and a period of  $\sim 230$  nm, which is comparable to the illumination structures used in ROSE and SIMFLUX. We, however, were able to extract all the localization information encoded in photons by the structured illumination. Doing this, we have experimentally realized the full potential of camera-based MELM methods and have in practice achieved a factor of  $\sim 4.4$  on  $N_{\text{effective}}$ , which

corresponds to an improvement by a factor of  $\sim 2.1$  on the localization precision.

Additionally, we employed C-MELM with a structured illumination, which was distinctly non-harmonic. This shows that C-MELM does not rely on a specific structured illumination, as long as it can be characterized and modeled. With this non-harmonic illumination structure, we obtained an  $N_{\text{effective}}$  of  $\sim 1.7$ , which is the optimal improvement possible for a contrast of  $\sim 0.75$  and a period of  $\sim 400$  nm.

Thus, C-MELM makes optimal use of the resources in a given experiment, we have shown. Furthermore, C-MELM is readily applicable to other experiments that use wide-field structured illumination to enhance localization (e.g., SIMPLE, ROSE, SIMFLUX), since it only relies on a rigorous analysis in conjunction with a locally-calibrated model for the structured illumination but not on a specific structured illumination. Thus, all the benefits of C-MELM may be realized with both previous and future implementations of localization microscopy with any source of structured illumination<sup>5,30–33</sup>. The resulting gain in photon efficiency may be utilized to achieve better spatial resolution, or faster imaging, or both. In the context of various single-molecule super-resolution modalities (e.g., PALM<sup>20</sup>, STORM<sup>21</sup>, and DNA PAINT<sup>22</sup>), our calibrated illumination structures provide yet another advantage: They may be used to verify the presence/absence of blinking and/or bleaching of a molecule of interest or of any influential nearby molecules. To do this, one takes advantage of the fact that the different intensities from a molecule measured under different exposures are coupled in a known manner for given position of the molecule. Consequently, they may be used to indicate absence of blinking in a measurement or, alternatively, to flag it for individual analysis or rejection. This permits realization of all the benefits of our protocol also in the context of super-resolution imaging, even in the presence of complex blinking dynamics.

It is a common misconception that the PSF in experiments similar to ours is an Airy function with its characteristic diffraction rings. Rather, the PSF has an intense central peak, like the Airy function, but no diffraction rings, only tails that decrease slowly, approximately with the distance to the center of the PSF cubed, starting with a “shoulder” to the peak<sup>9</sup>. The central peak and its “shoulder” is described well by a 2D-Gaussian standing on a constant “background”<sup>9</sup> (Supplementary Note 1, Methods). This “background” adds to any actual fluorescent background in images, but depends on the incident illumination, since it is part of the PSF. Consequently, source photons contribute to it in a manner that is proportional to the structured illumination at the position of the point-source. This effectively allows for extraction of structured illumination-encoded information from an additional  $\sim 20$  per cent of photons<sup>9</sup>, when localizing emitters in images with sufficiently low actual background (Supplementary Note 7). When this is possible, it constitutes another improvement relative to ROSE and SIMFLUX.

That PSF is the result of an isotropic superposition of light emitted by an isotropic superposition of fluorophores that essentially are dipole emitters. This isotropic superposition may be the result of a single fluorophore that is free to rotate and does so sufficiently fast relative to the lifetime of its excited state that any dependence on the polarization of the excitation light field is lost. Alternatively, a collection of randomly oriented fluorophores in a fluorescent bead under isotropic illumination will result in the same PSF. A fluorescent bead imaged under total internal reflection fluorescence (TIRF) conditions has a similar PSF<sup>9</sup>.

On the other hand, the emission dipole moment of a single fluorophore may be fixed in orientation due to steric hindrances, electrostatic interactions, or deliberately with two linkers<sup>9,24,25,34–37</sup>. Such circumstances affect C-MELM analysis as well as conventional PSF fitting. If the fluorophore is fixed during the recording of each “frame”, an appropriate PSF for this purpose must be used for

accurate localization<sup>9,24,25,38</sup>. That PSF should also be used in C-MELM analysis, for localization and because its use guarantees an accurate quantification of the spot intensity. The fact that the spot's intensity depends on the orientation of the excitation dipole moment relative to the excitation field does not influence C-MELM, since this analysis depends only on relative intensities. If, instead, the fluorophore is fixed in orientation only during the recording of each image in a “frame”, the influence of excitation light field must also be accounted for. This also applies in the case where the fluorophore is partially free to rotate. If the fluorophore reorients between discrete states within an exposure time, C-MELM analysis seems challenging.

We note, finally, that our method is applicable in principle also to other experiments in which the PSF may be radically different, e.g., in the presence of significant aberrations<sup>39–41</sup> and/or in 3D imaging<sup>39–43</sup>, provided that the PSF is known or can be modeled sufficiently well.

## Conclusion

In conclusion, we have demonstrated that C-MELM optimally exploits the localization information in images obtained in experiments using wide-field structured illumination to enhance localization microscopy. Its ease-of-use and compatibility with existing and future implementations of this paradigm should ensure that all localization information is put to maximal use.

## Methods

**Sample preparation.** In our first experiment, red-fluorescent polymer nanoparticles with  $\phi = 46$  nm (Invitrogen, FluoroSphere carboxylated) were used as light emitters for calibration of the structured illumination. Their maximum excitation and emission wavelengths were 580 nm and 605 nm, respectively. The stock solution of nanoparticles was diluted  $10^4$  times in MilliQ and sonicated for at least 30 min. A fixed amount was diluted further 10 times in 99% ethanol for a final dilution of  $10^5$ . A high-precision coverslip (Marienfeld cat no. 0107052) was cleaned with UV/ozone for 60 min before use. To deposit nanoparticles on the coverslip, the coverslip was incubated with 5  $\mu$ L of the nanoparticle solution and dried at 50 °C for 1 h in an oven. Subsequently, the coverslip was mounted on a microscope slide with 10  $\mu$ L of 1xTE. Slides were sealed with epoxy glue and imaged right away.

For the secondary experimental setup, green-fluorescent polymer microspheres with  $\phi = 51$  nm (Duke Scientific Corporation cat no G50) were used as light emitters. Their maximum excitation and emission wavelengths were 468 nm and 508 nm, respectively. The stock solution of microspheres was diluted  $10^4$  times in PBS and sonicated for at least 30 min. To deposit microspheres on the coverslip, the coverslip was incubated with 10  $\mu$ L of the microsphere solution for 1 min on a glass slide to spread the microspheres evenly across the surface. The coverslip was briefly dipped in PBS and then in Milli-Q water, before it was dried under a nitrogen flow. Subsequently, the coverslip was mounted on a microscope slide with 8  $\mu$ L of Mowiol solution and left overnight to harden.

Single-molecule samples were obtained by grafting Streptavidin labeled with Atto-590 onto a BSA/BSA-biotin layer. 10  $\mu$ g/mL BSA was mixed with 1  $\mu$ g/mL BSA-biotin complex in a 10:1 ratio. 100  $\mu$ L was added to UV/ozone cleaned coverslips for 20 min and washed in 1xTE for 2 min. Next, 100  $\mu$ L of 1  $\mu$ g/mL Streptavidin labeled with Atto-590 was added to the coverslip and left covered for 10 min before washed in 1xTE for 2 min. The coverslip was mounted with degassed 1xTE, sealed with nail polish, and imaged right away.

**Microscope.** Fluorescence imaging was performed with a Nikon Eclipse Ti2-U inverted microscope with a 100x oil objective (Nikon Plan Apochromat Lambda 100x/1.45). The microscope was modified for structured illumination (see below, Fig. 2, Supplementary Figs. 2 and 5). A dichroic mirror (AHF, quad band F73-478) allowed us to use the objective in both excitation and emission pathways. Prior to recording, the emission of the sample was guided through an emission filter (AHF, quad band cat no. F72-866) and a 1.5x magnifying tube lens. The microscope was placed on an optical table. A motorized XY-stage was used to localize the emitters, while an XY-piezo stage (MCL, NanoH) was used for high-precision positioning during imaging. Focus was adjusted manually and inspected using the average spatial s.d. of spots in an image, to ensure that images were well-focused.

## Generation of structured illumination using a digital micromirror device

**(DMD).** A 561-nm laser (Cobolt, 06-DLP 561 nm) was used as excitation light source. The light was expanded with 2 lenses (Thorlabs;  $f = 30$  mm and  $f = 200$  mm, respectively). Two mirrors (Thorlabs, BBEO2) guided the expanded light onto a digital micromirror device (DMD, Texas Instruments Lightcrafter 9000). The DMD consists of an array of micrometer-sized square mirrors that can be either “on” (reflection to sample) or “off” (reflection away from sample). The angle



between the incident light and the DMD was  $\sim 24$  degrees, such that the most intense first diffraction order of the “on”-position mirrors was normal to the DMD plane. At this angle, and for the chosen wavelength, the blaze-grating angle condition was satisfied and ensured that i) the main diffraction angle is intense and ii) the two first diffraction orders created by the lines on the DMD are of equal intensity<sup>39,44</sup>. This light was sent through a telescope (Thorlabs,  $f = 300$  mm) and collimated by a third (projection) lens (Edmund optics,  $f = 300$  mm). The two lenses of the telescope, the projection lens, and the objective were all positioned in  $4f$  configurations, such that i) the DMD was imaged in the sample plane and ii) the back focal plane of the objective is conjugated with the focal plane of the telescope. Following Reymond et al.<sup>12</sup>, we utilize this plane to, first, control the polarization of light by introducing a linear polarizer and a quarter wave plate oriented at  $45$  degrees relative to the linear polarizer to create circularly polarized light. Secondly, the zeroth order diffraction beam was filtered out by insertion of a home-made spatial mask. The polarization of the first diffraction-order beams, used to create the line pattern on the sample, was controlled by a home-made segmented polarizer, as depicted in Supplementary Figure 2. Because the blaze-grating condition is satisfied, it was not necessary to adjust the intensity of the two first-diffraction spots independently<sup>39</sup>. Finally, a second dichroic mirror is placed perpendicularly to the dichroic mirror inserted in the microscope, to compensate for polarization changes induced by the original dichroic mirror<sup>45</sup>.

The DMD was used to create line patterns consisting of 3 row/column of mirrors in the “on”-position, followed by 6 rows/columns in the “off”-position (Fig. 2). This was repeated periodically across the face of the DMD. The mirror configuration of the DMD was controlled using BitMap Picture (BMP) files. The files were loaded into the software DL LightCrafter 6500 & 9000 version 4.0.0 and displayed on the DMD. The intensity of the illumination through the objective was  $\sim 2$  W/cm<sup>2</sup>.

For the secondary setup a 473-nm laser (Cobolt, 06-MLD 473 nm) was used as excitation source. The microscope setup described above was utilized also for this experiment, except that the excitation path bypassed the all optical components between the DMD and the microscope (the second telescope, linear polarizer, quarter-wave plate and the segmented polarizer). This resulted in a structured illumination created by three-beam interference<sup>28</sup>.

The intensity was reduced from 100 mW to 30 mW using neutral density filters and the polarization was made circular using a linear polarizer combined with a quarter wave plate oriented at  $45$  degrees relative to the linear polarizer. The DMD pattern for this setup was 1 mirror “on” and 7 mirrors “off”. The intensity of the illumination through the objective varied from  $4.6$  W/cm<sup>2</sup> to  $6.9$  W/cm<sup>2</sup>.

**EMCCD camera.** For imaging of fluorescent emitters, we used a highly sensitive EMCCD camera (Evolve 512, Photometrics). For all imaging, we used a field-of-view of  $512 \times 512$  square pixels of  $16 \mu\text{m}$  width. The combined magnification of the microscope (objective and tube lenses) resulted in an effective pixel width of  $107$  nm. Throughout measurements, the EM gain was set to  $500$ , which corresponded to a signal-to-photon conversion factor of  $72$ . The constant offset added to all pixel output values before readout was  $505$ . The camera’s pixel rows were aligned to the horizontal lines of the DMD. We corrected all theoretical variances by a factor of two<sup>446</sup>, due to excess noise originating in the electron multiplication process.

**Characterization of structured illumination.** Since the beads are small ( $\phi = 46$ – $51$  nm) relatively to the period of the illumination ( $\sim 230$  nm, respectively,  $400$  nm), the excitation intensity experienced by each bead is proportional to the intensity of the structured illumination at the bead’s position. Specifically, even for the largest particles in the reported size distribution, the pattern contrast is sampled with  $\sim 96\%$  accuracy, assuming uniform dye distribution in the volume of each bead (Supplementary Fig. 12). Consequently, the integrated intensity in each bead’s spot can be used as a direct estimate of the local illumination intensity (Fig. 2c, d). Using this, we measured the intensity of the illumination as a function of position by translating the beads in steps across the structured illumination and imaging them between steps (Fig. 2c). Specifically, the beads were translated through 31 positions with a step length of  $\sim 71$  nm along a diagonal line. At each position, we ten times imaged six/eight patterns: three/four phases of the structured illumination for each of two orthogonal directions in the image plane. Each phase shift was three/two mirror units on the DMD, i.e., a third/quarter period of the structured illumination (Fig. 2 and Supplementary Fig. 6). Each pattern was displayed on the DMD for  $49$  ns, which resulted in a time-lapse of  $50$  ms between images. For each position, each bead in the sample thus was imaged as  $60$  diffraction-limited spots in as many images. For analysis, we selected spots that were sufficiently isolated from each other as fiducials. The varying intensity of each spot as a function of the phase of the structured illumination allowed us to characterize the intensity profile of the experimentally realized structured illumination. In order to determine intensities, we applied a joint MLE-fit of six/eight 2D-Gaussian model-PSFs (see below) to each set of six/eight images (Supplementary Note 3). We fitted using the fact that the position-coordinates of the source and the width of its PSF were the same under all six/eight illuminations. Only the number of photons,  $N$ , and background,  $b$ , could differ between the six/eight illuminations (Fig. 2). For each pattern of structured illumination, we averaged the number of photons estimated for each particle in this manner over the ten repetitions and used that average to characterize the pattern (Fig. 2). We either modeled the pattern as a harmonic function (two-beam interference) or as a series of top-hat functions describing the lines of

illumination, convolved with a Gaussian PSF describing diffraction by the objective<sup>47</sup> (three-beam interference, Supplementary Note 9, Supplementary Fig. 7). This described data accurately (Fig. 2, Supplementary Figs. 3 and 6). The relevant parameters were obtained by weighted least-squares fitting of the model to data.

**C-MELM measurements.** The six/eight illumination patterns characterized above were used for C-MELM measurements. Each C-MELM measurement consisted of six/eight images in which the sample was exposed to three/four phases of the structured illumination for each of two orthogonal directions in the image plane, with an exposure time of  $\sim 49$  ms per image. In order to determine the position of an isolated point-source with C-MELM, first the position was crudely determined. When we used a densely populated sample as basis for characterization, a single characterization measurement was sufficient in terms of reasonable FOV-coverage. In that case, the five fiducials nearest to the determined position were selected in order to describe the local values of the structured illuminations as functions of phase and, by interpolation between fiducials, as function of position (Supplementary Fig. 13, Supplementary Note 10). In cases where the sample used for characterization was sparse, we used multiple FOVs to ensure sufficient coverage. In such cases, the same interpolation was carried out to determine the shape of the structured illumination, but its phase was estimated based on the variation of intensities of the emitter to be localized as a function of the phase-shifted illumination structures.

Then, a joint MLE fit of six/eight 2D-Gaussians model-PSFs (see below) was used to analyze the six/eight diffraction-limited spots produced by each fluorescent source to be localized. Again, we assumed identical positions and PSF widths in all spots from any given source. For a given source, however, the six/eight intensities recorded with the six/eight different illuminations were assumed related as the illuminations at the position of the source—this is the end to which we characterized the illuminations. This protocol simultaneously uses the positional information encoded in the intensity of a spot by the structured illumination and encoded in the position of the spot by any illumination (Supplementary Note 7). We repeated the C-MELM measurement and analysis for all chosen, well-isolated emitters in the sample that showed reasonable photostability.

Any drift of the structured illumination between characterization and measurement can lead to bias in the C-MELM estimate, due to discrepancies between characterized structured illumination position and actual structured illumination position at the time of measurement. To correct for this potential bias, we utilized the fact that positions of particles in the sample obtained with camera-based localization alone are unbiased. In the measurements in which the prior characterization was based on a single FOV of a densely populated sample, we determined the common bias for all investigated spot and corrected for it. Alternatively, in measurements where the characterization was based on several FOVs, the bias is already adjusted for by the determination of the phase of the structured illumination based on the emitter to be localized, as described above.

**PSF model for image-based localization and C-MELM analysis.** Throughout, we used a 2D-Gaussian-plus-a-constant as theoretical model-PSF. As described by Mortensen et al.<sup>9</sup>, this provides an accurate approximation to the actual PSF. We used MLE to fit this PSF to images recorded with uniform illumination (or any illumination, without using its structure). This localizes fluorescent point-sources optimally<sup>9</sup>. See Supplementary Notes 1–3 for details.

**Simulations.** For Monte Carlo simulations of experiments (Supplementary Figs. 1 and 10), we assumed Poisson statistics for the number of photons recorded in each pixel. Simulated experiments were analyzed identically to our experimental data using C-MELM and PSF-fitting (see above). Note that variances calculated using such simulations should be corrected by a factor of two, to account for excess noise in the EM process of an EMCCD camera, if one wishes to compare to experiments obtained using an EMCCD camera. Parameters used in the simulations are given in the relevant figures.

## Data availability

All data that support the findings of this study are available from the corresponding author upon request.

## Code availability

Source code for simulations and C-MELM analysis are available from the corresponding author upon request.

Received: 29 June 2020; Accepted: 1 February 2021;

Published online: 01 March 2021

## References

1. Deschout, H. et al. Precisely and accurately localizing single emitters in fluorescence microscopy. *Nat. Methods* **11**, 253–266 (2014).



2. Shashkova, S. & Leake, M. C. Single-molecule fluorescence microscopy review: shedding new light on old problems. *Biosci. Rep.* **37**, 1–19 (2017).
3. Elf, J. & Barkenfors, I. Single-molecule kinetics in living cells. *Annu. Rev. Biochem.* **88**, 635–659 (2019).
4. Von Diezmann, A., Shechtman, Y. & Moerner, W. E. Three-dimensional localization of single molecules for super-resolution imaging and single-particle tracking. *Chem. Rev.* **117**, 7244–7275 (2017).
5. Chen, B. C. et al. Lattice light-sheet microscopy: imaging molecules to embryos at high spatiotemporal resolution. *Science* **346**, 1257998 (2014).
6. Grimm, J. B. et al. A general method to fine-tune fluorophores for live-cell and in vivo imaging. *Nat. Methods* **14**, 987–994 (2017).
7. Huang, F. et al. Video-rate nanoscopy using sCMOS camera-specific single-molecule localization algorithms. *Nat. Methods* **10**, 653–658 (2013).
8. Balzarotti, F. et al. Nanometer resolution imaging and tracking of fluorescent molecules with minimal photon fluxes. *Science* **355**, 606–612 (2017).
9. Mortensen, K. I., Churchman, L. S., Spudich, J. A. & Flyvbjerg, H. Optimized localization analysis for single-molecule tracking and super-resolution microscopy. *Nat. Methods* **7**, 377–381 (2010).
10. Larson, D. R. The economy of photons. *Nat. Methods* **7**, 357–359 (2010).
11. Gu, L. et al. Molecular resolution imaging by repetitive optical selective exposure. *Nat. Methods* **16**, 1114–1118 (2019).
12. Reymond, L. et al. SIMPLE: Structured illumination based point localization estimator with enhanced precision. *Opt. Express* **27**, 24578 (2019).
13. Cnossen, J. et al. Localization microscopy at doubled precision with patterned illumination. *Nat. Methods* **17**, 59–63 (2020).
14. Reymond, L., Huser, T., Ruprecht, V. & Wieser, S. Modulation-enhanced localization microscopy (meLM). *J. Phys. Photonics* **2**, 041001 (2020).
15. Copeland, C. R. et al. Subnanometer localization accuracy in widefield optical microscopy. *Light Sci. Appl.* **7**, 31 (2018).
16. Kask, P., Palo, K., Hinnah, C. & Pommerencke, T. Flat field correction for high-throughput imaging of fluorescent samples. *J. Microsc.* **263**, 328–340 (2016).
17. Douglass, K. M., Sieben, C., Archetti, A., Lambert, A. & Manley, S. Super-resolution imaging of multiple cells by optimized flat-field epi-illumination. *Nat. Photonics* **10**, 705–708 (2016).
18. Khaw, I. et al. Flat-field illumination for quantitative fluorescence imaging. *Opt. Express* **26**, 15276 (2018).
19. Yildiz, A. et al. Myosin V walks hand-over-hand: single fluorophore imaging with 1.5-nm localization. *Science* **300**, 2061–2065 (2003).
20. Betzig, E. et al. Imaging intracellular fluorescent proteins at nanometer resolution. *Science* **313**, 1642–1645 (2006).
21. Rust, M. J., Bates, M. & Zhuang, X. Sub-diffraction-limit imaging by stochastic optical reconstruction microscopy (STORM). *Nat. Methods* **3**, 793–795 (2006).
22. Schnitzbauer, J., Strauss, M. T., Schlichthaefer, T., Schueder, F. & Jungmann, R. Super-resolution microscopy with DNA-PAINT. *Nat. Protoc.* **12**, 1198–1228 (2017).
23. Parthasarathy, R. Rapid, accurate particle tracking by calculation of radial symmetry centers. *Nat. Methods* **9**, 724–726 (2012).
24. Mortensen, K. I., Sung, J., Flyvbjerg, H. & Spudich, J. A. Optimized measurements of separations and angles between intra-molecular fluorescent markers. *Nat. Commun.* **6**, 1–9 (2015).
25. Mortensen, K. I., Sung, J., Spudich, J. A. & Flyvbjerg, H. How to measure separations and angles between intramolecular fluorescent markers. *Methods Enzymol.* **581**, 147–185 (2016).
26. Rao, C. R. *Linear Statistical Inference and its Applications*. (Wiley, 1973).
27. Eilers, Y., Ta, H., Gwosch, K. C., Balzarotti, F. & Hell, S. W. MINFLUX monitors rapid molecular jumps with superior spatiotemporal resolution. *Proc. Natl Acad. Sci. USA* **115**, 6117–6122 (2018).
28. Heintzmann, R. & Huser, T. Super-resolution structured illumination microscopy. *Chem. Rev.* **117**, 13890–13908 (2017).
29. Li, M., Li, Y., Liu, W., Zhanghao, K. & Xi, P. Structured illumination microscopy using digital micro-mirror device and coherent light source. *Appl. Phys. Lett.* **116**, 233702 (2020).
30. Gustafsson, M. G. L. Surpassing the lateral resolution limit by a factor of two using structured illumination microscopy. *J. Microsc.* **198**, 82–87 (2000).
31. Frohn, J. T., Knapp, H. F. & Stemmer, A. True optical resolution beyond the Rayleigh limit achieved by standing wave illumination. *Proc. Natl Acad. Sci. USA* **97**, 7232–7236 (2000).
32. Shao, L., Kner, P., Rego, E. H. & Gustafsson, M. G. L. Super-resolution 3D microscopy of live whole cells using structured illumination. *Nat. Methods* **8**, 1044–1048 (2011).
33. Fiolka, R., Shao, L., Hesper Rego, E., Davidson, M. W. & Gustafsson, M. G. L. Time-lapse two-color 3D imaging of live cells with doubled resolution using structured illumination. *Proc. Natl Acad. Sci. USA* **109**, 5311–5315 (2012).
34. Toprak, E. et al. Defocused orientation and position imaging (DOPI) of myosin V. *Proc. Natl Acad. Sci. USA* **103**, 6495–6499 (2006).
35. Backer, A. S., Backlund, M. P., Lew, M. D. & Moerner, W. E. Single-molecule orientation measurements with a quadrated pupil. *Opt. Lett.* **38**, 1521–1523 (2013).
36. Aguet, F., Geissbühler, S., Märki, I., Lasser, T. & Unser, M. Steerable filters for orientation estimation and localization of fluorescent dipoles. *Opt. Express* **17**, 6829–6848 (2009).
37. Backlund, M. P. et al. Simultaneous, accurate measurement of the 3D position and orientation of single molecules. *Proc. Natl Acad. Sci. USA* **109**, 19087–19092 (2012).
38. Enderlein, J., Toprak, E. & Selvin, P. R. Polarization effect on position accuracy of fluorophore localization. *Opt. Express* **14**, 8111 (2006).
39. Babcock, H. P. & Zhuang, X. Analyzing single molecule localization microscopy data using cubic splines. *Sci. Rep.* **7**, 1–8 (2017).
40. Li, Y. et al. Real-time 3D single-molecule localization using experimental point spread functions. *Nat. Methods* **15**, 367–369 (2018).
41. Xu, F. et al. Three-dimensional nanoscopy of whole cells and tissues with in situ point spread function retrieval. *Nat. Methods* **17**, 531–540 (2020).
42. Pavani, S. R. P. et al. Three-dimensional, single-molecule fluorescence imaging beyond the diffraction limit by using a double-helix point spread function. *Proc. Natl Acad. Sci. USA* **106**, 2995–2999 (2009).
43. Kirshner, H., Aguet, F., Sage, D. & Unser, M. 3-D PSF fitting for fluorescence microscopy: Implementation and localization application. *J. Microsc.* **249**, 13–25 (2013).
44. Sandmeyer, A. et al. DMD-based super-resolution structured illumination microscopy visualizes live cell dynamics at high speed and low cost. 1–32 <https://doi.org/10.1101/797670> (2019).
45. Zhanghao, K. et al. Super-resolution imaging of fluorescent dipoles via polarized structured illumination microscopy. *Nat. Commun.* **10**, 4694 (2019).
46. Mortensen, K. I. & Flyvbjerg, H. ‘Calibration-on-the-spot’: How to calibrate an EMCCD camera from its images. *Sci. Rep.* **6**, 26860 (2016).
47. Fry, G. A. Square-wave gratings convoluted with a Gaussian spread function. *J. Opt. Soc. Am.* **58**, 1415–1416 (1968).

## Acknowledgements

This work was funded by the Novo Nordisk Foundation Challenge Programme (NNF16OC0022166). We thank A. Kristensen for generously sharing microscopy components with us.

## Author contributions

H.F. and K.I.M. conceived the idea. M.S., R.M. and K.I.M. designed research. A.C.H. and R.M. built the experimental setup and performed experiments. M.S. and K.I.M. developed the theory. M.S. analyzed the data. K.I.M. supervised the data analysis. M.S. wrote the initial manuscript draft. Everybody discussed results and contributed to and approved the final manuscript.

## Competing interests

The authors declare no competing interests.

## Additional information

**Supplementary information** The online version contains supplementary material available at <https://doi.org/10.1038/s42005-021-00546-y>.

**Correspondence** and requests for materials should be addressed to K.I.M.

**Reprints and permission information** is available at <http://www.nature.com/reprints>

**Publisher's note** Springer Nature remains neutral with regard to jurisdictional claims in published maps and institutional affiliations.



**Open Access** This article is licensed under a Creative Commons Attribution 4.0 International License, which permits use, sharing, adaptation, distribution and reproduction in any medium or format, as long as you give appropriate credit to the original author(s) and the source, provide a link to the Creative Commons license, and indicate if changes were made. The images or other third party material in this article are included in the article's Creative Commons license, unless indicated otherwise in a credit line to the material. If material is not included in the article's Creative Commons license and your intended use is not permitted by statutory regulation or exceeds the permitted use, you will need to obtain permission directly from the copyright holder. To view a copy of this license, visit <http://creativecommons.org/licenses/by/4.0/>.

© The Author(s) 2021

## Terms and Conditions

Springer Nature journal content, brought to you courtesy of Springer Nature Customer Service Center GmbH ("Springer Nature").

Springer Nature supports a reasonable amount of sharing of research papers by authors, subscribers and authorised users ("Users"), for small-scale personal, non-commercial use provided that all copyright, trade and service marks and other proprietary notices are maintained. By accessing, sharing, receiving or otherwise using the Springer Nature journal content you agree to these terms of use ("Terms"). For these purposes, Springer Nature considers academic use (by researchers and students) to be non-commercial.

These Terms are supplementary and will apply in addition to any applicable website terms and conditions, a relevant site licence or a personal subscription. These Terms will prevail over any conflict or ambiguity with regards to the relevant terms, a site licence or a personal subscription (to the extent of the conflict or ambiguity only). For Creative Commons-licensed articles, the terms of the Creative Commons license used will apply.

We collect and use personal data to provide access to the Springer Nature journal content. We may also use these personal data internally within ResearchGate and Springer Nature and as agreed share it, in an anonymised way, for purposes of tracking, analysis and reporting. We will not otherwise disclose your personal data outside the ResearchGate or the Springer Nature group of companies unless we have your permission as detailed in the Privacy Policy.

While Users may use the Springer Nature journal content for small scale, personal non-commercial use, it is important to note that Users may not:

1. use such content for the purpose of providing other users with access on a regular or large scale basis or as a means to circumvent access control;
2. use such content where to do so would be considered a criminal or statutory offence in any jurisdiction, or gives rise to civil liability, or is otherwise unlawful;
3. falsely or misleadingly imply or suggest endorsement, approval, sponsorship, or association unless explicitly agreed to by Springer Nature in writing;
4. use bots or other automated methods to access the content or redirect messages
5. override any security feature or exclusionary protocol; or
6. share the content in order to create substitute for Springer Nature products or services or a systematic database of Springer Nature journal content.

In line with the restriction against commercial use, Springer Nature does not permit the creation of a product or service that creates revenue, royalties, rent or income from our content or its inclusion as part of a paid for service or for other commercial gain. Springer Nature journal content cannot be used for inter-library loans and librarians may not upload Springer Nature journal content on a large scale into their, or any other, institutional repository.

These terms of use are reviewed regularly and may be amended at any time. Springer Nature is not obligated to publish any information or content on this website and may remove it or features or functionality at our sole discretion, at any time with or without notice. Springer Nature may revoke this licence to you at any time and remove access to any copies of the Springer Nature journal content which have been saved.

To the fullest extent permitted by law, Springer Nature makes no warranties, representations or guarantees to Users, either express or implied with respect to the Springer nature journal content and all parties disclaim and waive any implied warranties or warranties imposed by law, including merchantability or fitness for any particular purpose.

Please note that these rights do not automatically extend to content, data or other material published by Springer Nature that may be licensed from third parties.

If you would like to use or distribute our Springer Nature journal content to a wider audience or on a regular basis or in any other manner not expressly permitted by these Terms, please contact Springer Nature at

[onlineservice@springernature.com](mailto:onlineservice@springernature.com)

B.2 Quantitative imaging of lipidated peptides:  
Towards a mechanistic understanding of their  
transport through an epithelial cell layer

## **Quantitative imaging of lipidated peptides: Towards a mechanistic understanding of their transport through an epithelial cell layer**

Adam Coln Hundahl, Arjen Weller, Jannik Bruun Larsen, Claudia U Hjørringgaard, Morten B Hansen, Ann-Kathrin Mündler, Kasper Kristensen, Eva Arnspang Christensen\*, Thomas Lars Andresen, Kim I. Mortensen, Rodolphe Marie

### Authors contributions:

Adam (plan and performed all experiments in the main text, wrote the first draft)

Thomas, Kim, Jannik and Rodolphe (plan research)

Arjen Weller (organoplate data)

Claudia U Hjørringgaard, Morten B Hansen, Ann-Kathrin Mündler (sCT synthesis, labelling and HPLC)

Kasper Kristensen (FCS data)

Eva Arnspang Christensen (hosting of TIRF experiments)

### Affiliations:

Technical University of Denmark, Department of Health Technology, Ørstedes Plads, Building 345C, DK-2800 Kgs. Lyngby, Denmark.

\*University of Southern Denmark, Department of Green Technology, Campusvej 55, 5230 Odense M, Denmark.

### **Abstract**

Oral drug delivery increases patients' compliance and is thus the preferred administration route for most drugs. However, absorption is hindered by the intestinal barrier for drugs like peptides. In this case, chemical modification such as the addition of lipid side chains is one strategy to increase the drugs transport through and improve bioavailability after oral delivery. While the effect of lipidation on transport has been established, a mechanistic understanding of this effect is still lacking. Such mechanistic understanding could bypass a time-consuming trial and error approach to developing novel drug delivery schemes. To this end, end-point detection of biopharmaceuticals transported through fully polarized endothelial cells monolayer is typically used. However, these methods are time-consuming and tedious. Furthermore, most established methods cannot be combined easily with high-resolution fluorescence imaging that could provide a mechanistic insight into cellular uptake and transport. Here we address this challenge in two ways; first we develop an axial PSF deconvolution scheme to quantify the transport of peptides through a monolayer of Caco-2 cells using single-cell analysis with live cell confocal fluorescence microscopy. Then we show that cells cultured for two days on glass are a minimal model to study the transport of peptides as they achieve a tight monolayer and exhibit the same transport of peptides observed for cells grown longer under microfluidic conditions. We apply this simple method to investigate the effects of side chain lipidation of the model peptide drug salmon calcitonin (sCT) with 4-carbon and 8-carbon-long fatty acid chains. Furthermore, we compare experiments performed at lower temperature and using inhibitors for some endocytotic pathways to pinpoint the main avenues for the transport of different analogs. We thus show that increasing the length of the lipid chain increases the transport of the drug significantly but also makes endocytosis the primary transport mechanism.

**Keywords:** drug delivery, lipidated peptides, intestinal barrier transport, Salmon Calcitonin, Caco-2 cells.

## Introduction

Often, therapeutic drugs are administered through injection (Mitrugotri, Burke, & Langer, 2014), a direct path into the bloodstream resulting in high bioavailability, defined as the fraction of drug that has effectively entered the cardiovascular system (Hinderliter & Saghir, 2014). However, the need for injections lowers customer compliance (Tibbitt, Dahlman, & Langer, 2016). Alternative administration routes such as nasal, inhalation, or oral delivery (Anselmo, Gokarn, & Mitrugotri, 2018) are increasingly explored. In particular, oral drug delivery has received much focus in the past decade due to its high patient compliance (Ismail & Csóka, 2017). Biopharmaceuticals administered orally must pass through the mucus layer and the epithelial cell layer forming the intestinal barrier. The epithelial cell layer create a tight barrier preventing molecules from passing through the interface of two cells (tight junctions) (Groschwitz & Hogan, 2009).

Consequently, the bioavailability of larger drugs like peptides administered orally is still suboptimal (around 1-2 %) (Renukuntla, Vadlapudi, Patel, Boddu, & Mitra, 2013).

A common strategy to improve bioavailability is to package the biopharmaceutical in nanoparticles to target the uptake via the clathrin-mediated endocytosis (Manzanares & Ceña, 2020). Another approach is to use promoter molecules and co-transport the molecule of interest (Drucker, 2020; Verma et al., 2021). Alternatively, the chemical structure of the drug can be modified with chemical groups in order to promote a transport route of interest. Recently, the lipidation of peptides (Diedrichsen et al., 2021; Menacho-Melgar, Decker, Hennigan, & Lynch, 2019) has been shown to improve peptide bioavailability by promoting interactions of the drug with the cell membrane. In an attempt to further improve on bioavailability the influence of the lipid chain length on the overall transport of salmon Calcitonin has been shown (Trier et al., 2015). The putative mechanism for increased transport is that partitioning of the lipidated peptide to the cell membrane occurs on both sides of the cell layer, eventually leading to the subsequent release of the lipidated peptide into the cytosol and then on the basal side of the cell layer. However, a mechanistic understand of the mode of action of peptide lipidation is still lacking before de novo design of such modification is possible. Bioavailability is typically measured using the human epithelial colorectal adenocarcinoma cell line CaCo-2 as a model of the gut epithelial cells (Behrens, Stenberg, Artursson, & Kissel, 2001). CaCo-2 cells are cultured on a porous membrane filter separating an apical chamber on top of the membrane and a basolateral chamber on the bottom is used to support the cells (Transwell plate). Cells are typically grow for 18-21 days with media change every 1-2 days before the cells grow into a polarized monolayer with tight barriers (Yang, Zhao, Yu, Sun, & Yu, 2017). The overall transport is then typically quantified by an end-point measurement such as mass spectrometry (Birch, Diedrichsen, Christophersen, Mu, & Nielsen, 2018). Several other methods based on the detection of fluorescence including ELISA (Gupta et al., 2013) are also used. While this approach has the advantage to be applicable to any drug without labelling, long cell culture time makes the experiment tedious and thus limits the applicability of the Transwell system for massively parallel studies and consequently leads to a trial-and-error approach to developing new drugs.

Instead, fluorescence microscopy can be used to quantify the biopharmaceutical in the different compartments of the cell (Capoulade, Wachsmuth, Hufnagel, & Knop, 2011). Fluorescence labeling

of the biopharmaceutical combined with confocal imaging allows for quantifying the amount of drug transported through a monolayer of Caco-2 cells, either by end-point measurement of the concentration of the biopharmaceutical on the basal side or by quantifying the amount of fluorescence in the cytosol of the cells by integrating intensity in a single z-plane (Brayden, Gleeson, & Walsh, 2014).

Moreover, high magnification confocal fluorescence microscopy can help pinpoint the uptake mechanism of the biopharmaceutical. In some cases, the biopharmaceutical may appear as puncta, which can suggest that the uptake mechanism is mediated by endocytosis (Brock, 2014; Potocky, Menon, & Gellman, 2003). Using multicolor imaging and colocalization analysis, confocal fluorescence microscopy provides high signal-to-noise ratio spatial resolution so it can reveal the biopharmaceuticals interactions with organelles (Kowada, Maeda, & Kikuchi, 2015; Zhang, Ma, & Chalfie, 2004). This was successfully used to investigate the transport of, e.g., PolIFN- $\alpha$  in Caco-2 cells (Liu et al., 2017; Thompson et al., 2011; Zimmermann et al., 2014). Eventually, live-cell imaging can provide a time resolution sufficient for elucidating the kinetics of the cellular uptake (Vtyurina, Åberg, & Salvati, 2021).

Still, the quantification of the transported peptide signal in a monolayer of cell may be complicated by the limited spatial resolution of fluorescence microscopy. Lateral resolution is approximately 200 nm, whereas axial resolution is much larger, around 400 nm at a 500 nm excitation, and it is so even for confocal imaging (Conchello & Lichtman, 2005). In a typical imaging experiment where the overall transport through a cell layer is observed axially, quantifying the fluorescence signal from the cytosol or around the cell membrane should be done carefully, whether it appears as a diffuse signal indicating a release of the peptide in the cytosol, or as puncta-like signal typical of the peptide found primarily in endosomes, for example resulting from endocytosis (Brock, 2014). Indeed, the cell surrounding's fluorescence signal significantly extends within the cell's interior and vice versa. Eventually, the signal from fluorescent molecules located outside the cell on both sides of the cell layer, i.e., the apical and basolateral sides, would overlap when the thickness of the cell approaches that of the size of the PSF, making image interpretation difficult.

Deconvoluting fluorescence images with the PSF (Conchello & Lichtman, 2005) is a way to extract the fluorescence intensity in the different compartments of the cell. It's been used to quantify the fluorescence of puncta-like structures, typically in experiments where transport occurs via endosomes (Helmuth, Burckhardt, Greber, & Sbalzarini, 2009). Still, little has been done to quantify the diffuse signal from the cell cytosol and the localized signal from the membrane (Smith, Hennen, Chen, & Mueller, 2015). In particular, there is a potential to use PSF deconvolution in combination with a physical model of the cell to extract all contributions to the overall fluorescence signal at once.

Here we quantify the signal of the lipidated forms of the 3.4 kDa peptide salmon Calcitonin sCT in a layer of Caco-2 cells by first measuring the PSF of the spinning disc microscope and then using this knowledge to perform a deconvolution combined with a simple physical model of the cell to interpret the fluorescence intensity of the cytosol, the cell membrane, and the transported molecule across the cell monolayer. We confirm the validity of the cell model by measuring the known transport properties of TAT, using Dextran, and Lucifer Yellow as negative controls for active

transport. We show how the intensity profile through a cell looks in different uptake scenarios. We then quantified the transport of salmon Calcitonin. We investigate the uptake of three various double-lipidated sCT analogs over 4 hours using spinning disc confocal fluorescence microscopy to quantify the effects of lipidation on the transport of sCT through Caco-2 cells. Furthermore, we use this method to demonstrate that the model can show differences in the transport pattern of the peptide by adding an inhibitor for endocytosis and lowering the temperature below physiological temperatures.

## Results

### *Cellular model and axial PSF deconvolution scheme*

We aim to quantify a fluorescently-labelled peptide transported through a monolayer of Caco-2 cells. To this end, we use time-lapse spinning disc confocal microscopy to image live cells exposed to the labelled peptide. Caco-2 cells were seeded in a commercial 8-well plate and left to grow for 48 hours. It was shown that Caco-2 cells grown in a Transwell plate system for as short as three days exhibit valid barrier integrity (Gupta, Doshi, & Mitragotri, 2013). The cell's nucleus and the plasma membrane are then stained using Hoechst (blue) and CellMask (red), respectively (Figure 1A). A solution of the drug of interest, labelled with a fluorophore, is added right before the imaging of the cells begin. Three-color confocal z-stacks are acquired as a time-lapse movie every 40 minutes for 4 hours at multiple field-of-view (FOVs) (Figure 1B). Within each FOV, we select a few cells and define one 10-by-10  $\mu\text{m}$  region of interest (ROI) per cell. The ROI is chosen away from the nucleus such that the presence of the nucleus does not lead to curved plasma membranes. We hereby ensure that the plasma membrane appear as a minimally thin layer in the axial intensity profile measured in all ROIs and can thus be modelled with the PSF of the microscope. Two axial intensity profiles are extracted for each cell in this ROI: one for the membrane, and one for the peptide (Figure 1C-D).

From the two axial intensity profiles we first see that in the case of a transported drug, a characteristic intensity peak appears in the peptide channel intensity profile. We then see that the cells cytoplasm is very thin compare to the axial resolution of the spinning disc microscope. This highlights the fact that we have to perform an axial PSF deconvolution of the peptide signal in order to access quantitative information of how much peptide is in the cytoplasm and under the cells. We thus use a physical model of the cell, the substrate and the solution above the cells to extract the contribution of the different regions to the overall axial intensity profiles in the three imaging channels. We first fit the cell membrane intensity profile using the PSF of our microscope. While models exist for the lateral and axial PSF, we ensure that the PSF is accounting for any aberrations of our set-up by using a measurement of the PSF estimated for each fluorescence channel using 100-nm polymer beads (Figure S1). The cell membranes are much thinner than the PSF and thus appears as two Gaussian-like intensity peak, which we fit as the position of the bottom and top membrane of the cell (Figure 1B). This then allows us to divide the intensity profile of the peptide channel into four sections that are relevant for quantifying how much peptide is transported through the cell monolayer: 1) the solution above the cell 2) the cytosol, 3) the space between the cell and the glass surface, and 4) the glass. With that in mind, we model the peptide intensity in each section to deconvolute the axial intensity profile and distinguish the signal from the peptide found at the bottom of the cell layer from the contribution from the solution (Figure 1D). We derived an analytical expression describing the intensity signal in each section (see Methods) so the

measured axial intensity profile can be fitted with the sum of all four contributions. Essentially, our physical model accounts for the following four effects that make interpretation of the axial intensity profile difficult: First, the signal from the peptide solution extends significantly into the cell and even the glass substrate (Figure 1D). We assume a uniform concentration in the solution and model this contribution as step function at the top membrane convolved with the axial PSF. Second, we assume the peptide concentration is uniform in the cytosol (Figure 1D). As a result, this contribution is modeled as a step function at the bottom membrane and another step function at the top membrane convolved with the PSF. Third, the space above the glass and below the bottom membrane gets presumably filled with peptide if transport is successful. Since the space below the cell is shallow compared to the PSF and cannot be resolved by confocal scanning, any peptide present here yields a PSF-like peak that colocalizes with the bottom membrane. Last, the fluorescence signal of the solution and the cells extends significantly into the glass due to the overlap of the illumination through the many pinholes of the Nipkow disc (Conchello & Lichtman, 2005). It varies slowly in space, so, for simplicity, we consider it constant and subtract this background from the rest of the intensity profile. Summing the intensity contributions from these four sections results in the fit to the intensity profile (Figure 1D solid green line).

#### ***Time-lapse imaging and axial intensity profile reveal transport of a peptide***

The assay allows for time dependent transport studies, thus we investigated the cross barrier transport kinetics of a fluorescently labeled peptide. Figure 2A shows the XZ projection of a single cell in a FOV for multiple time points: before adding peptide, then immediately after adding the peptide and readjusting z-focus and XY position to correct for addition mediated drift ie.  $t = 0$ ,  $t = 120$  min, and  $t = 240$  min. Prior to addition of the peptide we detect two red peaks in the membrane signal (red) close together, representing the two membranes of the cell, a low background fluorescence in the peptide channel (green) and a nucleus signal (blue) fluctuating around the background level. After addition of the fluorescent peptide we see an overall increase in the peptide intensity level in all four sections (in solution, in the cytosol, at the interface at the bottom of the cell and in the glass) underscoring the importance for devising our model capable of decoupling the contributions from the individual sections. For the subsequent time points we detect a constant peptide signal in solution, but an increasing signal at the interface at the bottom of the cell suggesting cross barrier transport of the peptide. This illustrates how the assay facilitates live cell imaging that can provide the intensity input necessary for creating an analytical model that can quantitatively describe peptide transport across a cellular barrier.

#### ***Fluorescence model allows quantification of the cellular transport of TAT***

To validate our assay we first performed a positive control with a peptide capable of cross barrier transport and a negative controls with compounds that should not be able to transverse an intact barrier. As the positive control we employed the transport of Trans-Activator of Transcription (TAT) peptide, previously shown to cross the intestinal barrier. We thus measure the transport of FITC-labelled TAT (TAT-FITC) across the Caco-2 cell monolayer, deconvolute the axial intensity profiles of the plasma membrane and the FITC signal to quantify the fluorescence signal in the solution, in the cytosol and at the bottom of the cell layer. We added  $3.5 \mu\text{M}$  of TAT to the cells and start recording z-stacks after focus is readjusted. Figure 3A shows the plasma membrane signal axial intensity profile through one ROI at  $t=0$  min. From this we extract the position of the top and bottom membrane (dashed vertical lines in Figure 3A). We then use the membrane positions to fit the FITC



signal with our model (Figure 3B) and extract the intensity of the peptide signal in solution, in the cytosol and below the cell (Figure 3C). Here, the peptide signal colocalized with the bottom membrane appears as a single PSF-shaped peak. To follow the time dependent evolution of the three main parameters extracted from the fit of the peptide signal, we measured a new Z-stack every 40 minutes allowing us to quantify the cross-barrier peptide transport over time. Comparing the intensity profiles for the same cell after 240 minutes of incubation (Figure 3D-E) with the ones found after 0 minutes (Figure 3A-C) we see that the peak-like signal corresponding to the TAT-FITC signal under the cells has increased above its initial value and even beyond the intensity in the solution. Next we performed a full quantification for all time points allowing us to simultaneously follow how the peptide intensity changed in solution, in the cytosol and at the interface at the bottom of the cell (Figure 3G). Performing the analysis for 10 different ROIs/cells in parallel we found a constant peptide intensity in the solution over time, as we would expect (blue, Figure 3G), but linear increase in the cytosol reaching a 25-fold increase when comparing the value at  $t=0$  min versus  $t=240$  min (red, Figure 3G). Finally we quantified that the TAT-FITC signal increased two-fold from the first measurement until  $t = 100$  min, before reaching a plateau (orange, Figure 3G). So using our assay, we can measure a time dependent transport of TAT that corroborates earlier findings that it is able to transport through Caco-2 cells.

The transport mechanism of TAT is debated. It has been proposed that the main transport mechanism is via endocytosis at the concentration we use in our experiment (Brock, 2014), so we expect the signal is due to TAT-FITC being accumulated as the endosomes are transported to the bottom membrane. However, from our data, we can only pinpoint that the TAT-FITC signal is collocated with the bottom membrane but cannot conclude whether the TAT-FITC is free in solution, bound to the membrane, or shed out of the cells in extracellular vesicles. However, we observed that the cytosol concentration increases 25x from  $t = 0$  min to  $t = 240$  min because we can simultaneously quantify the peptide signal in different parts of our cellular model. This observation indicates that TAT is taken up through endocytosis but escapes the endosome for cytosolic delivery as previously reported (Potocky et al., 2003).

To ensure that the detected transport of TAT-FITC to the bottom of the cell layer is not just an artifact of a non-tight barrier, we employed two classical small molecule reporters of barrier integrity (Betanzos et al., 2018). Keeping the same experimental setup as used for the TAT-FITC experiment we first added 5  $\mu$ M of 4.4 kDa Dextran-FITC and quantified the intensity signal in solution, in the cytosol and at the bottom of the cell over time (Figure 3H). We chose this particular Dextran molecular weight to match the molecular weight of TAT. As for TAT, the solution intensity is unchanged. The cytosolic Dextran content increases slightly from 2 A.U to 4 A.U over 4 hours, which has also been seen for an experiment with a similar timescale (Rousou et al., 2022). More interestingly, we detect no significant increase of the FITC signal collocated with the bottom membrane of the cell (orange dots), which shows that dextran does not accumulate at the bottom of the cells over time. To ensure a comprehensive validation of the barrier integrity of our model, we also performed a time course experiment where 100  $\mu$ M Lucifer Yellow (400 Da) is added to the cells (Figure 3I). Lucifer Yellow has a much smaller size than TAT or Dextran. We found that the fluorescence signal at the bottom of the cell layer is unchanged throughout the experiment, confirming that the cell layer is leak-tight even for even small molecules. From those two control experiments, we conclude that the increase of the FITC signal collocated with the bottom

membrane of the cells (Figure 3G orange dots) is a result of an accumulation of TAT-FITC below the cell layer as expected from the known transport properties of TAT (Brock, 2014).

#### ***Double lipidation of sCT also leads to accumulated signal under the cells***

Next we implemented the validated assay to perform a detailed investigation of how cross-barrier transport of the pharmaceutical relevant peptide Salmon Calcitonin was modified by double lipidations of varying length (Figure S2). We now address the transport of Salmon Calcitonin modified with two lipid side chains. We tested three analogs of sCT labelled with atto488: sCT(C0/C0), that has only been modified with atto488, sCT(C4/C4), which is modified with two C4 chains, and sCT(C8/C8) that modified with two C8 chains. Solution FCS and stepwise bleaching experiments both confirm that all sCT analogs are almost exclusively found as monomers in the condition used for imaging (see Supplementary Information).

The axial intensity profiles obtained for the three sCT analogs are qualitatively similar to those obtained with TAT. Figure S3A and D show an example of a single ROI at  $t = 0$  min and  $t = 240$  min, respectively, under the addition of sCT(C0/C0). After fitting of the intensity profiles for several ROIs, we follow the evolution of the intensity in the solution, the cytosol and at the bottom of the cell layer with time for the three analogs (Figure S3). In particular we look closer at the intensity of the peptide colocalizing with the bottom membrane as this was shown to increase significantly in the case of our positive control TAT (Figure 4). We see a linear increase of the sCT(C0/C0) signal over 4 hours corresponding to approximately 1.5 times the initial signal. Similarly, the addition of sCT(C4/C4) yield a relative increase of 1.5x (Figure 4). We see that the level of accumulated peptide at the bottom of the cells does not exceed the solution level for those two analogs. Furthermore, we also see that the signal in the cytosol does not change (as much?) indicating that the cytosolic content does not increase over time although the peptide makes it to the bottom of the cell. This suggests that the peptide is only transported through the cells but not released in the cytosol. In contrast to the first two analogs, we see in Figure 4 that the increase of the sCT(C8/C8) signal at the bottom of the cell over time is much stronger. The increase is constant over the 4 hours experiment and reaches approximately a relative increase of 3.7 times. This relative increase also has to be seen considering two other aspects of the experiment (Figure S3). First, the intensity in the solution is approximately four times lower as compared to that of sCT(C0/C0) and sCT(C4/C4). We assign this to the reduced solubility of sCT(C8/C8) due to the increasing size of the lipid chains. Second, the intensity level at the bottom of the cells surpasses that of the solution level already at our first measurement after addition of the peptide. One factor playing into that is that even without any peptide present, there is still some intensity signal arising from the cells, as seen in Figure 2B. Secondly, the rate of increase for sCT(C8/C8) is very steep compared to both sCT(C0/C0) and sCT(C4/C4); hence it is very likely that in the period of adding sCT(C8/C8) and before starting the measurement ( $t = 0$  min) some peptide has already transported through the monolayer. Similar to the other analogs, sCT(C8/C8) is not released inside the cytosol, as seen in Figure S3 panel I.

The results in Figure 4 show that our assay based on cells grown on glass for 2 days and an axial PSF deconvolution scheme is sufficient to quantify differences in transport of lipidated peptides. A growth of 2 days is short compared to the state of the art for differentiation and polarization of Caco-2 cells which is typically 21 days. To validate our assay, we applied our image analysis scheme on z-stacks acquired on fully differentiated cells. To this end, we used a commercial organ-on-a-chip platform to grow Caco-2 cells for XX days under alternate flow conditions that lead to polarized cells

with tight junctions (REF unpublished data Arjens paper). We then expose the cells to the labelled peptides and image as in our assay. We see that the intensity profiles are similar to those obtained in our simple cellular model on glass (Figure S4). We repeat the experiment for all three sCT analogs and summarized the result of the fitting in Figure S5. We show that also with polarized cells, lipidation of the sCT increases transport, leading to an increased peptide signal collocalizing with the bottom of the Caco-2 cells monolayer. The relative increase of the signal for sCT(C8/C8) is somewhat lower than for the cells grown on glass however, this is an important validation that our assay based on short-time grown cells is sufficient for a quantitative view on the overall transport properties of the lipidated peptides in a minimal gut-model.

We now look at the peptide signal in the cytosol. None of the sCT analogs showed an increase of peptide signal in the cytosol, as opposed to what the addition of TAT showed (Figure 3G). This suggests that the sCT analogs are either 1) taken up as endosomes and transported as endosomes through the monolayer, or 2) that the peptides interact with the membrane and diffuse through the membrane to the other side.

#### ***Temperature and endocytosis inhibitors affect transport in different ways for different sCT analogs***

Next we use our assay to address the mechanism governing sCT transport and how lipidation affects it. Thus we repeated our experiment for the three sCT analogs either at a decreased temperature (25 °C) or in the presence of Dynasore, both perturbations of the experiment are well-described ways to reduce the endocytic uptake into cells. We added 80 µM Dynasore, an inhibitor of the clathrin- and cavein-mediated endocytosis pathway, which is active in Caco-2 cells (Schmid & Conner, 2003). Dynasore has previously been shown to inhibit the endocytotic transport of small nanoparticles by approximately 50 to 60 % at this concentration (Chai et al., 2016).

We compared the relative increase of the signal at the bottom of the cells after 240 minutes incubation for the three sCT analogs at 37 °C, at 25 °C and at 37 °C in the presence of Dynasore (Figure 5 and Figure S6). Our main observation is that the addition of Dynasore is mostly affecting the transport of the sCT modified with the longest chain (3.7x to 2.5x), while it is also affecting the transport of the unlipidated sCT (1.5x to 1.2x) and not at all the sCT lipidated with the shortest chain. This is contrast with the effect of temperature that seems to affect equally all three analogs. Here these results suggest that the endocytic pathway plays a more important role in the transport of the sCT bearing longer lipid side chains than for the analog with short lipid side chains.

While Figures 4 showed that the transport of sCT can be increased by a factor of 2.5 by lipidating sCT with two C8 chains, Figure 5 suggests that our cellular model combined with live cell imaging and image analysis is able to show differences in the transport mechanism by using inhibitors of cellular transport pathways. However, we cannot pinpoint if the peptide is inside the cell, outside the cell, free in solution or associated with the plasma membrane. Thus, to address this, we incubated the cells with sCT(C8/C8) for four hours, before we washed 1x with PBS to remove the non-transported peptide in solution and then shrunk the cells by disrupting the tight junctions using 1.5 µM EDTA (Figure 6A). This allowed us to measure intensity profiles for cells just as EDTA had been added and 10 minutes after (Figure 6B and C). Here we see that at the same position, the intensity profile is the same when the cell is there as when the cell have shrunk and the plasma membrane has partially detached from the surface. This shows that the peptide is transported

through the cell layer and sticks to the surface after being transported and so it was shed out of the cell.

## **Discussion**

The single lipidation of sCT at the N-terminus with a C8 lipid chain has been previously shown to increase the overall transport through Caco-2 cells by 10-fold (Trier et al., 2015). Here we investigate the transport of sCT modified with two lipid side chains at position 20 and 26. The hypothesis is that the presence of two side chains rather than a single terminal one would orient the peptide molecule to the lipid bilayer and increase its interaction with the cell membrane even for shorter lipid chains than for single lipidation. The binding of lipidated peptides to the membrane leads to transport, but there are several hypotheses for the mechanism involved. In one scenario, the association of the peptide with the lipid membrane is an equilibrium (partition) such that the peptide stochastically crosses the membrane and dissociates on the other side. This exchange across the lipid membrane should occur on both sides of the cells. In this scenario, the overall transport of the lipidated peptide occurs through the cells, i.e., intracellularly. We expect to detect a diffuse signal inside the cytosol in this case. However, in another scenario, the lipidated peptide associates with the lipid-membrane and is transported towards the basolateral of the cells by diffusion along the lipid-membrane, that is intercellularly. In both cases, we expect to measure a signal for the peptide partitioning on the cell membrane; the peptide signal should colocalize with the cell membrane signal. Alternatively, the peptide is transported via endocytosis, and in this case, we expect the peptide signal to appear strongly as puncta in the cells.

### ***[remind what the problem is]***

At first glance, real time fluorescence confocal imaging of a fluorescently labelled peptide could easily pinpoint the main fate of the peptide in Caco-2 cells and lead to a mechanistic understanding of the transport. However, current platforms used for differentiating cells are not readily amenable to high magnification imaging. Additionally, even with high magnification confocal microscopy the axial resolution complicates the quantitative analysis of the fluorescence signal when transport through cells in the direction of the imaging.

### ***[what we did]***

Here we establish a simple cellular model that is both fast and suitable for high magnification microscopy. This cellular model also allows us to use a physical model of the cell layer that is suitable for axial PSF deconvolution of the intensity profile through the cell layer. A physical model combined with deconvolution allows us to extract the individual contributions of the solution, the cytosol and the cell bottom membrane to the overall intensity profile.

Cells are grown for a short time and on a solid substrate. This is considerably shorter than what usually done and although others have shown that 3 days growth is sufficient for cells to be polarized (Gupta et al., 2013), we may compromise on the validity of our cellular model. So we validated its use for studying cross-barrier peptide transport and we use a positive control (TAT) and negative controls (Dextran and Lucifer Yellow). Our results confirm that our model can quantify the cytosolic peptide content (Figure 3) and the amount of peptide that ends up collocated with the bottom of the cells (Figure 3 and 4).

Our physical model of the cell assumes that 1) the cytosol is a medium with a uniform peptide intensity 2) separated by a flat and thin membrane at the bottom and the top. For this model to be valid, we arbitrarily choose to sample the axial intensity profile through the cytosol, away from the

nucleus. By doing this we neglect the non-uniform peptide signal that occurs when peptides are accumulating in puncta-like structures. Puncta-like peptide signal is seen for the C8 analog and Figure S7 shows the intensity profiles sampled over the nucleus. In this case the physical model for deconvolution has to be modified to include a PSF-like peak colocalizing with the top of the cell seen on the peptide channel. This peak coincides for the endosome signal that collocates with the top membrane and agrees with what we see in the images of the TAT-FITC and the sCT(C8/C8); the endosomes are gathered around the nucleus (Figure S8 and S9). This effect makes the interpretation of the peptide signal peak at the bottom of the cell more difficult and so, we opted to sample through the cytosol to quantify the transport of the lipidated peptides in the cytosol without influence of the puncta-like structures. Conversely, most of the PSF deconvolution work done in the context of cellular transport studies is focusing on tracking of puncta-like signals and colocalization with organelles. Here instead we focus on measuring the diffuse peptide signal that is in the cytosol and the peptide signal collocated at the basolateral side of the cell layer.

Figure 5 gives us some insight into possible mechanisms of how the lipidation of sCT affects the transport mechanisms. Transport is inhibited fully or partially by lowering the temperature. Temperature affects all transport pathways equally, whether endocytosis or diffusion in the membrane. In contrast, addition of an endocytosis inhibitor like Dynasore affects primarily the accumulation of sCT(C8/C8) and sCT(C0/C0) while it is not affecting the transport of sCT(C4/C4). Given that transport of sCT(C4/C4) is lowered when decreasing the temperature but unchanged when adding Dynasore, it suggests that the transport mechanism of sCT(C4/C4) could be diffusion through the membrane while the transport of sCT(C8/C8) is partially (but not only) through endocytosis. An explanation of how this would happen would be by the two sCT(C4/C4) fatty acid lipid chains that interact with the cell membrane and diffuse to the other side of the cell layer inside the cell membrane. If the peptide were to diffuse in the cytosol, we would have been able to quantify the release of peptides inside the cells. Furthermore, by looking at the solution level (blue data points in Figure S3H), we can see that the accumulated peptide under the cells (orange data points in Figure S3H) does not exceed this level. This suggests that the transport of the peptide occurs under passive transport dictated by diffusion through the membrane of the cells.

The transport of sCT(C0/C0) and sCT(C8/C8) decreases when the temperature is lowered or when Dynasore is added. This strongly suggests that the predominant transport mechanism is endocytosis. sCT(C8/C8) exhibits the highest accumulation under the cells. The intensity of the peptide signal under the cells exceeds by far that of the peptide solution itself, suggesting that the accumulation results from an active transport, such as endocytosis. Qualitatively this also agrees with what is seen in Figure 2. sCT(C0/C0) and sCT(C4/C4) show little to no signs of peptide in endosomes (Figure S9 A-D), but sCT(C8/C8) shows a lot of puncta-like structures, which we interpret as endosomes (Figure S9 E-F).

Finally, the addition of the endocytosis inhibitor does not suppress the accumulation of peptides below the cells for sCT(C8/C8) totally suggests that an additional mechanism could be at play, for example, association of the lipidated peptide to the membrane followed by diffusion along the lipid membrane. To assess this, our assay could be adapted for other fluorescence imaging modalities such as tracking of single molecules using single molecule microscopy.

#### **Similarity with other modifications and transport studies**

It has been shown by several others who are utilizing Transwell systems that the overall transport of sCT through a Caco-2 monolayer can be increased by biotinylation (Cetin, Youn, Capan, & Lee, 2008), PEGylation (Youn, Jung, Oh, Yoo, & Lee, 2006) or other modifications (Kim et al., 2005; Song, Chung, & Shim, 2005). It was shown by Shah et al. (Shah & Khan, 2004) that native Salmon Calcitonin should occur through passive diffusion based on temperature measurements. Furthermore, the change in transport mechanisms as fatty acid lipid chains are added is supported by Cetin et al., (Cetin et al., 2008) where they modify it with a small hydrophobic molecule, biotin. They show that the amount of transported biotinylated sCT increases 4-fold compared to native sCT. Furthermore, other peptides have also shown that modifying with a hydrophobic molecule changes the transport mechanism (S. Ramanathan et al., 2001; Srinivasan Ramanathan et al., 2001). In our model, we do more than quantifying the amount of transported drug; we also show that we can develop a mechanistic understanding of the transport by doing live single-cell imaging, thus obtaining knowledge from both a qualitative also a quantitative point of view using a simple assay with a short time from cell seeding to imaging. The quantitative data could further design new and novel drug candidates for orally administered drugs.

## **Conclusion**

In conclusion, we show that double lipidation of Salmon Calcitonin with lipid chains can alter the amount of peptide transported across a Caco-2 monolayer. Furthermore, we show that the underlying transport mechanism is affected by the length of the lipid chains. We achieve this by applying a simple model of the cellular layer to deconvolute the axial intensity profile and access the peptide signal contribution in the solution, the cytosol, and the bottom membrane of the cells. This model allowed us to interpret the fluorescence signal obtained by confocal imaging across a cell layer as thin as the axial resolution of our microscope. This model further showed that we get leak-tight barriers by utilizing a simple cell model where cells are only grown for two days. These results show that lipidating the peptides may increase the bioavailability of the peptide. Still, more importantly, we provide a model and a tool for an easy and quantitative experimental setup, which will enhance the knowledge of how to increase the bioavailability of biopharmaceuticals administered orally.

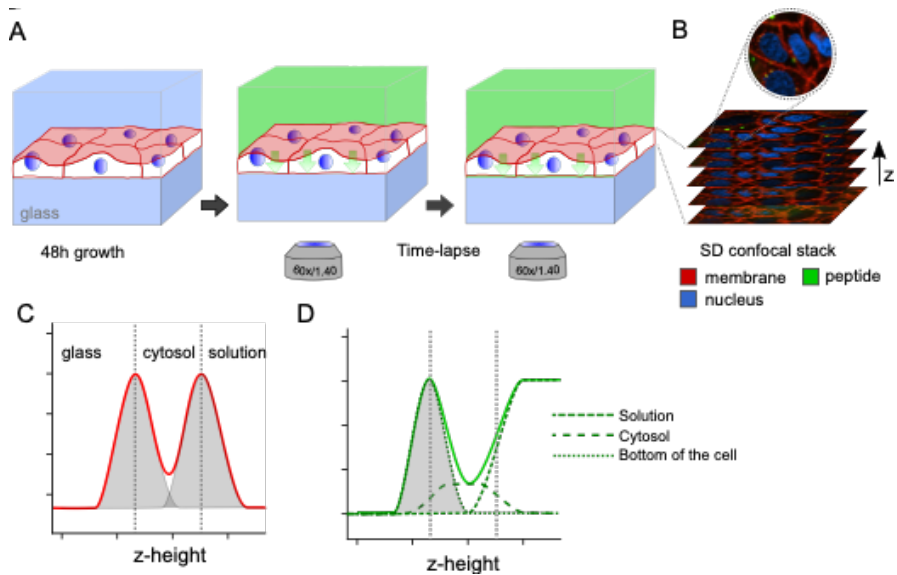


Figure 1 Assay for peptide transport imaging with spinning disc confocal microscopy of live cells A) Caco-2 cells are grown on a glass surface then exposed to fluorescently labelled peptide. B) Timelapse confocal imaging yield confocal stacks in three colors. Axial intensity profiles of C) the membrane channel D) the peptide channel are deconvoluted with the experimental PSF (grey) to extract the position of the cell membranes (dotted lines) and the individual peptide signal (dotted green) in the solution, the cytosol and the bottom of the cell representing the accumulated peptide at the bottom cell membrane.

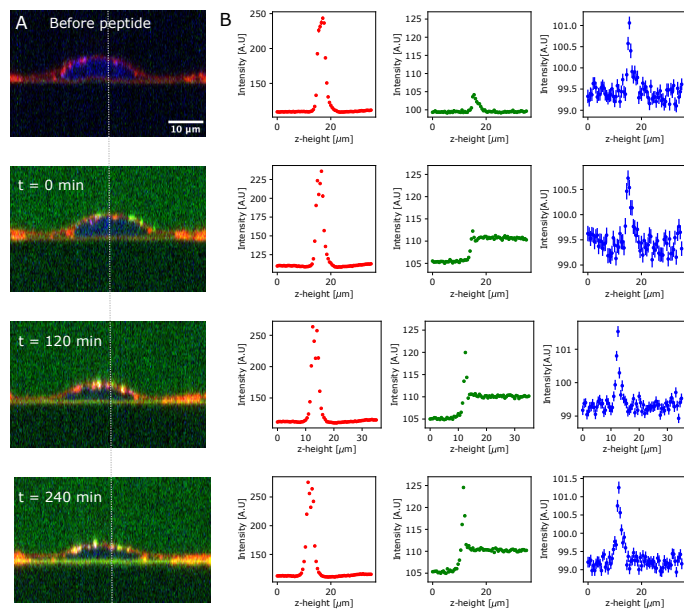


Figure 2 – Live cell imaging shows the accumulation of peptide signal under the Caco-2 cell layer. A) XZ projection of the same cell at four different time points ie before addition of the labelled peptide and after at  $t = 0$ , 120, and 240 minutes. B) Intensity profiles for the membrane (red), peptide (green) and nucleus (blue) fluorescent channels above the nucleus. The intense green spike developing over time indicates accumulation of the peptide at the bottom of the cell layer.



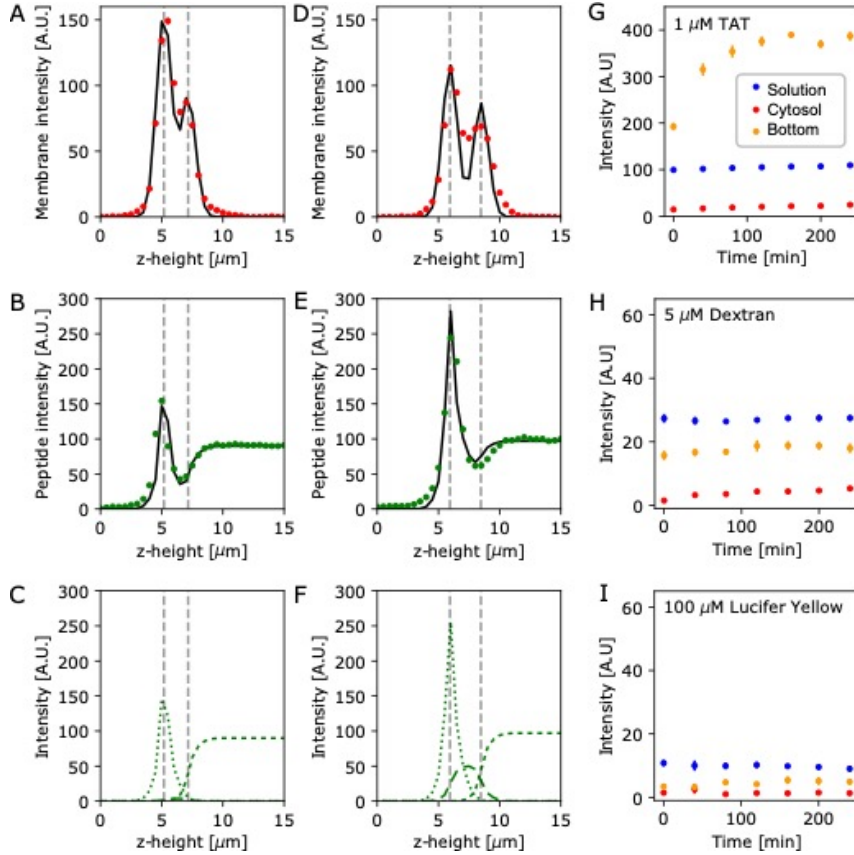


Figure 3 Validation of the cellular model and the axial PSF deconvolution scheme. A) Membrane intensity and fit yielding the position of the cell membrane (dotted line) at  $t=0$  min. B) Peptide signal intensity and fit under the incubation with  $1 \mu\text{M}$  TAT-FITC at  $t=0$  min. C) Individual components of the fit to the peptide signal showing the peptide signal in the solution, the cytosol and at the bottom of the cell. D-F) Same graphs as in A-C) but at  $t=240$  min. G) The TAT-FITC intensity at the interface at the bottom of the cell (orange), in solution (blue) and in the cytosol (red) as a function of time averaged over  $N = 10$  cells. H) Same as G but for the experiment with Dextran and  $N = 12$  cells. I) Same as G but for the experiment with Lucifer Yellow and  $N = 5$  cells. Error bars are standard error of the mean (s.e.m.).

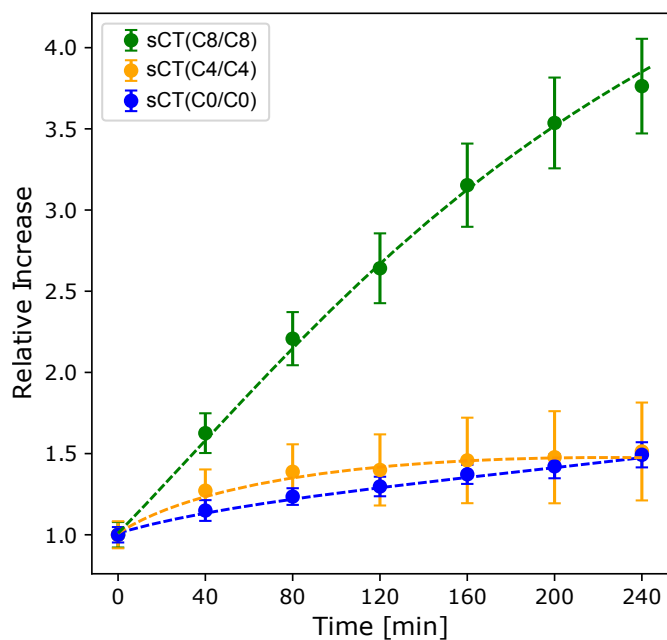


Figure 4 The relative increase of the peptide signal collocated with the bottom membrane of the cell shown for the three sCT analogs over time. The relative difference in peptide signal at the interface at the bottom of the cell calculated by normalizing all time points with the intensity at  $t = 0$  min for sCT(C0/C0) (blue,  $N = 24$ ), sCT(C4/C4) (orange,  $N = 38$ ) and sCT(C8/C8) (green,  $N = 38$ ). Dashed lines are guide to the eye curves.

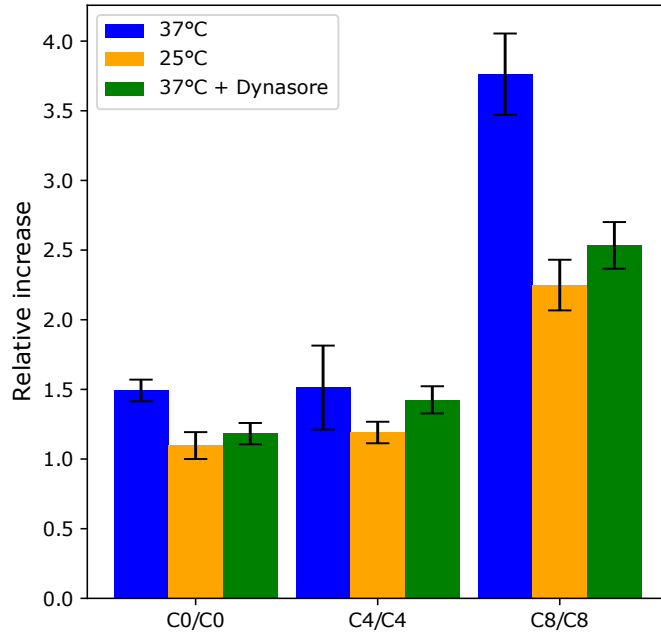


Figure 5 Temperature and endocytosis inhibitor Dynasore change the relative transport of sCT analogs. Relative increase of the peptide signal at the bottom of the cells measured at  $t = 240$  min for sCT(C0/C0), sCT(C4/C4) and sCT(C8/C8). The blue bars represent the relative increase at 37 °C ( $N = 24$ , and 38). The orange bars represent the relative increase at the reduced temperature of 25 °C ( $N = 24$ , 20 and 19). The green bars represent the relative increase at 37 °C with 80  $\mu$ M Dynasore added. Here  $N = 18$ , 17 and 31 for sCT(C0/C0), sCT(C4/C4) and sCT(C8/C8), respectively.

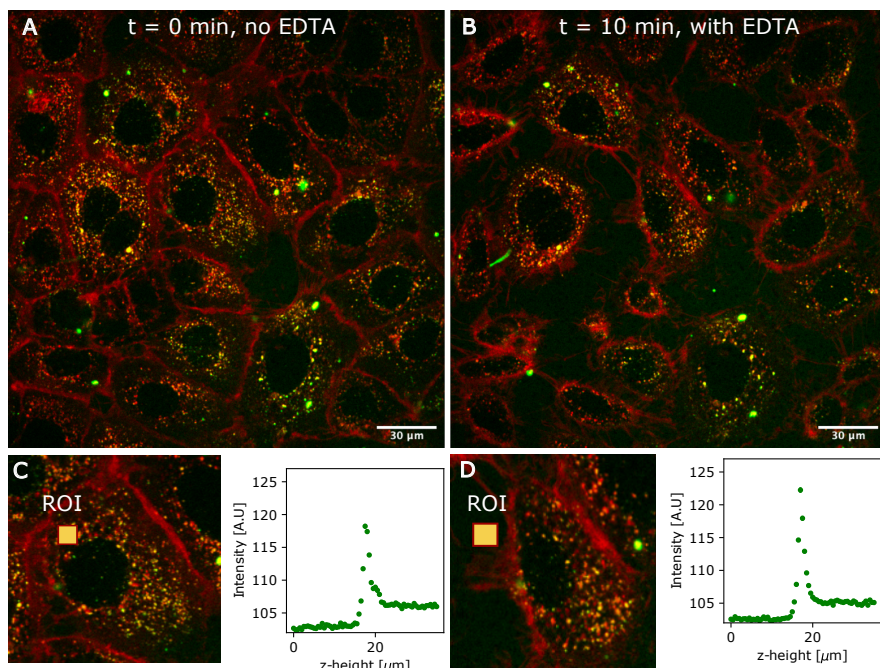


Figure 6 Peptide signal persist after cells are exposed to EDTA. A) Maximum projection image before adding EDTA. B) Same FOV after 10 minutes incubation with  $1.5 \mu\text{M}$  EDTA. C) Cropped image of the cell of interest and axial intensity profile in the ROI at  $t = 0$  and D) at  $t = 10$  min after cell has detached from the surface.

## Materials and methods

### Cell culture

The Caco-2 cells were kept in a T75 culture flask (Nunc EasyFlask 75 cm<sup>2</sup> Cat. Nr. 156472) with 12 mL Minimum Essential Medium (MEM) with 10% FBS, 1% L-glutamine, 1% non-essential amino acids and 1% Penicillin/streptomycin. The cells were placed in an incubator at 37 degrees with 95% O<sub>2</sub>, 5% CO<sub>2</sub>, and 5 % humidity. The cells were grown to approximately 90% confluency before splitting for the transport experiment.

### Synthesis of salmon calcitonin

#### Abbreviations:

DMF, dimethyl formamide; DIPEA, diisopropyl ethyl amine; TFA, trifluoroacetic acid; DIC, diisopropylcarbodiimide; Oxyma, ethyl cyanohydroxyiminoacetate; TIPS, triisopropyl silane; HFIP, hexafluoroisopropanol.

#### Materials

Fmoc-protected amino acids, oxyma and DIC were purchased from Iris-Biotech. The resin was purchased from Rapp Polymere. Solvents and all other reagents were purchased from Sigma Aldrich. Standard Fmoc amino acids: Fmoc-Ala-OH, Fmoc-Arg(Pbf)-OH, Fmoc-Asn(Trt)-OH, Fmoc-Asp(OtBu)-OH, Fmoc-Cys(Trt)-OH, Fmoc-Gln(Trt)-OH, Fmoc-Glu(OtBu)-OH, Fmoc-Gly-OH, Fmoc-His(Trt)-OH, Fmoc-Ile-OH, Fmoc-Leu-OH, Fmoc-Lys(Boc)-OH, Fmoc-Met-OH, Fmoc-Phe-OH, Fmoc-Pro-OH, Fmoc-Ser(tBu)-OH, Fmoc-Thr(tBu)-OH, Fmoc-Trp(Boc)-OH, Fmoc-Tyr(tBu)-OH, Fmoc-Val-OH.

Special Fmoc amino acids: Fmoc-Oc2O-OH (Fluorenylmethyloxycarbonyl-amino-3,6-dioxoactanoic acid), Fmoc-L-Leu-L-Ser[PSI(Me, Me)Pro]-OH, Fmoc-Glu-OtBu, Fmoc-Asp-OtBu.

#### Synthesis of lipidated amino acids

Fmoc-AA-OtBu (AA = Glu or Asp, 1 eq.) was dissolved in dichloromethane. PyBOP (1 eq.), DIPEA (3 eq.) and amino-lipid (butylamine or octylamine) (1.1 eq.) were added, and the reaction mixture was stirred overnight. The mixture was evaporated *in vacuo*, re-dissolved in EtOAc, washed with 1M KHSO<sub>4</sub> (2x), with sat. NaHCO<sub>3</sub> (2x), with brine (2x), dried over MgSO<sub>4</sub>, filtered, and evaporated *in vacuo*.

The ester-product was re-dissolved in 10 mL DCM. 5 mL TFA was added, stirred for one h, and evaporated *in vacuo*. The product was re-dissolved in 5 mL of DMF and precipitated with water. The precipitate was centrifuged (5 min, 6000 rpm), and the supernatant was decanted. The product was lyophilized to yield colourless powders. The correct masses were identified using MALDI-TOF MS.

#### Solid phase peptide synthesis

Peptides were synthesized on a Biotage Initiator + Alstra microwave-assisted peptide synthesizer in 10 mL fritted syringes on a 0.05 mmol scale. Tentagel S-RAM resin was used (0.23 mmol/g). Fmoc-deprotection was performed by adding 5 mL of deprotection solution (20% piperidine in DMF, 0.1 M Oxyma) to the resin 75 °C for 30 sec. The resin was drained and washed once with 5 mL DMF. Another 5 mL of deprotection solution was added 75 °C for 2 min. Afterward, the resin was drained and washed five times with 5 mL DMF. Coupling of amino acids was performed by adding amino acid solution (4 eq. of Fmoc-AA-OH, 4 eq. Oxyma in DMF, 0.3M concentration), DIC solution (5 eq., 2M DIC in DMF) and heating the mixture to 75°C for 5 min. The solution was drained and the resin was washed once with 5 mL DMF. The coupling was repeated. After the second coupling the resin was washed 4 times with 5 mL DMF. Extended coupling times were applied for Fmoc-Arg(Pbf)-OH,

Fmoc-L-Leu-L-Ser[PSI(Me, Me)Pro]-OH and the lipidated amino acids Fmoc-Asp(C4)-OH, Fmoc-Asp(C8)-OH, Fmoc-Glu(C4) and Fmoc-Glu(C8)-OH. These amino acids were coupled at room temperature for 25 min followed by 75 °C for 5 min. The resin was drained, washed 4 times with DMF (5 mL) and the coupling was repeated.

#### **Formation of disulfide on resin**

After coupling of Fmoc-Oc2O-OH, the resin was washed five times with DCM (5 mL). 5 mL of iodine solution (1:4 HFIP/1% I<sub>2</sub> in DCM) was added to the resin, shaken for 2 min, filtered, and washed once with a 1:1 HFIP/DCM solution. The resin was then left to shake for 15 min with a 1:1 HFIP/DCM solution. The solution was drained, and the resin was washed five times with DCM and five times with DMF. Afterward, Fmoc was removed by adding 5 mL 20% piperidine in DMF (with 0.1% Oxyma), and the tube was shaken for 2x 20 min. The resin was washed with DMF, DCM, DMF, DCM, i-PrOH, DCM, and Et<sub>2</sub>O.

#### **Atto coupling, peptide cleavage, purification and analysis.**

Atto488 (5 mg, 5.1 μmol), dry DIPEA (5 eq., 20.4 μmol, 3.55 μL) were dissolved in dry DMF (200 μL) and added to 45 mg resin (approx. 5.7 μmol). The tube was shaken overnight in the dark. The resin was washed 5 times with 5 mL of DMF, 5 times with 5 mL DCM and air-dried. The resin was treated with 0.6 mL cleavage cocktail (90% TFA, 5% water, 5% TIPS) for 240 min. The crude peptide was precipitated in cold diethylether, centrifuged, and decanted. The residue was air-dried and re-dissolved in 20% MeCN in MQ. The crude peptide was purified on a Dionex Ultimate 3000 system equipped with a RQ variable wavelength detector and an automated fraction collector using a Phenomenex, Gemini NX 5u, C18, 110Å, AXIA, 250 mm x 21 mm column at a 20 mL/min flowrate. RP-HPLC gradients were run using a solvent system consisting of solution A (H<sub>2</sub>O + 0.1% TFA) and B (MeCN + 0.1% TFA). Pure fractions were combined and lyophilized. Peptides were analyzed on a Shimadzu NexeraX2 reverse-phase HPLC (RP-HPLC) system equipped with Shimadzu LC-30AD pumps, a Shimadzu SIL-30AC autosampler, a CTO-20AC column oven and a Shimadzu PDA detector (monitoring at 214 nm, 280 nm and 492 nm) using a Waters XBridge BEH C18, 2.5μm 3.0x150mm XP Column at a flow rate of 0.5 mL/min. RP-HPLC gradients were run using a solvent system consisting of solution A (5% MeCN in H<sub>2</sub>O + 0.1% TFA) and B (MeCN + 0.1% TFA). Mass analysis was performed with autoflex-MALDI-TOF (Bruker) or UHPLC-Microtof-Q III LC-MS system (Bruker).

#### **Cell seeding**

At 90% confluency, the medium in the T75 flask was removed, and the cells were washed with 10 mL of a cell suitable PBS (D8537-500ML Sigma) preheated to 37 degrees. The PBS was removed and replaced with 1 mL trypsin/EDTA and placed in the incubator at 37 degrees with 95% O<sub>2</sub>, 5% CO<sub>2</sub>, and 5 % humidity for approximately 5 minutes or until the cells were detached from the surface of the flask. The trypsin/EDTA solution was deactivated by adding 9 mL cell medium. The cell density per mL was found using a NucleoCounter. 30000 cells were seeded per well and grown for two days.

#### **Cell staining**

Cells were stained for 30 minutes with 1μg/mL Hoechst 33342 (H1399, Thermo Fisher, 10 μg/mL) in Fluorobrite (ThermoFisher, A1896701). After staining the cells were washed once in clean fluorobrite. After staining with fluorobrite, the cells were labelled with CellMask DeepRed plasma membrane stain (ThermoFisher, C10046) diluted 2000 times for approximately 10 minutes. After the staining, the cells were washed in fluorobrite 3 times.

## Imaging

For the transport studies, a confocal spinning disk (inverted Nikon Ti2 with Yokogawa CSU-W1 SD system with 50  $\mu\text{m}$  pinholes) with a 60x 1.4 NA oil objective (CFI Plan Apochromat Lambda 60x Oil) was used. The microscope was connected to a heater and  $\text{CO}_2$  to maintain favorable conditions for the cells. The heater was set to 37  $^\circ\text{C}$ , and the  $\text{CO}_2$  was set to 5%. A water reservoir was also present to maintain humidity while imaging. Three different lasers were used. 405 nm laser at 8% to excite the nucleus stained with Hoechst. A 488 nm laser at 10% was used to excite the peptides. A 640 nm laser was used to excite the CellMask DeepRed, labeling the membrane of the cells. A quadband emission filter was used to capture the emitted light for faster acquisition with a sCMOS (Photometrics Prime 95B) camera.

Several fields of views (FOVs) at 1200x1200 pixels (180 nm x 180 nm pixel size) were picked out using the mark and find positioning plugin in the Nikon software. After all the FOVs were picked, a z-stack was taken of all the FOVs marked. The z-stack consisted of 71 steps, where each step was 0.5  $\mu\text{m}$ . After taking the z-stack, the peptide was added carefully. After adding the peptide, all FOVs were corrected back to the original position in x,y, and z if needed. After the correction, a time series was set up to run for 4 hours, imaging every FOV with a z-stack every 40 minutes yielding seven time points.

## Point spread function measurement

The width of the point spread function (PSF) is dependent on many parameters of the confocal microscope, including the excitation and emission wavelength. Hence, we pragmatically measure the axial PSF for the 488 nm and the 640 nm excitation of our spinning disc confocal microscope. To this end, 100 nm fluorescent polymer beads (ThermoFisher, T7279) were used. The beads were small enough to be considered point sources due to the diffraction limit and have the advantage that they can be imaged at four different wavelengths. A z-stack was taken to estimate the PSF in the z-direction. The axial intensity profile essentially shows the axial PSF as seen in Figure S0. The PSF is approximated with the sum of two Gaussians, as seen in the equation below.

$$f(x) = a \left( c \left( \frac{1}{\sigma\sqrt{2\pi}} \right) \exp^{-\frac{1}{2} \left( \frac{x-\mu}{\sigma} \right)^2} + (1-c) \left( \frac{1}{(\sigma * \sigma_{corr})\sqrt{2\pi}} \right) \exp^{-\frac{1}{2} \left( \frac{x-(\mu+\mu_{shift})}{(\sigma * \sigma_{corr})} \right)^2} \right) + b$$

One gaussian is tall and slim, whereas the second one is small and wide. This means that the width ( $\sigma$ ) of the two Gaussians are not the same. To express the double gaussian with only one  $\sigma$ , a factor was multiplied by the width of the small and wide gaussian. This factor is called  $\sigma_{corr}$  and is defined as:  $\sigma_{corr} = \frac{\sigma_{wide}}{\sigma_{narrow}}$ . Furthermore, the center position  $\mu$  of the two Gaussians is shifted compared to one another. Hence, a shift parameter  $\mu_{shift}$  is introduced and is defined as the difference between the two positions. The factor  $c$  is a weight determining how much of each of the gaussian should be represented in the sum of the Gaussians.

The overall shape of the fit to the axial PSF for the 488 nm and 640 nm excitation was used to deconvolute the axial intensity profiles through the cells.

## Deconvolution of the axial intensity profiles

After acquiring all of the images, each FOV was analyzed and processed individually. In each FOV for every eligible cell, a small region of interest (ROI) of 10x10 pixels was picked out. Typically, the ROI

was close to the nuclei but not in the nuclei. After picking out the ROIs, the intensity signal in the ROI was stored for each of the three channels in each z plane of the z-stack. The intensity from the blue channel was used to verify that the ROI was not placed inside the nucleus. However, the intensity trace from the nuclei channel can still give a small (4-5 intensity units) increase when the ROI is inside the cell as seen in Figure 1C left panel.

We first fit the axial intensity profile from the membrane channel to locate the cell's lower and upper membrane layers. We select the ROIs so that the membrane can be modelled by an infinitely thin plane thus the intensity profile is fitted with two axial PSFs and a constant background:

$$f(x) = a1 \left( c \left( \frac{1}{\sigma\sqrt{2\pi}} \right) \exp^{-\frac{1}{2} \left( \frac{x-\mu_1}{\sigma} \right)^2} + (1-c) \left( \frac{1}{(\sigma * \sigma_{corr})\sqrt{2\pi}} \right) \exp^{-\frac{1}{2} \left( \frac{x-(\mu_1+\mu_{shift})}{(\sigma * \sigma_{corr})} \right)^2} \right) \\ + a2 \left( c \left( \frac{1}{\sigma\sqrt{2\pi}} \right) \exp^{-\frac{1}{2} \left( \frac{x-\mu_2}{\sigma} \right)^2} + (1-c) \left( \frac{1}{(\sigma * \sigma_{corr})\sqrt{2\pi}} \right) \exp^{-\frac{1}{2} \left( \frac{x-(\mu_2+\mu_{shift})}{(\sigma * \sigma_{corr})} \right)^2} \right) + b$$

Five parameters are fitted; a1, the amplitude of the Gaussians describing the lower cell membrane, a2 describing the amplitude of the second gaussian,  $\mu_1$  is the position of the lower membrane,  $\mu_2$  is the position of the upper membrane, and b is the background signal. The remaining parameters in the function are found experimentally from the PSF at the 640 nm excitation.

Next, the axial intensity signal from the peptide channel is used to quantify peptide signal in the solution, the cytosol and collocated with the bottom membrane. The contribution from the solution is described by a step function convoluted with the axial PSF. Similarly the cytosol contribution is defined by two step functions convoluted with the PSF. The signal collocated with the bottom membrane is modeled by the PSF. The function describing the intensity profile of the peptide channel is thus described by:

$$f(x) = \left( \begin{aligned} & \frac{a1}{2} * \left( c * \left( 1 + \operatorname{erf} \left( \frac{x-\mu_1}{\sqrt{2} * \sigma} \right) \right) + (1-c) * \left( 1 + \operatorname{erf} \left( \frac{x-(\mu_1+\mu_{shift})}{\sqrt{2} * (\sigma * \sigma_{corr})} \right) \right) \right) \\ & + \frac{a2}{2} * \left( c * \left( 1 + \operatorname{erf} \left( \frac{x-\mu_2}{\sqrt{2} * \sigma} \right) \right) + (1-c) * \left( 1 + \operatorname{erf} \left( \frac{x-(\mu_2+\mu_{shift})}{\sqrt{2} * (\sigma * \sigma_{corr})} \right) \right) \right) \\ & + a3 \left( c \left( \frac{1}{\sigma\sqrt{2\pi}} \right) \exp^{-\frac{1}{2} \left( \frac{x-\mu_1}{\sigma} \right)^2} + (1-c) \left( \frac{1}{(\sigma * \sigma_{corr})\sqrt{2\pi}} \right) \exp^{-\frac{1}{2} \left( \frac{x-(\mu_1+\mu_{shift})}{(\sigma * \sigma_{corr})} \right)^2} \right) \end{aligned} \right) \\ + b$$

Here, a1 is the amplitude of the first error function, which describes the plateau in the cell's cytosol. Parameter a2 is the amplitude of the second error function, which represents the plateau in the solution. Parameter a3 is the amplitude of the peak that colocalized with the bottom membrane of the cell. Lastly, b is the background intensity. All other parameters in the function are known from prior fitting of the membrane signal (the positions of the membranes) and of the shape of the axial PSF at the 488 nm excitation. From the fit we obtain the fitted values of a1, a2 and a3.



## References

- Anselmo, A. C., Gokarn, Y., & Mitragotri, S. (2018). Non-invasive delivery strategies for biologics. *Nature Reviews Drug Discovery*, 18(1), 19–40. <https://doi.org/10.1038/nrd.2018.183>
- Behrens, I., Stenberg, P., Artursson, P., & Kissel, T. (2001). Transport of lipophilic drug molecules in a new mucus-secreting cell culture model based on HT29-MTX cells. *Pharmaceutical Research*, 18(8), 1138–1145. <https://doi.org/10.1023/A:1010974909998>
- Betanzos, A., Zanatta, D., Bañuelos, C., Hernández-Nava, E., Cuellar, P., & Orozco, E. (2018). Epithelial Cells Expressing EhADH, An Entamoeba histolytica Adhesin, Exhibit Increased Tight Junction Proteins. *Frontiers in Cellular and Infection Microbiology*, 8(September), 1–17. <https://doi.org/10.3389/fcimb.2018.00340>
- Birch, D., Diedrichsen, R. G., Christophersen, P. C., Mu, H., & Nielsen, H. M. (2018). Evaluation of drug permeation under fed state conditions using mucus-covered Caco-2 cell epithelium. *European Journal of Pharmaceutical Sciences*, 118(January), 144–153. <https://doi.org/10.1016/j.ejps.2018.02.032>
- Brayden, D. J., Gleeson, J., & Walsh, E. G. (2014). A head-to-head multi-parametric high content analysis of a series of medium chain fatty acid intestinal permeation enhancers in Caco-2 cells. *European Journal of Pharmaceutics and Biopharmaceutics*, 88(3), 830–839. <https://doi.org/10.1016/j.ejpb.2014.10.008>
- Brock, R. (2014). The uptake of arginine-rich cell-penetrating peptides: Putting the puzzle together. *Bioconjugate Chemistry*, 25(5), 863–868. <https://doi.org/10.1021/bc500017t>
- Burchfield, J. G., Lopez, J. A., Mele, K., Vallotton, P., & Hughes, W. E. (2010). Exocytotic vesicle behaviour assessed by total internal reflection fluorescence microscopy. *Traffic*, 11(4), 429–439. <https://doi.org/10.1111/j.1600-0854.2010.01039.x>
- Capoulade, J., Wachsmuth, M., Hufnagel, L., & Knop, M. (2011). Quantitative fluorescence imaging of protein diffusion and interaction in living cells. *Nature Biotechnology*, 29(9), 835–839. <https://doi.org/10.1038/nbt.1928>
- Cetin, M., Youn, Y. S., Capan, Y., & Lee, K. C. (2008). Preparation and characterization of salmon calcitonin-biotin conjugates. *AAPS PharmSciTech*, 9(4), 1191–1197. <https://doi.org/10.1208/s12249-008-9165-2>
- Chai, G. H., Xu, Y., Chen, S. Q., Cheng, B., Hu, F. Q., You, J., ... Yuan, H. (2016). Transport Mechanisms of Solid Lipid Nanoparticles across Caco-2 Cell Monolayers and their Related Cytotoxicology. *ACS Applied Materials and Interfaces*, 8(9), 5929–5940. <https://doi.org/10.1021/acsami.6b00821>
- Conchello, J. A., & Lichtman, J. W. (2005). Optical sectioning microscopy. *Nature Methods*, 2(12), 920–931. <https://doi.org/10.1038/nmeth815>
- Diedrichsen, R. G., Harloff-Helleberg, S., Werner, U., Besenius, M., Leberer, E., Kristensen, M., & Nielsen, H. M. (2021). Revealing the importance of carrier-cargo association in delivery of insulin and lipidated insulin. *Journal of Controlled Release*, 338(July), 8–21. <https://doi.org/10.1016/j.jconrel.2021.07.030>
- Drucker, D. J. (2020). Advances in oral peptide therapeutics. *Nature Reviews Drug Discovery*, 19(4), 277–289. <https://doi.org/10.1038/s41573-019-0053-0>
- Groschwitz, K. R., & Hogan, S. P. (2009). Intestinal barrier function: Molecular regulation and disease

- pathogenesis. *Journal of Allergy and Clinical Immunology*, 124(1), 3–20. <https://doi.org/10.1016/j.jaci.2009.05.038>
- Gupta, V., Doshi, N., & Mitragotri, S. (2013). Permeation of Insulin, Calcitonin and Exenatide across Caco-2 Monolayers: Measurement Using a Rapid, 3-Day System. *PLoS ONE*, 8(2). <https://doi.org/10.1371/journal.pone.0057136>
- Helmuth, J. A., Burckhardt, C. J., Greber, U. F., & Sbalzarini, I. F. (2009). Shape reconstruction of subcellular structures from live cell fluorescence microscopy images. *Journal of Structural Biology*, 167(1), 1–10. <https://doi.org/10.1016/j.jsb.2009.03.017>
- Hinderliter, P., & Saghir, S. A. (2014). Pharmacokinetics. *Encyclopedia of Toxicology: Third Edition*, 3, 849–855. <https://doi.org/10.1016/B978-0-12-386454-3.00419-X>
- Ismail, R., & Csóka, I. (2017). Novel strategies in the oral delivery of antidiabetic peptide drugs – Insulin, GLP 1 and its analogs. *European Journal of Pharmaceutics and Biopharmaceutics*, 115, 257–267. <https://doi.org/10.1016/j.ejpb.2017.03.015>
- Je, H. J., Kim, E. S., Lee, J. S., & Lee, H. G. (2017). Release Properties and Cellular Uptake in Caco-2 Cells of Size-Controlled Chitosan Nanoparticles. *Journal of Agricultural and Food Chemistry*, 65(50), 10899–10906. <https://doi.org/10.1021/acs.jafc.7b03627>
- Joyce, P., Jömettsa, S., Isaksson, S., Hossain, S., Larsson, P., Bergström, C., & Höök, F. (2021). TIRF Microscopy-Based Monitoring of Drug Permeation Across a Lipid Membrane Supported on Mesoporous Silica. *Angewandte Chemie*, 133(4), 2097–2101. <https://doi.org/10.1002/ange.202011931>
- Kataoka, M., Fukahori, M., Ikemura, A., Kubota, A., Higashino, H., Sakuma, S., & Yamashita, S. (2016). Effects of gastric pH on oral drug absorption: In vitro assessment using a dissolution/permeation system reflecting the gastric dissolution process. *European Journal of Pharmaceutics and Biopharmaceutics*, 101, 103–111. <https://doi.org/10.1016/j.ejpb.2016.02.002>
- Kim, S., Lee, H., Lee, S., Kim, S. K., Lee, Y. K., Chung, B. H., ... Byun, Y. (2005). Enhancing effect of chemically conjugated deoxycholic acid on permeability of calcitonin in Caco-2 cells. *Drug Development Research*, 64(2), 129–135. <https://doi.org/10.1002/ddr.10423>
- Kowada, T., Maeda, H., & Kikuchi, K. (2015). BODIPY-based probes for the fluorescence imaging of biomolecules in living cells. *Chemical Society Reviews*, 44(14), 4953–4972. <https://doi.org/10.1039/c5cs00030k>
- Liu, X., Zheng, S., Qin, Y., Ding, W., Tu, Y., Chen, X., ... Cai, X. (2017). Experimental evaluation of the transport mechanisms of PolFN- $\alpha$  in Caco-2 cells. *Frontiers in Pharmacology*, 8(NOV), 1–11. <https://doi.org/10.3389/fphar.2017.00781>
- Macia, E., Ehrlich, M., Massol, R., Boucrot, E., Brunner, C., & Kirchhausen, T. (2006). Dynasore, a Cell-Permeable Inhibitor of Dynamin. *Developmental Cell*, 10(6), 839–850. <https://doi.org/10.1016/j.devcel.2006.04.002>
- Manzanares, D., & Ceña, V. (2020). Endocytosis: The nanoparticle and submicron nanocompounds gateway into the cell. *Pharmaceutics*, 12(4), 1–22. <https://doi.org/10.3390/pharmaceutics12040371>
- McClellan, S., Prosser, E., Meehan, E., O'Malley, D., Clarke, N., Ramtoola, Z., & Brayden, D. (1998). Binding and uptake of biodegradable poly-DL-lactide micro- and nanoparticles in intestinal epithelia. *European Journal of Pharmaceutical Sciences*, 6(2), 153–163. [https://doi.org/10.1016/S0928-0987\(97\)10007-0](https://doi.org/10.1016/S0928-0987(97)10007-0)
- Menacho-Melgar, R., Decker, J. S., Hennigan, J. N., & Lynch, M. D. (2019). A review of lipidation in

- the development of advanced protein and peptide therapeutics. *Journal of Controlled Release*, 295(December 2018), 1–12. <https://doi.org/10.1016/j.jconrel.2018.12.032>
- Mitragotri, S., Burke, P. A., & Langer, R. (2014). Overcoming the challenges in administering biopharmaceuticals: Formulation and delivery strategies. *Nature Reviews Drug Discovery*, 13(9), 655–672. <https://doi.org/10.1038/nrd4363>
- Potocky, T. B., Menon, A. K., & Gellman, S. H. (2003). Cytoplasmic and Nuclear Delivery of a TAT-derived Peptide and a  $\beta$ -Peptide after Endocytic Uptake into HeLa Cells. *Journal of Biological Chemistry*, 278(50), 50188–50194. <https://doi.org/10.1074/jbc.M308719200>
- Preta, G., Cronin, J. G., & Sheldon, I. M. (2015). Dynasore - Not just a dynamin inhibitor. *Cell Communication and Signaling*, 13(1), 1–7. <https://doi.org/10.1186/s12964-015-0102-1>
- Ramanathan, S., Pooyan, S., Stein, S., Prasad, P. D., Wang, J., Leibowitz, M. J., ... Sinko, P. J. (2001). Targeting the sodium-dependent multivitamin transporter (SMVT) for improving the oral absorption properties of a retro-inverso Tat nonapeptide. *Pharmaceutical Research*, 18(7), 950–956. <https://doi.org/10.1023/A:1010932126662>
- Ramanathan, S., Srinivasan, Qiu, B., Pooyan, S., Zhang, G., Stein, S., Leibowitz, M. J., & Sinko, P. J. (2001). Targeted PEG-based bioconjugates enhance the cellular uptake and transport of a HIV-1 TAT nonapeptide. *Journal of Controlled Release*, 77(3), 199–212. [https://doi.org/10.1016/S0168-3659\(01\)00474-6](https://doi.org/10.1016/S0168-3659(01)00474-6)
- Renukuntla, J., Vadlapudi, A. D., Patel, A., Boddu, S. H. S., & Mitra, A. K. (2013). Approaches for enhancing oral bioavailability of peptides and proteins. *International Journal of Pharmaceutics*, 447(1–2), 75–93. <https://doi.org/10.1016/j.ijpharm.2013.02.030>
- Rousou, C., Maar, J. De, Qiu, B., Wurff-jacobs, K. Van Der, Ruponen, M., Urtti, A., ... Deckers, R. (2022). *The Effect of Microbubble-Assisted Ultrasound on Molecular Permeability across Cell Barriers*.
- Schmid, S. L., & Conner, S. D. (2003). Regulated portals of entry into the cell. *Nature*, 422(March), 37–44. Retrieved from [www.nature.com/nature](http://www.nature.com/nature)
- Shah, R. B., & Khan, M. A. (2004). Regional permeability of salmon calcitonin in isolated rat gastrointestinal tracts: transport mechanism using Caco-2 cell monolayer. *The AAPS Journal*, 6(4), 2–6.
- Smith, E. M., Hennen, J., Chen, Y., & Mueller, J. D. (2015). Z-scan fluorescence profile deconvolution of cytosolic and membrane-associated protein populations. *Analytical Biochemistry*, 480, 11–20. <https://doi.org/10.1016/j.ab.2015.03.030>
- Song, K. H., Chung, S. J., & Shim, C. K. (2005). Enhanced intestinal absorption of salmon calcitonin (sCT) from proliposomes containing bile salts. *Journal of Controlled Release*, 106(3), 298–308. <https://doi.org/10.1016/j.jconrel.2005.05.016>
- Thompson, C., Cheng, W. P., Gadad, P., Skene, K., Smith, M., Smith, G., ... Knott, R. (2011). Uptake and transport of novel amphiphilic polyelectrolyte-insulin nanocomplexes by caco-2 cells-towards oral insulin. *Pharmaceutical Research*, 28(4), 886–896. <https://doi.org/10.1007/s11095-010-0345-x>
- Tibbitt, M. W., Dahlman, J. E., & Langer, R. (2016). Emerging Frontiers in Drug Delivery. *Journal of the American Chemical Society*, 138(3), 704–717. <https://doi.org/10.1021/jacs.5b09974>
- Trier, S., Linderroth, L., Bjerregaard, S., Strauss, H. M., Rahbek, U. L., & Andresen, T. L. (2015). Acylation of salmon calcitonin modulates in vitro intestinal peptide flux through membrane permeability enhancement. *European Journal of Pharmaceutics and Biopharmaceutics*, 96, 329–337. <https://doi.org/10.1016/j.ejpb.2015.09.001>

- Turner, J. R. (2009). Intestinal mucosal barrier function in health and disease. *Nature Reviews Immunology*, 9(11), 799–809. <https://doi.org/10.1038/nri2653>
- Verma, S., Goand, U. K., Husain, A., Katekar, R. A., Garg, R., & Gayen, J. R. (2021). Challenges of peptide and protein drug delivery by oral route: Current strategies to improve the bioavailability. *Drug Development Research*. <https://doi.org/10.1002/ddr.21832>
- Vtyurina, N., Åberg, C., & Salvati, A. (2021). Imaging of nanoparticle uptake and kinetics of intracellular trafficking in individual cells. *Nanoscale*, 13(23), 10436–10446. <https://doi.org/10.1039/d1nr00901j>
- Yang, Y., Zhao, Y., Yu, A., Sun, D., & Yu, L. X. (2017). Oral drug absorption: Evaluation and prediction. *Developing Solid Oral Dosage Forms: Pharmaceutical Theory and Practice: Second Edition*, 331–354. <https://doi.org/10.1016/B978-0-12-802447-8.00012-1>
- Youn, Y. S., Jung, J. Y., Oh, S. H., Yoo, S. D., & Lee, K. C. (2006). Improved intestinal delivery of salmon calcitonin by Lys18-amine specific PEGylation: Stability, permeability, pharmacokinetic behavior and in vivo hypocalcemic efficacy. *Journal of Controlled Release*, 114(3), 334–342. <https://doi.org/10.1016/j.jconrel.2006.06.007>
- Zhang, S., Ma, C., & Chalfie, M. (2004). Combinatorial marking of cells and organelles with reconstituted fluorescent proteins. *Cell*, 119(1), 137–144. <https://doi.org/10.1016/j.cell.2004.09.012>
- Zimmermann, C., Rudloff, S., Lochnit, G., Arampatzi, S., Maison, W., & Zimmer, K. P. (2014). Epithelial transport of immunogenic and toxic gliadin peptides in vitro. *PLoS ONE*, 9(11), 1–17. <https://doi.org/10.1371/journal.pone.0113932>

**Supplementary Information to ‘Quantitative imaging of lipidated peptides: Towards a mechanistic understanding of their transport through an endothelial cell layer’**

**Uptake of peptide measured on Caco-2 cells grown in an microfluidic platform**

**Cell culture**

The three-lane OrganoPlate (4004-400-B, Mimetas BV) was used for all experiments. First, an ECM-gel was prepared consisting of 4 mg/mL Collagen 1 (3447-020-01, R&D Systems), 100 mM HEPES (H0887, Sigma) and 3.7 mg/mL NaHCO<sub>3</sub>. The ECM-mixture was loaded into the ECM-channel and placed for 30 min in the incubator to polymerize. To avoid gel drying the 30 µL HBSS was added to the ECM-channel to until usage of the plate for cell loading. Next, Caco-2 cells were detached with 0.25% trypsin EDTA, diluted to a final concentration of  $1 \times 10^7$  cells/mL and dispensed into the upper channel of the chip. The OrganoPlate was placed inside the incubator and incubated vertically for 3 h to allow cell attachment against the ECM. The cultivation of cells in the OrganoPlate was continued horizontally for 4 days on an interval rocker ( $\pm 7^\circ$  angle, 8 min rocking interval) at 37°C, 5% CO<sub>2</sub>. The medium was replaced every 2-3 days. For all experiments, chips with tight barrier properties were used, which were assessed by imaging the distribution of 0.5 mg/mL 4.4 kDa TRITC-Dextran (T1037, Sigma) in the chip as previously described (Trietsch et al., 2017)

**sCal imaging in OrganoPlate**

The medium of the chip were aspirated and washed two times with HBSS. Cells inside the chips were stained with Cellmask Deep Red Plasma membrane Stain (C10046, Thermo Fisher, 1:1000) and Hoechst (H1399, Thermo Fisher, 10 µg/mL) for 30 min at 37°C, 5% CO<sub>2</sub>. Next, the chips were washed twice with imaging media and images of three different x-y positions per chip were acquired. Afterwards, imaging media in the cell channel was replaced by the sCal peptide and imaged continuously over 3-4 hours using a Spinning Disk microscope.

**Investigation of Atto 488-labeled lipidated analogues of sCT by fluorescence correlation spectroscopy (FCS)**

The solution state of peptides may be evaluated using a number of different biophysical and analytical techniques. However, it is not possible to apply the traditional characterization techniques to fluorescently labeled peptides because (i) the peptides are available in insufficient amounts and (ii) the fluorophore may interfere with the readout. On the other hand, the fluorophore opens new methodological opportunities, for example, allowing the peptides to be evaluated using fluorescence correlation spectroscopy (FCS).

In brief, FCS measures the temporal fluctuations from a confocal detection volume. The intensity time trace is then used to estimate an autocorrelation curve. For a single species of fluorescent particles, the autocorrelation curve can be fitted by the function (Krichevsky & Bonnet, 2002)

$$G(\tau) = \frac{1}{N} \left(1 + \frac{\tau}{\tau_D}\right)^{-1} \left(1 + \frac{\tau}{S^2 \tau_D}\right)^{-\frac{1}{2}} \quad (1)$$

where  $\tau$  is the lag time,  $N$  is the average number of fluorescent particles in the detection volume,  $S$  is the ratio of the axial to radial dimensions of the detection volume, and  $\tau_D$  is the typical lateral diffusion time of the particles through the detection volume. The value of  $\tau_D$  is related to the diffusion coefficient,  $D$ , via the relation (Krichevsky & Bonnet, 2002)

$$\tau_D = \frac{\omega_{xy}^2}{4D} \quad (2)$$

where  $\omega_{xy}$  is the lateral radius of the detection volume.

The following text describes the usage of FCS for characterization of Atto 488-labeled lipidated analogues of salmon calcitonin (sCT). Specifications of the FCS setup can be found elsewhere (Kristensen et al., 2016).

#### Characterization of detection volume

To determine  $S$ , a 10 nM sample with Alexa Fluor 488 hydrazide was repeatedly measured, and the resulting autocorrelation curves were fitted using Equation 1 as previously described (Kristensen et al., 2017).. From this, the value of  $S$  was determined to be 8.8.

To determine  $\omega_{xy}$ , samples with Alexa Fluor 488 hydrazide in the range 0-1000 nM were investigated. The resulting autocorrelation curves were fitted using Equation 1 with  $S = 8.8$ . The values of  $N$  and  $\tau_D$  were plotted as a function of the molecular concentration,  $C$ , see Figure S9.

Using the relation<sup>1</sup>

$$V = \frac{N}{C} \quad (3)$$

the size of the detection volume,  $V$ , was estimated to be 1.1 fL. Finally, using the relation (Krichevsky & Bonnet, 2002)

$$V = \pi^{3/2} S \omega_{xy}^3 \quad (4)$$

$\omega_{xy}$  was estimated to be 280 nm. Importantly,  $\tau_D$  was found to be independent of  $C$ , as it should be. Also worth noting, the diffusion time at 1  $\mu$ M Alexa Fluor 488 was subject to some uncertainty, demonstrating that this concentration is approaching the limit of the FCS setup.

#### Evaluation of the solution state of the peptides

FCS was performed using the samples described in Table 1

Atto 488-labeled sCT	Concentration	Solvent
Native	1 $\mu$ M	FluoroBrite
C4/C4	1 $\mu$ M	FluoroBrite
C8/C8	~500 nM	HBSS

**Table 1.** Peptide samples investigated by FCS.

The peptide concentrations were chosen to allow for direct comparison to the microscopy experiments. To reduce intensity drift due to peptide adsorption to the coverslips, the sample chambers were pre-incubated with peptide solutions. Even after pre-incubation of the chambers, sample drift represented a challenge, and I generally had to wait for ~30-60 min before the signal was sufficiently stable for performing FCS.

Figure S9 shows the autocorrelation curves measured for each peptide. The curves were fitted using Equation 1 with  $S = 8.8$ . The fitted curves were in good agreement with the experimental ones, suggesting that the samples were of a fairly monodisperse nature. Table 2 shows the results of the fitting. Using Equation 2, the diffusion coefficients of the peptides were estimated, see Figure S10.

Atto 488-labeled sCT	$N$	$\tau_D$ ( $\mu$ s)
Native	414 $\pm$ 30	122 $\pm$ 23
C4/C4	633 $\pm$ 25	121 $\pm$ 10
C8/C8	447 $\pm$ 8	90 $\pm$ 1

**Table 2.** Results of fitting the acquired autocorrelation curves with Equation 1. The data are the average of two measurements, and the experimental uncertainties represent the standard deviation.

It has been suggested that the diffusion coefficient of peptides is empirically related to their molecular weight,  $M$ , via the relation (Hosoya et al., 2004)

$$\log(D) = -0.434 \log(M) - 4.059 \quad (5)$$

where  $M$  is in units of Da and  $D$  in  $\text{cm}^2 \text{s}^{-1}$ . The diffusion coefficients calculated using this equation were compared to the measured ones, see Figure S10. This calculation tentatively suggests that the native and C4/C4-modified analogues of sCT were incorporated in small oligomers with 2-4 peptides, whereas the C8/C8-modified analogue of sCT was in an almost monomeric state.

The conclusions of the diffusion analysis is, at least to some extent, supported by apparent particle numbers in the detection volume. For the native sCT, the estimated particle number corresponds to  $\sim 600 \text{ nM}$ , that is, half of that expected for a monomeric peptide solution. For the C4/C4-modified analogue, on the other hand, the estimated particle number corresponds to  $\sim 1 \mu\text{M}$ . This would suggest that this peptide is in a monomeric state. For the C8/C8-modified analogue, the estimated particle concentration corresponds to  $\sim 700 \text{ nM}$ , but the interpretation of this value may be somewhat uncertain due to uncertainties in the measured peptide concentration.

Overall, the FCS data points towards the conclusion that all peptides are either monomeric or at most assembled in small oligomers with 2-4 peptides.

#### **Additional relevant observations**

It should finally be mentioned that I in a few instances observed some bright particles in the sample with the C8/C8-modified sCT analogue. These particles could potentially represent prefibrillar intermediates. However, they were quite rare, and as such, they were neglected in the data analysis. The bright particles were not detected in samples with native and C4/C4-modified sCT.

#### **Size of the peptide aggregates measured by Photobleaching Step Analysis (PBSA):**

The transport of peptides through cells may depend on the agglomeration state of the peptides in solution. In our study we thus address the agglomeration of the lipidated Salmon calcitonin. To this end we perform stepwise bleaching of peptides adsorbed to a glass surface using total internal reflection fluorescence (TIRF) microscopy.

It has been shown that TIRF microscopy can be utilized to identify the number of monomers in a protein by photobleaching step analysis (Ulbrich & Isacoff, 2007). TIRF microscopy illuminates the sample in a shallow layer above the glass-water interface. It thus yields a high signal to noise (SNR) ratio compared to epifluorescence (Takashi Funatsu, Yoshie Harada, Makio Tokunaga, 1995) (Fish KN, 2009).

Peptides labelled with atto-488 are adsorbed from solution onto a clean glass surface then imaged until all peptide spots has bleached. To this end an 8-well glass bottom slide (Ibidi) was cleaned following a protocol from Snaar-Jagalska et al (Snaar-Jagalska, Cambi, Schmidt, & De Keijzer, 2013). In brief, the glass slides are sonicated for 15 min in a 1% triton solution followed by rinsing in Milli-Q water. The glass slides are then sonicated for 15 min in Milli-Q water followed by another 15 min sonication with 0.1M KOH. Finally, the glass slides are sonicated in Milli-Q water for 15 min and dried under a nitrogen flow.

Next, 100  $\mu\text{L}$  of approximately 100 fM peptide was added to a clean well and incubated for approximately 10 minutes to allow the peptides to adhere to the glass surface. After 10 minutes, the peptide solution was removed and fresh imaging medium was added (FluoroBrite, Sigma-Aldrich). Note, we use the same buffer as used in the experiment leading to the spinning disc confocal imaging data discussed in the main text.

TIRF imaging is performed on a homebuilt setup based on an inverted epifluorescence microscope (Nikon Eclipse). A 473 nm laser beam (Cobolt 06-MLD 100 mW) is expanded and focused in the back focal plane of the objective (Nikon 100x/ 1.45 plan apochromat) using a  $f = 300 \text{ mm}$  lens (Thorlabs, AC508-300-A-ML). The beam is tilted using a mirror placed in a  $4f$  configuration with the objective and the focusing lens to achieve TIRF illumination. The power density at the sample plane were approximately  $40 \text{ W/cm}^2$ . Images are recorded with an EMCCD (Photometrics, 512 Evolve) at 50 ms exposure and an EM gain of 300. The experiment is repeated using a different instrument. Here a commercially built TIRF microscope (Nikon

Eclipse Ti2-E) equipped with a 100x objective (CFI SR HP Apochromat TIRF 100xc oil 1.49 NA), a 488nm laser source and a Camera ORCA-Flash 4.0 sCMOS camera (Hamamatsu) camera is used. The power density is estimated to approximately 0.1 W/cm<sup>2</sup>.

The peptide concentration is adjusted thus that peptides appear as isolated bright spots on the surface. Figure S13A shows the first frame in a bleaching movie where the bright spots represent peptides with an atto488 fluorophore attached to it. We record the fluorescence of those spots for 25 seconds (ie. 500 frames) or until all the spots have bleached. In our analysis we only consider isolated spots at the center of the field of view where the illumination is highest ( the white circle in Figure 13B). Conversely, each isolated spot may contain more than one peptide which are not optically resolved but will be resolved by the analysis of the intensity time trace during bleaching of the fluorophores.

The intensity of a spot is summed in a 7x7 pixels region for each frame, which was then used to estimate the number of steps and the step intensity in the intensity trace of a spot using a step-finding algorithm (Ulbrich & Isacoff 2007). The number of steps is then equal to the number of monomers in the peptide analogue as the atto488 label was attached during the synthesis of the peptide. Figure S14 shows the result of the analysis for a single spot. The intensity is summed in a region around the spot larger than the diffraction limit (Figure S14 A) yielding an intensity trace as seen in Figure S14 B. Here, we make sure that the spot has no neighboring spots that may contribute to the intensity trace. A step-finding algorithm is applied of the intensity trace where time points are binned by two to reduce noise on the time trace.

The algorithm estimates the background from the end of the intensity trace (right of dotted line in Figure S14C). The number of steps and the step size in the intensity trace left of the dotted line is then fitted using an iterative maximum likelihood estimator fit of the data with an increasing number of steps. The range of step finding as shown by the dotted line in Figure S14 C should be careful picked for the algorithm to correctly find the steps. As a consequence we inspect the result of the fitting by eye to confirm the number of steps (Figure S14 C). The red dashed horizontal line represents the estimated background level. We analyse a total of N = 88 spots for 5 different field-of-views for sCal(C4,C4)-atto488 and Repeat the experiment for sCal(C0/C0)-atto488 and sCal(C8/C8)-atto488 and summarize the distribution of the number of steps and the step size in photons (Figure S15-S17 panel A and B).

#### Conversion of step size to photon count

The step finding analysis gives step sizes in units of arbitrary intensity, so we calculate a number of photons for the step size. The conversion is dependent on the gain of the camera, the offset of the camera and the quantum efficiency (QE) of the camera. Since an EMCCD camera was used for this experiment the EM gain is also included in the conversion. The combined gain for the camera and the EM gain is measured to be 25 for our specific camera at 300 EM gain and camera gain of 1. The quantum efficiency of our EMCCD camera is 90% at the used wavelength, thus the conversion from intensity to photons is done by the following equation:

$$photon = \frac{\frac{intensity}{total\ gain}}{QE}$$

Figure S16 A shows the distribution of photon in the spots for sCal(C4/C4)-atto488 for 5 field-of-views.

Figure S16 B shows the number of steps found for all sCal(C4/C4)-atto488 and here it is clear to see that the sCal(C4,C4)-atto488 is found primarily as monomers with only a few dimers present. Figure S16 C shows the intensity of the spot as a function of the distance from the center of the illumination seen in Figure S13



B. The blue dot represents the center of the illumination and from this we can see that the further away we get from the center the less intensity we gain from each single spot. This explains why the distribution of the photons is as wide as it is. Figure S15-S17 D show the intensity of the step as a function of number of steps for all three analogs. This shows again that almost all of the steps are single steps, but has a wide range of step sizes, which is explained by the non-uniform illumination.

We find that all three peptides are found as monomers (Figure S18) when dispersed in Fluorobrite, the medium used for the spinning discs imaging data shown in the main text. The PBSA data agrees with our FCS analysis described previously.

In Figure S19 we combine the results of the three analogues (sCal(C0/C0)-atto488, sCal(C4/C4)-atto488 and sCal(C8/C8)-atto488) from our home-built TIRF. sCal(C0/C0)-atto488 and sCal(C4/C4)-atto488 show very similar distributions, but sCal(C8/C8)-atto488 show a shifted distribution toward lower photon count (Figure S19 A). To investigate this the local background found at the peptide is estimated as the shift may be due to a minor sample-to-sample variation of the TIRF illumination since the effective Power density at the glass-water interface is highly dependent on the incidence angle (Figure S19 B) (Török, 2007). We can see that sCal(C8/C8)-atto488 (green) has a slightly higher background compared to that of sCal(C0/C0)-atto488 and sCal(C4/C4)-atto488 (blue and orange, respectively). To verify if this is the cause of the shift in distribution the sum of the photon counts of the background and the spot is seen in Figure S19 C. The distribution of sCal(C8/C8)-atto488 is indeed shifted towards the other two peptides, however still not fully overlapping. Even though a full overlap is not seen we still conclude a monodisperse distribution of the sizes of the three peptides.

#### **References:**

- Krichevsky and Bonnet. Rep. Prog. Phys (2002) 65:251-297.
- Kristensen et al. Nanoscale (2016) 8:19726-19736.
- Kristensen et al. Methods Mol. Biol. (2017) 1548:159-180.
- Hosoya et al. J. Pharm. Pharmacol. (2004) 56:1501-1507.
- Fish KN. (2009). Total Internal Reflection Fluorescence (TIRF) Microscopy. Curr Protoc Cytom., 0(12), Unit 12.18. <https://doi.org/10.1002/0471142956.cy1218s50.Total>
- Snaar-Jagalska, B. E., Cambi, A., Schmidt, T., & De Keijzer, S. (2013). Single-molecule imaging technique to study the dynamic regulation of gpcr function at the plasma membrane. In *Methods in Enzymology* (1st ed., Vol. 521). <https://doi.org/10.1016/B978-0-12-391862-8.00003-X>
- Takashi Funatsu, Yoshie Harada, Makio Tokunaga, K. S. & T. Y. (1995). Imaging of single fluorescent molecules and individual ATP turnovers by single myosin molecules in aqueous solution. *Nature*, 374, 555–559.
- Ulbrich, M. H., & Isacoff, E. Y. (2007). Subunit counting in membrane-bound proteins. *Nature Methods*, 4(4), 319–321. <https://doi.org/10.1038/nmeth1024>
- Török, Peter, and Fu-Jen Kao. 2007. *Optical Imaging and Microscopy : Techniques and Advanced Systems*. Optical Imaging and Microscopy. Springer.
- S. J. Trietsch, E. Naumovska, D. Kurek, M. C. Setyawati, M. K. Vormann, K. J. Wilschut, H. L. Lanz, A. Nicolas, C. P. Ng, J. Joore, S. Kustermann, A. Roth, T. Hankemeier, A. Moisan, and P. Vulto, “Membrane-free culture and real-time barrier integrity assessment of perfused intestinal epithelium tubes,” *Nature Communications*, vol. 8, no. 1, pp. 1–7, 2017

#### **Supplementary figures**

##### **List of supplementary figures**

Figure S1. Spinning disc axial PSF measurement and fit for the 488 nm and 640 nm excitation.  
Figure S2. Chemical structure of Salmon Calcitonin analogs.  
Figure S3. Single ROI intensity profiles in the peptide channel for sCT analogs.  
Figure S4. Axial intensity profiles and analysis for sCal(C8/C8)-atto488 on fully polarized Caco-2 cells in a microfluidic platform.  
Figure S5. Relative increase of peptide signal at the bottom of the cells measured on fully polarized Caco-2 cells in a microfluidic platform.  
Figure S6. Effects of clathrin-mediated endocytosis inhibitor and decreased temperature on the accumulation of peptide under the cells.  
Figure S7. Intensity profiles and fitting parameters of sCT(C8/C8) through nucleus.  
Figure S8. Caco-2 cells incubated with 1  $\mu$ M of FITC-labelled TAT imaged after t = XX min .  
Figure S9. SD-LSCM images of Caco-2 cells incubated with each of the three analogues showing qualitative differences in the peptide signal.  
Figure S10. FCS - Characterization of the confocal detection volume using Alexa Fluor 488 hydrazide.  
Figure S11. FCS - Autocorrelation curves recorded for Atto 488-labeled analogues of sCT.  
Figure S12. FCS - Evaluation of the diffusion properties of the Atto 488-labeled analogues of sCT.  
Figure S13. Typical field-of-view of a sample used for stepwise bleaching.  
Figure S14. Example of photobleaching step analysis (PBSA) for a single spot.  
Figure S15. PBSA of sCal(C0/C0)-atto488 on a home-built TIRF.  
Figure S16. PBSA of sCal(C4/C4)-atto488 on a home-built TIRF.  
Figure S17. PBSA of sCal(C8/C8)-atto488 on a home-built TIRF.  
Figure S18. Size distribution of sCal(C0/C0)-atto488, sCal(C4/C4)-atto488 and sCal(C8/C8)-atto488 obtained by PBSA.  
Figure S19. Distribution of step size, background and total photon counts in the PBSA experiment.

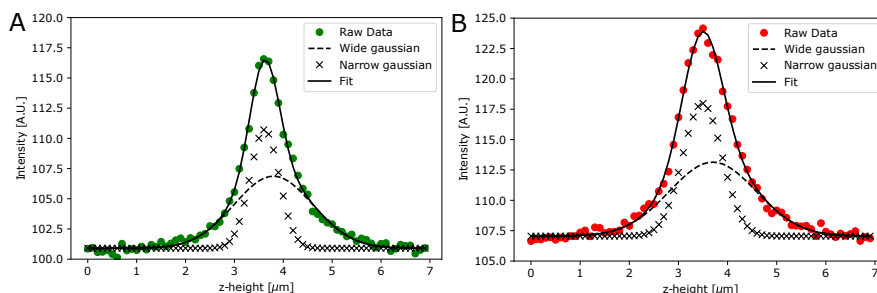


Figure S1. Spinning disc axial PSF measurement and fit for the 488nm and 640nm excitation. Axial PSF of the spinning disc microscope measurement on a single 100-nm bead at 488nm excitation (A) and 640 nm excitation (B).

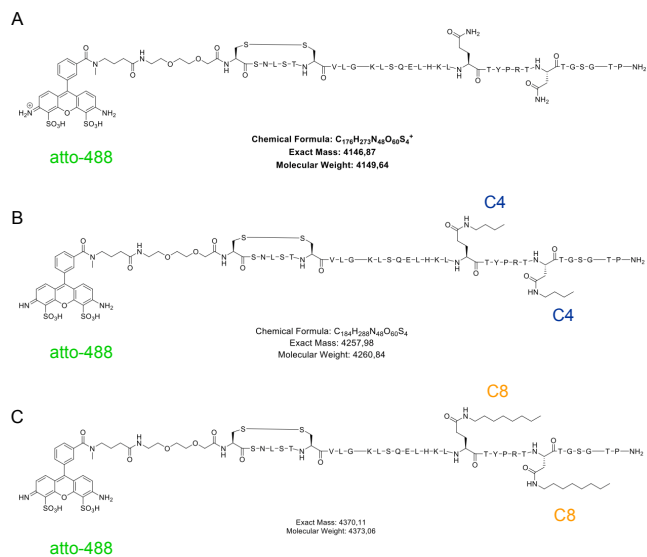


Figure S2. Chemical structure of the Salmon Calcitonin analogs labelled with atto-488. A) sCT(C0/C0), B) sCT(C4/C4) and C) sCT(C8/C8).

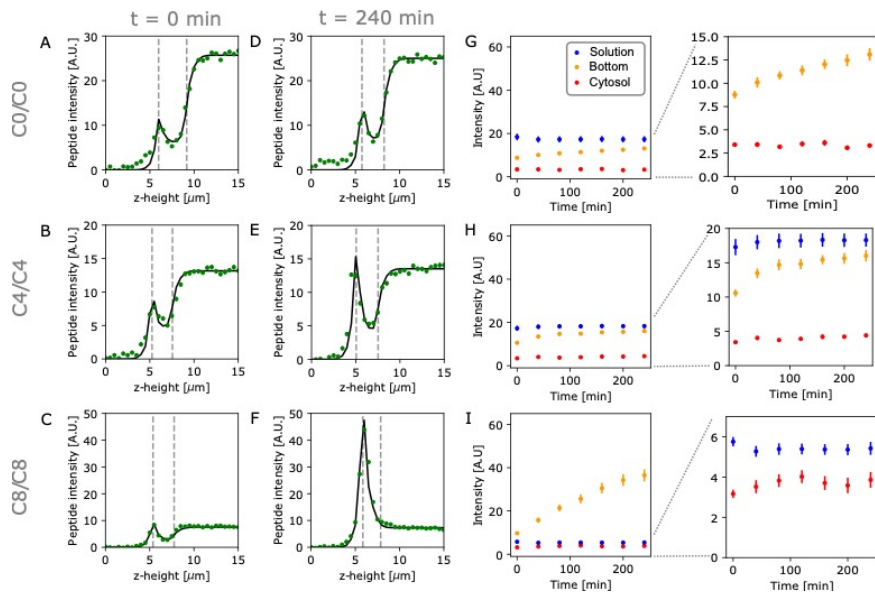


Figure S3. Single ROI intensity profiles in the peptide channel for the SCT analogs. A - C) at  $t = 0$  min D-F) at  $t = 240$  min. G-I) Fitted parameters over time for each of the peptide sCT(C0/C0), sCT(C4/C4) and sCT(C8/C8). Orange data points represent the peptide signal at the bottom of the cells. Panels to the right shows a zoom in of the same data at low intensities.

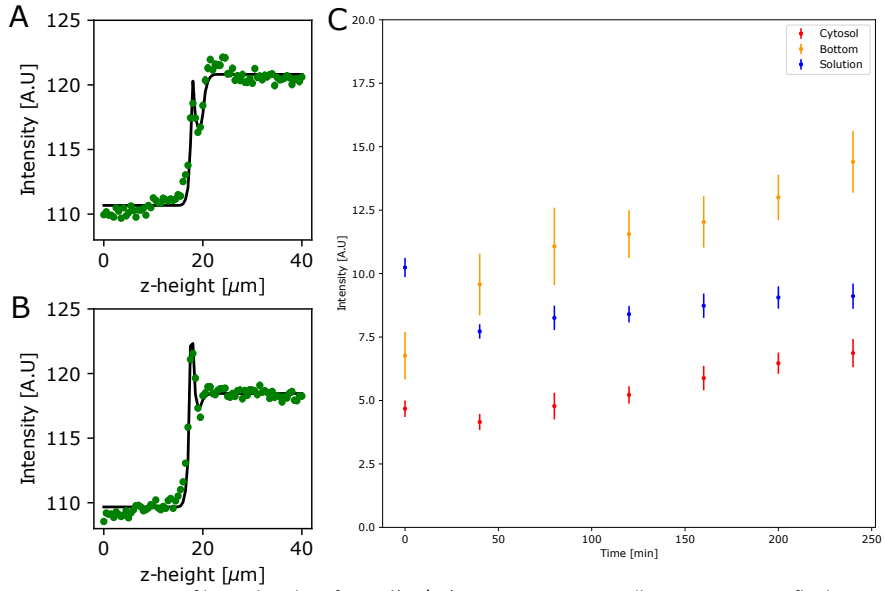


Figure S4 Intensity profiles and analysis for sCal(C8/C8)-atto488 on Caco-2 cells grown in a microfluidic platform. A) Intensity profile at  $t = 0$  min for a single ROI, right after adding sCal(C8/C8)-atto488 to the solution. B) same ROI but at  $t = 240$  minutes. C) Summary of the fitted parameters over time for  $N = 9$  cells. Error bars are the s.e.m.

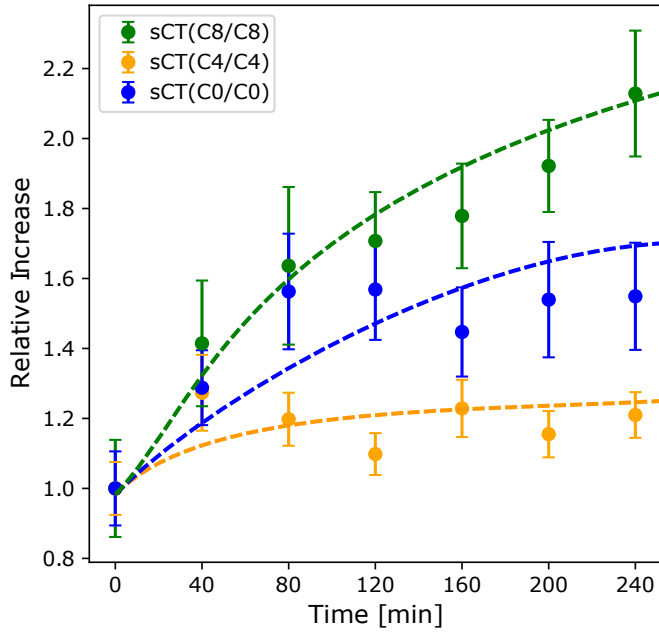


Figure S5 Relative increase of peptide signal at the bottom of the cells measured on fully polarized cells in a microfluidic platform. The blue data points shows the sCT(C0/C0) on N = 16 cells, the orange data points shows the data for sCT(C4/C4) on N = 17 cells and the green data points shows sCT(C8/C8) for N = 9 cells (see Figure S4). Error bars are standard error on the mean (s.e.m). Dashed lines are guide to the eye.

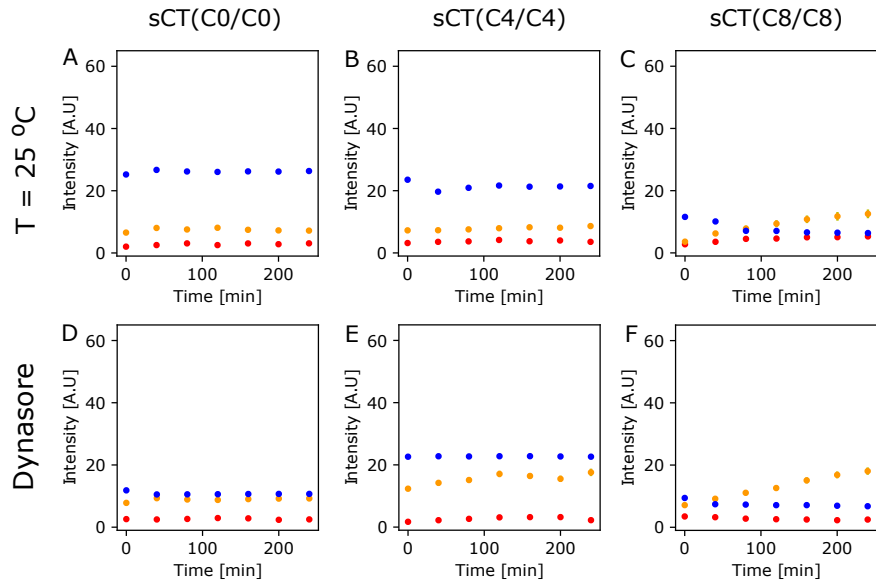


Figure S6 Effects of decreased temperature and addition of the clathrin-mediated endocytosis inhibitor Dynasore on the peptide signal. A) Shows the transport of sCal(C0/C0) at 25 degrees with no transport seen. B) Shows the increase of sCal(C4/C4) at 25 degrees showing a very slight increase over time. C) Shows the transport of sCal(C8/C8) at 25 degrees. The peptide is clearly transported through the and increases steadily. D) Should show the data for sCal(C0/C0) with dynasore added. No transport of sCal(C0/C0)-atto488 is observed. E) Shows the uptake of sCal(C4/C4) in the presence of the inhibitor dynasore. The addition of the inhibitor does not seem to change the uptake of sCal(C4/C4). F) Shows the uptake of sCal(C8/C8) in the presence of dynasore. The peptide is still transported through the cells, however no as much as without the inhibitor.

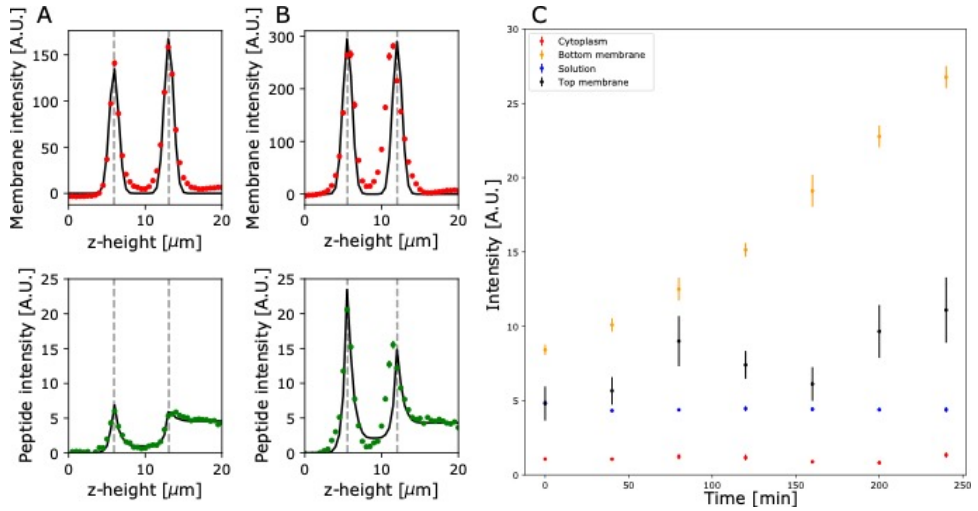


Figure S7 Intensity profiles sampled through the nucleus and fit. A) the membrane and peptide intensity profile in red and green, respectively, just after adding sCT(C8/C8). Black line is the fit to the intensity profile. The model of the peptide channel includes a PSF-like peak at the top membrane. B) shows the same cell at t = 240 minutes. C) The four parameters extracted from the peptide channel fit: the peptide signal at the bottom of the cells, the peptide intensity level inside the cell, peptide signal at the top membrane of the cell and the solution level. Data shows the mean and the s.e.m for N = 9 cells.

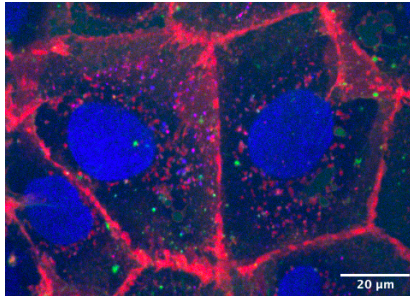


Figure S8 Caco-2 cells incubated with 1  $\mu\text{M}$  of TAT-FITC and imaged after t = XX min . TAT-FITC is taken up by the cell through endocytosis (green dots). Further more a diffusive signal is also observed in the cytosol of the cells. The cell membrane and nucleus are shown in red and blue respectively.

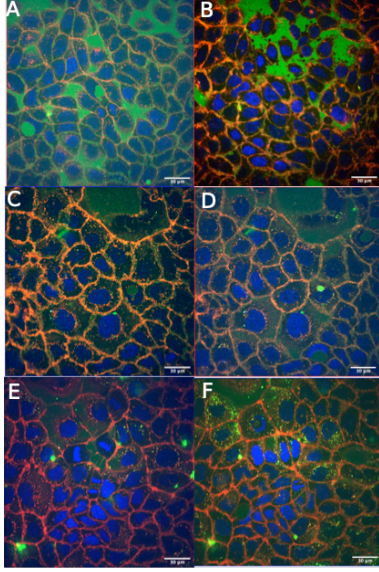


Figure S9. Images of Caco-2 cells incubated with each of the three sCT analogues showing qualitative differences in the peptide signal. Each image single slice images at  $z = 17 \mu\text{m}$  from starting acquisition. A: sCal(C0/C0)-atto488 at  $t = 0 \text{ min}$  and B: same at  $t = 240 \text{ min}$ . C: sCal(C4/C4)-atto488 at  $t = 0 \text{ min}$  and D: Same at  $t = 240 \text{ min}$ . E: sCal(C8/C8)-atto488 at  $t = 0 \text{ min}$  and F: Same at  $t = 240 \text{ min}$ .

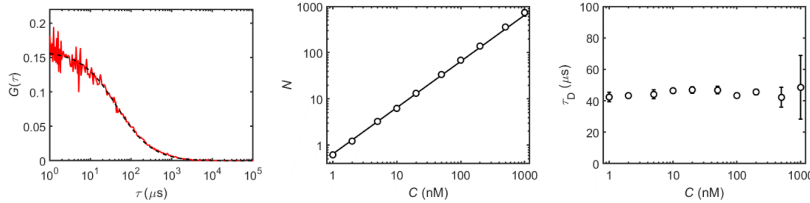


Figure S10. Characterization of the confocal detection volume using Alexa Fluor 488 hydrazide. (Left) Autocorrelation curve recorded from 10 nM Alexa Fluor 488. The dashed lined shows the best fit of Equation 1. (Middle) Particle concentration in the detection volume as a function of the Alexa Fluor 488 molar concentration. (Right) Diffusion time as a function of the Alexa Fluor 488 molar concentration. The data were generally recorded with a 1 min acquisition time, except for concentrations  $\geq 500 \text{ nM}$ , which were recorded with a 5 min acquisition time. Also, the data  $\geq 200 \text{ nM}$  were recorded using a lower laser intensity to avoid overloading of the detector. Except for the left panel, the data are the average of three measurements. The error bars represent the standard deviation and are not shown if they are smaller than the symbols.



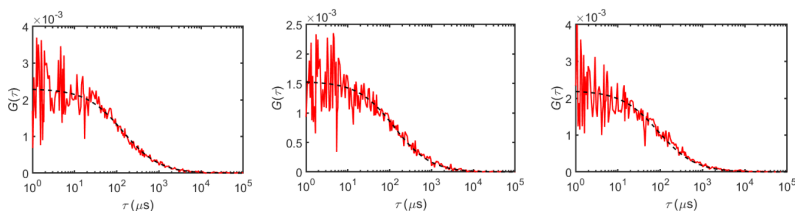


Figure S11. Autocorrelation curves recorded for Atto 488-labeled analogues of sCT. (Left) Native sCT. (Middle) C4/C4-modified sCT. (Right) C8/C8-modified sCT. The curves were recorded using an acquisition time of 5 min. The dashed black line shows the best fit of Equation 1.

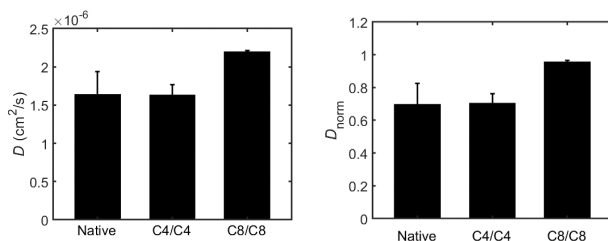


Figure S12. FCS evaluation of the diffusion properties of the Atto 488-labeled analogues of sCT. (Left) Estimated diffusion coefficients. (Right) Estimated diffusion coefficient normalized to those expected for monomeric peptides.

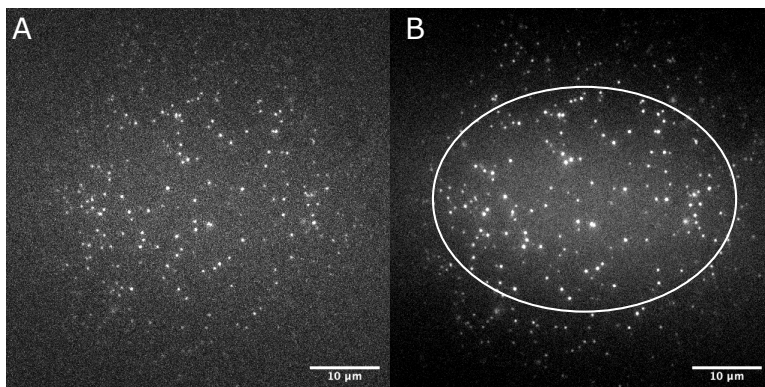


Figure S13. Typical field-of-view of a sample used for stepwise bleaching. A) The first frame of a sample with sCal(C4/C4)-atto488. B) Average of the 10 first frames of the same field of view as in A. The white circle indicates spots eligible for analysis.

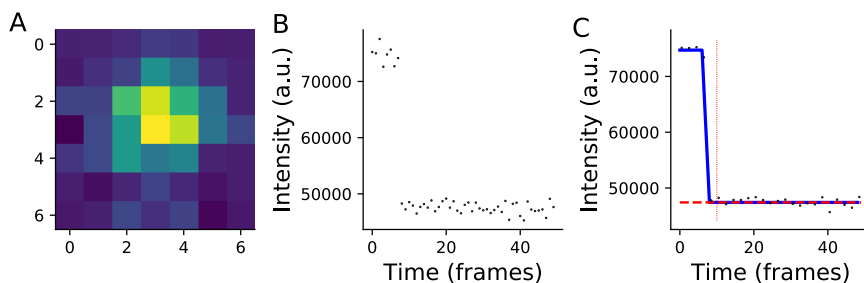


Figure S14. Analysis of the stepwise bleaching experiment. Upper left shows the raw intensity trace of the spot seen in the upper right image. The lower graph shows the results of the analysis with the number of steps and step size found in the analysis.

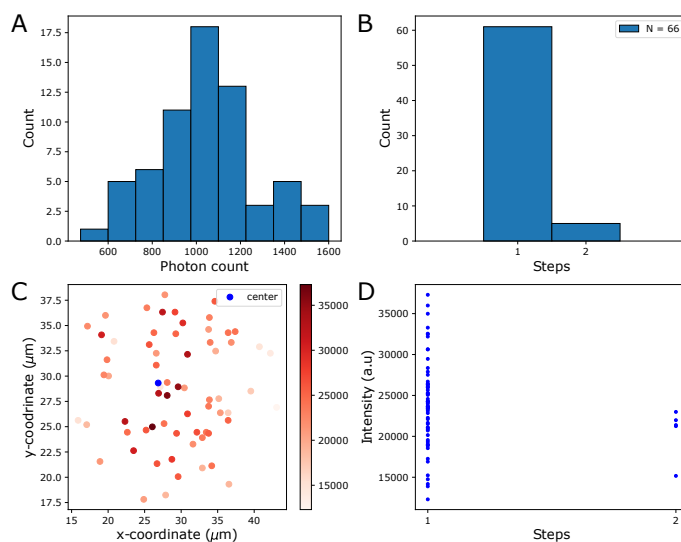


Figure S15. Result of analysis of all N=66 spots for sCal(C0/C0)-atto488 on homebuilt TIRF. A) shows the distribution of photons emitted from the peptides. B) shows the number of steps found for all peptide spots. C) shows the intensity of the spots as a function of the distance to the center of illumination. D) shows the intensity of the spots as a function of number of steps.

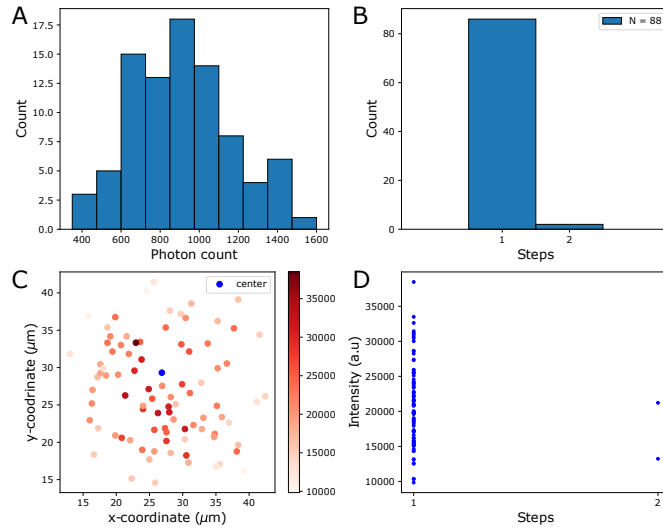


Figure S16. Result of analysis of all N=88 spots for sCal(C4/C4)-atto488 imaged on homebuilt TIRF. A) shows the distribution of photons emitted from the peptides. B) shows the number of steps found for all peptide spots. C) shows the intensity of the spots as a function of the distance to the center of illumination. D) shows the intensity of the spots as a function of number of steps.

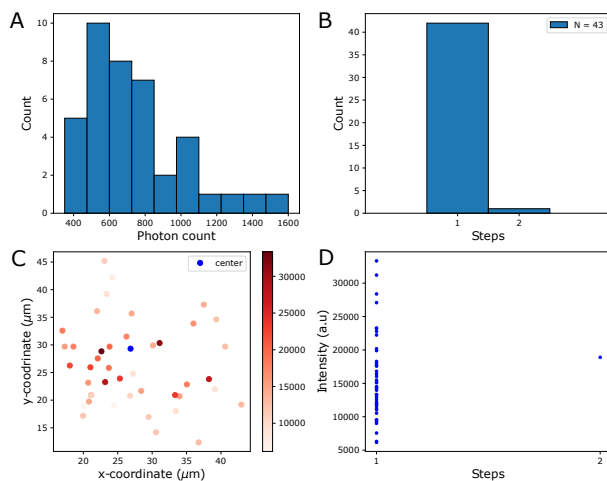


Figure S17. Result of analysis of all N=43 spots for sCal(C8/C8)-atto488 on homebuilt TIRF. A) shows the distribution of photons emitted from the peptides. B) shows the number of steps found for all peptide spots. C) shows the intensity of the spots as a function of the distance to the center of illumination. D) shows the intensity of the spots as a function of number of steps.

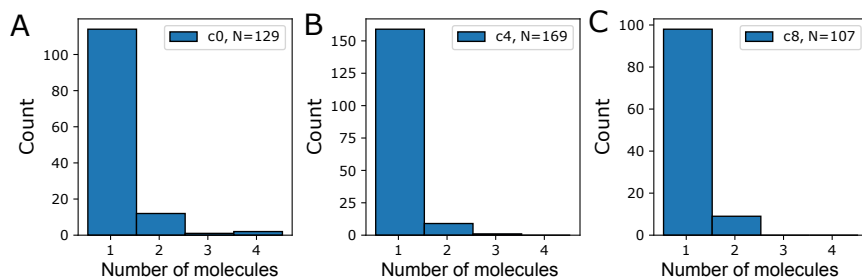


Figure S18. Size distribution of sCal(C0/C0)-atto488, sCal(C4/C4)-atto488 and sCal(C8/C8)-atto488.

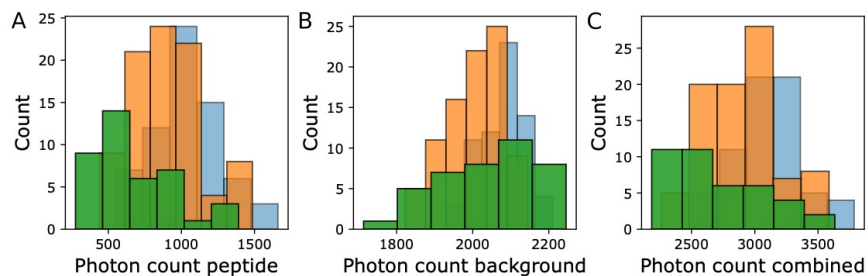


Figure S19. Distribution of step size, background and total photon counts for sCal(C0/C0)-atto488 (blue), sCal(C4/C4)-atto488 (orange) and sCal(C8/C8)-atto488 (green).

# Bibliography

---

- [1] M. Schmidt, A. C. Hundahl, H. Flyvbjerg, R. Marie, and K. I. Mortensen, “Camera-based localization microscopy optimized with calibrated structured illumination,” *Communications Physics*, vol. 4, no. 1, pp. 1–10, 2021.
- [2] S. Mitragotri, P. A. Burke, and R. Langer, “Overcoming the challenges in administering biopharmaceuticals: Formulation and delivery strategies,” *Nature Reviews Drug Discovery*, vol. 13, no. 9, pp. 655–672, 2014.
- [3] P. Hinderliter and S. A. Saghir, “Pharmacokinetics,” *Encyclopedia of Toxicology: Third Edition*, vol. 3, pp. 849–855, 2014.
- [4] M. W. Tibbitt, J. E. Dahlman, and R. Langer, “Emerging Frontiers in Drug Delivery,” *Journal of the American Chemical Society*, vol. 138, no. 3, pp. 704–717, 2016.
- [5] A. C. Anselmo, Y. Gokarn, and S. Mitragotri, “Non-invasive delivery strategies for biologics,” *Nature Reviews Drug Discovery*, vol. 18, no. 1, pp. 19–40, 2018.
- [6] R. Ismail and I. Csóka, “Novel strategies in the oral delivery of antidiabetic peptide drugs – Insulin, GLP 1 and its analogs,” *European Journal of Pharmaceutics and Biopharmaceutics*, vol. 115, pp. 257–267, 2017.
- [7] J. Renukuntla, A. D. Vadlapudi, A. Patel, S. H. Boddu, and A. K. Mitra, “Approaches for enhancing oral bioavailability of peptides and proteins,” *International Journal of Pharmaceutics*, vol. 447, no. 1-2, pp. 75–93, 2013.
- [8] M. Kataoka, M. Fukahori, A. Ikemura, A. Kubota, H. Higashino, S. Sakuma, and S. Yamashita, “Effects of gastric pH on oral drug absorption: In vitro assessment using a dissolution/permeation system reflecting the gastric dissolution process,” *European Journal of Pharmaceutics and Biopharmaceutics*, vol. 101, pp. 103–111, 2016.
- [9] J. R. Turner, “Intestinal mucosal barrier function in health and disease,” *Nature Reviews Immunology*, vol. 9, no. 11, pp. 799–809, 2009.
- [10] K. R. Groschwitz and S. P. Hogan, “Intestinal barrier function: Molecular regulation and disease pathogenesis,” *Journal of Allergy and Clinical Immunology*, vol. 124, no. 1, pp. 3–20, 2009.

- [11] A. Fedi, C. Vitale, G. Ponschin, S. Ayehunie, M. Fato, and S. Scaglione, "In vitro models replicating the human intestinal epithelium for absorption and metabolism studies: A systematic review," *Journal of Controlled Release*, vol. 335, pp. 247–268, 2021.
- [12] S. Fowler, W. L. K. Chen, D. B. Duignan, A. Gupta, N. Hariparsad, J. R. Kenny, W. G. Lai, J. Liras, J. A. Phillips, and J. Gan, "Microphysiological systems for adme-related applications: current status and recommendations for system development and characterization," *Lab Chip*, vol. 20, pp. 446–467, 2020.
- [13] D. Manzanares and V. Ceña, "Endocytosis: The nanoparticle and submicron nanocompounds gateway into the cell," *Pharmaceutics*, vol. 12, no. 4, pp. 1–22, 2020.
- [14] H. T. McMahon and E. Boucrot, "Molecular mechanism and physiological functions of clathrin-mediated endocytosis," *Nature reviews Molecular cell biology*, vol. 12, no. 8, pp. 517–533, 2011.
- [15] D. J. Drucker, "Advances in oral peptide therapeutics," *Nature Reviews Drug Discovery*, vol. 19, no. 4, pp. 277–289, 2020.
- [16] S. Verma, U. K. Goand, A. Husain, R. A. Katekar, R. Garg, and J. R. Gayen, "Challenges of peptide and protein drug delivery by oral route: Current strategies to improve the bioavailability," *Drug Development Research*, vol. 82, no. 7, pp. 927–944, 2021.
- [17] J. M. Harris and R. B. Chess, "Effect of pegylation on pharmaceuticals," *Nature reviews Drug discovery*, vol. 2, no. 3, pp. 214–221, 2003.
- [18] R. G. Diedrichsen, S. Harloff-Helleberg, U. Werner, M. Besenius, E. Leberer, M. Kristensen, and H. M. Nielsen, "Revealing the importance of carrier-cargo association in delivery of insulin and lipidated insulin," *Journal of Controlled Release*, vol. 338, pp. 8–21, 2021.
- [19] R. Menacho-Melgar, J. S. Decker, J. N. Hennigan, and M. D. Lynch, "A review of lipidation in the development of advanced protein and peptide therapeutics," *Journal of Controlled Release*, vol. 295, pp. 1–12, 2019.
- [20] S. Trier, L. Linderroth, S. Bjerregaard, H. M. Strauss, U. L. Rahbek, and T. L. Andresen, "Acylation of salmon calcitonin modulates in vitro intestinal peptide flux through membrane permeability enhancement," *European Journal of Pharmaceutics and Biopharmaceutics*, vol. 96, pp. 329–337, 2015.
- [21] I. Behrens, P. Stenberg, P. Artursson, and T. Kissel, "Transport of lipophilic drug molecules in a new mucus-secreting cell culture model based on HT29-MTX cells," *Pharmaceutical Research*, vol. 18, no. 8, pp. 1138–1145, 2001.

- [22] Y. Yang, Y. Zhao, A. Yu, D. Sun, and L. X. Yu, "Oral drug absorption: Evaluation and prediction," *Developing Solid Oral Dosage Forms: Pharmaceutical Theory and Practice: Second Edition*, pp. 331–354, 2017.
- [23] S. McClean, E. Prosser, E. Meehan, D. O'Malley, N. Clarke, Z. Ramtoola, and D. Brayden, "Binding and uptake of biodegradable poly-DL-lactide micro- and nanoparticles in intestinal epithelia," *European Journal of Pharmaceutical Sciences*, vol. 6, no. 2, pp. 153–163, 1998.
- [24] V. Gupta, N. Doshi, and S. Mitragotri, "Permeation of Insulin, Calcitonin and Exenatide across Caco-2 Monolayers: Measurement Using a Rapid, 3-Day System," *PLoS ONE*, vol. 8, no. 2, 2013.
- [25] A. Sánchez, A. Calpena, M. Mallandrich, and Clares, "Validation of an ex vivo permeation method for the intestinal permeability of different bcs drugs and its correlation with caco-2 in vitro experiments," *Pharmaceutics*, vol. 11, p. 638, 11 2019.
- [26] D. Birch, R. G. Diedrichsen, P. C. Christophersen, H. Mu, and H. M. Nielsen, "Evaluation of drug permeation under fed state conditions using mucus-covered Caco-2 cell epithelium," *European Journal of Pharmaceutical Sciences*, vol. 118, no. January, pp. 144–153, 2018.
- [27] H. J. Je, E. S. Kim, J. S. Lee, and H. G. Lee, "Release Properties and Cellular Uptake in Caco-2 Cells of Size-Controlled Chitosan Nanoparticles," *Journal of Agricultural and Food Chemistry*, vol. 65, no. 50, pp. 10899–10906, 2017.
- [28] X. Liu, S. Zheng, Y. Qin, W. Ding, Y. Tu, X. Chen, Y. Wu, L. Yanhua, and X. Cai, "Experimental evaluation of the transport mechanisms of PoIFN- $\alpha$  in Caco-2 cells," *Frontiers in Pharmacology*, vol. 8, no. NOV, pp. 1–11, 2017.
- [29] C. Thompson, W. P. Cheng, P. Gadad, K. Skene, M. Smith, G. Smith, A. McKinnon, and R. Knott, "Uptake and transport of novel amphiphilic polyelectrolyte-insulin nanocomplexes by caco-2 cells-towards oral insulin," *Pharmaceutical Research*, vol. 28, no. 4, pp. 886–896, 2011.
- [30] C. Zimmermann, S. Rudloff, G. Lochnit, S. Arampatzi, W. Maison, and K. P. Zimmer, "Epithelial transport of immunogenic and toxic gliadin peptides in vitro," *PLoS ONE*, vol. 9, no. 11, pp. 1–17, 2014.
- [31] J. Capoulade, M. Wachsmuth, L. Hufnagel, and M. Knop, "Quantitative fluorescence imaging of protein diffusion and interaction in living cells," *Nature Biotechnology*, vol. 29, no. 9, pp. 835–839, 2011.
- [32] E. Abbe, "Beiträge zur theorie des mikroskops und der mikroskopischen wahrnehmung," *Archiv f. mikrosk. Anatomie*, vol. 9, pp. 413–468, 12 1873.



- [33] P. A. Shamlou, L. H. Breen, W. V. Bell, M. Pollo, and B. A. Thomas, "A new scaleable freeze-thaw technology for bulk protein solutions," *Biotechnology and Applied Biochemistry*, vol. 46, no. 1, pp. 13–26, 2007.
- [34] R. Rabkin, T. I. Gottheiner, and V. S. Fang, "Removal and excretion of immunoreactive rat growth hormone by the isolated kidney," *American Journal of Physiology-Renal Physiology*, vol. 240, no. 4, pp. F282–F287, 1981. PMID: 7013498.
- [35] M. J. Rust, M. Bates, and X. Zhuang, "Sub-diffraction-limit imaging by stochastic optical reconstruction microscopy (storm)," *Nature methods*, vol. 3, no. 10, pp. 793–796, 2006.
- [36] M. Heilemann, S. Van De Linde, M. Schüttelpelz, R. Kasper, B. Seefeldt, A. Mukherjee, P. Tinnefeld, and M. Sauer, "Subdiffraction-resolution fluorescence imaging with conventional fluorescent probes," *Angewandte Chemie International Edition*, vol. 47, no. 33, pp. 6172–6176, 2008.
- [37] E. Betzig, G. H. Patterson, R. Sougrat, O. W. Lindwasser, S. Olenych, J. S. Bonifacino, M. W. Davidson, J. Lippincott-Schwartz, and H. F. Hess, "Imaging intracellular fluorescent proteins at nanometer resolution," *science*, vol. 313, no. 5793, pp. 1642–1645, 2006.
- [38] S. T. Hess, T. P. Girirajan, and M. D. Mason, "Ultra-high resolution imaging by fluorescence photoactivation localization microscopy," *Biophysical journal*, vol. 91, no. 11, pp. 4258–4272, 2006.
- [39] J. S. Biteen, M. A. Thompson, N. K. Tselentis, G. R. Bowman, L. Shapiro, and W. Moerner, "Super-resolution imaging in live *caulobacter crescentus* cells using photoswitchable eyfp," *Nature methods*, vol. 5, no. 11, pp. 947–949, 2008.
- [40] K. I. Mortensen, L. S. Churchman, J. A. Spudich, and H. Flyvbjerg, "Optimized localization analysis for single-molecule tracking and super-resolution microscopy," *Nature methods*, vol. 7, no. 5, pp. 377–381, 2010.
- [41] M. G. Gustafsson, "Surpassing the lateral resolution limit by a factor of two using structured illumination microscopy," *Journal of microscopy*, vol. 198, no. 2, pp. 82–87, 2000.
- [42] R. Heintzmann and C. G. Cremer, "Laterally modulated excitation microscopy: improvement of resolution by using a diffraction grating," in *Optical biopsies and microscopic techniques III*, vol. 3568, pp. 185–196, SPIE, 1999.
- [43] D. Li, L. Shao, B.-C. Chen, X. Zhang, M. Zhang, B. Moses, D. E. Milkie, J. R. Beach, J. A. Hammer III, M. Pasham, *et al.*, "Extended-resolution structured illumination imaging of endocytic and cytoskeletal dynamics," *Science*, vol. 349, no. 6251, p. aab3500, 2015.

- [44] L. Schermelleh, A. Ferrand, T. Huser, C. Eggeling, M. Sauer, O. Biehlmaier, and G. P. Drummen, "Super-resolution microscopy demystified," *Nature cell biology*, vol. 21, no. 1, pp. 72–84, 2019.
- [45] N. P. Wells, G. A. Lessard, P. M. Goodwin, M. E. Phipps, P. J. Cutler, D. S. Lidke, B. S. Wilson, and J. H. Werner, "Time-resolved three-dimensional molecular tracking in live cells," *Nano letters*, vol. 10, no. 11, pp. 4732–4737, 2010.
- [46] K. Welsher and H. Yang, "Multi-resolution 3d visualization of the early stages of cellular uptake of peptide-coated nanoparticles," *Nature nanotechnology*, vol. 9, no. 3, pp. 198–203, 2014.
- [47] F. Balzarotti, Y. Eilers, K. C. Gwosch, A. H. Gynnå, V. Westphal, F. D. Stefani, J. Elf, and S. W. Hell, "Nanometer resolution imaging and tracking of fluorescent molecules with minimal photon fluxes," *Science*, vol. 355, no. 6325, pp. 606–612, 2017.
- [48] K. C. Gwosch, J. K. Pape, F. Balzarotti, P. Hoess, J. Ellenberg, J. Ries, and S. W. Hell, "Minflux nanoscopy delivers 3d multicolor nanometer resolution in cells," *Nature methods*, vol. 17, no. 2, pp. 217–224, 2020.
- [49] R. Schmidt, T. Weihs, C. A. Wurm, I. Jansen, J. Rehman, S. J. Sahl, and S. W. Hell, "Minflux nanometer-scale 3d imaging and microsecond-range tracking on a common fluorescence microscope," *Nature communications*, vol. 12, no. 1, pp. 1–12, 2021.
- [50] L. Reymond, T. Huser, V. Ruprecht, and S. Wieser, "Modulation-enhanced localization microscopy," *Journal of Physics: Photonics*, vol. 2, p. 041001, jul 2020.
- [51] L. Gu, Y. Li, S. Zhang, Y. Xue, W. Li, D. Li, T. Xu, and W. Ji, "Molecular resolution imaging by repetitive optical selective exposure," *Nature Methods*, vol. 16, no. 11, pp. 1114–1118, 2019.
- [52] L. Reymond, J. Ziegler, C. Knapp, F.-C. Wang, T. Huser, V. Ruprecht, and S. Wieser, "SIMPLE: Structured illumination based point localization estimator with enhanced precision," *Optics Express*, vol. 27, no. 17, p. 24578, 2019.
- [53] J. Cnossen, T. Hinsdale, R. Thorsen, M. Siemons, F. Schueder, R. Jungmann, C. S. Smith, B. Rieger, and S. Stallinga, "Localization microscopy at doubled precision with patterned illumination," *Nature Methods*, vol. 17, no. 1, pp. 59–63, 2020.
- [54] M. Li, Y. Li, W. Liu, A. Lal, S. Jiang, D. Jin, H. Yang, S. Wang, K. Zhanghao, and P. Xi, "Structured illumination microscopy using digital micro-mirror device and coherent light source," *Applied Physics Letters*, vol. 116, no. 23, p. 233702, 2020.

- [55] M. M. Frigault, J. Lacoste, J. L. Swift, and C. M. Brown, "Live-cell microscopy - tips and tools," *J Cell Sci*, vol. 122, pp. 753–767, Mar 2009.
- [56] A. Ettinger and T. Wittmann, "Fluorescence live cell imaging," *Methods in cell biology*, vol. 123, pp. 77–94, 2014.
- [57] N. Vtyurina, C. Åberg, and A. Salvati, "Imaging of nanoparticle uptake and kinetics of intracellular trafficking in individual cells," *Nanoscale*, vol. 13, no. 23, pp. 10436–10446, 2021.
- [58] J. Jonkman, C. M. Brown, G. D. Wright, K. I. Anderson, and A. J. North, "Tutorial: guidance for quantitative confocal microscopy," *Nature Protocols*, vol. 15, no. 5, pp. 1585–1611, 2020.
- [59] J. Pawley, *Handbook of biological confocal microscopy*, vol. 236. Springer Science & Business Media, 2006.
- [60] A. Nakano, "Spinning-disk confocal microscopy mdash; a cutting-edge tool for imaging of membrane traffic," *Cell Structure and Function*, vol. 27, no. 5, pp. 349–355, 2002.
- [61] J. A. Conchello and J. W. Lichtman, "Optical sectioning microscopy," *Nature Methods*, vol. 2, no. 12, pp. 920–931, 2005.
- [62] J. A. Helmuth, C. J. Burckhardt, U. F. Greber, and I. F. Sbalzarini, "Shape reconstruction of subcellular structures from live cell fluorescence microscopy images," *Journal of Structural Biology*, vol. 167, no. 1, pp. 1–10, 2009.
- [63] E. M. Smith, J. Hennen, Y. Chen, and J. D. Mueller, "Z-scan fluorescence profile deconvolution of cytosolic and membrane-associated protein populations," *Analytical Biochemistry*, vol. 480, pp. 11–20, 2015.
- [64] P. Kner, B. B. Chhun, E. R. Griffis, L. Winoto, and M. G. L. Gustafsson, "Super-resolution video microscopy of live cells by structured illumination," *Nature Methods*, vol. 6, no. 5, pp. 339–342, 2009.
- [65] K. S. & T. Y. Takashi Funatsu, Yoshie Harada, Makio Tokunaga, "Imaging of single fluorescent molecules and individual ATP turnovers by single myosin molecules in aqueous solution," *Nature*, vol. 374, pp. 555–559, 1995.
- [66] Fish KN, "Total Internal Reflection Fluorescence (TIRF) Microscopy," *Curr Protoc Cytom.*, vol. 0, no. 12, p. Unit 12.18, 2009.
- [67] D. Axelrod, *Chapter 7 Total Internal Reflection Fluorescence Microscopy*, vol. 89. Elsevier Inc., 1 ed., 2008.

- [68] B.-C. Chen, W. R. Legant, K. Wang, L. Shao, D. E. Milkie, M. W. Davidson, C. Janetopoulos, X. S. Wu, J. A. Hammer III, Z. Liu, *et al.*, “Lattice light-sheet microscopy: imaging molecules to embryos at high spatiotemporal resolution,” *Science*, vol. 346, no. 6208, p. 1257998, 2014.
- [69] E. Collett, *Field Guide to Polarization*. Field Guides, Society of Photo Optical, 2005.
- [70] A. G. York, S. H. Parekh, D. D. Nogare, R. S. Fischer, K. Temprine, M. Mione, A. B. Chitnis, C. A. Combs, and H. Shroff, “Resolution doubling in live, multicellular organisms via multifocal structured illumination microscopy,” *Nature Methods*, vol. 9, no. 7, pp. 749–754, 2012.
- [71] L. Schermelleh, R. Heintzmann, and H. Leonhardt, “A guide to super-resolution fluorescence microscopy,” *Journal of Cell Biology*, vol. 190, no. 2, pp. 165–175, 2010.
- [72] A. R. Halpern, M. Y. Lee, M. D. Howard, M. A. Woodworth, P. R. Nicovich, and J. C. Vaughan, “Versatile, do-it-yourself, low-cost spinning disk confocal microscope,” *Biomed. Opt. Express*, vol. 13, pp. 1102–1120, Feb 2022.
- [73] A. Budó and I. Ketskeméty, “Influence of secondary fluorescence on the emission spectra of luminescent solutions,” *The Journal of Chemical Physics*, vol. 25, no. 3, pp. 595–596, 1956.
- [74] A. Betanzos, D. Zanatta, C. Bañuelos, E. Hernández-Nava, P. Cuellar, and E. Orozco, “Epithelial cells expressing ehadh, an entamoeba histolytica adhesin, exhibit increased tight junction proteins,” *Frontiers in Cellular and Infection Microbiology*, vol. 8, 2018.
- [75] H. Rastogi, J. Pinjari, P. Honrao, S. Praband, and R. Somani, “The impact of permeability enhancers on assessment for monolayer of colon adenocarcinoma cell line (caco-2) used in in vitro permeability assay,” *Journal of Drug Delivery and Therapeutics*, vol. 3, pp. 20–29, May 2013.
- [76] R. Brock, “The uptake of arginine-rich cell-penetrating peptides: Putting the puzzle together,” *Bioconjugate Chemistry*, vol. 25, no. 5, pp. 863–868, 2014.
- [77] M. A. Davis, “Hardware triggering: maximizing speed and efficiency for live cell imaging,” *Nature Methods*, vol. 14, no. 12, p. 1223, 2017.
- [78] K. Bittermann and K.-U. Goss, “Predicting apparent passive permeability of caco-2 and mdck cell-monolayers: A mechanistic model,” *PLOS ONE*, vol. 12, pp. 1–20, 12 2017.
- [79] W. J. Conover and R. L. Iman, “Multiple-comparisons procedures. informal report,” 2 1979.

- [80] B. J. Iacopetta and E. Morgan, "The kinetics of transferrin endocytosis and iron uptake from transferrin in rabbit reticulocytes," *Journal of Biological Chemistry*, vol. 258, no. 15, pp. 9108–9115, 1983.
- [81] J. Saraste, G. E. Palade, and M. G. Farquhar, "Temperature-sensitive steps in the transport of secretory proteins through the golgi complex in exocrine pancreatic cells," *Proceedings of the National Academy of Sciences*, vol. 83, no. 17, pp. 6425–6429, 1986.
- [82] W. F. Wolkers, H. Oldenhof, F. Tang, J. Han, J. Bigalk, and H. Sieme, "Factors affecting the membrane permeability barrier function of cells during preservation technologies," *Langmuir*, vol. 35, pp. 7520–7528, 06 2019.
- [83] E. Macia, M. Ehrlich, R. Massol, E. Boucrot, C. Brunner, and T. Kirchhausen, "Dynasore, a Cell-Permeable Inhibitor of Dynamin," *Developmental Cell*, vol. 10, no. 6, pp. 839–850, 2006.
- [84] M. H. Ulbrich and E. Y. Isacoff, "Subunit counting in membrane-bound proteins," *Nature Methods*, vol. 4, no. 4, pp. 319–321, 2007.
- [85] B. E. Snaar-Jagalska, A. Cambi, T. Schmidt, and S. De Keijzer, *Single-molecule imaging technique to study the dynamic regulation of gpcr function at the plasma membrane*, vol. 521. Elsevier Inc., 1 ed., 2013.
- [86] S. Watanabe, T. Takahashi, and K. Bennett, "Quantitative evaluation of the accuracy and variance of individual pixels in a scientific CMOS (sCMOS) camera for computational imaging," *Single Molecule Spectroscopy and Superresolution Imaging X*, vol. 10071, p. 100710Z, 2017.
- [87] S. J. Trietsch, E. Naumovska, D. Kurek, M. C. Setyawati, M. K. Vormann, K. J. Wilschut, H. L. Lanz, A. Nicolas, C. P. Ng, J. Joore, S. Kustermann, A. Roth, T. Hankemeier, A. Moisan, and P. Vulto, "Membrane-free culture and real-time barrier integrity assessment of perfused intestinal epithelium tubes," *Nature Communications*, vol. 8, no. 1, pp. 1–7, 2017.